Generalisation of the Cumulants of Flow Amplitudes to the higher orders

Cindy Mordasini

Technische Universität München
Fakultät für Physik
Dense and Strange Hadronic Matter (E62)

Technische Universität München
Fakultät für Physik
Dense and Strange Hadronic Matter (E62)

Generalisation of the Cumulants of Flow Amplitudes to the higher orders

Cindy Victorine Simone Mordasini

Vollständiger Abdruck der von der Fakultät für Physik der Technischen Universität München zur Erlangung des akademischen Grades eines

Doktors der Naturwissenschaften (Dr. rer. nat.)

genehmigten Dissertation.

Vorsitzender:	apl. Prof. Dr. Norbert Kaiser
Prüfer der Dissertation:	1. TUM Junior Fellow Ante Bilandzic, Ph.D.
	2. Prof. Dr. Bastian Märkisch

Die Dissertation wurde am 15.02.2021 bei der Technischen Universität München eingereicht und durch die Fakultät für Physik am 01.04.2021 angenommen.

Here, on the edge of what we know,
in contact with the ocean of the unknown,
shines the mystery and beauty of the world.
And it's breathtaking.
Carlo Rovelli

Abstract

The collective behaviour of the particles produced in ultra-relativistic heavy-ion collisions is one of the probes used to study the properties of the created quark–gluon plasma (QGP), a state of strongly interacting matter characterised by deconfined quarks and gluons. Studies on the hydrodynamic response of the QGP to the initial state anisotropies, known as the anisotropic flow phenomenon, have allowed the determination of some of its transport properties, like the ratio of its shear viscosity over entropy density η/s. The observation that its value must be low to explain the experimental results has shown that QGP is one of the most perfect liquids found until now.

Anisotropic flow analyses have benefited from the development of the multiparticle correlations techniques, followed by the introduction of the formalism of uni- and multivariate cumulants. Extensive measurements for various centre of mass energies and collision systems have shown the necessity to study not only the flow amplitudes and symmetry planes but also the genuine correlations that may exist between different harmonics.

This work presents the mathematical formalism used in the generalisation of the Symmetric Cumulants (SCs), observables initially developed to probe the genuine correlations between two flow amplitudes v_m and v_n, to three and more flow amplitudes. This latter choice results in the development of a new and alternative approach for flow analyses, where the flow amplitudes squared are directly used as fundamental observables in cumulant expansion. This method is qualified of "alternative" as the flow observables were previously defined using the azimuthal angles and single-event averages in the cumulant expansions. The presented toy Monte Carlo simulations check the different required properties of multivariate cumulants and ensure the validity of this novel approach. The robustness of these observables to few-particle nonflow correlations is furthermore verified with the help of the HIJING event generator.

These generalised SCs are then used to measure experimentally for the first time the event-by-event genuine correlations between three distinct flow amplitudes in Pb–Pb collisions at $\sqrt{s_{\mathrm{NN}}} = 2.76$ TeV with the ALICE data recorded in 2010. Comparisons with model predictions show the development of genuine correlations between v_2, v_3 and v_4 during the hydrodynamic evolution of the QGP. The same phenomenon is also hinted with the measurements of such correlations between v_2, v_3 and v_5, with the additional potential to learn more about the non-linear response of v_5 from v_2 and v_3. The results for $\mathrm{SC}(2,4,6)$ and $\mathrm{SC}(3,4,5)$ indicate an absence of genuine correlations between the concerned amplitudes. Besides, all these measurements carry additional and independent constraints for the parametrization of the theoretical models.

Finally, the alternative approach developed for the higher order SCs is applied to the case of the genuine correlations between distinct moments of the flow amplitudes. Toy Monte Carlo and HIJING studies are used to control the validity of this extension to the Asymmetric Cumulants (ACs). First predictions at the initial and final states for different combinations of the proposed two-harmonic ACs are also presented.

Zusammenfassung

Das kollektive Verhalten von Teilchen, die in ultrarelativistischen Schwerionen-Kollisionen erzeugt werden, ist eine der Sonden, die verwendet wird, um die Eigenschaften des erzeugten Quark-Gluon-Plasmas (QGP) zu untersuchen, einem Zustand stark wechselwirkender Materie, der durch freie Quarks und Gluonen gekennzeichnet ist. Studien über die hydrodynamische Reaktion des QGP auf Anfangszustandsanisotropien, bekannt als das Phänomen des anisotropen Flusses, haben die Bestimmung einiger seiner Transporteigenschaften ermöglicht, wie das Verhältnis seiner Scherviskosität zur Entropiedichte η/s. Die Beobachtung, dass sein Wert niedrig sein muss, um die experimentellen Ergebnisse zu erklären, hat gezeigt, dass QGP eine der perfektesten Flüssigkeiten ist, die bis jetzt gefunden wurden.

Anisotrope Flussanalysen haben von der Entwicklung der Mehrteilchen-Korrelations-Techniken profitiert, sowie von der Einführung des Formalismus der uni- und multivariaten Kumulanten. Umfangreiche Messungen bei verschiedenen Schwerpunktsenergien und in verschiedenen Kollisionssystemen haben die Notwendigkeit gezeigt, nicht nur die Flussamplituden und Symmetrieebenen zu untersuchen, sondern auch die echten Korrelationen, die zwischen verschiedenen Harmonischen bestehen können.

Diese Arbeit stellt den mathematischen Formalismus vor, der bei der Verallgemeinerung der Symmetrischen Kumulanten (SCs) verwendet wird, Observablen, die ursprünglich entwickelt wurden, um die echten Korrelationen zwischen zwei Flussamplituden v_m und v_n auf drei und mehr Flussamplituden zu untersuchen. Diese letztere Wahl führt zur Entwicklung eines neuen und alternativen Ansatzes für Flussanalysen, bei dem die quadrierten Flussamplituden direkt als fundamentale Observablen in der Kumulantenexpansion verwendet werden. Diese Methode ist als "alternativ" zu bezeichnen, da die Flussobservablen zuvor über die azimutalen Winkel und Einzelereignis-Mittelwerte in den Kumulantenexpansionen definiert wurden. Die vorgestellten vereinfachte Monte-Carlo-Simulationen überprüfen die verschiedenen erforderlichen Eigenschaften der multivariaten Kumulanten und gewährleisten die Gültigkeit dieses neuartigen Ansatzes. Die Robustheit dieser Observablen gegenüber Wenig-Teilchen-Nichtfluss-Korrelationen wird darüber hinaus mit Hilfe des HIJING-Ereignisgenerators verifiziert.

Diese verallgemeinerten SCs werden dann verwendet, um zum ersten Mal die echten Korrelationen zwischen drei verschiedenen Flussamplituden in Pb–Pb Kollisionen bei $\sqrt{s_{\mathrm{NN}}} = 2.76$ TeV mit den ALICE-Daten aus dem Jahr 2010 experimentell zu messen. Vergleiche mit Modellvorhersagen zeigen die Entwicklung von echten Korrelationen zwischen v_2, v_3 und v_4 während der hydrodynamischen Entwicklung des QGP. Das gleiche Phänomen wird auch bei den Messungen solcher Korrelationen zwischen v_2, v_3 und v_5 angedeutet, mit dem zusätzlichen Potenzial, mehr über die nicht-lineare Reaktion von v_5 aus v_2 und v_3 zu erfahren. Die Ergebnisse für SC$(2, 4, 6)$ und SC$(3, 4, 5)$ zeigen, dass es keine echten Korrelationen zwischen den betroffenen Amplituden gibt. Außerdem bringen alle diese Messungen zusätzliche und voneinander unabhängige Einschränkungen für die Parametrisierung der theoretischen Modelle.

Schließlich wird der alternative Ansatz, der für die SCs höhere Ordnung entwickelt wurde, auf den Fall der echten Korrelationen zwischen verschiedenen Momenten der Flussamplituden angewendet. Mit Hilfe von Monte-Carlo- und HIJING-Studien wird die Gültigkeit dieser Er-

weiterung auf die Asymmetrischen Kumulanten (ACs) überprüft. Erste Vorhersagen für die Anfangs- und Endzustände für verschiedene Kombinationen der vorgeschlagenen zweiharmonischen ACs werden ebenfalls vorgestellt.

Acknowledgements

"Behind every great thesis is a great team," could be the saying, as these results would have not seen the day without the help and support of many great people.

First of all, I would like to thank my supervisor, Dr. Ante Bilandzic, for the chance to explore the wonders of anisotropic flow and heavy-ion collisions. During these three years and in all the rocky situations we encountered (and there were quite a few of them), he has been there with his endless support and wide expertise of the topic. I am also incredibly grateful for all the useful tutorials and advice, our lengthy morning discussions about physics and work, and all the conferences and PhD schools I attended. My analysis would have not reached such levels without him, nor would I.

I would like to express my gratitude to Prof. Laura Fabbietti for her support. She showed me that nothing is impossible with work and passion. I also learned a lot from her strict criteria and great suggestions for high-quality presentations. I am proud to be part of her group and look forward to continue this journey here, in Munich.

Speaking about groups, I would like to address many thanks to the other core members of the MuPa "flow" group, Marcel Lesch, Laura Šerkšnytė and Seyed Farid Taghavi, for the enormous support and great discussions. Especially, a huge thanks to my colleague, "student" and great friend Marcel for all our chats and his excellent advice. I know our working duo is not done rocking the flow scene, and I cannot wait to see what next we will achieve together. A special thanks to my friend and fellow PhD student Laura for her unwavering help and stimulating exchanges. I would not be where I am today without her. And finally, a big thank you to Farid for answering all my sudden questions about models and flow, and for teaching me on the academic and research worlds.

I would like to give many deep thanks to the *Dense and Strange Hadronic Matter* group as well, for the amazing working atmosphere and all the fantastic moments both in Garching and in conferences. Special thanks to my coffee fellows Bernhard Hohlweger, Andreas Mathis and Dimitar Mihaylov, who took me under their wing and guided my first steps as a baby PhD student and young experimentalist in ALICE, and to Stefan Heckel for all the shared wisdom in heavy-ion physics and the fruitful discussions during our hot flavoured water breaks. I would like to thank also Petra Zweckinger and Sigrid Weichs for the immense help with all the administrative formalities.

I would like to highlight the contribution from the ALICE Collaboration for the feedback and help in this adventure with the higher order Symmetric Cumulants. The list is too long to name everyone, but I would like to acknowledge Davide Caffarri, Anthony Timmins and Panos Christakoglou for teaching me their wisdom concerning the Barlow test, and answering all my naïve questions with infinite patience. Many big thanks to Dong Jo Kim as well for the great help and without whom the full experimental reanalysis of the Symmetric Cumulants in an incredibly tight timeline would have not been possible at all.

This list would not be complete without mentioning all my friends and family in Switzerland, who never failed to prove me space–time does not matter when you care about someone. Their endless support always kept me on the right tracks to reach my goals, especially when I was stumbling and filled with doubts. Last but far from least, I would like to express my deepest gratitude to my mother, Christine. I do not have words strong enough to tell how much her love and never-ending support mean to me. I would have not come as far as I have without her and for that, I would like to dedicate her this thesis.

Contents

List of Figures

List of Tables

Chapter 1

Introduction

The Standard Model of particle physics (SM) is a theoretical model used to describe the properties of elementary particles and their interactions. Since its formulation in the 1970s, it is still successful as it can explain with a great precision numerous observables. It also allows the predictions of many particles and phenomena. However, the SM is not complete. As a start, it does not contain gravity — one of the four fundamental forces. Recent discoveries also indicate that the SM needs to be extended. For example, the observations of neutrino oscillations show that neutrinos must be massive particles, while SM neutrinos are massless. The Dark Matter and Dark Energy needed to explain the respectively 26% and 69% unknown parts of the Universe are also absent from the SM. All the theories trying to explain these phenomena are gathered under the name of *Physics beyond the Standard Model*. The SM is a minimal model, meaning it contains only the particles needed for its consistency [1]. Figure 1.1 presents an overview of this particle content. This includes twelve fermions (and their corresponding antifermions), four gauge bosons, and the Higgs boson [2–4]. The latter is a spin 0 particle and one of the essential elements of the SM. It was introduced to explain the origin of the mass of all particles. Its first experimental observation by ATLAS and CMS in 2012 [5, 6] contributed further to the success of the SM.

The fermions of spin 1/2 are classified into two groups: the quarks and the leptons. Quarks can have one of the six following flavours: up (u), charm (c), top (t), down (d), strange (s) and bottom (b). The first three have a positive electric charge of $2/3$ of the elementary charge, while the last three have a negative charge of $-1/3$ of the elementary charge. For the leptons, three flavours with an electric charge of -1 can be distinguished: the electron (e), the muon (μ) and the tau (τ). Each one of them has an associated chargeless and massless neutrino. Additionally, the fermions are divided into three generations, also called families, formed with two quarks (a positive one and a negative one), one charged lepton and its corresponding neutrino.

The SM is a local quantum field theory (QFT). It has the gauge symmetry $SU(3)_C \otimes SU(2)_L \otimes U(1)_Y$ [1]. $SU(3)_C$ corresponds to the group associated with the strong interaction with the colour charge. $SU(2)_L \otimes U(1)_Y$ represents the reunion of the electromagnetic and weak forces, where the index L stands for the participation of the left-handed fermions in the weak interaction and Y for the hypercharge. These three fundamental forces — strong, weak and electromagnetic — are all mediated with spin 1 bosons. In QFT, these bosons can be identified with the generators of the corresponding groups. Therefore, for each interaction, their number is equal to the number of generators. The weak interaction acts on all fermions with the exchange of the $W^{\pm}$ and Z^0 bosons. Because of the masses of the carriers, the weak force is short-ranged and act only at distances smaller than the size of the nucleons. Electrically charged particles can interact through electromagnetism. Its neutral mediator, the photon γ, has no rest mass. This implies that the electromagnetic force is long-ranged. The third fundamental interaction

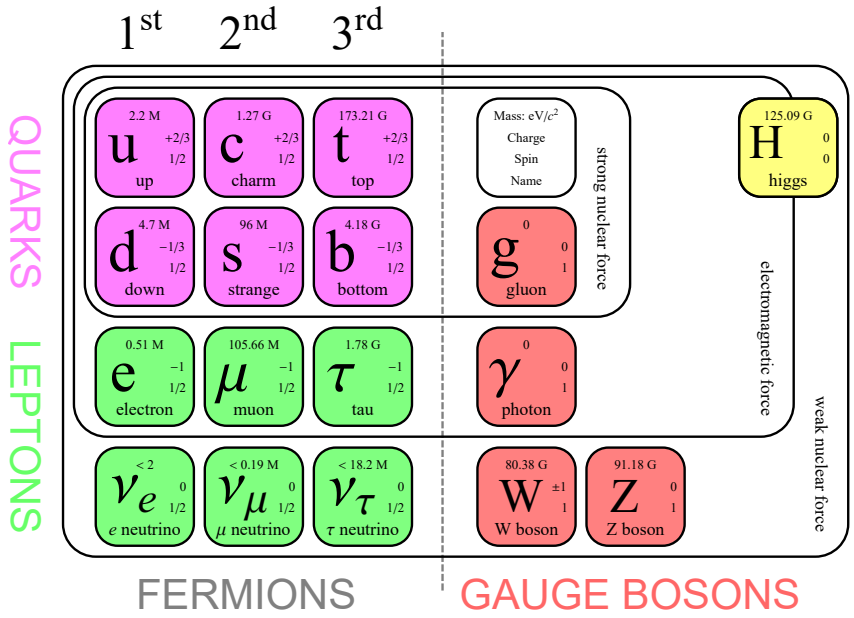

Figure 1.1: Fundamental particles of the Standard Model [7]. The fermions are the constituents of matter, while the gauge bosons describe the interactions.

included in the SM is the strong force. Its exchange particles are the gluons g, which can act between the quarks, but also between other gluons. In opposition to electromagnetism and gravity, which become weaker when the distance increases, the strong interaction presents a peculiar behaviour. At short ranges, the coupling constant of the force becomes small, and the interactions of quarks and gluons can be treated perturbatively [8]. However, at wavelengths of the order of 1 fm, the interacting partons appear as tightly bound composite particles, the hadrons. This phenomenon, known as *colour confinement*, will be discussed in more details in Section 1.1.

This chapter is organised as follows. The theory of the strong interaction, the quantum chromodynamics (QCD), is presented in Section 1.1. The properties and formation of the quark–gluon plasma (QGP) are described in Section 1.2. Relativistic heavy-ion collisions and their physics are treated in Section 1.3. Section 1.4 introduces the concept of the anisotropic flow phenomenon. A selection of previous flow measurements and their physics messages are shown in Section 1.5.

1.1 Quantum chromodynamics

The strong interaction between the quarks and gluons is described with a non-Abelian $SU(3)_C$ gauge theory called QCD [8, 9]. The name *chromodynamics* comes from its associated charge, the colour. There are three values of colour, named in analogy with the three primary colours: red, blue and green. Independently of their flavour, quarks carry one value of colour, while antiquarks have one anticolour (antired, antiblue or antigreen). The mediators of QCD are the colour-charged gluons. In opposition to quantum electrodynamics (QED), where the photon is the single, neutral vector boson of the interaction, there are eight different gluons, which can be related to the eight 3×3 Gell-Mann matrices of $SU(3)$. For example, a gluon changing a blue quark into a green one is "green–antiblue". One consequence of this non-zero charge is that the gluons can interact with each other.

Hadrons are composite bound states of quarks and gluons. They are categorised into different families, the two main ones being the mesons and the baryons. Mesons result from a quark-antiquark pair, while baryons are formed from the binding of three quarks. As no single quark has been seen, hadrons must be colourless particles. A meson is composed of a pair of quarks of one colour and its corresponding anticolour, while each quark in a baryon has a different colour. Recently, exotic states with over three valence quarks have been observed in experiments. An exotic meson, the tetraquark $Z^{\pm}(4430)$, has been found in 2007 by the Belle experiment [10]. Concerning the exotic baryons, the LHCb Collaboration discovered in 2015 the two pentaquarks $P_c^+(4380)$ and $P_c^+(4450)$ [11].

The interactions between quarks and gluons are described in the QCD Lagrangian density [12], given by

$$\mathcal{L}_{QCD} = \sum_q \overline{q}(x)\left(i\gamma_\mu D^\mu - m_q\right) q(x) - \frac{1}{4g^2}\mathrm{tr}G^{\mu\nu}(x)G_{\mu\nu}(x), \tag{1.1}$$

where $q(x)$ is the local quark field, m_q the quark mass, γ_μ the Dirac matrices, g the coupling constant, tr the trace and D_μ the covariant derivative,

$$D_\mu = \partial_\mu - iA_\mu^a t^a, \tag{1.2}$$

with A_μ^a the gauge field and t^a the generators of $SU(3)$. Equation (1.1) can be divided into two contributions. The first term represents the interaction dynamics between the quarks and the gluons. Gluon field dynamics is described by the second term, with

$$G^{\mu\nu}(x) \equiv i\left[D^\mu, D^\nu\right] = \partial^\mu A^\nu(x) - \partial^\nu A^\mu(x) i\left[A^\mu(x), A^\nu(x)\right] \tag{1.3}$$

the gluon field strength tensor.

The strength of an interaction is characterised by its corresponding coupling constant. For example, in QED, the difficulty to separate two electric charges lessens the further they are from each other. This implies that the corresponding coupling constant, α_{QED}, is strong at short scales and decreases with the distance. The opposite behaviour is observed in QCD. At large energies or small distances, the coupling constant is weak. When the energy decreases or the distance increases, it becomes stronger, hence the name *strong interaction* [9, 12]. In QFT, the *beta function* expresses the dependence of the strong interaction coupling constant α_S as a function of the energy scale Q [8], with the following relation

$$Q^2\frac{\partial\alpha_S}{\partial Q^2} = \frac{\partial\alpha_S}{\partial \ln Q^2} = \beta(\alpha_S). \tag{1.4}$$

In the case of QCD, this beta function is written as the series

$$\beta(\alpha_S) = -\left(b_0\alpha_S^2 + b_1\alpha_S^3 + b_2\alpha_S^4 + \ldots\right) \tag{1.5}$$

with b_i the $(i+1)$-loop β-function coefficient [13]. One has to stress the importance of the minus sign in Eq. (1.5). From the proof that $b_0 > 0$ [8], the overall signature expresses the decrease of the coupling constant with the energy. At particularly high energies, the force is so small that the quarks become free particles. This phenomenon, known as *asymptotic freedom*, is a property of non-Abelian gauge theories [14–16]. Figure 1.2 shows the running of the coupling constant with the energy scale. Some theoretical models predict that the decrease of α_S with the energy will eventually make its value comparable to the coupling constants of the electromagnetic and the weak forces, for energies of the order of 10^{15}–10^{17} GeV [8]. As the three forces would then merge into a single interaction, these models are collectively known under the name of *Grand Unified Theories* or *Grand Unification*.

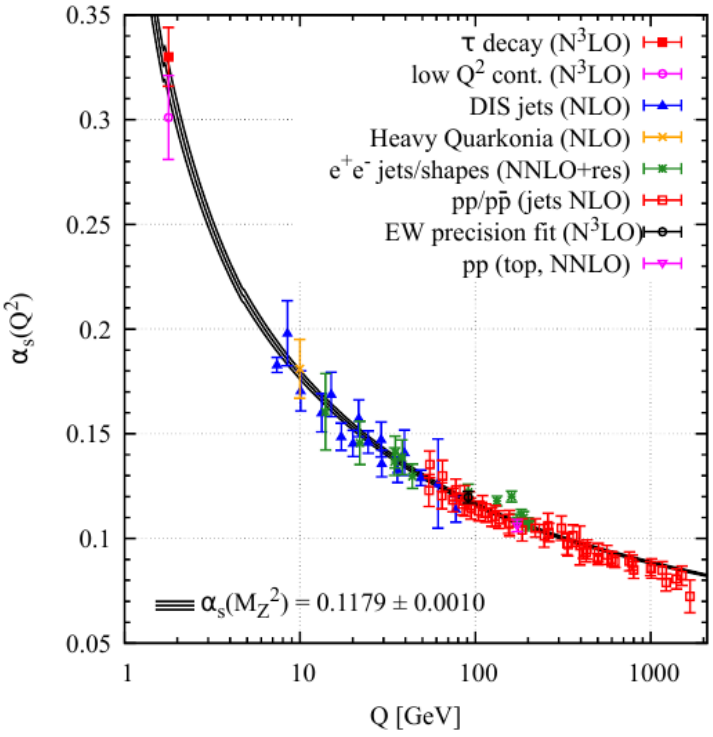

Figure 1.2: Running of the coupling constant α_S as a function of the energy scale Q determined using different physical processes [13].

As mentioned above, hadrons are colourless objects. It is then not possible to observe directly colour-charged particles. This confinement [17] can be understood with the following illustration (Fig. 1.3): for a pair of colour charges, the gluon field forms a tube, also called string, between them. Energy is provided to the quarks to separate them. Due to the behaviour of α_S, the length of the string increases until it reaches the point where it becomes energetically more favourable to create a new pair of quark-antiquark than further elongating the tube. Therefore, instead of detecting single quarks, new mesons are produced from the gain of energy. In collisions in particle accelerators, the available energy is high enough that this process can happen multiple times, creating objects called jets.

The running of α_S has not only implications on the phenomena related to the strong force

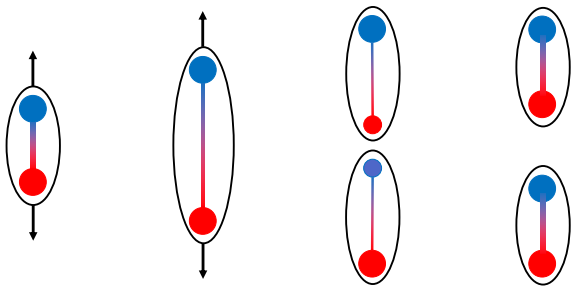

Figure 1.3: Illustration of the colour confinement for a pair of colour charges. The black arrows symbolise the energy given to the pair to separate it. Inspired from [17].

itself. It also prevents solving the QCD Lagrangian density with a unique approach. Two main regimes can therefore be identified. For small α_S, perturbation theory can be applied [9,15,18]. In this regime, the combination of short distances and small size of the coupling constant allows a good approximation of the infinite number of interaction terms by a finite sum. Many important measurements have been tested using perturbative QCD (pQCD), like the ratio of the production rate of $e^+e^- \longrightarrow$ hadrons and $e^+e^- \longrightarrow \mu^+\mu^-$.

For the range where the coupling constant is larger, non-perturbative techniques have to be used to solve the Lagrangian. An example is lattice QCD. This numerical approach is based on a four-dimensional space–time grid, also called the lattice [19,20]. Its size is $N_\sigma^3 \times N_\tau$ and the lattice spacing — i.e. the distance between the nodes — is generally denoted with a. Fields representing the quarks are placed on the nodes of the lattice, while the connections between them stand for the gluon fields. All physical quantities are then expressed in terms of the spacing, even if the latter is not used as a parameter in the discretized QCD partition function [19]. The spacing a can be changed by changing the coupling appearing in the QCD Lagrangian. Finally, continuum QCD is retrieved when the lattice spacing tends to zero.

1.2 Quark–gluon plasma

The running of α_S has important consequences on the behaviour of quark matter. It can be therefore of interest to study its thermodynamic properties as a function of the temperature T and the baryon chemical potential μ_B. The phase diagram of QCD matter is represented in Fig. 1.4. At low T and μ_B, the quarks and gluons are confined inside the hadrons. The ground state of this nuclear matter is the nucleus, at the conditions of $T \sim 0$ and $\mu_B = 938$ MeV [21]. For lower baryonic densities[1], the matter exists in a hadronic gas state. Further, for chemical

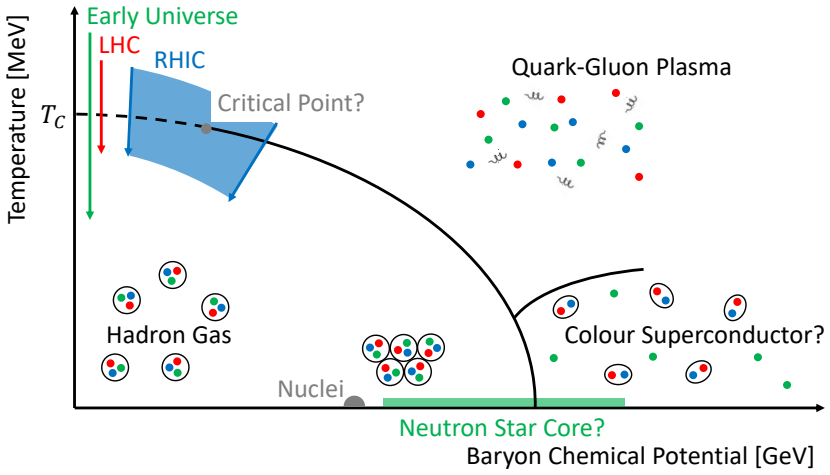

Figure 1.4: Schematic of the QCD phase diagram showing the different phases of quark matter as a function of the temperature and baryon chemical potential. The dashed line indicates the crossover phase transition. The interrogation marks indicate some remaining open questions. Inspired from [22].

potentials between $\mu_B = 938$ MeV and $\mu_B \geq 1$ GeV, the nuclei form tightly bound solids or Fermi liquids [21].

[1] It is possible to describe the thermodynamic properties of quark matter using its baryonic density instead of its baryon chemical potential. The phase diagram obtained this way is similar to the one presented in Fig. 1.4.

The question of the composition of the ultra-dense cosmological objects like neutron stars and black holes attracted the interest of the physics community at the end of the 1930s. Thereupon, understanding the properties of QCD matter at densities larger than the normal matter density became necessary [18, 23, 24]. At $T \approx 0$ MeV and $\mu \geq 1$ GeV, calculations predict the existence of a degenerate liquid and Cooper pairing of the quarks near the Fermi surface [21, 25]. In this state, the quarks create bosonic pairs forming a condensate. Because of its similarities with the superconductors made from electrons in a metal and the local colour symmetry breaking, this phase is dubbed the *colour superconductor* phase [26, 27].

With the introduction of the quark model in 1964 by Gell-Mann [28] and Zweig [29, 30], hadrons could be explained as bound states of quarks and gluons. The possibility of the existence of deconfined quarks was considered and in 1970, Itoh suggested their presence inside the neutron stars [31]. A few years later, the idea of a new state of matter composed only of unbound quarks appears as well [23, 32, 33]. This state was first dubbed *hadronic plasma*, in analogy with its electrodynamic counterpart where the electrons of a neutral gas become mobile charges for high enough temperatures [21, 33]. It has since then been renamed *quark–gluon plasma* [34].

For $\mu \sim 0$, calculations done with lattice QCD have predicted a crossover transition at $T < 200$ MeV [35] between the hadronic gas and the QGP. One of its interesting features is the restoration of chiral symmetry. In QFT, the left- and right-handed components of a massless fermion are independent [20, 36, 37]. Furthermore, confined quarks are massive particles. As a result, the chiral symmetry is spontaneously broken. In the transition from normal matter to QGP, the quarks deconfine and their masses go from the large values to nearly zero, hence the restoration of the symmetry.

As an expected solution of pQCD at high temperatures, the QGP was first thought to behave like a weakly interacting gas [12, 23, 38], based on asymptotic freedom and Debye screening of the colour charge. While QGP has been experimentally observed in 2000 at the Super Proton Synchrotron (SPS) at CERN [39], this idea held until the first high energy heavy-ion collisions at the Relativistic Heavy Ion Collider (RHIC) at the Brookhaven National Laboratory in 2004 [37, 40–42]. With the measurements of various effects like the collective flow or the jet quenching, it has been found with great surprise that the QGP behaves like a strongly interacting liquid. This explains why QGP is often called sQGP, from *strongly coupled quark–gluon plasma*. Furthermore, the comparison of the predictions from relativistic hydrodynamics with the data has shown that the ratio of the shear viscosity over entropy density η/s must be close to the lowest bound of $1/4\pi$ [43]. This makes the QGP the most perfect fluid known up to now [21, 40, 41].

Even though a certain number of predictions have already been confirmed or proven incorrect by measurements of nuclear collisions, many open questions remain about the phases of the QCD matter and their transitions. For example, in the case of high baryon density, lattice QCD cannot be used anymore. Computations made with diverse methods for two light quark flavours hint at the existence of a critical point followed by a first order phase transition between the hadronic and QGP phases [12, 21, 44–46]. However, the existence of this critical point is only theoretical and its exact position uncertain. Experimental searches are therefore done for this purpose at RHIC using the beam energy scan [35, 47–49]. In this experimental program, the available phase space is studied using heavy-ion collisions at different centre of mass energies, starting at $\sqrt{s_{\mathrm{NN}}} = 7.7$ GeV up to $\sqrt{s_{\mathrm{NN}}} = 200$ GeV, the largest energy reachable at RHIC [21].

Figure 1.4 also shows in green the direction of the evolution of the Early Universe and the conditions inside the neutron stars cores. QCD predicts that a high temperature QGP filled the Universe in the first few microseconds after the Big Bang [38, 50]. This state was present until the Universe cooled enough for the gluons and quarks to recombine into hadrons. Furthermore, while the outer crust of neutron stars is known to be made of electron gas, ions

and neutrons, the composition of the inner part is still an open question. Quark matter as QGP is one of the possibility investigated by theoreticians and experimentalists, alongside hyperons and neutrons [51]. Investigating the QGP is therefore fundamental to get a clearer picture of the phase diagram of the QCD matter, but also a better understanding of the evolution of the Universe itself for the key role it has in its description.

1.3 Physics of relativistic heavy-ion collisions

QGP can be produced experimentally through ultra-relativistic collisions of heavy ions. Since its discovery in 2000, it has been observed and studied for different nuclei and centre of mass energies $\sqrt{s_{\mathrm{NN}}}$, each accelerator having its particularities. For instance, collisions produced at the Large Hadron Collider (LHC) at CERN are usually done with lead ions at energies of the order of the TeV ($\sqrt{s_{\mathrm{NN}}} = 2.76$ TeV in 2010–2011, 5.02 TeV in 2015 and 2018). Xenon at $\sqrt{s_{\mathrm{NN}}} = 5.44$ TeV has also been used in 2017 [52]. Oxygen collisions are planned for the future Run 3 [53]. RHIC collided gold and other species like uranium at various energies between GeV and TeV. Some motivations for the use of various energies are the study of the onset of QGP formation or the influence of the ion shape on the QGP properties. The QGP produced in these relativistic heavy-ion collisions undergo a time evolution as illustrated in Fig. 1.5. Before the collision, the nuclei are stripped of the totality of their electrons and accelerated to velocities close to the speed of light. Relativistic Lorentz contraction becomes non-negligible at these energies and the collision of the two ions can be seen in the laboratory frame as the collision of two thin disks or two "pancakes" (see the two left panels in Fig. 1.5). This extreme Lorentz contraction has two major consequences on the system. First, the density of quarks and gluons is higher in the disks than in the initial ions at rest. Second, the collision time has a well-defined value, identical for all the nucleons [37].

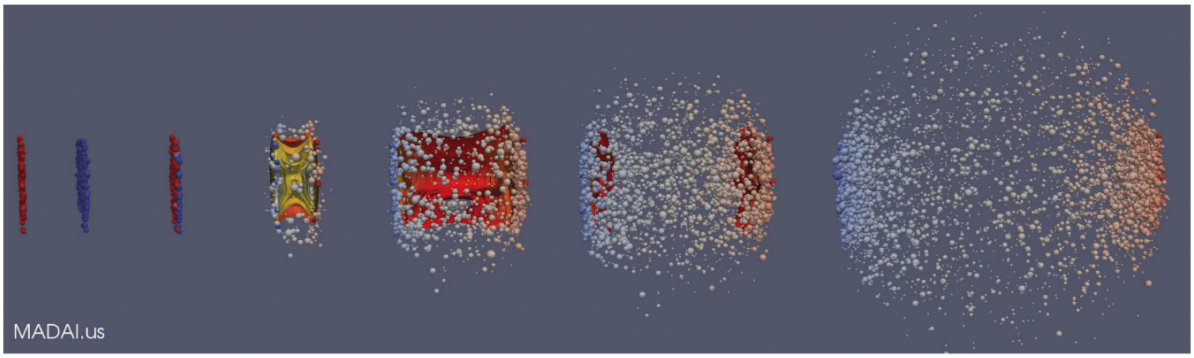

Figure 1.5: Simulation of the time evolution of a relativistic heavy-ion collision. Taken from [54], based on [55, 56].

As the geometry of the collision influences the evolution of the produced matter and the signatures one can extract from them, some technical concepts have to be introduced. Figure 1.6 shows the main keywords used to define the ideal geometry. The overlap of the ions at the time of the collision is characterised with the *impact parameter* b, defined as the distance between the centres of the two nuclei. Collisions with $b = 0$ are called head-on or central collisions, while peripheral collisions correspond to an impact parameter closer to the sum of the radii of the two ions. The *reaction plane*, or collision plane, is the plane spanned by the direction of the impact parameter vector $\mathbf{b}$ and the beam axis z [57]. Its angle with respect to the x-axis is denoted by Ψ_{RP}. Furthermore, the nucleons in the colliding ions can be divided

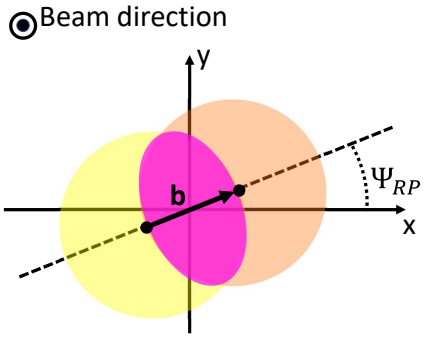

Figure 1.6: Ideal geometry of the collision between two heavy ions. The bold arrow indicates the impact parameter vector **b**. The reaction plane of angle Ψ_{RP} is denoted with the dashed line. Based on [57].

into two main groups. The ones which take part in the reaction are called the *participants* and they belong to the pink overlap region. The nucleons without any contribution in the collision are the *spectators*, indicated in yellow and orange in the figure. While both the impact parameter and the reaction plane can be used to make theoretical predictions, they are not directly measurable in experiments. However, it is possible to measure the number of produced particles, the energy released in the collision and the number of spectators [12]. Both the released energy, and the produced particle multiplicity are proportional to the number of participants, and their respective distributions can be used to categorise the events into *centrality classes*. The distribution of produced particles, for instance, is divided into consecutive steps in such a way that the 5% highest multiplicities events can be related to the 5% most central collisions [12,58]. In relativistic collisions, the centrality c is linked to the impact parameter b using the relation

$$c \simeq \frac{\pi b^2}{\sigma_{\text{inel}}}, \tag{1.6}$$

where σ_{inel} is the total inelastic nucleus-nucleus cross section [58]. Figure 1.7 illustrates the centrality classification and its connection to the impact parameter and shape of the overlap region of the collision.

For an event with a given impact parameter, the experimental multiplicity or number of participants can be related to the theoretical quantities like the number of wounded nucleons — nucleons who interacted at least once — and of binary collisions — collisions between two nucleons. This is done with the help of models like the Glauber model [12,59–62]. The nuclear density profile used in the Glauber model is given by the Woods–Saxon distribution [12] and the description of an inelastic collision of two nuclei is approximated as the superposition of successive independent interactions of the nucleons. Furthermore, two types of calculations can be found, leading to slightly different results. The first one is known as the *optical Glauber model* [60]. In this approach, the nucleon density is assumed to be continuous, meaning the nucleons do not have specific spatial coordinates. The second method is the *Monte Carlo Glauber* (MC-Glauber) [60]. Here, the two nuclei are built with the nucleons according to their corresponding density distributions. The collision for a random b is then described as this sequence of binary nucleon–nucleon collisions, where it is assumed that the nucleons have a straight path between the interactions [60,62]. Moreover, MC-Glauber takes as one of its inputs the nucleon-nucleon cross-sections obtained from pp collisions at various energies and assumes they remain constant after each collision.

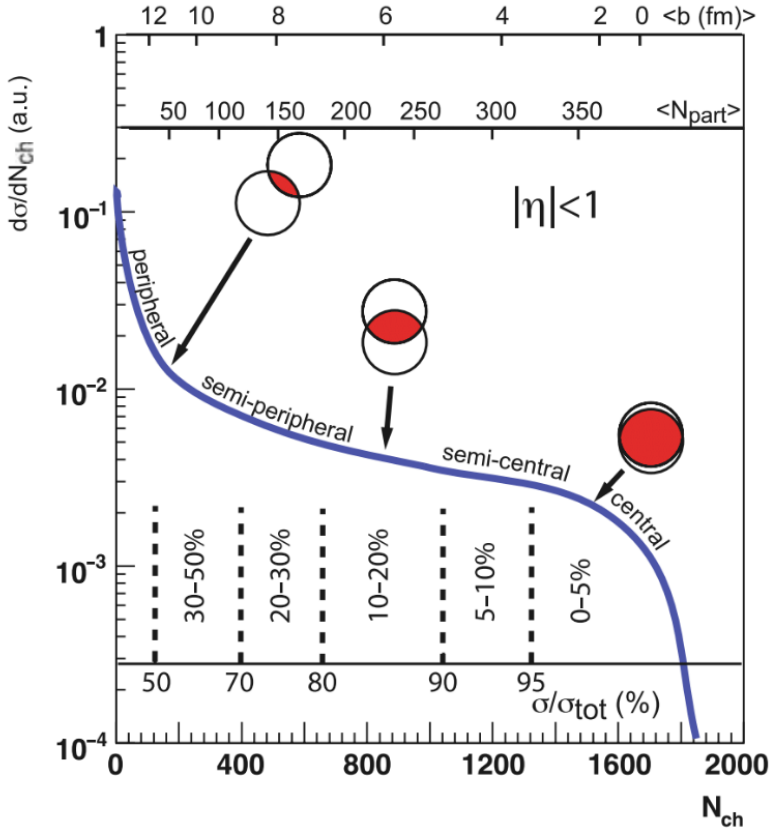

Figure 1.7: Sketch of the centrality definition based on the multiplicity produced in the collision [12]. The corresponding impact parameter b and number of participants N_{part} are shown.

Once the ions collide, the interactions can develop under different forms. Hard processes[2] with large transferred momenta $Q \gtrsim 10$ GeV [63] are the first processes to happen, due to the uncertainty principle. These so-called "hard" particles are at the origin of phenomena like jets, direct photons, pairs of dileptons and can be traced back to this pre-equilibrium phase. The bulk of the initial quarks and gluons liberated by the collision produces a volume of matter that evolves until a thermal equilibrium is reached. In this pre-equilibrium state, the hydrodynamics theory, used to describe successfully the QGP phase, cannot be applied and other models have been developed. Examples are the MC-Glauber introduced above, or the Colour Glass Condensate (CGC) approach. The latter is based on a different ordering of the time scales in the collision, characteristic of glass-like matter [20, 63–65]. As the accelerated ions are extremely Lorentz-contracted, their collision time becomes infinitely short, $\tau_0 \sim 1/\sqrt{s}$, where $\sqrt{s}$ is the centre of mass energy. Moreover, for a soft gluon with momentum k, the time scale of its evolution is $\tau_g \sim 1/k$, with as a consequence $\tau_g \gg \tau_0$ [20]. If the energy is sufficient, the density of partons becomes saturated and the partons are no longer independent. They start to act coherently, leading to a description with classical colour fields in the same plane as the colliding ions. In the CGC approach, when the two ions collide, their classical colour fields combine. As the disks go through each other, the hadrons separate, forming new longitudinal colour fields. The medium takes the form of a cylinder composed of three-dimensional classical colour fields as shown in Fig. 1.8. This short-lived pre-equilibrium state is the so-called *glasma* [20] (see third panel in Fig. 1.5).

[2]More energetic particles are called "hard" particles, while particles with less kinetic energy are the "soft" particles.

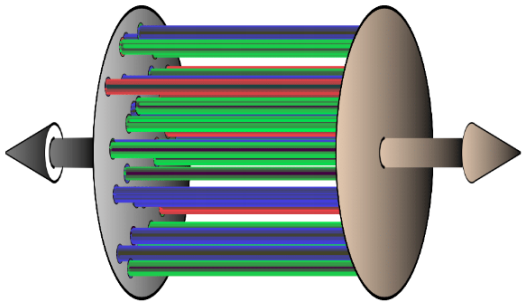

Figure 1.8: Longitudinal colour flux tubes developing between the two colliding ions in the CGC approach [63].

As the pre-equilibrium state continues to develop, the partons interact with each other and the volume of produced matter quickly reaches a local thermal equilibrium. It has to be noted that these interactions are not negligible. The thermalization time is about 1 fm/c although the medium is fast expanding, meaning the distances the partons have to cover increase continuously [63]. The phase after this thermalization is known as QGP, where relativistic viscous hydrodynamics can be applied. It is visible in the fourth panel in Fig. 1.5. The QGP continues to expand and the local thermal equilibrium disappears. The density and temperatures decrease until they reach the point where the gluons and quarks can recombine into hadrons. This corresponds to the crossover phase transition at T_C in the QCD phase diagram in Fig. 1.4. This phase, simply called *hadronisation*, happens between $\tau \simeq$ 10–20 fm/c and leads to the formation of a hot hadronic gas [63]. The energy density of the system continues to decrease as the gas expands. Its hadronic content is constantly changing due to inelastic interactions until the so-called *chemical freeze-out* [37,66]. At this point, the particle numbers and species become conserved, but the particle momenta can still be changed through elastic processes. The *thermal freeze-out* stops all elastic scatterings and the final state particles will fly freely to the detectors, with the only possible changes in the composition being due to particle decays and interactions with the matter composing the detector itself.

Finally, as the collision between two heavy nuclei recreates the conditions which are predicted to be the ones of the Big Bang and the time evolution of the produced matter is similar in the two cases, relativistic heavy-ion collisions are sometimes called *Little Bang* [40,42,67].

1.4 Anisotropic flow phenomenon

The idea to describe the evolution of the system created in the collision of two ions with hydrodynamics was first proposed in 1953 by Landau [68]. It was confirmed with the first measurements at RHIC where the hydrodynamic predictions were found to be in good agreement with the data. Ideal hydrodynamics is applicable only if the system is close to a local thermal equilibrium. This comes from the fact that hydrodynamics laws are based on the thermodynamic properties of the system, like its temperature, pressure and energy density, and these quantities are well defined only close to the equilibrium [69]. As a result, the hydrodynamic description is valid only from the thermalisation of the interacting matter to its freeze-out, and thus, initial conditions need to be provided. Various approaches can be used to obtain these initial conditions. Some examples are the MC-Glauber model which has already been discussed earlier, or the IP-Glasma based on the CGC approach [70]. Alternatively, transport models can also be employed. For instance, a multiphase transport model (AMPT) [71], which is based on different other

models, namely a Heavy-Ion Jet INteraction Generator (HIJING) [72,73] and the Zhang's parton cascade model [74] for the generation of the partons and their evolution up to the hadronisation. One common point of all these models is that one of their output is the initial transverse density distribution of the matter formed in the early times of the collision. The HIJING model is discussed in Section 6.1.

In semicentral and peripheral events, this transverse density, and the corresponding volume of interacting matter in the overlap region of the two colliding nuclei, is at leading order elliptical in the transverse plane, with the smaller axis of the ellipse parallel to the reaction plane [75] as shown in Fig. 1.6. However, this geometric asymmetry cannot explain the results observed in central events as the overlap region is mainly circular, and hence isotropic. This other source of anisotropy in the system is found in the nature of the colliding ions. They are not ideal, smooth spheres, but composite objects made of protons and neutrons. The positions of the nucleons fluctuate event-by-event, which leads to deformations of the overlap region. These fluctuations are present in all centralities, but they dominate in central events [75]. From these two sources and their effects, two different regimes can be distinguished: the *geometry-dominated* regime in non-central events and the *fluctuation-dominated regime* for the most head-on collisions [76,77].

One dimensionless quantity used to determine the size of the almond-shaped asymmetry is the so-called *ellipticity*, which is defined with respect to the reaction plane as

$$\epsilon_2^{RP} = \frac{\{x^2 - y^2\}}{\{x^2 + y^2\}}, \tag{1.7}$$

where x and y are the coordinates of the participating nucleons projected on the transverse plane and $\{\ldots\}$ represents the average over the initial energy density distribution $e(x, y)$ [75],

$$\{\ldots\} = \frac{\int dxdy\ e(x, y)\ldots}{\int dxdy\ e(x, y)}. \tag{1.8}$$

With this definition of the ellipticity, ϵ_2^{RP} can take any value between zero and one. In particular, $\epsilon_2^{RP} = 0$ means the system presents a perfectly symmetric energy density profile.

The deformations in the interacting volume shape due to the fluctuations lead to a generalisation of the ellipticity to higher orders. Thereupon, the initial density distribution can be described with the *eccentricities* $\mathcal{E}_n$ [75,78,79] defined as

$$\mathcal{E}_n \equiv \epsilon_n e^{in\Phi_n} \equiv -\frac{\{r^n e^{in\phi}\}}{\{r^n\}}, n > 1, \tag{1.9}$$

$$\mathcal{E}_1 \equiv \epsilon_1 e^{i\Phi_1} \equiv -\frac{\{r^3 e^{i\phi}\}}{\{r^3\}}. \tag{1.10}$$

In Eqs. (1.9) and (1.10), r and ϕ are the transverse coordinates. ϵ_n represents the magnitude of the n-th order asymmetry and Φ_n its orientation, also called the n-th order *participant plane* of the initial state. As for the original ellipticity, the initial anisotropy is maximum when $|\mathcal{E}_n| = \epsilon_n = 1$, and vanishing if $\epsilon_n = 0$. In addition of the ellipticity for $\mathcal{E}_2 = \epsilon_2^{RP}$, the first orders are respectively named the *triangularity* for $\mathcal{E}_3$, the *quadrangularity* for $\mathcal{E}_4$ and so on. The shapes of the initial volume of interacting matter for the first five orders of eccentricities are illustrated in Fig. 1.9.

The hydrodynamic evolution of the volume of interacting matter is driven by its equation of motion, namely the Navier-Stokes equation, its simplification in the limit of non-viscous fluid the Euler equation, and their consecutive generalisations. Furthermore, the spatial asymmetry is at the origin of pressure gradients inside the volume [21,80]. The insertion of these pressure gradients in the equations of motion shows then a transfer of the anisotropy in the coordinate

Figure 1.9: Characteristic shapes of the initial interaction volume for the orders $n = 1$ to $n = 5$ with the corresponding eccentricities $\mathcal{E}_n$ [75].

space into an anisotropy in momentum space. This transfer, known as the *anisotropic flow phenomenon* or simply the *anisotropic flow*, can therefore be interpreted as the medium response to the initial geometry of the system [75, 80]. Figure 1.10 summarises the full phenomenon.

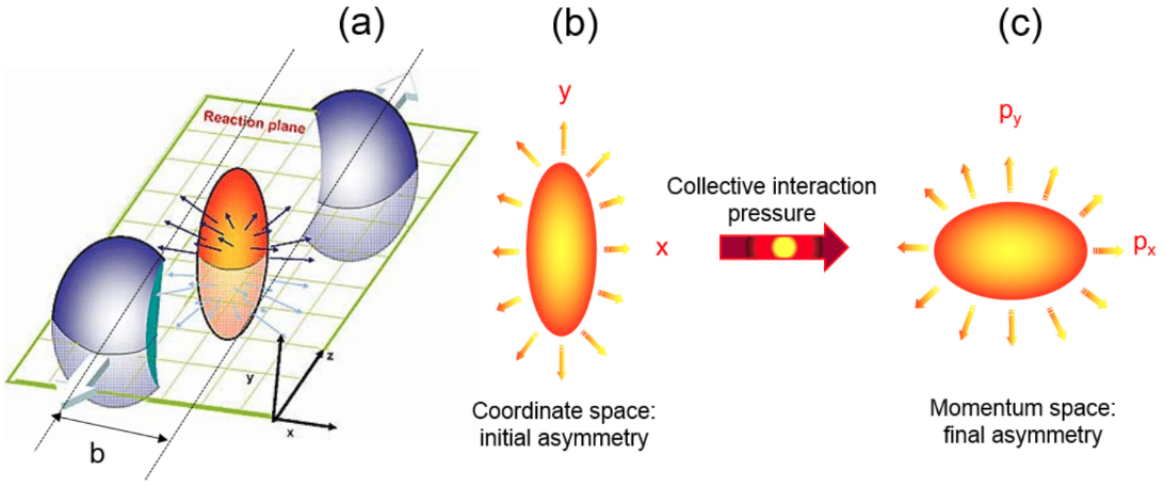

Figure 1.10: Illustration of the anisotropic flow phenomenon [81]: the dominant elliptic shape of the interaction volume in non-central collisions (a), the anisotropy in the coordinate space (b) and in the momentum space (c).

Similarly, as for the initial anisotropy in the coordinate space, the deformations of the final volume of interacting matter in the momentum space can be characterised with the *complex harmonic flow* coefficients V_n. The n-th order coefficient is defined as [75]

$$V_n \equiv v_n e^{in\Psi_n}. \tag{1.11}$$

The magnitude of the n-th order momentum asymmetry is given by the flow amplitude v_n and its direction by the corresponding symmetry plane Ψ_n. As for the eccentricities $\mathcal{E}_n$, each flow amplitude has its own name. For example, v_1 is the *directed flow*, v_2 the *elliptic flow*, v_3 the *triangular flow*, and so forth. Figure 1.11 shows the different orientations of the first three symmetry planes Ψ_1, Ψ_2 and Ψ_3. Furthermore, the fluctuations of ϵ_n and Φ_n imply that v_n and Ψ_n also vary event-by-event. It has to be noted that without these fluctuations, all Ψ_n would be equal to the reaction plane of the collision Ψ_{RP}. Generally, V_n, and thus v_n, depend on the transverse momentum p_T, the pseudorapidity η and the particle species, i.e. $V_n(p_\mathrm{T}, \eta, \text{species})$ and $v_n(p_\mathrm{T}, \eta, \text{species})$. They are then referred as *differential flow*. The corresponding *integrated flow* can be obtained by averaging these quantities over the corresponding phase space, which is generally the acceptance of the detector [83].

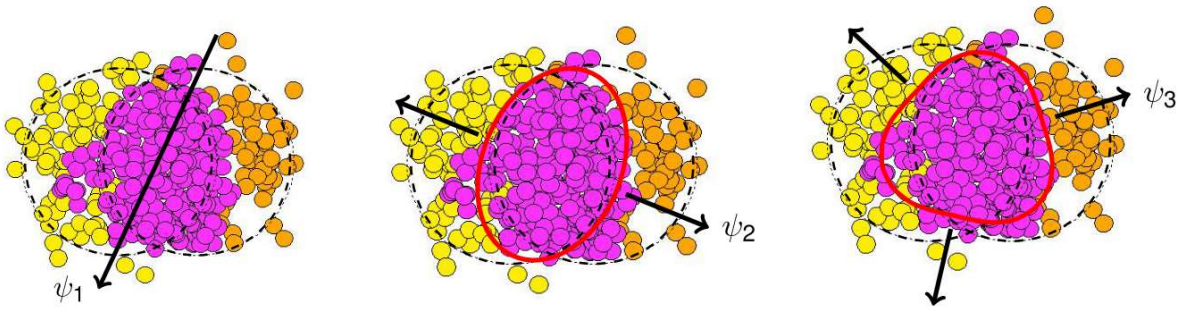

Figure 1.11: Examples of different orientations of the symmetry planes in the transverse view of the heavy-ion collision [82].

The initial eccentricities $\mathcal{E}_n$ and final flow coefficients V_n are not independent. More precisely, the flow coefficients are fully determined from the hydrodynamic equations of motion once the initial conditions are set. This means V_n can be expressed as a function of the eccentricities, i.e. $V_n = V_n(\mathcal{E}, \alpha)$, with $\mathcal{E}$ a set of eccentricities and α the dynamical properties of the interacting matter, for example, its transport coefficients or its equation of motion [75, 79]. Based on hydrodynamic simulations, the complex flow coefficients can be expanded into [75]

$$V_n(\mathcal{E}, \alpha) = \kappa(\alpha)\mathcal{E} + \mathcal{O}(\mathcal{E}^2) + \delta_n. \tag{1.12}$$

The variable δ_n is a complex residual introduced to take into account the effects from the fluctuations, supposed to be uncorrelated with $\mathcal{E}_n$. Furthermore, the expansion is possible only if $|\mathcal{E}_n| < 1$ for any n. In heavy-ion collisions, this is the case for $n \neq 2$, as these eccentricities originate from fluctuations. However, in non-central collisions, $\mathcal{E}_2$ comes from the geometry of the interacting volume and is the largest eccentricity. This implies that $\mathcal{E}_2$ dominates in the expansion and most notably is involved in non-linear terms for the higher order coefficients [75].

From these assumptions, the key question is where to stop the expansion in order to have a good approximation of the harmonic flow coefficients. The answer is based on the symmetry properties of the system. For a given event, V_n is symmetric under rotation, i.e. it is invariant under the transformation $\varphi \longrightarrow \varphi + 2\pi/n$. For a single order n, the resulting expansion can then be divided into the linear part proportional to the corresponding $\mathcal{E}_n$ and the non-linear part obtained from the symmetry constraints. The parameter $\kappa(\alpha)$ is also separated into its corresponding linear and non-linear components. From the expansions of the first flow harmonics[3], it has been shown that $V_2 \propto \mathcal{E}_2$ and $V_3 \propto \mathcal{E}_3$ for a given centrality range. Figure 1.12 shows this linear dependence for different parametrisations of the same MC-Glauber model in the case of identified pions with centrality in the range 20–30%. In the case of higher order $n \geq 4$, non-linear effects can be seen. A contribution from $(V_2)^2$ manifest itself in V_4, while mixing between V_2 and V_3 influences V_5 [42, 87]. Terms involving the second, third and fourth harmonics represent the non-linear parts of V_6. Simulations for V_4 are shown in Fig. 1.13.

The anisotropy in momentum space influences the emission of the final state particles which are detected in the experiment. The observable of interest in flow analyses is the azimuthal distribution of some physical quantity of the outgoing particles, where the quantity can be the transverse momentum or the multiplicity in some rapidity or pseudorapidity η range [88], to cite only a few examples. The most general distribution is thus the triple differential distribution $E\,\mathrm{d}^3N/\mathrm{d}^3\mathbf{p}$, where E is the energy (included to ensure the result is Lorentz invariant) and $\mathbf{p}$ the

[3]For the expansions themselves, see [75, 84, 85].

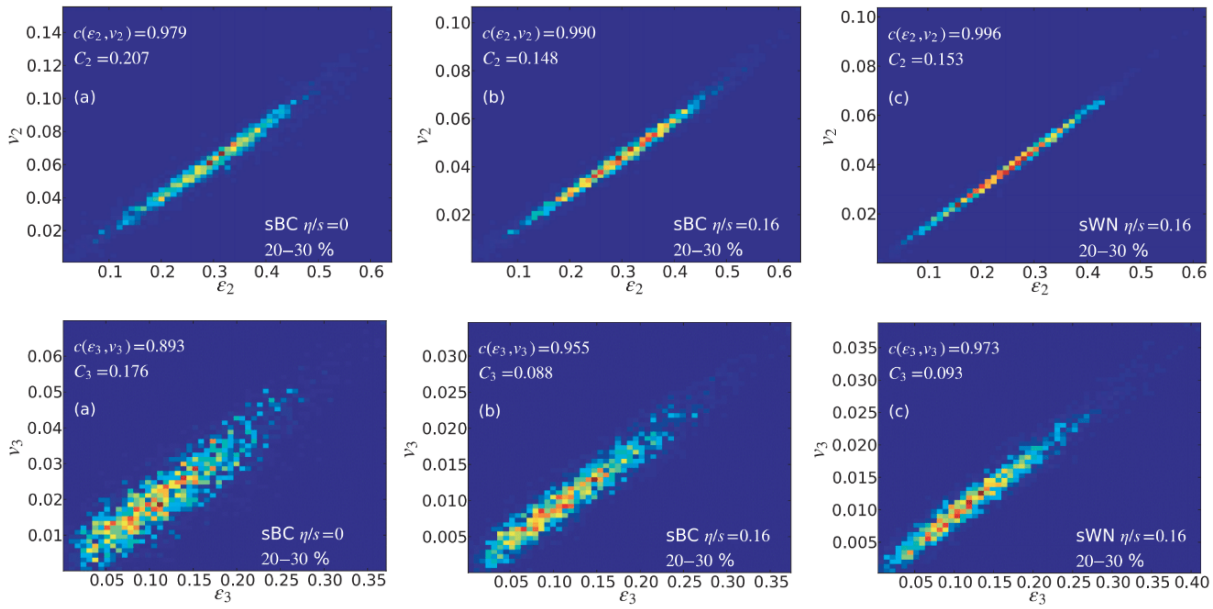

Figure 1.12: v_2 as a function of ϵ_2 (*top*) and v_3 as a function of ϵ_3 (*bottom*) for different parametrisations of the MC-Glauber model, with identified pions in the 20–30% centrality range [86].

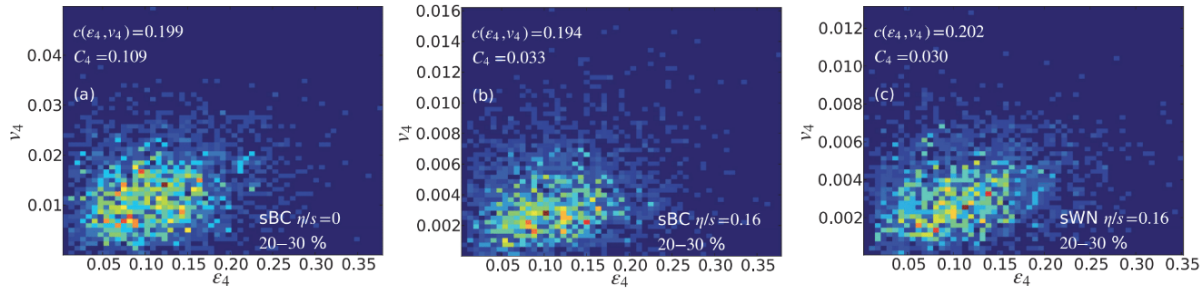

Figure 1.13: v_4 as a function of ϵ_4 for different parametrisations of the MC-Glauber model, with identified pions in the 20–30% centrality range [86].

3-momentum. As this azimuthal distribution is a periodic function, it can be expressed with a Fourier series. Originally given with the coefficients x_n and y_n in the transverse plane [88], the Fourier expansion is now usually written as [89]

$$E\frac{\mathrm{d}^3N}{\mathrm{d}^3\mathbf{p}} = \frac{1}{2\pi}\frac{\mathrm{d}^2N}{p_\mathrm{T}\mathrm{d}p_\mathrm{T}\mathrm{d}\eta}\left[1+2\sum_{n=1}^{\infty} v_n\cos\left(n(\varphi-\Psi_n)\right)\right], \tag{1.13}$$

with the flow amplitudes v_n and the symmetry planes Ψ_n being the two sets of Fourier coefficients of the series. Using the properties of Fourier series and trigonometric functions, the flow amplitudes can be expressed exactly with[4]

$$v_n = \langle\cos\left[n\left(\varphi-\Psi_n\right)\right]\rangle = \left\langle \mathrm{e}^{in(\varphi-\Psi_n)}\right\rangle. \tag{1.14}$$

In the above expression, $\langle\ldots\rangle$ represents the average over all particles in an event, also called *single-event* average. A second type of average is also introduced now: the *all-event average* $\langle\langle\ldots\rangle\rangle$ is the average over all particles in an event followed by the average over all events. These two notations will be used in the rest of this thesis.

[4]See Appendix B.1 for the demonstration.

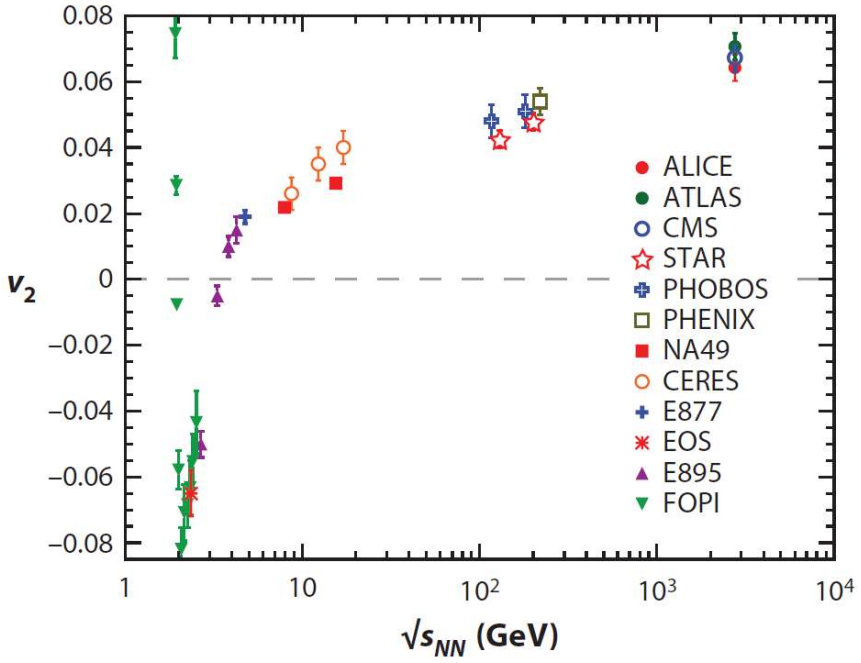

Figure 1.14: Integrated elliptic flow v_2 as a function of the centre of mass energy $\sqrt{s_{\mathrm{NN}}}$ for different heavy-ion experiments in the centrality range 20–30% [42].

1.5 Previous measurements in flow analyses

This section presents an overview of the most important heavy-ion results obtained in flow analyses. Even before the first evidence of the creation of the predicted QGP in heavy-ion collisions at the SPS collider [39] until now, extensive research has been made on the dynamical properties of this extreme state of matter using anisotropic flow as a probe.

Flow coefficients

First experimental heavy-ion studies of directed and elliptic flow can be traced back in the 1990s with measurements of gold or lead collisions at centre of mass energies ranging from a few hundreds of MeV to 200 GeV per nucleon [90–97]. The directed flow v_1 shows a change of sign around midpseudorapidity. For the elliptic flow, studies have found a sign transition with the increase of collision energy. For energies in the 1–2 GeV range, v_2 is negative, indicating emission of the particles out of the reaction plane, called *squeeze-out* effect. The participant nucleons interact and want to exit the fireball. As the spectators travel along the reaction plane, the participants can only be emitted perpendicular to it [98]. For energies higher than 2 GeV, an in-plane emission of the particles is observed, leading to positive values of the elliptic flow coefficient. For $\sqrt{s_{\mathrm{NN}}} < 1$ GeV, the centre of mass energy of the two ions is not sufficient to break them and they simply bounce off each other. The particles produced from the interactions of the nucleons are then dragged by the recoiling nuclei, imitating an in-plane emission with positive values of v_2. Figure 1.14 shows the evolution of the elliptic flow in the centrality range 20–30% for different heavy-ion experiments as a function of the centre of mass energy.

At the beginning of the 2000s, systematic measurements of the QGP properties in Au–Au collisions at $\sqrt{s_{\mathrm{NN}}} = 130$ GeV have been done by the experiments at RHIC. Among the different

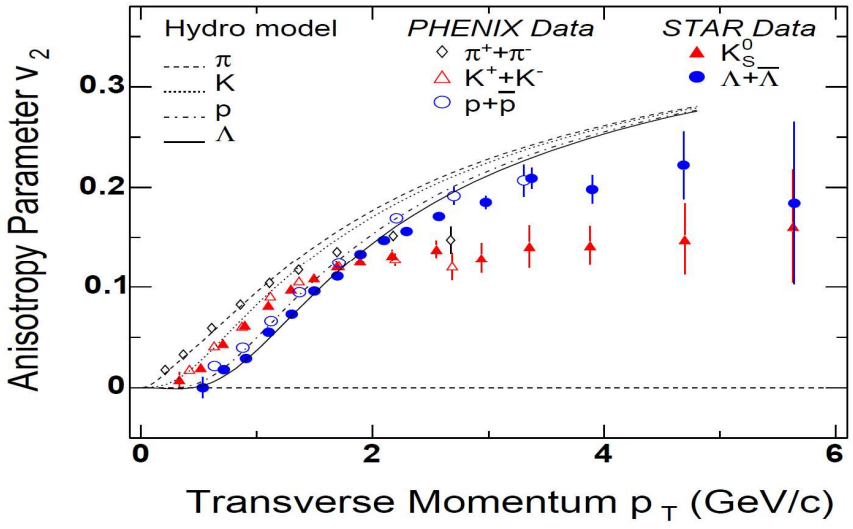

Figure 1.15: Differential elliptic flow v_2 as a function of the transverse momentum p_{T} for various identified hadrons for Au–Au collisions at $\sqrt{s_{\mathrm{NN}}} = 130$ GeV at RHIC. The results from STAR and PHENIX are shown with corresponding hydrodynamic simulations [41].

signatures that have been observed, the elliptic flow of various identified hadron species has been measured as a function of the transverse momentum p_{T} (see Fig. 1.15). The mass splitting predicted by hydrodynamics has been shown to be well reproduced by the data for low transverse momenta. Furthermore, it has been demonstrated that the data were in perfect agreement for $p_{\mathrm{T}} < 1.5$–2 GeV/c with predictions from ideal hydrodynamics with an equation of state including a transition from hadronic to quark matter. It has been concluded that the QGP created in the heavy-ion collisions was a nearly perfect liquid with a very small shear viscosity over entropy density.

Following the measurements at the SPS and RHIC accelerators, extensive studies have been made in both the theoretical and experimental sides. One can cite, for example, the first looks at higher order flow amplitudes. While they were known to be small, it was believed that the statistics achieved at RHIC was already sufficient to measure quantities like the quadrangular flow v_4 [99, 100] or the triangular flow v_3 [77]. The motivation behind these analyses is the possibility to apply independent constraints on the initial conditions, the system properties and the model calculations. Figure 1.16 shows the measurements of the integrated v_2, v_4 and v_6 as a function of the centrality by the STAR Collaboration in Au–Au collisions at $\sqrt{s_{\mathrm{NN}}} = 200$ GeV, using different analysis techniques (see Chapter 2). The ordering of the flow amplitudes is clearly visible, with v_2 having a dominant effect and v_6 compatible with zero for all centralities.

One interesting remark is, while the measurements of the even higher order harmonics quickly followed after the first results of elliptic flow at RHIC, it took a few more years for the same interest for the odd harmonics to develop as well. The first mention of the triangular flow v_3 and its corresponding triangularity in the initial state ϵ_3 can be traced back to 2010 in Ref. [77], with the first experimental measurements directly following. Figure 1.17 (a) shows the integrated values for v_2, v_3 and v_4 as a function of the centrality for Pb–Pb collisions at $\sqrt{s_{\mathrm{NN}}} = 2.76$ TeV [101]. The same ordering of amplitudes as seen for the even harmonics is also visible with v_3. Furthermore, using the linear response assumption for v_2 and v_3, the measurements of the ratio of v_2/ϵ_2 and v_3/ϵ_3, where the eccentricities are determined using various models for the initial conditions, seem to indicate more important viscous corrections for the third than thesecond order (see Fig. 1.17 (b)).

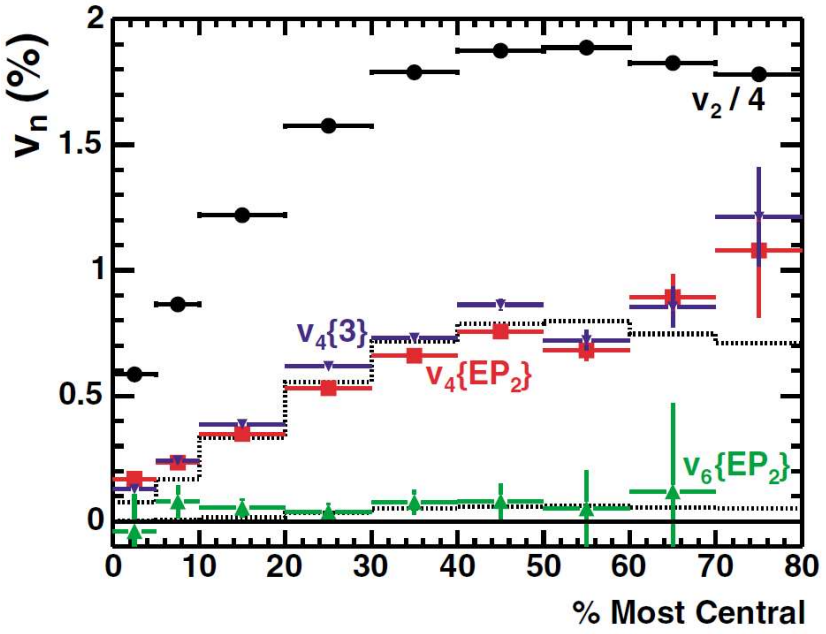

Figure 1.16: Integrated elliptic flow v_2, quadrangular flow v_4 and 6th order flow amplitude v_6 as a function of the centrality in Au–Au collisions at $\sqrt{s_{\mathrm{NN}}} = 200$ GeV by the STAR experiment [100].

In parallel of the measurements of the higher order flow amplitudes, more studies are made in the analysis techniques. One can cite, for instance, the introduction of observables based on the mathematical formalism of cumulants. As it extracts the genuine correlations between all the elements in it, the cumulant expansion is the most indicated method to remove the correlations involving only a few particles, also called nonflow. Borghini et al. presented in 2001 the first methods based on cumulants in Refs. [83, 102, 103], which have been extensively used in theoretical and experimental studies since then. Examples of observables, like $v_2\{2\}$ or $v_4\{3\}$ — the measurement of v_2 with a two-particle cumulant and of v_4 with a three-particle cumulant respectively — are visible in Figs. 1.16 and 1.17.

Correlations between symmetry planes

The flow amplitudes are not the only degrees of freedom of the Fourier series that have been studied with heavy-ion collisions. The first results on the symmetry planes can be attributed to the E877 Collaboration in 1997 [92]. Various measurements relative to Ψ_n have been done by the experiments at RHIC and the LHC. While some analyses were conducted due to the contribution of the symmetry planes in the evaluation of the amplitudes [100, 104], searches have also been done on the planes themselves and their correlations. Results of the cosine of the difference between two (or more) symmetry planes have hinted that the correlations in the momentum space are due to both the fluctuations of the initial geometry and the non-linear response of the flow harmonics themselves during the system evolution. Examples of results and observables can be found in Refs. [105–107] (see Fig. 1.18 for results from ATLAS). Theoretical developments taking into account correlations between the flow amplitudes have been published recently in Ref. [108].

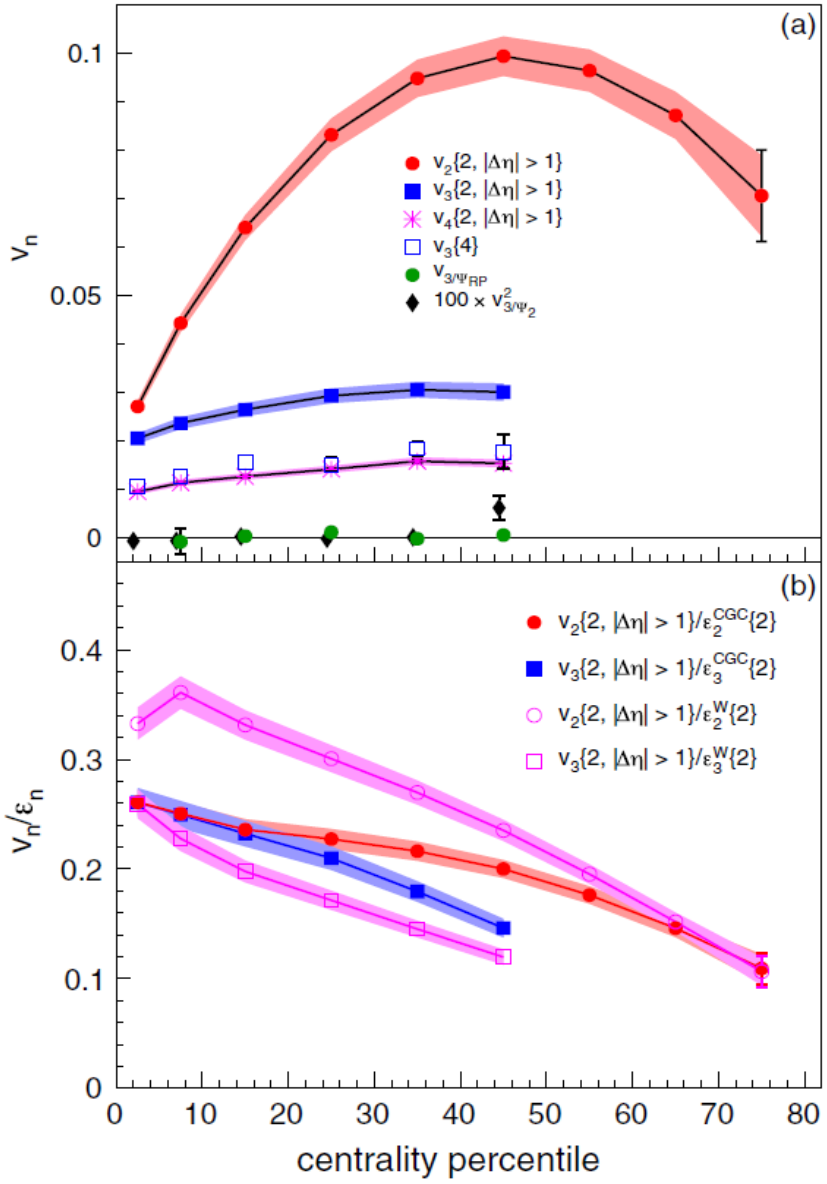

Figure 1.17: (a) Integrated elliptic flow v_2, triangular flow v_3 and quadrangular flow v_4 as a function of the centrality. (b) v_2 and v_3 divided by the corresponding eccentricities obtained with two different models for initial conditions. Both figures use data from Pb–Pb collisions at $\sqrt{s_{\mathrm{NN}}} = 2.76$ TeV [101].

Correlations between flow amplitudes

The idea to measure the correlations between two different flow amplitudes v_m and v_n has been first proposed by Niemi et al. in Ref. [86]. With the same linear correlator used to determine the linear response between v_n and ϵ_n, they concluded that the linear correlations between v_n and v_m were not governed only by the initial conditions, but also by the shear viscosity over entropy density of the QGP itself. Non-trivial, significant correlations between two different eccentricities ϵ_n and ϵ_m have also been observed in Ref. [109]. At the same time, correlations between flow amplitudes have been studied in Ref. [110] in the context of the newly developed *Generic Framework*. In this paper, Bilandzic et al. introduced a set of new observables based

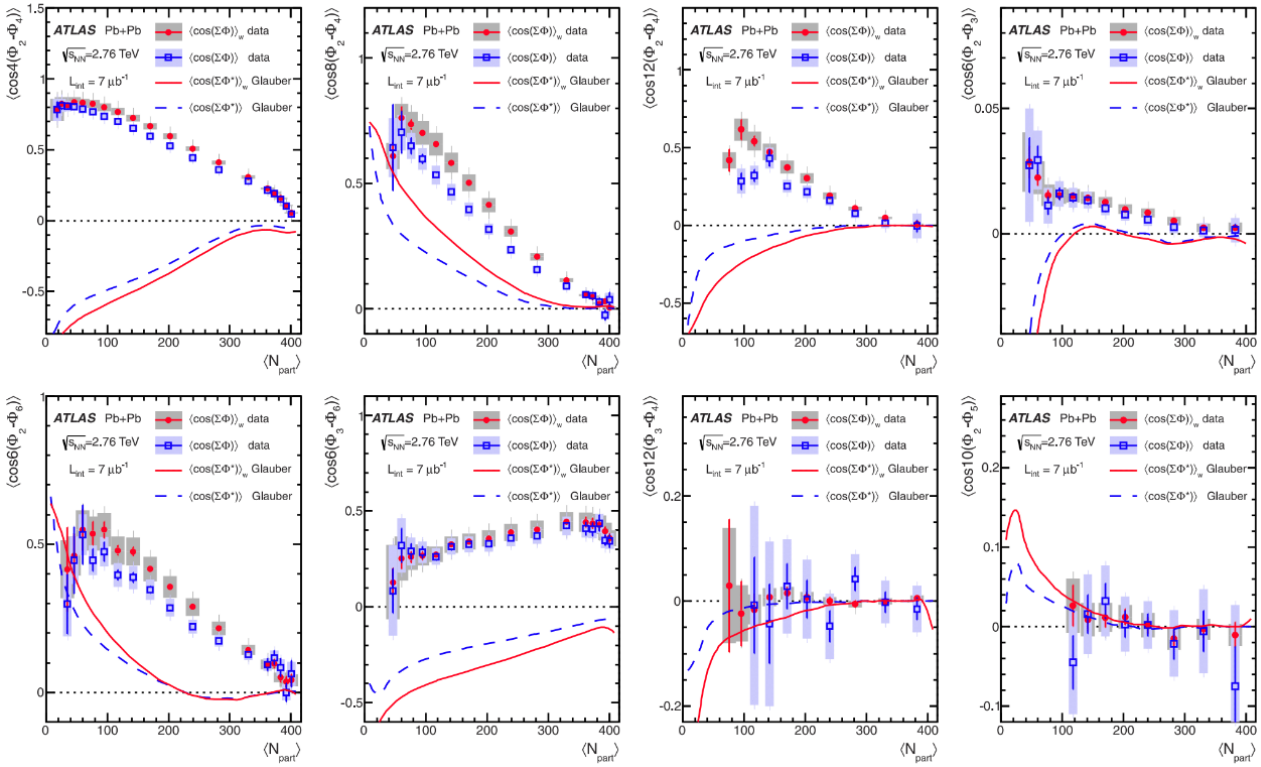

Figure 1.18: Dependence of eight symmetry planes correlators with respect to the number of participants N_{part} for Pb–Pb collisions at $\sqrt{s_{\rm NN}} = 2.76$ TeV by the ATLAS experiment [107].

on the cumulant expansion in terms of azimuthal angles for two different harmonics n and m. Initially called *Standard Candles*, these *Symmetric Cumulants* (SCs) have quickly become one of the most commonly used methods to measure the genuine correlations between v_n and v_m, as all contributions from the symmetry planes are cancelled out by definition. Another method is the Event Shape Engineering (ESE) first presented in Ref. [111]. Many analyses, both theoretical and experimental, have been made with these two different sets of observables. On the experimental side, measurements with the ESE techniques have first been reported in Pb–Pb collisions at $\sqrt{s_{\rm NN}} = 2.76$ TeV by the ATLAS Collaboration [112, 113]. Furthermore, ALICE announced similar measurements using the SCs for the same system and energies in Refs. [114, 115], quickly followed by systematic studies in Ref. [116][5].

The top panel of Fig. 1.19 represents the first results for the SCs as a function of the centrality obtained by ALICE for Pb–Pb collisions at $\sqrt{s_{\rm NN}} = 2.76$ TeV. The experimental measurements show that SC$(4, 2)$ has positive values for all centralities, which means the fluctuations between v_2 and v_4 are correlated event-by-event. More precisely, if the average of v_4, denoted by $\langle v_4 \rangle$, is smaller than v_4 in one event, the probability to find $\langle v_2 \rangle$ smaller than v_2 in the same event is increased. Furthermore, the values of SC$(3, 2)$ are all negative, suggesting that v_2 and v_3 are anticorrelated. Here, the probability to find $\langle v_3 \rangle$ larger than v_3 if $\langle v_2 \rangle$ is smaller than v_2 in a given event is enhanced. Nevertheless, the sign of the genuine correlations between two flow amplitudes is not the only conclusion one can draw from the top figure in Fig. 1.19. The results have been represented with the theoretical predictions for different parametrisations of the temperature dependence of η/s, denoted $\eta/s(T)$. These parametrisations are illustrated in the bottom left panel of Fig. 1.19 and they all have the same average $\langle \eta/s(T) \rangle = 0.20$ [118].

[5] For a historical summary of the studies about SCs, see the end of the introduction in Ref. [117].

Two conclusions can be drawn from the comparisons of the data to the theoretical predictions. First, the SCs are sensitive to $\eta/s(T)$, while the measurements of $v_n\{2\}$ are sensitive only to $\langle\eta/s(T)\rangle$, meaning there is no distinction between the details of the temperature dependence (see bottom right part of Fig. 1.19). Alternatively, there is then not a single parametrisation, which can describe both SC$(4,2)$ and SC$(3,2)$ in all centralities at the same time. From all these points, it is clear that the SCs give information that is not accessible from the measurements of the single flow amplitudes, and they allow the application of new constraints on the theoretical models used to describe the QGP evolution and properties.

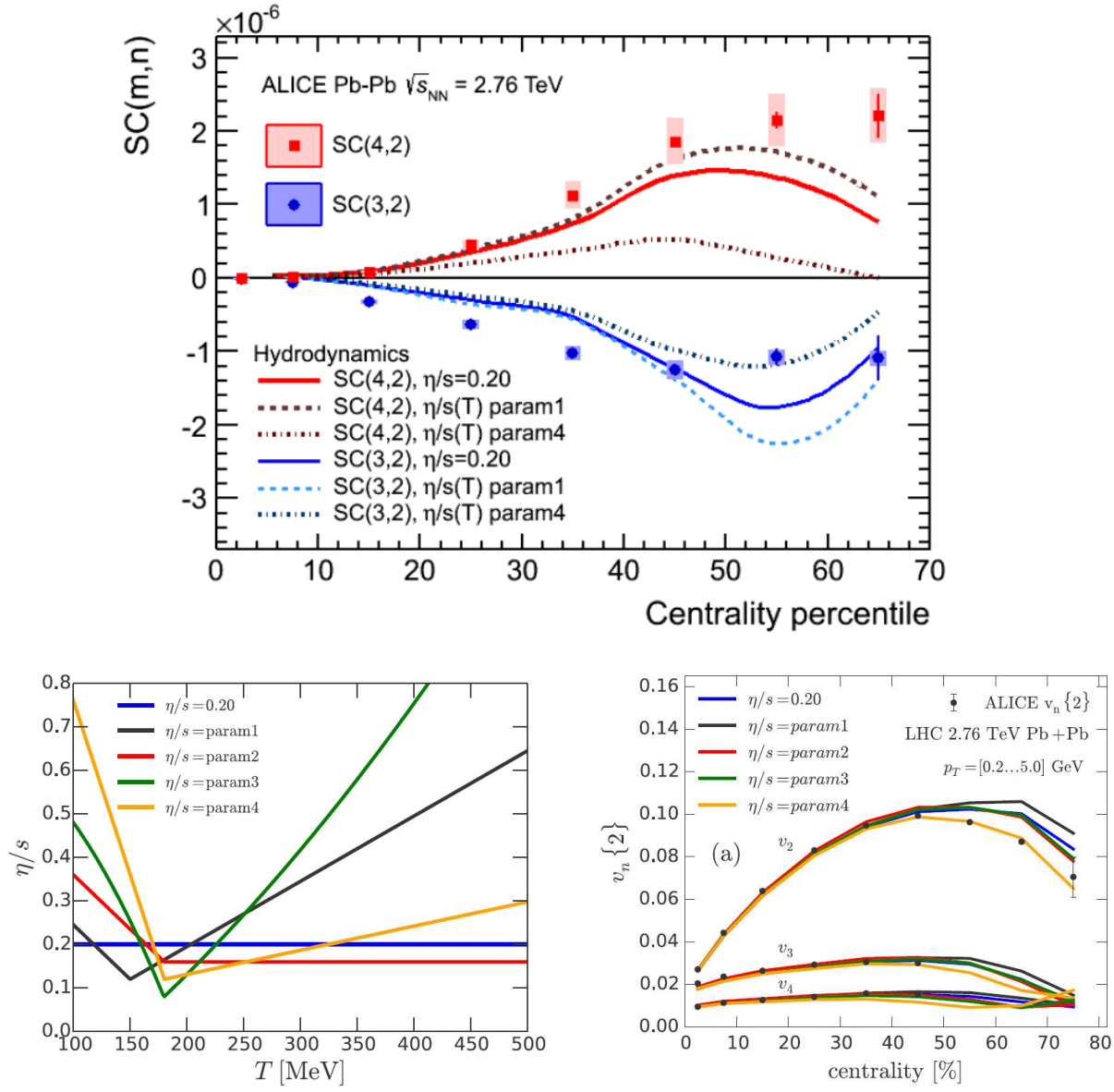

Figure 1.19: (*Top*) Centrality dependence of the correlations between v_4 and v_2 (SC$(4,2)$) in red and v_3 and v_2 (SC$(3,2)$) in blue from ALICE in Pb–Pb collisions at $\sqrt{s_{\rm NN}} = 2.76$ TeV [114]. The results are compared to the theoretical predictions with the parametrisations shown in Bottom left. (*Bottom left*) Various parametrisations of the temperature dependence of η/s, all with the same average $\langle\eta/s(T)\rangle = 0.20$ [118] (*Bottom right*) Centrality dependence of the two-particle cumulants of various v_n with the theoretical predictions corresponding to the parametrisations from bottom left [118].

From these conclusions, the next natural step is to probe the genuine correlations between more than two flow amplitudes. Similarly to the SCs, these new observables would indeed be sensitive to information that the previously used variables have no access to. Furthermore, as odd flow amplitudes develop only in the presence of fluctuations and even flow amplitudes can trivially be correlated from the presence of an elliptical geometry, measuring the correlations between even and odd harmonics would have the potential to separate between the magnitude and shape fluctuations of the initial geometry. From the measurements of genuine correlations between higher and lower order flow amplitudes, these novel observables would then help in the application of new and independent constraints on the non-linear response. An example of this point is the case SC$(2, 3, 5)$ which can help to probe the relation between v_5 and ϵ_2 and ϵ_3 (as v_2 and v_3 have a linear relation to ϵ_2 and ϵ_3 respectively).

The generalisation of the SCs to three and more flow amplitudes was first mentioned in Table 1 in Ref. [119]. This thesis presents the theoretical framework for this generalisation to any number of amplitudes. In a second step, this framework is extended to observables quantifying the genuine correlations between two and three flow amplitudes risen to distinct orders, the Asymmetric Cumulants (ACs). Finally, measurements of these generalised higher order SCs in Pb–Pb collisions collected by the ALICE experiment are presented along with the first predictions for the two-harmonic ACs.

Chapter 2

Theoretical Framework on Anisotropic Flow

As seen in Section 1.4, the quantification of the anisotropic flow in heavy-ion collisions relies on the measurement of its two sets of Fourier coefficients: the flow amplitudes v_n and the symmetry planes Ψ_n. Equation (1.14) relates v_n in an event with the azimuthal angles of the outgoing particles φ and the corresponding Ψ_n. While φ can be measured directly in the experiment, this is not the case for the symmetry planes. Many techniques have been designed over the years to determine them. One method traditionally used is the event plane (EP) method [89]. In this approach, the estimated symmetry plane Ψ_{EP}, also called the *event plane*, is given by

$$\Psi_n \simeq \Psi_{EP} \equiv \frac{1}{n} \arctan\left(\frac{\sum_i w_i \sin(n\varphi_i)}{\sum_i w_i \cos(n\varphi_i)}\right). \tag{2.1}$$

The summation index i represents the particles taken into account to determine the event plane, but not necessarily all the particles in the event itself. Moreover, as Ψ_{EP} is an approximation of the real Ψ_n, the difference between the two values needs to be corrected. The weights w_i are therefore introduced to ensure that the resolution $R = \langle \cos\left(n(\Psi_{EP} - \Psi_n)\right)\rangle$ is as good as possible. These weights can be optimised with a careful choice of the quantities used to compute them. It has to be noted that the weights generally differ between the odd and even harmonics [89]. The estimation of the anisotropic flow amplitude v_n, denoted with $v_n\{EP\}$, is calculated with [89]

$$v_n\{EP\} \equiv \frac{1}{R} \langle \cos\left(n(\varphi - \Psi_{EP})\right)\rangle. \tag{2.2}$$

This method is not without problems. First, the resolution of the event plane is limited, because of the finite number of detected final state particles. It follows that the observed flow amplitudes always show a bias. Furthermore, this method is valid only if the flow correlations dominate the system. In reality, other sources of correlations involving only a few particles, designed under the name of *nonflow*, are present as well in the system (see Section 2.1 for more details). They add systematic errors that need to be corrected with other techniques [89, 120].

However, the main issue with the event plane method is its inability to measure directly and event-by-event the symmetry planes in the collision. Alternative methods, the *multiparticle azimuthal correlations techniques*, have been developed to bypass this problem. They are presented in Section 2.1. Section 2.2 introduces the formalism of cumulants and its traditional use in flow analyses. In Section 2.3, the correlations between different flow amplitudes are discussed.

2.1 Multiparticle correlations techniques

The key idea behind the multiparticle correlations techniques is to determine the values of the flow amplitudes using only the azimuthal angles, with no knowledge of the symmetry planes. It is based on the assumption that the azimuthal correlations between two particles come from the azimuthal correlations each particle has with the reaction plane itself [83, 102]. One consequence of this assumption, known as *flow correlations* or *flow principle* in the literature, is the independence of the tracks of the outgoing particles.

For a one-particle three-momentum distribution $f(\mathbf{p}) \equiv \mathrm{d}N/\mathrm{d}^3\mathbf{p}$, Eq. (1.14) can be rewritten as

$$v_n(\mathcal{D}) \equiv \left\langle \mathrm{e}^{in(\varphi-\Psi_n)} \right\rangle_{\mathcal{D}} = \frac{\int_{\mathcal{D}} \mathrm{e}^{in(\varphi-\Psi_n)} f(\mathbf{p}) \mathrm{d}^3\mathbf{p}}{\int_{\mathcal{D}} f(\mathbf{p}) \mathrm{d}^3\mathbf{p}}, \tag{2.3}$$

where the brackets $\langle \ldots \rangle_{\mathcal{D}}$ represent the average over all particles in the event and $\mathcal{D}$ stands for the phase-space region where flow is measured, generally the detector phase-space in the (p_{T}, y)-plane. Indicating the two-particle distribution with $f(\mathbf{p}_1, \mathbf{p}_2) \equiv \mathrm{d}N/\mathrm{d}^3\mathbf{p}_1\mathrm{d}^3\mathbf{p}_2$, the two-particle correlation is calculated as follows [102]

$$\begin{aligned} \left\langle \mathrm{e}^{in(\varphi_1-\varphi_2)} \right\rangle_{\mathcal{D}_1\times\mathcal{D}_2} &= \frac{\int_{\mathcal{D}_1\times\mathcal{D}_2} \mathrm{e}^{in(\varphi_1-\varphi_2)} f(\mathbf{p}_1,\mathbf{p}_2) \mathrm{d}^3\mathbf{p}_1\mathrm{d}^3\mathbf{p}_2}{\int_{\mathcal{D}_1\times\mathcal{D}_2} f(\mathbf{p}_1,\mathbf{p}_2) \mathrm{d}^3\mathbf{p}_1\mathrm{d}^3\mathbf{p}_2} \\ &= \frac{\int_{\mathcal{D}_1\times\mathcal{D}_2} \mathrm{e}^{in(\varphi_1-\Psi_n)}\mathrm{e}^{-in(\varphi_2-\Psi_n)} f(\mathbf{p}_1) f(\mathbf{p}_2) \mathrm{d}^3\mathbf{p}_1\mathrm{d}^3\mathbf{p}_2}{\int_{\mathcal{D}_1\times\mathcal{D}_2} f(\mathbf{p}_1) f(\mathbf{p}_2) \mathrm{d}^3\mathbf{p}_1\mathrm{d}^3\mathbf{p}_2} \\ &= v_n(\mathcal{D}_1) v_n(\mathcal{D}_2). \end{aligned} \tag{2.4}$$

The assumption that only flow correlations are present in the system is used between the first and second equalities, allowing the factorisation of the distribution function, i.e. $f(\mathbf{p}_1, \mathbf{p}_2) = f(\mathbf{p}_1) f(\mathbf{p}_2)$. Furthermore, the two particles have the same phase–space, $\mathcal{D}_1 = \mathcal{D}_2$, meaning that

$$\left\langle \mathrm{e}^{in(\varphi_1-\varphi_2)} \right\rangle = v_n^2. \tag{2.5}$$

Equation (2.5) demonstrates that, in the case of a system with only flow correlations, the correlations between two particles come solely from their respective correlations to a common reaction plane. Moreover, the derivation in Eq. (2.4) can be easily extended to any even number of particles. For example, with the four-particle correlation, the final result is given by

$$\left\langle \mathrm{e}^{in(\varphi_1+\varphi_2-\varphi_3-\varphi_4)} \right\rangle = v_n^4. \tag{2.6}$$

Before going further, the following notation is introduced:

$$\langle 2 \rangle_{n,-n} \equiv \left\langle \mathrm{e}^{in(\varphi_1-\varphi_2)} \right\rangle, \tag{2.7}$$

$$\langle 4 \rangle_{n,n,-n,-n} \equiv \left\langle \mathrm{e}^{in(\varphi_1+\varphi_2-\varphi_3-\varphi_4)} \right\rangle. \tag{2.8}$$

These single-event averages can then be estimated with the sums over the azimuthal angles:

$$\langle 2 \rangle_{n,-n} = \frac{1}{\binom{M}{2} 2!} \sum_{\substack{j,k=1 \\ j\neq k}}^{M} \mathrm{e}^{in(\varphi_j-\varphi_k)}, \tag{2.9}$$

$$\langle 4 \rangle_{n,n,-n,-n} = \frac{1}{\binom{M}{4} 4!} \sum_{\substack{j,k,l,m=1 \\ j\neq k\neq l\neq m}}^{M} \mathrm{e}^{in(\varphi_j+\varphi_k-\varphi_l-\varphi_m)}. \tag{2.10}$$

The condition that all indices in the sum must be taken different is of an extreme importance in multiparticle correlations techniques. The case of the two-particle correlator $\langle 2 \rangle_{n,-n}$ will be used here as an illustration, but the argumentation can easily be extended to any number of particles in the correlator. If $j \neq k$ is not applied in Eq. (2.9), the term where $j = k$ will lead to the addition of $\mathrm{e}^{in(\varphi_j - \varphi_j)} = 1$ into the average. As one is the maximum value $\mathrm{e}^{in(\varphi_j - \varphi_k)}$ can take, this term will have a dominant effect in the computation of v_n^2. This severe systematic bias, known as *autocorrelations* or *self-correlations*, needs therefore to be removed.

The most general form for a k-particle correlator with a set of k harmonics $\{n_1, \ldots, n_k\}$ is defined as [110]

$$\langle k \rangle_{n_1,\ldots,n_k} \equiv \frac{\sum_{\substack{j_1,\ldots,j_k=1 \\ j_1 \neq \ldots \neq j_k}}^{M} w_{j_1} \ldots w_{j_k} \mathrm{e}^{i(n_1\varphi_{j_1} + \ldots + n_k\varphi_{j_k})}}{\sum_{\substack{j_1,\ldots,j_k=1 \\ j_1 \neq \ldots \neq j_k}}^{M} w_{j_1} \ldots w_{j_k}}, \tag{2.11}$$

with M being the multiplicity of the considered event. The k particle weights $\{w_{j_1}, \ldots, w_{j_k}\}$ are introduced to correct systematic biases from various detector inefficiencies. As such, they can be a function of the transverse momenta, pseudorapidities, azimuthal angles or particle species for example, i.e. $w = w(p_\mathrm{T}, \eta, \varphi, PID, \ldots)$. Examples of particle weights can be seen in Section 5.3.

One important remark is that the set of harmonics n_i cannot be randomly chosen. In the case of a detector with a uniform azimuthal acceptance, only the correlations that are isotropic — for which $n_1 + \ldots + n_k = 0$ — are non-zero in the passage from the single-event to the all-event average. All other combinations will cancel out due to the randomness of the reaction plane. Finally, it has to be noted that v_n is not directly accessible with this method. The correlations between two particles return v_n^2, between four particles v_n^4, and more generally, the k-particle correlations with a single harmonic n will give v_n^k.

This whole approach has recently been generalised to express both the flow amplitudes and symmetry planes for a set of k harmonics $\{n_1, \ldots, n_k\}$ using the k-particle correlator [79]

$$\langle k \rangle_{n_1,\ldots,n_k} \equiv \left\langle \mathrm{e}^{i(n_1\varphi_1 + \ldots + n_k\varphi_k)} \right\rangle = v_{n_1} \ldots v_{n_k} \mathrm{e}^{i(n_1\Psi_{n_1} + \ldots + n_k\Psi_{n_k})}. \tag{2.12}$$

Equation (2.12) is one of the main equations in flow analyses, as a whole set of new observables can be obtained by choosing carefully the number and values of the harmonics n_i. The question resides then in how one can compute the left term, and therefore Eq. (2.11), as exactly and as efficiently as possible. One naïve method is the use of nested loops with one loop per particle in the correlator $\langle k \rangle_{n_1,\ldots,n_k}$, with the additional condition to prevent the autocorrelations. However, this approach, while giving precise results, is not feasible in practice due to its large CPU costs. Each one of the k nested loops goes over the full multiplicity of outgoing particles, which can easily reach a few thousands in central heavy-ion collisions. Furthermore, v_n varies event-by-event and one generally looks at the all-event averages, meaning the k loops for the particles are nested in the main loop over all the events in consideration.

More efficient methods to compute Eq. (2.11) rely on an object called the *Q-vector*, or *flow vector*. For simplicity, the expressions and derivations shown now are done with the use of unit particle weights. The general case with non-unit particle weights will be treated in the next part.

For a harmonic n and a multiplicity M, the Q-vector Q_n is a complex quantity defined as

$$Q_n \equiv \sum_{k=1}^{M} \mathrm{e}^{in\varphi_k}. \tag{2.13}$$

The k-particle correlators can then be rewritten in terms of Q_n. For example, Eqs. (2.9) and (2.10) become

$$\langle 2 \rangle_{n,-n} = \frac{1}{\binom{M}{2} 2!} \left[|Q_n|^2 - M \right], \tag{2.14}$$

$$\langle 4 \rangle_{n,n,-n,-n} = \frac{1}{\binom{M}{4} 4!} \Big[|Q_n|^4 + |Q_{2n}|^2 - 2\Re\left[Q_{2n} Q_n^* Q_n^*\right] - 4(M-2)|Q_n|^2 + 2M(M-3) \Big]. \tag{2.15}$$

The demonstration for the two-particle correlations is shown in Appendix B.2. From these last expressions, two advantages of the Q_n can be deduced. First, instead of the multiple sums over the multiplicity of an event and nested loops, all the needed Q-vectors can be computed for different harmonics in a single passage over the M particles and then arranged to get the final correlators. Second, no additional condition to exclude the autocorrelations needs to be included in the calculation, as they are naturally removed in the derivation.

While expressing multiparticle correlators in terms of Q-vectors is more efficient than using nested loops, this method has also its drawbacks. One of them is its implementation. The number of terms in the analysis expressions quickly explodes with the order of the correlator and thus, their computation quickly becomes unfeasible. Furthermore, for a single multiparticle correlator, different harmonics are involved in the last expression and all the corresponding Q-vectors need to be calculated. For example, Q_n and Q_{2n} are needed to measure $\langle 4 \rangle_{n,n,-n,-n}$ in Eq. (2.15). Recursive algorithms have then been developed to address these issues. They make up the core of the so-called *Generic Framework* [110].

2.1.1 Generic Framework

The Generic Framework has been developed as an efficient way to compute exactly any k-particle correlator involving any choice of flow harmonics. Its most general form allows the use of non-unit particle weights to correct for detector effects. If not indicated otherwise, all expressions and notations introduced in this subsection are taken from Ref. [110].

The definition of the Q-vector Q_n from Eq. (2.13) can be generalised to include the set of M particle weights w_k using

$$Q_{n,p} \equiv \sum_{k=1}^{M} w_k^p \mathrm{e}^{in\varphi_k}. \tag{2.16}$$

As before, φ_k are their azimuthal angles with respect to the reaction plane and M is the number of detected particles. The following property derives naturally from this definition of the *weighted Q-vector*:

$$Q_{-n,p} = Q_{n,p}^*. \tag{2.17}$$

The following shortcut notation is introduced for the numerator and denominator of Eq. (2.11):

$$N \langle k \rangle_{n_1,\ldots,n_k} \equiv \sum_{\substack{j_1,\ldots,j_k=1 \\ j_1 \neq \ldots \neq j_k}}^{M} w_{j_1} \ldots w_{j_k} \mathrm{e}^{i(n_1\varphi_{j_1} + \ldots + n_k\varphi_{j_k})}, \tag{2.18}$$

$$D \langle k \rangle_{n_1,\ldots,n_k} \equiv \sum_{\substack{j_1,\ldots,j_k=1 \\ j_1 \neq \ldots \neq j_k}}^{M} w_{j_1} \ldots w_{j_k}. \tag{2.19}$$

Moreover, the denominator $D\langle k\rangle_{n_1,\ldots,n_k}$ can easily be expressed as a function of the numerator $N\langle k\rangle_{n_1,\ldots,n_k}$ by setting all harmonics n_i to zero in the latter, i.e.

$$D\langle k\rangle_{n_1,\ldots,n_k} = N\langle k\rangle_{0,\ldots,0}\,. \tag{2.20}$$

The numerators and denominators of the multiparticle correlators can then be rewritten in terms of the weighted Q-vectors. The two- and three-particle correlators are given here as examples. One has for the two-particle correlator

$$N\langle 2\rangle_{n_1,n_2} = Q_{n_1,1}Q_{n_2,1} - Q_{n_1+n_2,2}, \tag{2.21}$$
$$D\langle 2\rangle_{n_1,n_2} = N\langle 2\rangle_{0,0} = Q_{0,1}^2 - Q_{0,2}, \tag{2.22}$$

and for the three-particle correlator

$$\begin{aligned} N\langle 3\rangle_{n_1,n_2,n_3} &= Q_{n_1,1}Q_{n_2,1}Q_{n_3,1} + 2Q_{n_1+n_2+n_3,3} \\ &\quad - Q_{n_1+n_2,2}Q_{n_3,1} - Q_{n_1+n_3,2}Q_{n_2,1} - Q_{n_2+n_3,2}Q_{n_1,1}, \end{aligned} \tag{2.23}$$
$$D\langle 3\rangle_{n_1,n_2,n_3} = N\langle 3\rangle_{0,0,0} = Q_{0,1}^3 - 3Q_{0,2}Q_{0,1} + 2Q_{0,3}. \tag{2.24}$$

Looking at the previous equations allows the design of two different recursive algorithms to express the higher order correlators in terms of lower order ones. The first recursive algorithm is based on the observation that

$$N\langle 1\rangle_{n_1} = Q_{n_1,1}, \tag{2.25}$$
$$N\langle 2\rangle_{n_1,n_2} = N\langle 1\rangle_{n_1} Q_{n_2,1} - Q_{n_1+n_2,2}, \tag{2.26}$$
$$\begin{aligned} N\langle 3\rangle_{n_1,n_2,n_3} &= N\langle 2\rangle_{n_1,n_2} Q_{n_3,1} + 2Q_{n_1+n_2+n_3,3} \\ &\quad - Q_{n_1+n_3,2}N\langle 1\rangle_{n_2} - Q_{n_2+n_3,2}N\langle 1\rangle_{n_1}\,. \end{aligned} \tag{2.27}$$

In this case, $N\langle k\rangle_{n_1,\ldots,n_k}$ can be found through the ordering of the partitions of the set $\{n_1,\ldots,n_k\}$. The second recursive algorithm is obtained from Eq. (2.18) for the numerator. After some rewriting of the sums, one can find that

$$\begin{aligned} N\langle k\rangle_{n_1,\ldots,n_k} &= Q_{n_k,1}N\langle k-1\rangle_{n_1,\ldots,n_{k-1}} - N\langle k-1\rangle_{n_1+n_k,\ldots,n_{k-1}} \\ &\quad - N\langle k-1\rangle_{n_1,n_2+n_k,\ldots,n_{k-1}} - \ldots - N\langle k-1\rangle_{n_1,\ldots,n_{k-1}+n_k}\,. \end{aligned} \tag{2.28}$$

The pseudocodes for both algorithms can be found in Ref. [110]. The computation of the multiparticle correlators used in this thesis uses an implementation of the second algorithm[1].

2.1.2 Transition to all-event averages

All equations presented above are for single-event averages. However, as already mentioned, the final quantities of interest must take into account all the events selected for the analysis. The single-event observables must therefore be averaged over these events. For a k-particle correlator, the all-event average is defined as [121]

$$\langle\langle k\rangle\rangle_{n_1,\ldots,n_k} \equiv \frac{\sum_{i=1}^{N_{\text{events}}}\left(W_{\langle k\rangle_{n_1,\ldots,n_k}}\right)_i\left(\langle k\rangle_{n_1,\ldots,n_k}\right)_i}{\sum_{i=1}^{N_{\text{events}}}\left(W_{\langle k\rangle_{n_1,\ldots,n_k}}\right)_i}, \tag{2.29}$$

where N_{events} is the number of analysed events, $\left(\langle k\rangle_{n_1,\ldots,n_k}\right)_i$ are the single-average k-particle correlators for each one of these events and $\left(W_{\langle k\rangle_{n_1,\ldots,n_k}}\right)_i$ the corresponding event weights.

[1] Credits to K. Gulbrandsen for the initial implementation of the C++ recursive algorithm used in this work.

In heavy-ion collisions, the number of outgoing particles varies event-by-event. If a simple averaging between the single-event correlator was done, the events with lower multiplicities would count as much as the events with higher multiplicities, which may bias the final results. Two techniques can then be used. The first one is to take the same number of particles in each event. In this case, unit event weights can be used. The other method is to choose multiplicity-dependent event weights. It has been shown that the choice of weights that minimise the statistical spread corresponds to the number of combinations of k particles one can do in an event with multiplicity M. It is possible to show that in the general case of non-unit particle weights, the event weight corresponds to the denominator $D\langle k\rangle_{n_1,\ldots,n_k}$. With unit particle weights, the event weights for the two- and four-particle correlators are given respectively by

$$W_{\langle 2\rangle_{n_1,n_2}} = M(M-1), \tag{2.30}$$

$$W_{\langle 4\rangle_{n_1,n_2,n_3,n_4}} = M(M-1)(M-2)(M-3), \tag{2.31}$$

where it has been used that the sum of particle weights $M' \equiv \sum_{j=1}^{M} w_j$ is equal to the usual multiplicity for $w_j = 1$.

2.1.3 Flow and nonflow

As seen in Section 2.1, the multiparticle correlations techniques rely on the flow principle. This idea is for example used in the derivation of the two-particle correlator, where it allows the factorisation of the two-particle probability density function (p.d.f.) into the product of two identical univariate p.d.f. (Eq. (2.4)). However, this assumption completely neglects the other sources of correlations that can exist between the azimuthal angles of two or more particles, with no dependence on the reaction plane and its orientation. Examples of such effects are the momentum conservation, resonances decays and jets, final states interactions, but also the quantum correlations between identical particles also known as the Hanbury-Brown and Twiss effects [122, 123]. As flow is related to the collective behaviour of all the outgoing particles and all these sources generally involve only a few particles, they are gathered under the name of *nonflow*. Figure 2.1 illustrates the flow collectivity (left) and an example of nonflow (right).

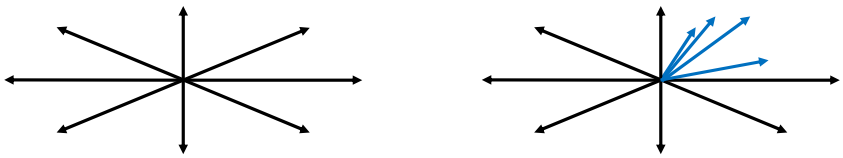

Figure 2.1: (*Left*) Illustration of the collective flow between all outgoing particles. (*Right*) Example of nonflow with four directly correlated particles shown in blue.

In presence of nonflow, the factorisation of the multivariate p.d.f. breaks down, which leads to a systematic bias in the evaluation of the flow amplitudes v_n, i.e. $f(\mathbf{p}_1,\ldots,\mathbf{p}_k) \neq f(\mathbf{p}_1)\cdots f(\mathbf{p}_k)$ for k particles. In terms of azimuthal angles, this can be written as $f(\varphi_1,\ldots,\varphi_k) \neq f(\varphi_1)\cdots f(\varphi_k)$.

For an event with multiplicity M, the nonflow contribution to a k-particle correlator δ_k is expressed with the scaling [102, 117]

$$\delta_k \sim \frac{1}{M^{k-1}}. \tag{2.32}$$

This behaviour can be understood with the following probability example based on the right panel of Fig. 2.1. If one of the four "blue" particles is taken in the computation of the four-

particle correlator for an event with M particles in total, the probability δ_4 to exactly take the three other "blue" particles goes as

$$\delta_4 \sim \frac{3}{M-1}\frac{2}{M-2}\frac{1}{M-3} \approx \frac{1}{M^3}, \tag{2.33}$$

if M is large enough. This approximation can be made as correlators involve generally only a few particles, while the multiplicities in heavy-ion collisions can easily reach a few hundred of detected particles.

Based on the scaling in Eq. (2.32), it is visible that the contribution from nonflow in the system decreases with the number of particles in the correlator. This conclusion is not unexpected, as it is more probable for a particle to decay into or be reconstructed as two than four or more particles. One could therefore use higher numbers of particles in the correlators to compute the flow coefficients without nonflow bias. However, this method is not recommendable in practise as it becomes quickly statistically demanding. The reason is that the higher order correlators estimate smaller and smaller terms like v^4, v^6 and so on, using correlators with values between 1 and -1. More effective techniques have therefore been developed to decrease, and even remove, nonflow contributions. They are discussed in the next section.

2.2 Formalism of cumulants

While the use of higher order correlators decreases the influence of nonflow, it requires previous knowledge of its sources. A new method based on the formalism of cumulants has then been developed to help with this problem [83,102,103]. In order to give a general understanding of the concept of cumulants, a simple step-by-step approach is first illustrated with the one-, two- and three-particle cumulants. In the second part of this section, the mathematical formalism is presented. Finally, it will be shown how these developments can be applied to flow analyses.

2.2.1 Conceptual approach

For any number of particles k, the particle distribution $f(\varphi_1, \ldots, \varphi_k)$ can be divided into the sum of its correlated and uncorrelated contributions. The division is trivial with one particle, i.e. $f(\varphi_1) = f_c(\varphi_1)$, where f_c indicates the particles in the term are correlated with each other. In the case of two particles, the distribution becomes [83,102]

$$\begin{aligned} f(\varphi_1, \varphi_2) &= f_c(\varphi_1) f_c(\varphi_2) + f_c(\varphi_1, \varphi_2) \\ &= f(\varphi_1) f(\varphi_2) + f_c(\varphi_1, \varphi_2), \end{aligned} \tag{2.34}$$

where the relation for one particle has been used in the second equality. The second term $f_c(\varphi_1, \varphi_2)$ is the so-called *cumulant*, which represents the genuine correlation between all the particles in the distribution. While it may seem more complicated at the first glance, the decomposition of the three-particle distribution follows the same pattern, i.e.

$$\begin{aligned} f(\varphi_1, \varphi_2, \varphi_3) = {} & f(\varphi_1) f(\varphi_2) f(\varphi_3) + f_c(\varphi_1, \varphi_2) f(\varphi_3) \\ & + f_c(\varphi_1, \varphi_3) f(\varphi_2) + f_c(\varphi_2, \varphi_3) f(\varphi_1) \\ & + f_c(\varphi_1, \varphi_2, \varphi_3). \end{aligned} \tag{2.35}$$

This decomposition, along with the one for the two-particle case, is illustrated in Fig. 2.2. Inserting Eq. (2.34) allows the rewriting of Eq. (2.35) into

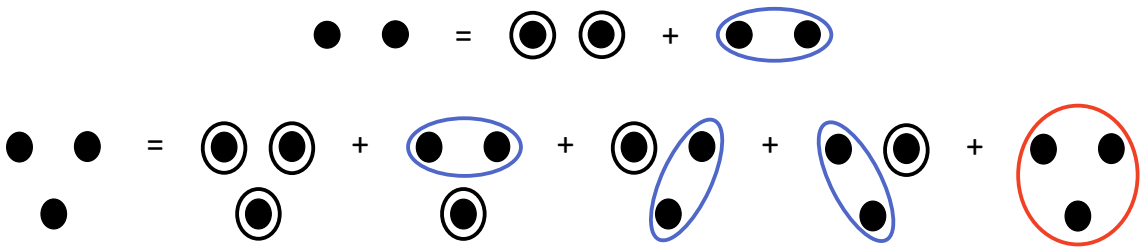

Figure 2.2: Decomposition of the two-particle distribution (*top*) and the three-particle distribution (*bottom*) into their correlated and uncorrelated parts. The ellipses indicate the genuine correlations between the particles inside. Inspired from [102].

$$\begin{aligned} f_c(\varphi_1,\varphi_2,\varphi_3) = f(\varphi_1,\varphi_2,\varphi_3) &- f(\varphi_1,\varphi_2) f(\varphi_3) \\ &- f(\varphi_1,\varphi_3) f(\varphi_2) - f(\varphi_2,\varphi_3) f(\varphi_1) \\ &+ 2 f(\varphi_1) f(\varphi_2) f(\varphi_3). \end{aligned} \tag{2.36}$$

The term $f_c(\varphi_1,\varphi_2,\varphi_3)$ is then the three-particle cumulant. The genuine k-particle correlations can therefore be understood as what remains of the k-particle distribution once all the l-particle correlations, $l < k$, have been subtracted.

2.2.2 Mathematical formalism

While the recursive procedure followed above could be generalised to express the higher order genuine correlations, it becomes easier to get them using the mathematical formalism presented by Kubo in Ref. [124]. The following definitions and notations are taken from Refs. [124, 125]. For a set of N random variables $X_1,\ldots,X_N$ and multivariate p.d.f. $f(X_1,\ldots,X_N)$, the moments are defined with

$$\mu_{\nu_1,\ldots,\nu_N} \equiv \int X_1^{\nu_1}\cdots X_N^{\nu_N} f(X_1,\ldots,X_N)\, dX_1\cdots dX_N. \tag{2.37}$$

Using the *moment generating function* $M(\xi_1,\ldots,\xi_N) \equiv \left\langle \mathrm{e}^{\sum_{j=1}^{N}\xi_j X_j}\right\rangle$, this definition can be rewritten as

$$\mu_{\nu_1,\ldots,\nu_N} = \frac{\partial^{\nu_1}}{\partial\xi_1^{\nu_1}}\cdots\frac{\partial^{\nu_N}}{\partial\xi_N^{\nu_N}} M(\xi_1,\ldots,\xi_N)\Big|_{\xi_1=\ldots=\xi_N=0}. \tag{2.38}$$

The *cumulant generating function* $K(\xi_1,\ldots,\xi_N)$ is then defined in terms of the moment generating function with

$$K(\xi_1,\ldots,\xi_N) \equiv \ln M(\xi_1,\ldots,\xi_N) = \ln\left\langle \mathrm{e}^{\sum_{j=1}^{N}\xi_j X_j}\right\rangle. \tag{2.39}$$

Similarly as for the moments μ, the cumulants are then obtained through

$$\kappa_{\nu_1,\ldots,\nu_N} = \frac{\partial^{\nu_1}}{\partial\xi_1^{\nu_1}}\cdots\frac{\partial^{\nu_N}}{\partial\xi_N^{\nu_N}} K(\xi_1,\ldots,\xi_N)\Big|_{\xi_1=\ldots=\xi_N=0}. \tag{2.40}$$

The following notations will be used interchangeably through this thesis:

$$\mu_{\nu_1,\ldots,\nu_N} \equiv \mu(X_1^{\nu_1},\ldots,X_N^{\nu_N}) \equiv \langle X_1^{\nu_1}\cdots X_N^{\nu_N}\rangle, \tag{2.41}$$

$$\kappa_{\nu_1,\ldots,\nu_N} \equiv \kappa(X_1^{\nu_1},\ldots,X_N^{\nu_N}) \equiv \langle X_1^{\nu_1}\cdots X_N^{\nu_N}\rangle_c. \tag{2.42}$$

The first cumulants expressed in terms of moments are given here as examples [125]:

$$\begin{aligned}
\kappa_1 &= \mu_1, \\
\kappa_2 &= \mu_2 - {\mu_1}^2, \\
\kappa_{1,1} &= \mu_{1,1} - \mu_{0,1}\mu_{1,0}, \\
\kappa_{2,1} &= 2\mu_{0,1}{\mu_{1,0}}^2 - 2\mu_{1,1}\mu_{1,0} - \mu_{0,1}\mu_{2,0} + \mu_{2,1}, \\
\kappa_{1,2} &= 2\mu_{1,0}{\mu_{0,1}}^2 - 2\mu_{1,1}\mu_{0,1} - \mu_{0,2}\mu_{1,0} + \mu_{1,2}, \\
\kappa_{1,1,1} &= 2\mu_{0,0,1}\mu_{0,1,0}\mu_{1,0,0} - \mu_{0,1,1}\mu_{1,0,0} - \mu_{0,1,0}\mu_{1,0,1} - \mu_{0,0,1}\mu_{1,1,0} + \mu_{1,1,1}.
\end{aligned} \tag{2.43}$$

Furthermore, $\kappa_{1,1}$ and $\kappa_{1,1,1}$ can be identified with the expressions given by Eqs. (2.34) and (2.35) respectively.

Mathematical properties of cumulants

Consider a variable made from a set of N stochastic observables $X_1, \ldots, X_N$. In order to be a valid multivariate cumulant, this candidate variable must check out the following list of properties. It has to be noted that the demonstration of all these properties can be found in the Appendix A of Ref. [125].

Statistical independence. The cumulant $\kappa_{\nu_1,\ldots,\nu_N}$ represents the genuine correlations between all the elements $X_1, \ldots, X_N$. Therefore, if the set of N observables can be divided into two or more statistically independent subsets, the resulting cumulant must be zero. A consequence of this is that $\kappa_{\nu_1,\ldots,\nu_N} = 0$ if and only if at least one X_j is statistically independent from the others.

Reduction. If some of the random observables $X_1, \ldots, X_N$ are set identical to each other, the reduced cumulant corresponds to the expression of a lower order cumulant, i.e.

$$\kappa_{\nu_1,\ldots,\nu_N} = \langle X_1^{\nu_1} \cdots X_N^{\nu_N} \rangle_c = \left\langle X_1^{\tilde{\nu}_1} \cdots X_M^{\tilde{\nu}_M} \right\rangle_c = \kappa_{\tilde{\nu}_1,\ldots,\tilde{\nu}_M}, \tag{2.44}$$

with $M < N$ and $\tilde{\nu}_j$ being the sum of all exponents of X_j. Furthermore, if all observables are set equal to X, the final result is a univariate cumulant of X of order $\nu_1 + \cdots + \nu_N$ with

$$\kappa_{\nu_1,\ldots,\nu_N} = \langle X_1^{\nu_1} \cdots X_N^{\nu_N} \rangle_c = \left\langle X^{\nu_1+\cdots+\nu_N} \right\rangle_c = \kappa_{\nu_1+\cdots+\nu_N}. \tag{2.45}$$

Semi-invariance. Consider a cumulant $\kappa_{\nu_1,\ldots,\nu_N}$ with $\sum_{i=1}^{N} \nu_i \geq 2$, meaning either at least one index $\nu_i \geq 2$, either at least two indices are equal to one. This cumulant is semi-invariant, i.e.

$$\kappa\left((X_1 + c_1)^{\nu_1}, \ldots, (X_N + c_N)^{\nu_N}\right) = \kappa\left(X_1^{\nu_1}, \ldots, X_N^{\nu_N}\right), \tag{2.46}$$

with $c_1, \ldots, c_N$ being a set of N constants. In the case where only one $\nu_i = 1$ and all the others $\nu_j = 0$, this property becomes

$$\kappa(1, \ldots, 1, X_i + c_i, 1, \ldots, 1) = c_i + \kappa(1, \ldots, 1, X_i, 1, \ldots, 1). \tag{2.47}$$

From this expression, the semi-invariance of a cumulant of a single variable is deduced to be

$$\kappa((X + c)^{\nu}) = \kappa(X^{\nu}), \tag{2.48}$$

where $\nu \geq 2$ and c is a constant.

Homogeneity. Let $c_1, \ldots, c_N$ be a set of N constants. The homogeneity property is then written as

$$\kappa((c_1 X_1)^{\nu_1}, \ldots, (c_N X_N)^{\nu_N}) = c_1^{\nu_1} \cdots c_N^{\nu_N} \kappa(X_1^{\nu_1}, \ldots, X_N^{\nu_N}). \tag{2.49}$$

In the case of a univariate cumulant, this property translates into

$$\kappa((cX)^{\nu}) = c^{\nu}\kappa(X^{\nu}), \tag{2.50}$$

with c a constant.

Multilinearity. For any linear variable, the multilinearity is satisfied if the cumulant of the sum of this variable is equal to the sum of the cumulant of each term. For example, if the first variable is linear (denoted by X_i) and the $N-1$ are either linear ($\nu_i = 1$) or non-linear ($\nu_i > 1$) (denoted by $Z_j^{\nu_j}$), the property is given by

$$\kappa(\sum_i X_i, Z_2^{\nu_2}, ..., Z_N^{\nu_N}) = \sum_i \kappa(X_i, Z_2^{\nu_2}, ..., Z_N^{\nu_N})\,. \tag{2.51}$$

This property can easily be generalised to more linear variables.

Additivity. For a univariate cumulant, if all the X_i are statistically independent, it follows that

$$\kappa((\sum_i X_i)^N) = \sum_i \kappa(X_i^N). \tag{2.52}$$

This requirement generalises straightforwardly for two and more statistically independent stochastic observables. In this case, the N-th order cumulant of the sum is again the sum of their N-th order cumulants.

Change of basis. Let $\kappa_{\nu_1,...,\nu_N}$ be a cumulant of the set of variables $X_1, \ldots, X_N$. Consider now these $X_1, \ldots, X_N$ to be themselves function of a set of N observables $Y_1, \ldots, Y_N$. It can be then shown that $\kappa_{\nu_1,...,\nu_N}$ is generally not a cumulant of this second basis, $Y_1, \ldots, Y_N$.

2.2.3 Application to flow analyses

Two of the most used observables in flow analyses are $v_n\{2\}$ and $v_n\{4\}$. They correspond to the estimations of the flow amplitude v_n with two- and four-particle cumulants, respectively. As the correlators used to calculate the cumulants are expressed in terms of Q-vectors, the method is often referred to as the *Q-cumulants*. The starting point of $v_n\{2\}$ is $\kappa_{1,1}$ with $X_1 = \mathrm{e}^{in\varphi_1}$ and $X_2 = \mathrm{e}^{-in\varphi_2}$. This choice of sign is made to ensure the isotropy of the final correlator. Using the notation introduced above, the single-event two-particle cumulant is given by

$$\left\langle \mathrm{e}^{in(\varphi_1-\varphi_2)} \right\rangle_c = \left\langle \mathrm{e}^{in(\varphi_1-\varphi_2)} \right\rangle - \left\langle \mathrm{e}^{in\varphi_1} \right\rangle \left\langle \mathrm{e}^{-in\varphi_2} \right\rangle. \tag{2.53}$$

Because of the randomness of the reaction plane, each half of the second term goes to zero in the transition from the single- to the all-event average. The two-particle cumulant itself is therefore expressed with

$$c_n\{2\} \equiv \left\langle \left\langle \mathrm{e}^{in(\varphi_1-\varphi_2)} \right\rangle \right\rangle_c = \left\langle \left\langle \mathrm{e}^{in(\varphi_1-\varphi_2)} \right\rangle \right\rangle = \left\langle v_n^2 \right\rangle, \tag{2.54}$$

where Eq. (2.12) has been used in the last equality. This relation means that

$$v_n\{2\} = \sqrt{c_n\{2\}}. \tag{2.55}$$

The development of the four-particle cumulant follows the same strategy, starting from $\kappa_{1,1,1,1}$, i.e.

$$\begin{aligned}\kappa_{1,1,1,1} = &-6\mu_{0,0,0,1}\mu_{0,0,1,0}\mu_{0,1,0,0}\mu_{1,0,0,0} + 2\mu_{0,0,1,1}\mu_{0,1,0,0}\mu_{1,0,0,0} + 2\mu_{0,0,1,0}\mu_{0,1,0,1}\mu_{1,0,0,0} \\ &+ 2\mu_{0,0,0,1}\mu_{0,1,1,0}\mu_{1,0,0,0} - \mu_{0,1,1,1}\mu_{1,0,0,0} + 2\mu_{0,0,1,0}\mu_{0,1,0,0}\mu_{1,0,0,1} - \mu_{0,1,1,0}\mu_{1,0,0,1} \\ &+ 2\mu_{0,0,0,1}\mu_{0,1,0,0}\mu_{1,0,1,0} - \mu_{0,1,0,1}\mu_{1,0,1,0} - \mu_{0,1,0,0}\mu_{1,0,1,1} + 2\mu_{0,0,0,1}\mu_{0,0,1,0}\mu_{1,1,0,0} \\ &- \mu_{0,0,1,1}\mu_{1,1,0,0} - \mu_{0,0,1,0}\mu_{1,1,0,1} - \mu_{0,0,0,1}\mu_{1,1,1,0} + \mu_{1,1,1,1}.\end{aligned} \tag{2.56}$$

Using the identification $X_1 = \mathrm{e}^{in\varphi_1}$, $X_2 = \mathrm{e}^{in\varphi_2}$, $X_3 = \mathrm{e}^{-in\varphi_3}$ and $X_4 = \mathrm{e}^{-in\varphi_4}$, all the terms that are not isotropic cancel out when the all-event average is taken, resulting in a four-particle cumulant given by

$$\begin{aligned} c_n\{4\} &\equiv \left(\langle\langle 4\rangle\rangle_{n,n,-n,-n}\right)_c = \langle\langle 4\rangle\rangle_{n,n,-n,-n} - 2\left(\langle\langle 2\rangle\rangle_{n,-n}\right)^2, \\ &= \left\langle v_n^4 \right\rangle - 2\left\langle v_n^2 \right\rangle^2. \end{aligned} \tag{2.57}$$

The flow amplitude v_n estimated from $c_n\{4\}$ is then obtained with

$$v_n\{4\} = \sqrt[4]{-c_n\{4\}}. \tag{2.58}$$

Using the same procedure, one can obtain the estimations of v_n using more particles. For example, the six- and eight-particle estimations are defined as

$$v_n\{6\} = \sqrt[6]{c_n\{6\}/4}, \tag{2.59}$$

$$v_n\{8\} = \sqrt[8]{-c_n\{8\}/33}, \tag{2.60}$$

where the six-particle cumulant $c_n\{6\}$ is based on $\kappa_{1,1,1,1,1,1}$ and the eight-particle cumulant $c_n\{8\}$ on $\kappa_{1,1,1,1,1,1,1,1}$.

The order of the cumulant in the notation of the estimate of the flow amplitude shows its importance when considering the interacting system as a whole. In the ideal situation without nonflow nor statistical fluctuations, it can be shown that all estimates are equal, i.e. $v_n = v_n\{2\} = v_n\{4\} = v_n\{6\} = v_n\{8\}$ and so forth. In presence of nonflow and statistical fluctuations, the estimates will show systematic biases. This effect is visible for example in Figs. 2 and 3 in Ref. [126].

2.3 Symmetric Cumulants

While the cumulants have shown their usefulness in reducing the nonflow contribution in the computation of the flow amplitudes, it is not their only strength. By nature, they probe the genuine correlations between the elements involved. They can therefore analyse the relations between two different flow amplitudes v_m and v_n. The observables designed for this purpose are the SCs.

In the traditional approach based on azimuthal angles, the two-harmonic SC is constructed from the fourth order cumulant $\kappa_{1,1,1,1}$. The choice of variables made for $v_n\{4\}$ in Eq. (2.56) is generalised for two different harmonics m and n into $X_1 = \mathrm{e}^{im\varphi_1}$, $X_2 = \mathrm{e}^{in\varphi_2}$, $X_3 = \mathrm{e}^{-im\varphi_3}$ and $X_4 = \mathrm{e}^{-in\varphi_4}$. Following the same procedure as in the previous section, the remaining expression is given by [114, 116]

$$\mathrm{SC}(m,n) \equiv \left(\langle\langle 4\rangle\rangle_{m,n,-m,-n}\right)_c = \langle\langle 4\rangle\rangle_{m,n,-m,-n} - \langle\langle 2\rangle\rangle_{m,-m}\langle\langle 2\rangle\rangle_{n,-n}. \tag{2.61}$$

Using again Eq. (2.12), SCs can be expressed in terms of the flow amplitudes themselves with

$$\mathrm{SC}(m,n) = \left\langle v_m^2 v_n^2 \right\rangle - \left\langle v_m^2 \right\rangle \left\langle v_n^2 \right\rangle. \tag{2.62}$$

It has to be noted that, while SCs are built from a four-particle cumulant with the azimuthal angles as fundamental observables, they can be interpreted as second order cumulants of the flow amplitudes squared, i.e. v_m^2 and v_n^2. As such, they present some interesting properties of cumulants. For example, if flow fluctuations are absent or if their magnitudes are uncorrelated,

the resulting SC will be zero by definition. Furthermore, as visible in Eq. (2.62), they do not show any contribution from the symmetry planes Ψ_m and Ψ_n or any relation they may have. Therefore, any measurement of a non-zero SC can be straightforwardly interpreted as the existence of genuine correlations between the two flow amplitudes.

Equation (2.62) can easily be rewritten as

$$\mathrm{SC}(m,n) = \left\langle \left(v_m^2 - \left\langle v_m^2 \right\rangle\right)\left(v_n^2 - \left\langle v_n^2 \right\rangle\right)\right\rangle . \tag{2.63}$$

Doing so allows an easier interpretation of the signature of the corresponding cumulant [110,114]. A positive $\mathrm{SC}(m,n)$ implies that the event-by-event fluctuations of v_m and v_n are correlated. This means that if, in a given event, v_m is found to be larger than its sample mean $\langle v_m \rangle$, it is then more probable to find equally v_n larger than $\langle v_n \rangle$ in the same event. This is, for example, the case for $\mathrm{SC}(4,2)$ as shown in the top panel in Fig. 1.19. On the other hand, a negative value of $\mathrm{SC}(m,n)$ is a sign of anticorrelation between v_m and v_n, i.e. finding v_m larger than $\langle v_m \rangle$ increases the probability to have v_n smaller than $\langle v_n \rangle$ in the same event. $\mathrm{SC}(3,2)$ is a good example of such a signature.

The cumulant properties and signatures are not the only interesting elements about the SCs. As they are initially constructed out of a four-particle cumulant, they are less sensitive to nonflow effects than their individual two- and four-particle correlators taken individually. Using the nonflow scaling of Eq. (2.32) explained in Section 2.1, one can express the nonflow scaling of a two-harmonic SC, δ_2^{SC}, as

$$\delta_2^{\mathrm{SC}} \sim \delta_4 + (\delta_2)^2 = \frac{\alpha}{M^3} + \frac{\beta}{M^2}, \tag{2.64}$$

where δ_4 and δ_2 are the generic nonflow scalings of the four- and two-particle azimuthal correlators, respectively.

In theoretical studies, the eccentricities ϵ_n in the initial state are accessible for each harmonic n. It is, therefore, possible to obtain predictions of their genuine correlations with

$$\mathrm{SC}_\epsilon(m,n) \equiv \left\langle \epsilon_m^2 \epsilon_n^2 \right\rangle - \left\langle \epsilon_m^2 \right\rangle \left\langle \epsilon_n^2 \right\rangle . \tag{2.65}$$

However, the results obtained in the initial and in the final states cannot be straightforwardly compared, as they present different scales. To solve this issue, the normalised SCs (NSCs), defined as

$$\mathrm{NSC}(m,n) \equiv \frac{\mathrm{SC}(m,n)}{\langle v_m^2 \rangle \langle v_n^2 \rangle}, \tag{2.66}$$

$$\mathrm{NSC}_\epsilon(m,n) \equiv \frac{\mathrm{SC}_\epsilon(m,n)}{\langle \epsilon_m^2 \rangle \langle \epsilon_n^2 \rangle}, \tag{2.67}$$

are used. With the help of the NSCs, it becomes possible to study the effects of the collective evolution in the genuine correlations present in the initial stages of the collision. For instance, a superposition of the predictions for $\mathrm{NSC}_\epsilon(m,n)$ and $\mathrm{NSC}(m,n)$ shows that the principal contribution to the correlations comes from the initial state. Such results can then help to apply constraints on the models used to describe the initial state. On the other hand, major differences in the comparisons between the two sets of results show that the hydrodynamic evolution has an impact on the interplay between the flow magnitudes.

Furthermore, the NSCs are not only useful to compare the correlations between the initial and final states of the collisions. While the flow amplitudes, and consecutively the SCs, show a dependence to the p_{T} range used in the analysis, their ratio is completely insensitive to it. This property allows the comparison of results obtained in different p_{T} ranges, for instance, between data from different experiments.

Chapter 3

A Large Ion Collider Experiment

The experimental part of the present work is based on data collected with A Large Ion Collider Experiment (ALICE) at the LHC. After an overview of CERN and the LHC itself in Section 3.1, ALICE and the main detectors used in the analysis are reviewed in more details in Section 3.2.

3.1 The Large Hadron Collider

Known under the names of "European Organisation for Nuclear Research" or "European Laboratory for Particle Physics", the CERN[1] complex is an institution dedicated to the understanding of the most fundamental components of matter and their interactions [127–129]. The main campus is near Geneva, on the border between Switzerland and France. It consists of a full chain of accelerators (Fig. 3.1), designed to bring various species of particles to higher and higher energies. These particles collide then at four specific Interaction Points (IPs) where the major detectors are situated. The last accelerator of the chain and the one of interest here, the LHC, can work with various nuclei, from the protons to the heavier ions like xenon or lead. Depending on the species, the beams do not start at the same place.

The protons originate from the ionisation of hydrogen atoms from a gas bottle at the start of the linear accelerator Linac2, where they are accelerated to 50 MeV. This beam of protons goes then to the Proton Synchrotron Booster (PSB), formed of four superimposed synchrotron rings. At their ejection from the PSB, the protons have an energy of 1.4 GeV and are grouped in large bunches from the four rings [127]. The next element of the chain is the Proton Synchrotron (PS), which serves multiple roles. Besides accelerating the proton beams to 25 GeV, it prepares the bunches for the SPS and the LHC. These bunches received from the PSB are split consecutively until 2808 of them, each containing about 1.15×10^{11} protons, are travelling in one of the two rings of the LHC with a spacing of 25 ns. They are then injected into the SPS where they reach an energy of 450 GeV before being used for physics studies or sent to the final accelerator of the chain, the LHC, where they are brought to energies of the order of the TeV before being collided.

Already in the early stages of the design of the LHC itself, plans have been made to allow the collisions of heavy ions. Initially, only fully stripped lead ion beams were thought, but as already mentioned, xenon has also been recently used. A purified lead sample is placed at the beginning of another linear accelerator, the Linac3, and heated. This produces a gas, which is ionised with the help of an electron current. The resulting lead ions Pb^{29+} are accelerated

[1] These letters stand for the French name "Centre Européen pour la Recherche Nucléaire", a temporary organisation created in 1952.

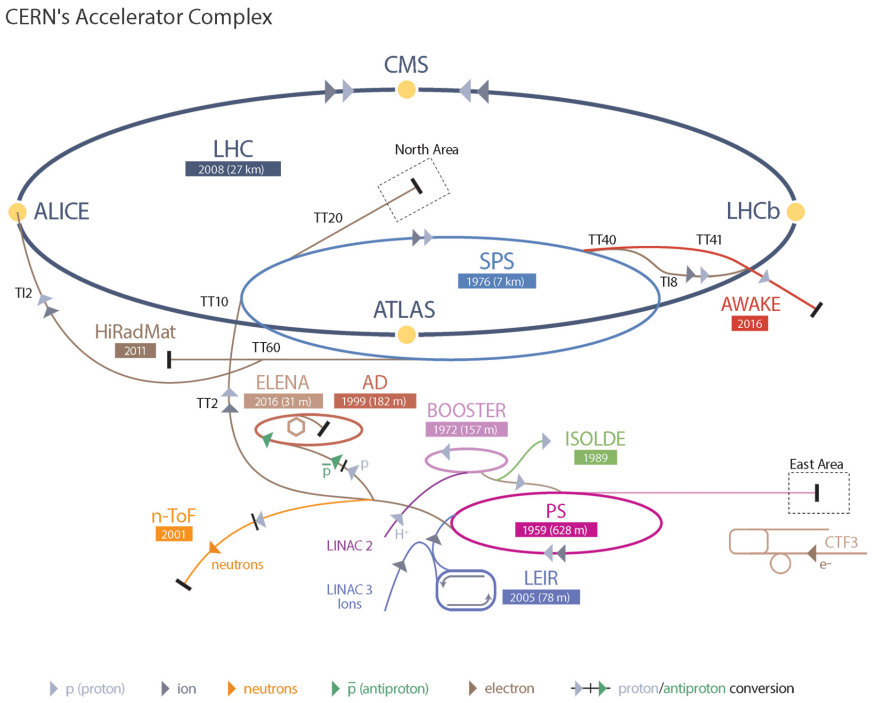

Figure 3.1: Full chain of the accelerators used at CERN to bring the particles to energies of the order of the TeV [130].

through the Linac3 to an energy per nucleon of 4.2 MeV/u. They are sent through a carbon foil for a second ionisation, leading to a Pb^{54+} beam. The partially ionised atoms are accelerated in the Low Energy Ion Ring (LEIR) up to 72 MeV/u, before following the same chain as the proton beam. The PS brings them to an energy per nucleon of 5.9 GeV/u and the SPS to 177 GeV/u. Between these two steps, the beam passes through another carbon foil to be fully ionised (Pb^{82+}). Finally, the 592 bunches of lead ions are injected to the LHC where they are accelerated to an energy of 2.56 TeV/u. It has to be noted that during the Run 2 data taking period of the LHC (2015–2018), the centre of mass energies have been increased to $\sqrt{s} = 13$ TeV for the collisions between proton beams, and $\sqrt{s_{\mathrm{NN}}} = 5.02$ TeV for the Pb–Pb collisions and $\sqrt{s_{\mathrm{NN}}} = 8.16$ TeV for the p–Pb collisions.

The LHC is a synchrotron-type accelerator with a circumference of 26.7 km [127]. It has been built in the tunnel of the former Large Electron Positron (LEP) machine, at the average depth of 100 m. The setup is made of eight arcs and eight straight sections with a length of about 528 m. Four of these sections, the IPs, are used for the collisions of the two beams. Finally, eight arcs are inserted between these sections for the bending of the trajectories of the two beams. This leads to a total of eight sectors for the full LHC, also called its eight octants.

As a collider, the LHC consists of two rings for the beams travelling with opposite direction. Due to the lack of space in the tunnel, these two rings are not completely separated. This has an impact on the design of the about 9600 superconducting magnets cooled at 1.9 K [129]. The generated magnetic fields can reach 8.33 T from the choice of superfluid helium for the cooling of the magnets and the technologies for the cables. Exactly 1232 of these magnets are the main dipoles, which ensure the quasi-circular trajectory of the particles. The beams are focused with the help of quadrupole and sextupole magnets. Radiofrequency cavities (eight per beam) accelerate the particles and compensate the energy losses through synchrotron radiation.

One of the most important concepts for an accelerator is its luminosity $\mathcal{L}$ [131] defined as

$$\frac{dR}{dt} = \mathcal{L}\sigma, \tag{3.1}$$

with $\frac{dR}{dt}$ the event rate and σ the cross section of the collision. In the ideal case of a head-on collision with two Gaussian beams, the luminosity is estimated with

$$\mathcal{L} = \frac{N_1 N_2 f N_b}{4\pi\sigma_x\sigma_y}. \tag{3.2}$$

In the formula above, $N_{1,2}$ is the number of particles in each colliding bunch, f the revolution frequency, N_b the number of bunches. The standard deviation along the x and y axis $\sigma_{x,y}$ corresponds to the dimensions of a bunch in the transverse plane. In practice, many parameters have to be taken into account. The collision offset, the beam profiles, and the crossing effects are examples of elements which can influence the final luminosity. For the LHC in Run 2, the luminosity was about 1.2×10^{34} cm^{-2}s^{-1} for the collisions between protons. In the case of Pb–Pb collisions, the nominal luminosity has been designed to reach $\mathcal{L} = 10^{27}$ cm^{-2}s^{-1}.

The two beams can collide at four positions along the LHC, the IPs cited above, where the main experiments of the LHC are situated. The two high luminosity detectors are A Toroidal LHC ApparatuS (ATLAS) [132] and Compact Muon Solenoid (CMS) [133]. Respectively located at Point 1 and Point 5, they are the two general-purpose experiments designed to study a broad range of physics topics. They are also at the origin of the observation of the Higgs boson in 2012. The LHC also has a dedicated heavy-ion detector, ALICE at Point 2, which will be discussed in the next section. Finally, the Large Hadron Collider beauty (LHCb) experiment [134] studies the differences between matter and antimatter at Point 8. As stated in the Chapter 1, LHCb is the detector which discovered the first exotic hadrons. Three smaller experiments are also placed along the LHC: the Large Hadron Collider forward (LHCf) [135] at Point 1, the TOTal Elastic and diffractive cross section Measurement (TOTEM) [136] at Point 5 and the Monopole and Exotics Detector at the LHC (MoEDAL) [137] at Point 8.

The LHC is currently in its second Long Shutdown (LS2) (2018–2021/2022) where the accelerators and the experiments are upgrading their hardware and software. For the future Run 3 data taking, the LHC is planned to be able to work with its nominal values for the energies of $\sqrt{s} = 14$ TeV for the collisions between protons, and $\sqrt{s_{\mathrm{NN}}} = 5.5$ TeV for p–Pb and Pb–Pb collisions, along with increased luminosity.

3.2 The ALICE detector

In opposition to RHIC, which is a fully dedicated heavy-ion accelerator, the LHC has only one experiment specialised for such collisions, ALICE [138–141]. Its main physics goal is the study of the properties of the interacting matter at extreme temperatures. Therefore, it has been designed to measure in the same place a broad range of observables previously analysed in different accelerators like RHIC or the SPS. Among the requirements were, for example, the abilities to track and identify particles with transverse momenta as low as 100 MeV/c to as high as around 100 GeV/c, and to reconstruct particles with a short lifetime, while taking into account the large number of charged tracks produced in central and semicentral collisions. As stated above, the nominal luminosity of the LHC in Pb–Pb collisions has been planned to reach $\mathcal{L} = 10^{27}$ cm^{-2}s^{-1}. In the Run 2 data taking, about 1 nb^{-1} of integrated luminosity has been taken with ALICE. This is about ten times more data than in Run 1, where the value was of about 75 μb^{-1} [142].

ALICE is a massive detector situated underground at Point 2. It measures $16 \times 16 \times 26$ m^3 and weights about 10000 t. The full detector (Fig. 3.2) can be divided into two main parts. The first system, the central barrel, is placed in the solenoid magnet from the L3 experiment

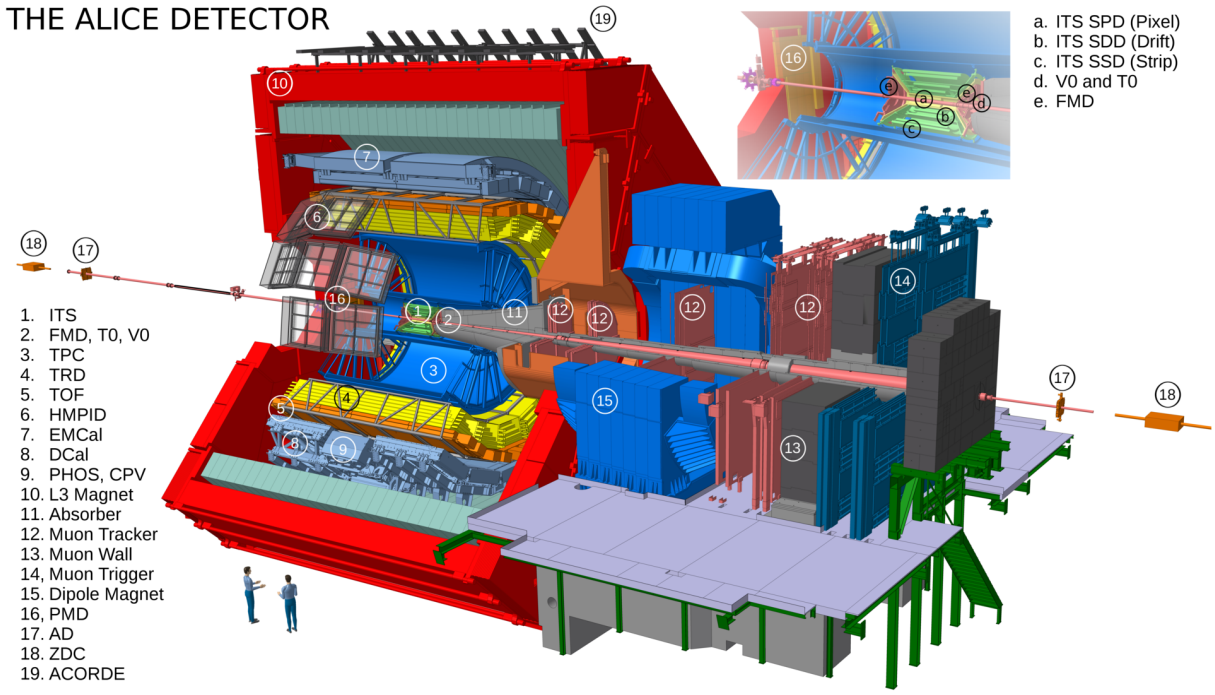

Figure 3.2: Schematic view of the ALICE detector during Run 2 [143].

at the LEP which produces a nominal magnetic field of 0.5 T. The central part of ALICE has a coverage in polar angles between 45 and 135°, which corresponds to a pseudorapidity range $|\eta| \leq 0.9$ [138, 140]. This allows the detection of hadrons, electrons and photons. The detector in the central barrel closest to the beam pipe is the Inner Tracking System (ITS), followed by the Time Projection Chamber (TPC), the Transition Radiation Detector (TRD) and the Time Of Flight (TOF). Situated between the space frame holding the previously cited central detectors and the magnet are the Electromagnetic Calorimeter (EMCal) and the Dijet Calorimeter (DCal), the latter being added during the Long Shutdown 1 (LS1) between Run 1 and Run 2. Besides these main systems are found two smaller detectors: the High Momentum Particle Identification (HMPID) and the Photon Spectrometer (PHOS). It has to be noted that only these four last detectors do not have a full 360° azimuthal coverage. The second part is the forward muon spectrometer placed at large rapidities. It consists of its own dipole magnet, five tracking chambers and an iron filter for the absorption of the remaining hadrons followed by two trigger stations. This setup allows measurements between 2 and 9°, or $-4 \leq \eta \leq -2.4$ [138].

Finally, several small detectors, generally situated close to the beam, complete the list. These are the Zero Degree Calorimeter (ZDC) for the measurement of the impact parameters, the Photon Multiplicity Detector (PMD) counting the number of photons, the Forward Multiplicity Detector (FMD), and the T0 and the V0 detectors for fast triggers. Above the L3 magnet is the ALICE Cosmic Ray Detector (ACORDE). This array of plastic scintillators serves as a trigger for cosmic rays measurements.

The following subsections present in more details the subdetectors directly involved in this analysis.

3.2.1 The Inner Tracking System

The ITS is the first tracking detector, directly surrounding the beam pipe and the nominal interaction point [138,140]. As such, its tasks are the reconstruction of the primary vertex with a high resolution better than 100 µm and of the secondary vertices coming from the decays of hyperons and heavy mesons like the D or B mesons. The ITS also deals with the tracking and identification of the low-momentum particles and the improvement of the reconstruction of the particles reaching the TPC through the resolution of their momentum and angle.

As all the main detectors in the central barrel, a pseudorapidity coverage of $|\eta| \leq 0.9$ is assured for all the vertices situated at most ± 5.3 cm of the nominal interaction point, along the beam pipe. The ITS is made of six layers of silicon detectors (Fig. 3.3), divided into three groups of two layers, each with their own technology: the Silicon Pixel Detector (SPD), the Silicon Drift Detector (SDD) and the Silicon Strip Detector (SSD). Several parameters have

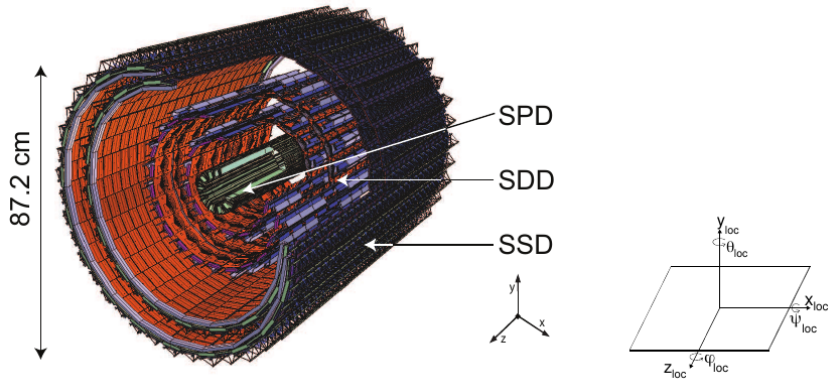

Figure 3.3: (*Left*) Layout of the ITS and orientation of the ALICE global (*middle*) and the ITS local (*right*) reference systems [144]. The origin of the global reference system is situated in the middle of the ITS such that the z-direction is aligned with the beam line.

been taken into account in the design of the layers to ensure a good efficiency in the track finding and a high resolution for the determination of the impact parameter. For instance, the matching between the tracks in the ITS and the TPC affects the determination of the outer radius of the former. For its inner radius, it is the dimensions of the beam pipe, which has a diameter of 6 cm, that must be taken into consideration. Another element is the number of tracks produced in a collision. The largest values are reached during head-on Pb–Pb collisions, where an event can have more than 10000 detected tracks before the application of any analysis selection. The granularity of the detector must then be able to deal with a track density of maximum 8000 tracks per unit of rapidity [138]. Furthermore, this density varies severely with the distance, meaning different technologies are needed depending on the position of the layers.

SPD layers

The SPD are the two innermost layers of the ITS, respectively placed at $r = 3.9$ cm and $r = 7.6$ cm from the beam pipe. They play an extremely important role in the measurement of the position of the primary vertex, as well as of the distance of closest approach (DCA) of the secondary tracks from the weak decays of the heavier particles. Finally, the SPD can be used as a centrality estimator (see Fig. 5.1) It has to be noted that its first layer has a larger pseudorapidity coverage of $|\eta| < 1.98$ [138] for the measurements of the multiplicities of charged particles, complementary to the FMD. There, the density of produced particles can reach up

to 80 particles/cm^{-2} in a largely radiative environment, requiring detectors with both high precision and high granularity. This leads to the choice of a hybrid pixel detector made out of silicon. The most basic block of the SPD is a two-dimensional matrix or sensor ladder. This matrix possesses 256×160 cells of 50 µm in the $r\varphi$ to 425 µm in the z-direction [138]. The cells are divided into five sub-matrices of 256 ($r\varphi$) × 32 (z) cells, each connected to a front-end readout chip. Besides, longer cells are employed near the borders to ensure a full coverage between the readout chips. The sensor ladders are then mounted two-by-two to create half-staves, themselves mounted on a support sector which serves also for the cooling of the system. As visible in Fig. 3.4, the sectors in the inner layer are composed of two staves, the ones in the outer layer of four staves.

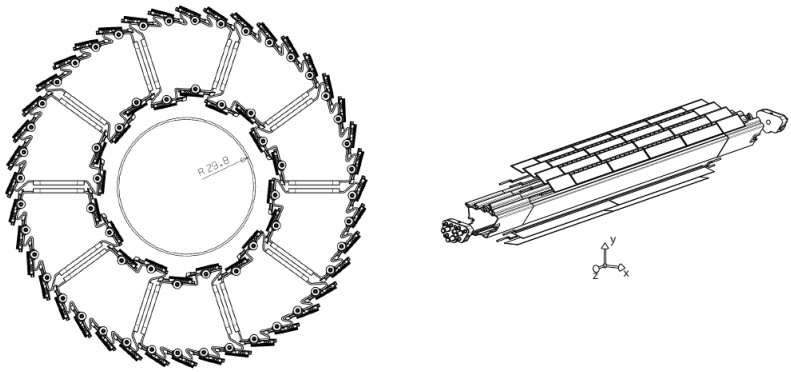

Figure 3.4: (*Left*) Layout of the SPD and (*right*) representation of a support sector made of carbon fibres [144].

SDD layers

The SDD are the two middle layers of the ITS, designed to have good multitrack capabilities. Moreover, half of the dE/dx samples (two out of four) are used for the particle identification (PID) in the ITS are obtained with the SDD. They are situated at $r = 15.0$ cm and $r = 23.9$ cm from the beamline. In this range, the charged particle density is supposed to be at maximum 7 cm^{-2}. The SDD modules are separated into two drift regions. The application of a drift field of about 500 V/cm allows the displacement of the electrons in opposite directions. These modules are set up on linear supports, the ladders. The inner SDD layer consists of fourteen ladders of six modules, while the outer layer has twenty-two ladders of eight modules. This sums up to a total sensitive area larger than 580 µm in the $r\varphi$- and z-directions, ensuring full coverage in azimuthal angles for the central barrel pseudorapidity range.

SSD layers

The last two layers of the ITS are composed of the SSD, located at $r = 38.0$ cm and $r = 43.0$ cm from the beam pipe. They are fundamental to help in the matching of the tracks measured in the ITS and the ones in the TPC. The SSD module is made of a double-sided strip detector. Each side has 768 strips with a pitch of 95 µm. To get the best resolution possible in the $r\varphi$-plane, the strips are set up nearly parallel to the beamline. The installation of the modules on the ladders is similar to the one used for the SDD. Thirty-four ladders, each with twenty-two modules in the beam direction, compose the inner layer. For the outer layer, thirty-eight ladders with twenty-five modules are used.

3.2.2 The Time Projection Chamber

The TPC [138] is the main tracking detector in ALICE, able to provide measurements of the charged particles momentum and PID, and the determination of the primary vertex while being a centrality estimator as well. It presents the same pseudorapidity range as the other detectors in the central barrel ($|\eta| < 0.9$) over its full length. For shorter track length, this range is even increased to $|\eta| < 1.5$. Furthermore, a full 2π coverage is ensured for the azimuthal angles. These requirements give to the TPC the status of the main apparatus used in hadronic measurements in any type of collision system. They aim at getting a better understanding of the source from where the produced particles are emitted, as well as its space–time evolution until freeze-out. These analyses rely on single- and two-particle spectra and correlations and event-by-event fluctuations and therefore impose requirements on the TPC. Examples are the need for a large acceptance and resolution in low and high momentum and pseudorapidity, the complete azimuthal acceptance and good PID capabilities.

Lepton-related observables can also be studied with the help of the TPC. These include the measurements of high-mass and high-p_{T} electron pairs and the production of charm- and beauty-flavoured particles. In this goal, the TPC must have a large acceptance for high-p_{T} tracks over his full length to ensure a good matching with the TRD. Furthermore, the PID capacities of the TPC are essential to ensure the electrons whose impact parameters are determined by the ITS can be used for separation of the primary J/ψ mesons to the ones coming from the decays of B particles. The matching to the electron candidates identified in the TRD imposes requirements on the rate capabilities of the TPC. This means maximum rates of 200 Hz must be reached for central Pb–Pb collisions. Events from the collisions between protons set a trigger limit to the rate of 1000 Hz as the total space charge is lower than for heavy-ion collisions.

Figure 3.5 shows the layout of the TPC. The dimensions of the cylinder are of about 85 cm for the inner radius, about 250 cm for the outer radius and a total length of 500 cm along the beamline, centred at the IP. The detector volume, about 88 m^3, is filled with a gaseous mixture

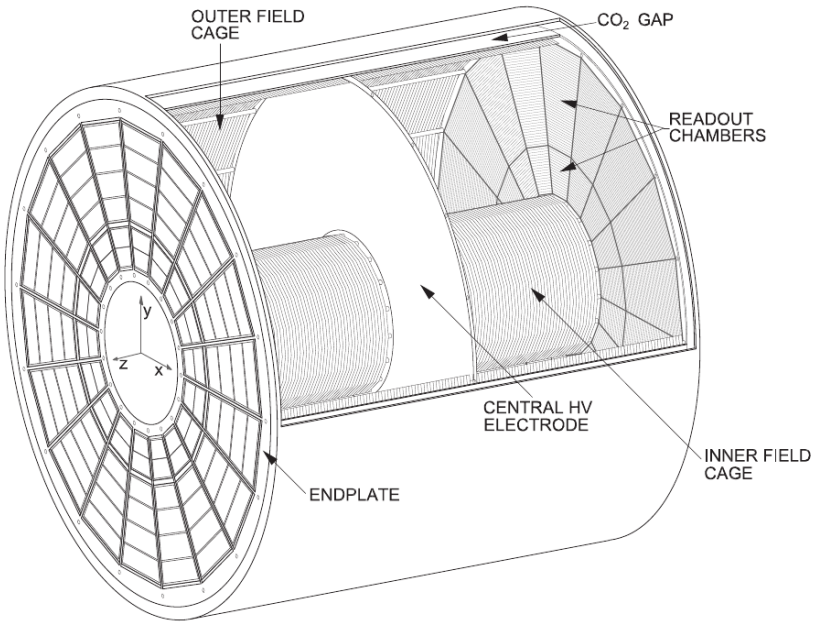

Figure 3.5: Schematic layout of the TPC [145].

of Ne/CO_2 with a ratio 90%/10%. A highly uniform electrostatic drift field is created by the

combination of the central high voltage electrode dividing the active volume in two, and the inner and outer field cages. Due to the choice of filling gas, high voltage gradients of approximately 400 V/cm must be obtained for the field cage, with a voltage of 100 kV at the central electrode. This choice of design means that the primary electrons produced by the ionisation of the gas have a drift distance of maximum 250 cm and a drift time of maximum 90 µs before reaching the endplates containing the readout chambers. The position (x, y, z) — or (r, φ, z) in cylindrical coordinates — of the drifting electron, which has been created through the ionisation of the gas, can then be obtained from the readout chambers. The transverse coordinates x and y (i.e. r and φ) correspond to the position of the pad where the electron arrived, while the longitudinal information z is provided with the measurement of the time of flight.

These chambers consist of multi-wire proportional chambers, with a cathode pad readout. They are divided azimuthally into thirty-six sectors, eighteen per side. Due to the radial dependency of the track density, two regions are distinguished for each sector: the Inner Read Out Chambers (IROCs) (from 84.1 cm to 132.1 cm) and the Outer Read Out Chambers (OROCs) (134.6 cm to 246.6 cm). To get the resolution required for the PID and the determination of the position, while ensuring the occupancy stays the lowest possible, about 560000 pads are employed in total. Finally, a gating grid is added to the system. Upon reception of a triggered system, the grids are open to let the electrons access the chambers from 6.5 µs after the collision for the duration of one drift-time interval, before closing again until the next collision and trigger. The goal is here to prevent space charges from secondary ionisations in the gas or from ion back flow to drift back into the active volume where they can introduce perturbation in the homogeneous field. This phenomenon, known as the *space charge distortion*, introduces a bias in the measured position of the track which needs to be corrected later on if not prevented. It has to be noted that the multi-wire proportional chambers used during Run 1 and Run 2 are currently replaced with the Gas Electron Multiplier (GEM) technology [146, 147]. This choice is motivated by the capacity of the GEM to work in the continuous read-out mode required by the increased event rate of Run 3.

3.2.3 The V0 detector

The V0 [138, 148] is a small two-part detector, which fills several purposes in ALICE. First of all, it helps in providing various triggers for the rest of the experiment: minimum bias for the central barrel and validation signal for the muon trigger in pp events, but also two centrality triggers for Pb–Pb collisions. Besides the trigger system, it serves as a control for the luminosity in the experiment.

The two arrays, V0A and V0C, are situated at different distances of the IP, along the beamline: V0A at 329 cm and V0C at 90 cm on the side of the muon spectrometer [148]. They cover the pseudorapidity ranges $2.8 < \eta < 5.1$ and $-3.7 < \eta < -1.7$, respectively, for a collision happening exactly at the interaction point. Because of these positions, the background can become non-negligible. Examples include the important production of secondary particles because of the presence of a sizeable amount of detector material in front of the arrays, or the interactions between the beam and the residual gas within the beamline [148]. These sources can bias the multiplicity measurement or provide the wrong trigger, and therefore, they need to be reduced.

The two arrays are made of four rings divided into eight sectors in the azimuthal direction. Figure 3.6 shows a schematic of the layout of each array. The design of the V0C is influenced by its position in front of the hadronic absorber: the sectors are separated to allow the passage of the scintillating fibres while ensuring the largest azimuthal coverage possible. Because of its further location, the V0A does not present such constraints. The scintillating fibres collect and

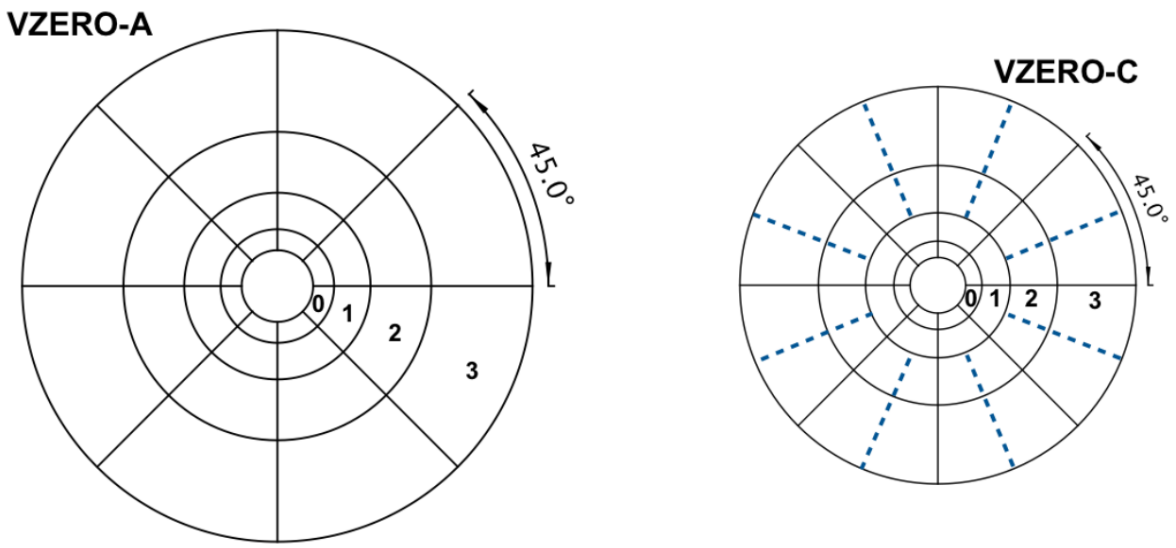

Figure 3.6: Layout of the V0A and V0C arrays [148].

guide the produced light to photomultipliers set at 3–5 m from the V0 arrays. It has to be noted that specific photomultipliers able to work in presence of a magnetic field need to be used, as the V0 system is situated within the L3 solenoid.

Among the triggers provided by the V0 cited above, some are specific to Pb–Pb collisions. One of the major criteria in the configuration of the triggers is the efficiency for hadronic interaction, which must be as high as possible. Therefore, two out of the three following conditions: (1) hits are detected in two pixel chips in the outer layer of the SPD, (2) a signal is detected in the V0A, (3) a signal is detected in the V0C. This list of requirements gives an estimation of the deposited average energy of a minimum ionising particle. It has to be noted that this minimum bias trigger was not constant during the full Pb–Pb data taking period in 2010. The increase of beam luminosity near the end of said period forced the criteria for the trigger to be reduced to the coincidence between SPD, V0A and V0C. The reason for this choice is that the electromagnetic dissociation of the lead nuclei created background signals which should be reduced as much as possible. Finally, this trigger implied an event rate of 50 Hz, divided as follows: 4 Hz from nuclear interactions, 45 Hz from electromagnetic phenomena, and 1 Hz from the beam background [149].

As stated above, the V0 detector can also be used for the centrality determination of the events produced in Pb–Pb collisions [149, 150]. To achieve this, the triggered events are further selected using the information from another detector, the ZDC, to remove the beam background. The obtained distribution of amplitudes in the V0 is shown in Fig. 3.7. This figure recalls Fig. 1.7. The procedure using the Glauber fit can therefore be applied to define each centrality class of events.

3.2.4 Online and offline data processing

As stated above in this chapter, the LHC performed collisions at various energies of the order of TeV. Collisions between protons at $\sqrt{s} = 8$ TeV, protons and lead at $\sqrt{s_{\mathrm{NN}}} = 5.02$ TeV and lead ions at $\sqrt{s_{\mathrm{NN}}} = 2.76$ TeV are examples taken by ALICE between 2009 and 2013. During Run 2 (2015–2018), the energies have been increased to $\sqrt{s} = 13$ TeV for pp collisions, $\sqrt{s_{\mathrm{NN}}} = 8.16$ TeV for p–Pb collisions and $\sqrt{s_{\mathrm{NN}}} = 5.02$ TeV for Pb–Pb collisions to cite only a

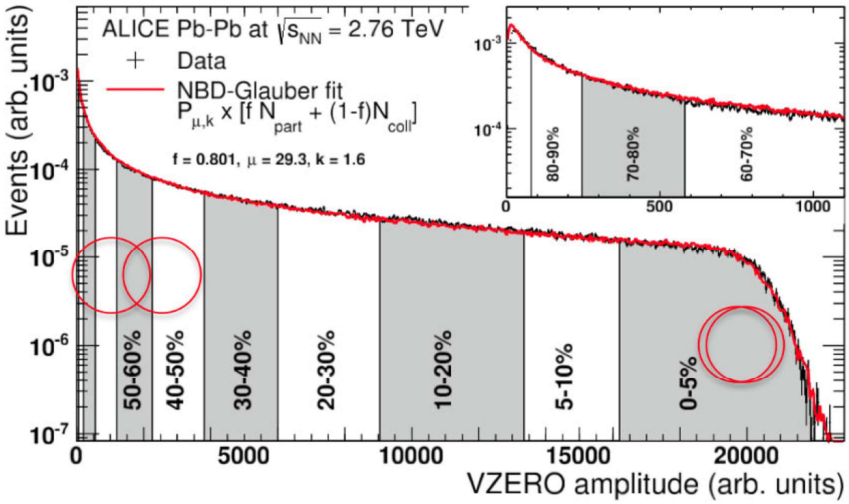

Figure 3.7: Distribution of the summed amplitudes in the V0 [150]. The Glauber fit is shown in red. Each segment indicates a different centrality class as described in Section 1.3.

few examples. The luminosity is therefore high enough that not all the produced events can be recorded and stored on tape. This procedure can be divided into two major categories, both with their requirements and specificities: the online and offline frameworks. This section describes the steps used during data taking to select and reconstruct the events to be used in analyses.

The online framework intervenes during the data taking itself. As such, it must be fast and efficient to select the events to keep for further treatment. The first step is the ALICE trigger system. It aims at reducing the number of events to give the next steps in the chain, the Data AcQuisition (DAQ) and the High Level Trigger (HLT), while ensuring the kept data are potentially interesting for the analyses done in ALICE. The Central Trigger Processor (CTP) receives the information for the various triggers from the different detectors. As these subsystems are not busy for the same time periods, the CTP must be able to process all the triggers concurrently in ways optimised for the different running modes of ALICE (pp, heavy ions,...) [138]. To allow the tracking detectors to deal with the large multiplicities generated in central Pb–Pb collisions, the trigger has to be able to work on a short time scale, about less than 1.2 μs. However, not all trigger inputs are already available, leading to a division of the trigger in two parts, the Level 0 (L0) signal which must work at 1.2 μs and the Level 1 (L1) signal at 6.5 μs which waits for the remaining trigger inputs. Furthermore, due to these high multiplicities, it becomes impossible to reconstruct the events containing more than one central collision. A "past-future protection" with a Level 2 (L2) trigger at the end ($\sim$ 88 μs) ensures that the event can be taken.

The variety of physics topics studied in ALICE for the different collision systems imposes different requirements on the events to keep. At least fifty trigger classes were envisioned for the Run 1 data taking period [138]. Examples are the minimum bias trigger already discussed above and used in this work, the cosmic trigger or the beam gas trigger. It is important to notice that the trigger classes do not have all the same frequency. Some of them (e.g. the minimum bias trigger) are so common that the performance of the acquisition system is their major limitation. As a result, they can potentially use a large fraction of the total bandwidth. On the other hand, rarer trigger classes are limited by the luminosity of the run and the detector live time. As

such, they would use a smaller fraction of the bandwidth. An equilibrium must then be found between these types of classes. This is achieved by the trigger and the DAQ systems.

The HLT must fulfil three roles within the data processing. It must select the portions of an event or the regions of interest which are relevant for the physics analyses. To achieve this, it helps with the removal of the pile-up in pp collisions or the filtering of the low momentum tracks, for instance. It also works on compressing the data as much as possible without losing physics information. Finally, it tightens the momentum cut in the muon spectrometer, improves the PID, the momentum resolution and IP determination of the TRD electrons in the TPC. This analysis of physics observables aims at rejecting fake events. The events or regions of interest accepted that the HTL are finally compressed and sent to the permanent storage.

The physics data resulting from the online system, as well as the ones from the various event generators used in ALICE, are reconstructed and analysed with the ALICE offline framework called AliRoot. In opposition to the other LHC experiments, which use two lines of software for their physics analyses, ALICE decided to develop and maintain only one framework, fully based on the ROOT framework. Some of the motivations behind this choice are the capacity of ROOT to deal with large amounts of data in any step of the data analysis and its efficiency as an object-oriented C++ language. It has to be noted that ALICE developed as well its own environment, AliEn [151], on a Grid computing infrastructure to ease the access and analysis of all the produced data. This procedure has even been facilitated further with the integration of the LEGO train framework [152], which optimises the use of resources in the case of an analysis over large samples of data, like a full period itself.

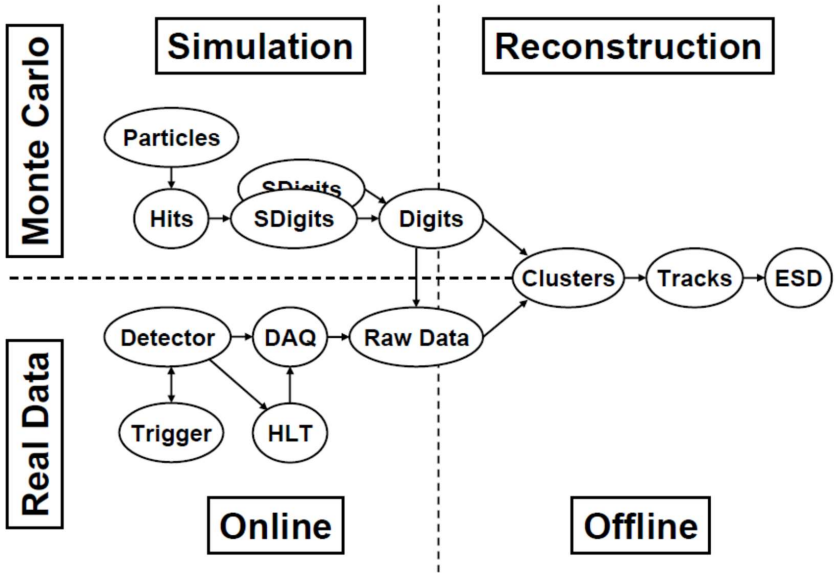

Figure 3.8: Data processing chain used to reconstruct both the simulated and real data [140].

Figure 3.8 shows the data processing framework for both the simulated and real data. In the former case, the particles are first produced by a Monte Carlo (MC) generator, meaning all their properties, like PID or momentum, are exactly known. This level of information represents what would be ideally measured and is designated under the names of *kinematics*, *generator* or *MC truth* level. Some generators and hydrodynamic models are presented in Section 6.1. These data are sent in the simulation chain reproducing the detector response of ALICE. Examples of programs used in this goal are GEANT3 [153] and its follow-up GEANT4 [154, 155]. They reduce the particle information to what is actually measured in the experiment. It has to be

noted that this step requires a full and exact simulation of each ALICE detector (dimensions, material budget,...) within the program.

The "raw data", simulated or real, are then processed by the reconstruction algorithms. The first step is the local reconstruction for each detector, like the clusterisation. Afterwards, the primary vertex is reconstructed, followed by the execution of the tracking and particle identification operations. Finally, the secondary vertices are reconstructed. More information about each of these steps can be found in Refs. [139, 140].

The structure of the reconstructed real data is organised in the following scheme: year, period, and runs. A *run* is defined as an uninterrupted data taking time interval where the conditions within ALICE are stable and identical. It can range from few minutes to few hours long, depending on the status of the detectors and the LHC itself. A new run is started if any change is made on the configuration of the system. Runs sharing the same global conditions (centre of mass energy, colliding system, ...) are grouped into a *period*. For instance, the full set of Pb–Pb collisions at $\sqrt{s_{\mathrm{NN}}} = 2.76$ TeV are gathered into the LHC10h period, where the number indicates the year of data taking (here 2010) and the last letter the index of the period in said year. MC simulations are stored into sets with identical conditions used for the detector response and follow their own naming scheme. An example is the LHC11a10a_bis dataset, which groups the HIJING simulations anchored to — i.e. obtained with the same conditions as — the LHC10h dataset.

The first data sample (period, run, ...) which is usable by the analysers is saved as Event Summary Data (ESDs) files, which contain all reconstructed information. As these files have a massive size, they are filtered into smaller samples, the Analysis Object Data (AODs) with only the quantities needed for physics analyses. Depending on the set of criteria, different filtering are present in a single AOD and are designated by a filterbit number. Examples used in this work are the TPC-standalone (or TPC-only) tracks with a selection based only the information from the TPC itself, or the hybrid tracks where the tracking information from the TPC and ITS are combined to get the best resolution in transverse momentum and to correct the non-uniform acceptance (NUA) in azimuthal angles coming from dead or malfunctioning regions of the SPD. Their filterbits are the 128 and the 768, respectively.

The final output of this *reconstruction* level (or *detector* level), be it ESDs or AODs, can then be used for physics analyses. It has to be noted that the comparison between the kinematics and reconstruction levels in simulated data can be used to determine the detector and software performances or to get the factors to correct for detector effects. Detailed explanation and methodology of the latter are given in Section 5.3.

Moreover, all the processing steps described above have been used to reconstruct and analyse the data taken during Run 1 and Run 2 at the LHC. However, due to the increase of the centre of mass energy and luminosity and the upgrades of various detectors, a new programming system will be required for Run 3. Called O2 for "online-offline" [156], it answers, for example, the need of a fast trigger decision and the disappearance of the notion of "event" due to the planned high rate and pile-up level in small and large colliding systems.

Chapter 4

Cumulants of Flow Amplitudes

This chapter presents the theoretical method introduced to generalise the two-harmonic SCs to any number of harmonics. Section 4.1 highlights the details of this new mathematical approach following Refs. [117, 125, 157]. Afterwards, this procedure is extended to the ACs. These latter observables aim to probe the genuine correlations between various moments of different flow amplitudes. This extension is explained similarly as for the SCs in Section 4.2.

4.1 Higher order Symmetric Cumulants

The lower order SCs (Eq. (2.62)) have been obtained with the traditional approach based on cumulants in flow analyses. Like discussed in Section 2.2, the azimuthal angles of the measured particles are identified as the fundamental stochastic variables in the definition of $\kappa_{1,1,1,1}$ (Eq. (2.56)). The expression resulting from this procedure is then interpreted in terms of the flow degrees of freedom: the flow amplitudes and the symmetry planes. However, this method presents a problem that should not be underestimated. The SC observables measure the genuine correlations between flow amplitudes. By definition, they must then be cumulants of these quantities. However, as seen in Section 2.2, a cumulant of the variables $X_1, \ldots, X_N$ with $X_1(Y_1, \ldots, Y_N), \ldots, X_N(Y_1, \ldots, Y_N)$ is generally not a cumulant in the basis $Y_1, \ldots, Y_N$. This means, for example, that the observation of a cumulant being zero would be misinterpreted as the absence of correlations between its variables.

This observation shows the need for a clear guideline to generalise the SCs to three and more flow harmonics while preserving their properties as cumulants. This leads thus to the first requirement of the novel approach introduced in Ref. [117]: any expression used to define a higher order SC must be a cumulant involving only the flow amplitudes, and not the azimuthal angles or the symmetry planes. Furthermore, as their names indicate, the SCs must be identical under the permutation of the concerned flow amplitudes. With two and three harmonics, this translates into $\mathrm{SC}(m,n) = \mathrm{SC}(n,m)$ and $\mathrm{SC}(k,l,m) = \mathrm{SC}(k,m,l) = \mathrm{SC}(l,k,m) = \mathrm{SC}(l,m,k) = \mathrm{SC}(m,k,l) = \mathrm{SC}(m,l,k)$. While this may seem a minor condition in appearance, it leads in fact to major consequences in the expressions of the SCs themselves. A two-harmonic SC must contain exactly two different flow amplitudes v_m and v_n, a three-harmonic SC three amplitudes, and so forth. Besides, all the amplitudes must be raised to the same power. This latter point is in fact good news, as it allows the direct use of Eq. (2.9) from Ref. [124].

4.1.1 Main idea for the new generalisation approach

The starting point of the novel approach is the expression of $\mathrm{SC}(m,n)$. While obtained with the traditional method, it happens to also be a cumulant of the flow amplitudes squared. This can be shown straightforwardly. The identification $X_1 = v_m^2$ and $X_2 = v_n^2$ in the expansion of $\kappa_{1,1}$ (Eq. (2.43)) leads directly to Eq. (2.62). Despite being an accidental coincidence, this characteristic of $\mathrm{SC}(m,n)$ is taken as the basis for the generalisation of the SCs to three and more amplitudes through the following proposition: for a number of flow magnitudes j, the corresponding $\mathrm{SC}(n_1,\ldots,n_j)$ is calculated by identifying $X_1 = v_{n_1}^2, X_2 = v_{n_2}^2, \ldots, X_j = v_{n_j}^2$ in the expression of the j-th order cumulant $\kappa_{1,\ldots,1}$.

For simplicity, the demonstration of the validity of the proposed idea is provided here only for the three-harmonic $\mathrm{SC}(k,l,m)$ as an example. Nevertheless, it can be easily extended to any number of flow harmonics. The resulting expressions for the four- and five-harmonics SCs can be found in Appendix B of Ref. [117]. Following the claim above, the definition of $\mathrm{SC}(k,l,m)$ is determined by setting $X_1 = v_k^2$, $X_2 = v_l^2$ and $X_3 = v_m^2$ in $\kappa_{1,1,1}$ (Eq. (2.43)):

$$\begin{aligned}\mathrm{SC}(k,l,m) \equiv \left\langle v_k^2 v_l^2 v_m^2 \right\rangle_c \equiv \left\langle v_k^2 v_l^2 v_m^2 \right\rangle - \left\langle v_k^2 v_l^2 \right\rangle \left\langle v_m^2 \right\rangle - \left\langle v_k^2 v_m^2 \right\rangle \left\langle v_l^2 \right\rangle \\ - \left\langle v_l^2 v_m^2 \right\rangle \left\langle v_k^2 \right\rangle + 2 \left\langle v_k^2 \right\rangle \left\langle v_l^2 \right\rangle \left\langle v_m^2 \right\rangle .\end{aligned} \tag{4.1}$$

This expression is symmetric under any permutation of the different harmonics. However, this quick check is not sufficient to prove that the novel approach leads to valid cumulants according to the formalism of Kubo [124]. In the following demonstration, only the names of the requirements are indicated. More details can be found in Section 2.2 and in Ref. [125].

Statistical independence. Without loss of generality, the fluctuations of v_k^2 and v_l^2 are chosen correlated, while v_m^2 fluctuate independently of the other two. Equation (4.1) becomes

$$\begin{aligned}\mathrm{SC}(k,l,m) = \left\langle v_k^2 v_l^2 \right\rangle \left\langle v_m^2 \right\rangle - \left\langle v_k^2 v_l^2 \right\rangle \left\langle v_m^2 \right\rangle - \left\langle v_k^2 \right\rangle \left\langle v_m^2 \right\rangle \left\langle v_l^2 \right\rangle \\ - \left\langle v_l^2 \right\rangle \left\langle v_m^2 \right\rangle \left\langle v_k^2 \right\rangle + 2 \left\langle v_k^2 \right\rangle \left\langle v_l^2 \right\rangle \left\langle v_m^2 \right\rangle = 0. \qquad \square\end{aligned} \tag{4.2}$$

Furthermore, if all three harmonics fluctuate independently, the derivation results again in

$$\begin{aligned}\mathrm{SC}(k,l,m) = \left\langle v_k^2 \right\rangle \left\langle v_l^2 \right\rangle \left\langle v_m^2 \right\rangle - \left\langle v_k^2 \right\rangle \left\langle v_l^2 \right\rangle \left\langle v_m^2 \right\rangle - \left\langle v_k^2 \right\rangle \left\langle v_m^2 \right\rangle \left\langle v_l^2 \right\rangle \\ - \left\langle v_l^2 \right\rangle \left\langle v_m^2 \right\rangle \left\langle v_k^2 \right\rangle + 2 \left\langle v_k^2 \right\rangle \left\langle v_l^2 \right\rangle \left\langle v_m^2 \right\rangle = 0. \qquad \square\end{aligned} \tag{4.3}$$

This proves that the candidate equation does not contain any internal bias and that an absence of genuine correlations between the three amplitudes can be safely deduced when the expression is consistent with zero. This confirms Theorem 1 in Ref. [124].

Reduction. The three flow magnitudes are now set equal to each other $v_k^2 = v_l^2 = v_m^2 \equiv v^2$, leading to

$$\mathrm{SC}(k,l,m) = \left\langle v^6 \right\rangle - 3 \left\langle v^4 \right\rangle \left\langle v^2 \right\rangle + 2 \left\langle v^2 \right\rangle^3 . \qquad \square \tag{4.4}$$

This is the expression for the κ_3 with v^2 as fundamental stochastic variable and therefore a valid cumulant.

Semi-invariance. Let c_k, c_l and c_m be three constants. It follows that

$$\begin{aligned}
\left\langle (v_k^2+c_k)(v_l^2+c_l)(v_m^2+c_m)\right\rangle_c &= \left\langle (v_k^2+c_k)(v_l^2+c_l)(v_m^2+c_m)\right\rangle \\
&\quad - \left\langle (v_k^2+c_k)(v_l^2+c_l)\right\rangle \left\langle (v_m^2+c_m)\right\rangle \\
&\quad - \left\langle (v_k^2+c_k)(v_m^2+c_m)\right\rangle \left\langle (v_l^2+c_l)\right\rangle \\
&\quad - \left\langle (v_l^2+c_l)(v_m^2+c_m)\right\rangle \left\langle (v_k^2+c_k)\right\rangle \\
&\quad + 2\left\langle (v_k^2+c_k)\right\rangle \left\langle (v_l^2+c_l)\right\rangle \left\langle (v_m^2+c_m)\right\rangle \\
&= \mathrm{SC}(k,l,m) \\
&\quad + c_k\left(\left\langle v_l^2 v_m^2\right\rangle - 2\left\langle v_l^2\right\rangle\left\langle v_m^2\right\rangle + 2\left\langle v_l^2\right\rangle\left\langle v_m^2\right\rangle - \left\langle v_l^2 v_m^2\right\rangle\right) \\
&\quad + c_l\left(\left\langle v_k^2 v_m^2\right\rangle - 2\left\langle v_k^2\right\rangle\left\langle v_m^2\right\rangle + 2\left\langle v_k^2\right\rangle\left\langle v_m^2\right\rangle - \left\langle v_k^2 v_m^2\right\rangle\right) \\
&\quad + c_m\left(\left\langle v_k^2 v_l^2\right\rangle - 2\left\langle v_k^2\right\rangle\left\langle v_l^2\right\rangle + 2\left\langle v_k^2\right\rangle\left\langle v_l^2\right\rangle - \left\langle v_k^2 v_l^2\right\rangle\right) \\
&\quad + c_k c_l\left(3\left\langle v_m^2\right\rangle - 3\left\langle v_m^2\right\rangle\right) + c_k c_m\left(3\left\langle v_l^2\right\rangle - 3\left\langle v_l^2\right\rangle\right) \\
&\quad + c_l c_m\left(3\left\langle v_k^2\right\rangle - 3\left\langle v_k^2\right\rangle\right) + c_k c_l c_m(3-3) \\
&= \mathrm{SC}(k,l,m). \qquad \square
\end{aligned} \tag{4.5}$$

Homogeneity. Let c_k, c_l and c_m be three constants. The homogeneity criterion goes as

$$\begin{aligned}
\left\langle (c_k v_k^2)(c_l v_l^2)(c_m v_m^2)\right\rangle_c &= \left\langle c_k c_l c_m v_k^2 v_l^2 v_m^2\right\rangle - \left\langle c_k c_l v_k^2 v_l^2\right\rangle\left\langle c_m v_m^2\right\rangle - \left\langle c_k c_m v_k^2 v_m^2\right\rangle\left\langle c_l v_l^2\right\rangle \\
&\quad - \left\langle c_l c_m v_l^2 v_m^2\right\rangle\left\langle c_k v_k^2\right\rangle + 2\left\langle c_k v_k^2\right\rangle\left\langle c_l v_l^2\right\rangle\left\langle c_m v_m^2\right\rangle \\
&= c_k c_l c_m \mathrm{SC}(k,l,m). \qquad \square
\end{aligned} \tag{4.6}$$

Multilinearity. Take $v_k^2, v_l^2, v_m^2, v_n^2$ four different flow amplitudes. It follows

$$\begin{aligned}
\mathrm{SC}(k+n,l,m) &= \left\langle (v_k^2+v_n^2)v_l^2 v_m^2\right\rangle - \left\langle (v_k^2+v_n^2)v_l^2\right\rangle\left\langle v_m^2\right\rangle - \left\langle (v_k^2+v_n^2)v_m^2\right\rangle\left\langle v_l^2\right\rangle \\
&\quad - \left\langle v_l^2 v_m^2\right\rangle\left\langle (v_k^2+v_n^2)\right\rangle + 2\left\langle (v_k^2+v_n^2)\right\rangle\left\langle v_l^2\right\rangle\left\langle v_m^2\right\rangle \\
&= \mathrm{SC}(k,l,m) + \mathrm{SC}(n,l,m). \qquad \square
\end{aligned} \tag{4.7}$$

The expression of $\mathrm{SC}(n_1,\ldots,n_j)$ obtained through the alternative approach proposed above passes all the requirements needed to be a valid multivariate cumulant of v_n^2. This is the essential key of this method: the cumulant formalism is applied directly on the v_n^2 and not on the azimuthal correlators anymore. The azimuthal angles are now only a tool to get the experimental estimators (see Section 4.1.2). Furthermore, the fact that the fundamental observables are not the flow amplitudes v_n but their square is an important nuance that needs to be stressed out. It can be shown that, already with two harmonics, $\mathrm{SC}(m,n)$ cannot meet the criterion about semi-invariance if applied with the flow amplitudes themselves as stochastic variables (see Appendix B.3).

While this method is designed to generalise the concept of SCs of the flow amplitudes to higher orders, it is not its only use. As with the two-harmonic SCs, it is possible to get predictions of the genuine correlations between different eccentricities in theoretical models. The corresponding formulas are determined by replacing the flow magnitudes v_n^2 by their counterparts in the initial state ϵ_n^2. Equation (4.1), for example, becomes for three eccentricities

$$\begin{aligned}
\mathrm{SC}_\epsilon(k,l,m) \equiv \left\langle \epsilon_k^2\epsilon_l^2\epsilon_m^2\right\rangle_c &\equiv \left\langle \epsilon_k^2\epsilon_l^2\epsilon_m^2\right\rangle - \left\langle \epsilon_k^2\epsilon_l^2\right\rangle\left\langle \epsilon_m^2\right\rangle - \left\langle \epsilon_k^2\epsilon_m^2\right\rangle\left\langle \epsilon_l^2\right\rangle \\
&\quad - \left\langle \epsilon_l^2\epsilon_m^2\right\rangle\left\langle \epsilon_k^2\right\rangle + 2\left\langle \epsilon_k^2\right\rangle\left\langle \epsilon_l^2\right\rangle\left\langle \epsilon_m^2\right\rangle .
\end{aligned} \tag{4.8}$$

Furthermore, these new SC observables can be normalised in order to compare initial and final states or results that are not measured for the same kinematic ranges. This allows, for instance, better quantification of the part of the correlations that developed only during the collective evolution [117]. The normalised SCs are computed with

$$\mathrm{NSC}(k,l,m) \equiv \frac{\mathrm{SC}(k,l,m)}{\langle v_k^2\rangle \langle v_l^2\rangle \langle v_m^2\rangle}, \tag{4.9}$$

$$\mathrm{NSC}_\epsilon(k,l,m) \equiv \frac{\mathrm{SC}_\epsilon(k,l,m)}{\langle \epsilon_k^2\rangle \langle \epsilon_l^2\rangle \langle \epsilon_m^2\rangle}. \tag{4.10}$$

4.1.2 Determination of the experimental expression

The expressions in terms of the flow amplitudes presented above can be used directly in theoretical studies, as the flow amplitudes can be estimated for each event as an output of the hydrodynamic models. However, this is not the case for experimental analyses. There, the azimuthal angles φ detected in an event are the only accessible variables which can be used to compute the multiparticle correlators. The flow magnitudes and symmetry planes are then estimated from the multiparticle azimuthal correlators and the analytic relation Eq. (2.12). In order to compare the theoretical predictions with the experimental results, one needs to ensure that the experimental expression in terms of azimuthal correlators is another form of the theoretical definition with the flow amplitudes. The two-harmonic SCs have been calculated with the traditional method, meaning their expression in terms of φ was determined at the same time. Since the new approach focuses on the flow magnitudes in the cumulant expansion, the next step in the generalisation is thus the determination of the experimental expression of the higher order SCs. The procedure is done here with three different harmonics and can again be easily generalised for more amplitudes.

Different definitions can be obtained from the insertion of Eq. (2.12) in the theoretical expression of $\mathrm{SC}(k,l,m)$ (Eq. (4.1)). From now on, three candidates are investigated. They are called here the *usual*, *alternative* and the *mixed* expressions of $\mathrm{SC}(k,l,m)$, respectively given by the following combinations of azimuthal correlators:

$$\begin{aligned}
\mathrm{SC}(k,l,m)_{usual} = &\left\langle\left\langle e^{i(k\varphi_1+l\varphi_2+m\varphi_3-k\varphi_4-l\varphi_5-m\varphi_6)}\right\rangle\right\rangle \\
&- \left\langle\left\langle e^{i(k\varphi_1+l\varphi_2-k\varphi_3-l\varphi_4)}\right\rangle\right\rangle \left\langle\left\langle e^{i(m\varphi_1-m\varphi_2)}\right\rangle\right\rangle \\
&- \left\langle\left\langle e^{i(k\varphi_1+m\varphi_2-k\varphi_3-m\varphi_4)}\right\rangle\right\rangle \left\langle\left\langle e^{i(l\varphi_1-l\varphi_2)}\right\rangle\right\rangle \\
&- \left\langle\left\langle e^{i(l\varphi_1+m\varphi_2-l\varphi_3-m\varphi_4)}\right\rangle\right\rangle \left\langle\left\langle e^{i(k\varphi_1-k\varphi_2)}\right\rangle\right\rangle \\
&+ 2\left\langle\left\langle e^{i(k\varphi_1-k\varphi_2)}\right\rangle\right\rangle \left\langle\left\langle e^{i(l\varphi_1-l\varphi_2)}\right\rangle\right\rangle \left\langle\left\langle e^{i(m\varphi_1-m\varphi_2)}\right\rangle\right\rangle,
\end{aligned} \tag{4.11}$$

$$\begin{aligned}
\mathrm{SC}(k,l,m)_{alternative} = &\left\langle\left\langle e^{i(k\varphi_1-k\varphi_2)}\right\rangle \left\langle e^{i(l\varphi_1-l\varphi_2)}\right\rangle \left\langle e^{i(m\varphi_1-m\varphi_2)}\right\rangle\right\rangle \\
&- \left\langle\left\langle e^{i(k\varphi_1-k\varphi_2)}\right\rangle \left\langle e^{i(l\varphi_1-l\varphi_2)}\right\rangle\right\rangle \left\langle\left\langle e^{i(m\varphi_1-m\varphi_2)}\right\rangle\right\rangle \\
&- \left\langle\left\langle e^{i(k\varphi_1-k\varphi_2)}\right\rangle \left\langle e^{i(m\varphi_1-m\varphi_2)}\right\rangle\right\rangle \left\langle\left\langle e^{i(l\varphi_1-l\varphi_2)}\right\rangle\right\rangle \\
&- \left\langle\left\langle e^{i(l\varphi_1-l\varphi_2)}\right\rangle \left\langle e^{i(m\varphi_1-m\varphi_2)}\right\rangle\right\rangle \left\langle\left\langle e^{i(k\varphi_1-k\varphi_2)}\right\rangle\right\rangle \\
&+ 2\left\langle\left\langle e^{i(k\varphi_1-k\varphi_2)}\right\rangle\right\rangle \left\langle\left\langle e^{i(l\varphi_1-l\varphi_2)}\right\rangle\right\rangle \left\langle\left\langle e^{i(m\varphi_1-m\varphi_2)}\right\rangle\right\rangle,
\end{aligned} \tag{4.12}$$

$$
\begin{aligned}
\mathrm{SC}(k,l,m)_{mixed} = &\left\langle\left\langle \mathrm{e}^{i(k\varphi_1+l\varphi_2-k\varphi_3-l\varphi_4)}\right\rangle\left\langle \mathrm{e}^{i(m\varphi_1-m\varphi_2)}\right\rangle\right\rangle \\
&- \left\langle\left\langle \mathrm{e}^{i(k\varphi_1-k\varphi_2)}\right\rangle\left\langle \mathrm{e}^{i(l\varphi_1-l\varphi_2)}\right\rangle\right\rangle\left\langle\left\langle \mathrm{e}^{i(m\varphi_1-m\varphi_2)}\right\rangle\right\rangle \\
&- \left\langle\left\langle \mathrm{e}^{i(k\varphi_1-k\varphi_2)}\right\rangle\left\langle \mathrm{e}^{i(m\varphi_1-m\varphi_2)}\right\rangle\right\rangle\left\langle\left\langle \mathrm{e}^{i(l\varphi_1-l\varphi_2)}\right\rangle\right\rangle \\
&- \left\langle\left\langle \mathrm{e}^{i(l\varphi_1-l\varphi_2)}\right\rangle\left\langle \mathrm{e}^{i(m\varphi_1-m\varphi_2)}\right\rangle\right\rangle\left\langle\left\langle \mathrm{e}^{i(k\varphi_1-k\varphi_2)}\right\rangle\right\rangle \\
&+ 2\left\langle\left\langle \mathrm{e}^{i(k\varphi_1-k\varphi_2)}\right\rangle\right\rangle\left\langle\left\langle \mathrm{e}^{i(l\varphi_1-l\varphi_2)}\right\rangle\right\rangle\left\langle\left\langle \mathrm{e}^{i(m\varphi_1-m\varphi_2)}\right\rangle\right\rangle .
\end{aligned}
\tag{4.13}
$$

These three examples differ from the order of their multiparticle correlators. For instance, the usual expression maximises the number of particles in the correlators for each term before taking the all-event averages. The alternative formula involves only the product of single-event two-particle azimuthal correlators in the estimation of the final all-event averages. As its name indicates, the mixed expression is an example half-way between the usual and the alternative relations. Furthermore, as seen in Chapter 2, in the case of a detector with uniform acceptance like ALICE, only the azimuthal k-particle correlators that are isotropic do not cancel out in the passage from the single-event to the all-event averages. It has to be noted that this is the case for all the candidates presented above.

These three candidate expressions in Eqs. (4.11)–(4.13) yield to the same expression as in Eq. (4.1). It becomes then necessary to check which one of them, if not all, presents the needed cumulant properties and can be reliably used in flow analyses to measure the genuine correlations between the magnitudes. The higher order SCs are a generalisation of the well-known two-harmonic case. The latter can thus be used to establish a list of requirements that the final experimental expression must follow, as shown in Ref. [117]. Some of them concern the cumulant properties, while others can be related to the flow techniques used in the analysis, like the choice of event weights.

The determination of the unique experimental expression through the mentioned requirements is established with the help of carefully thought toy MC (TMC) studies. The starting point of the TMC setup is the implementation of the Fourier distribution given by Eq. (1.13) to sample the azimuthal angles of each simulated particle. For simplicity, only three independent free parameters v_2, v_3 and v_4 are employed in the definition, i.e.

$$
f(\varphi) = \frac{1}{2\pi}\left[1 + 2v_2\cos(2\varphi) + 2v_3\cos(3\varphi) + 2v_4\cos(4\varphi)\right] . \tag{4.14}
$$

This TMC setup is reduced to the most simple form needed to determine which expression must be used to calculate the genuine correlations between three different flow harmonics in the experiment. As all the azimuthal correlators in the three candidate definitions are isotropic, the symmetry planes can be set to zero without ill effects. Other input parameters of the TMC setup involve the event multiplicity M and the number of simulated events N_{events}. While the latter is straightforward, different options are available for M. The default setting is that all events have the same number of particles as it allows the use of unit event weights. The alternative configuration is an event-by-event multiplicity uniformly sampled in the range (M_{min}, M_{max}) given by the user. This more realistic option is used to determine the correct event weights.

The execution of the TMC setup goes then as follows. For each event, M, v_2, v_3 and v_4 are set according to the needs of the current check. The azimuthal angles are sampled from the Fourier series of Eq. 4.14 and used to compute all the needed multiparticle correlators with the Generic Framework described in Section 2.1. As already mentioned, the choice of the event weights for the transition from the single-event to the all-event averages is left open as an input. Equations (4.11)–(4.13) are subsequently computed from the retrieved multiparticle

correlations and compared to the expected output of the TMC study. Figure 4.1 illustrates this full setup. Each check used to determine the correct experimental expression is now presented in the following sections.

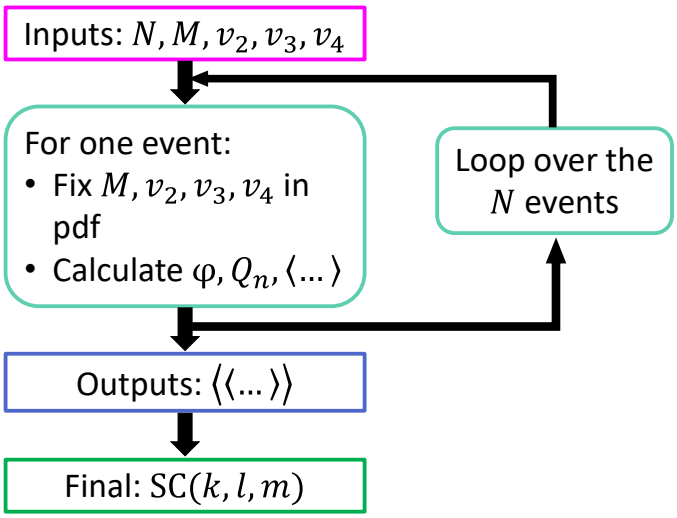

Figure 4.1: Illustration of the setup for the TMC studies used to check the properties of $\mathrm{SC}(k, l, m)$.

Study of the cumulants properties

The observable $\mathrm{SC}(k, l, m)$ probes the genuine correlations between the fluctuations of the three given flow amplitudes. Therefore, it must be zero in these different cases:

- case 1 where v_k, v_l, v_m are constant amplitudes,
- case 2 where v_k, v_l, v_m fluctuate independently, and
- case 3 where v_k, v_l fluctuate independently and v_m is genuinely correlated to v_k, for example.

These properties are shown for $\mathrm{SC}(2, 3, 4)$ with the following configurations of the TMC setup. For $N_{events} = 10^8$ events in total and $M = 100, 250, 500, 750, 1000$ particles per event, the flow amplitudes are set to

- $v_2, v_3, v_4 = 0$: case 1 shown in Fig. 4.2 (top left),
- $v_2 = 0.15, v_3 = 0.13, v_4 = 0.1$: case 1 shown in Fig. 4.2 (top right),
- $v_2, v_3, v_4 = (0.05, 0.09)$: case 2 shown in Fig. 4.2 (bottom left), and
- $v_2, v_3 = (0.05, 0.09)$ and $v_4 = v_2 - (0.005, 0.025)$: case 3 shown in Fig. 4.2 (bottom right).

The different panels in Fig. 4.2 show that $\mathrm{SC}(2, 3, 4)$ computed with the usual expression is in agreement with zero for all multiplicities, while the alternative and mixed definitions present a systematic bias as a function of M. This implies that only Eq. (4.11) does not contain any

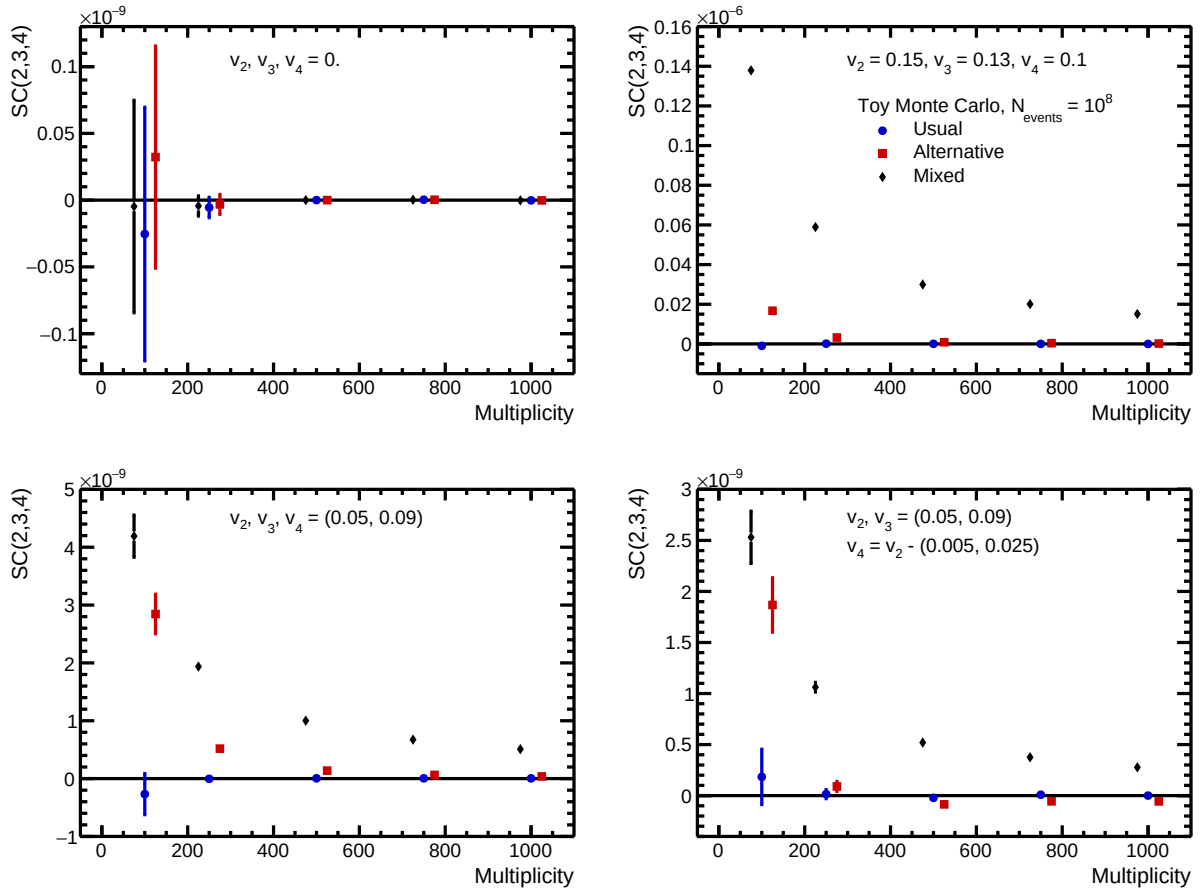

Figure 4.2: Multiplicity dependence of $\mathrm{SC}(2,3,4)$ for Eqs. (4.11)–(4.13) with different configurations of the TMC setup: zero amplitudes (*top left*), constant non-zero amplitudes (*top right*), independently fluctuating amplitudes (*bottom left*) and only two correlated amplitudes (*bottom right*). The notation (M_{min}, M_{max}) indicates the range for the event-by-event uniform sampling [117].

built-in correlations when the fluctuations of the harmonics are absent or fully independent, or when only two of them are genuinely correlated.

The results obtained with the previous TMC study are confirmed by configuring the setup such that the three flow magnitudes v_2, v_3 and v_4 are now genuinely correlated. For the same number of events N and sample of multiplicities, the harmonics are now set to $v_2 = (0.03, 0.1)$, $v_3 = v_2 - (0, 0.02)$ and $v_4 = v_2 - (0.005, 0.025)$. The final $\mathrm{SC}(2,3,4)$ is compared to the expected value analytically computed [158] using that

$$\langle v_2^m v_3^n v_4^p \rangle \equiv \int v_2^m v_3^n v_4^p f(v_2) f(v_2 - v_3) f(v_2 - v_4) dv_2 dv_3 dv_4, \tag{4.15}$$

with $f(x)$ a piecewise-defined function. The final results are shown in the left panel of Fig. 4.3 for all three expressions and in the right panel for the usual expression only. As in Fig. 4.2, the results with the usual expression are in agreement within the statistical errors with the expected value. The alternative and mixed definitions show the same systematic bias already seen above. All these checks lead to the conclusion that only the usual definition with the maximisation of the number of particles in each azimuthal correlator preserves the cumulant properties in all multiplicities. Therefore, from now on, the other requirements are checked only

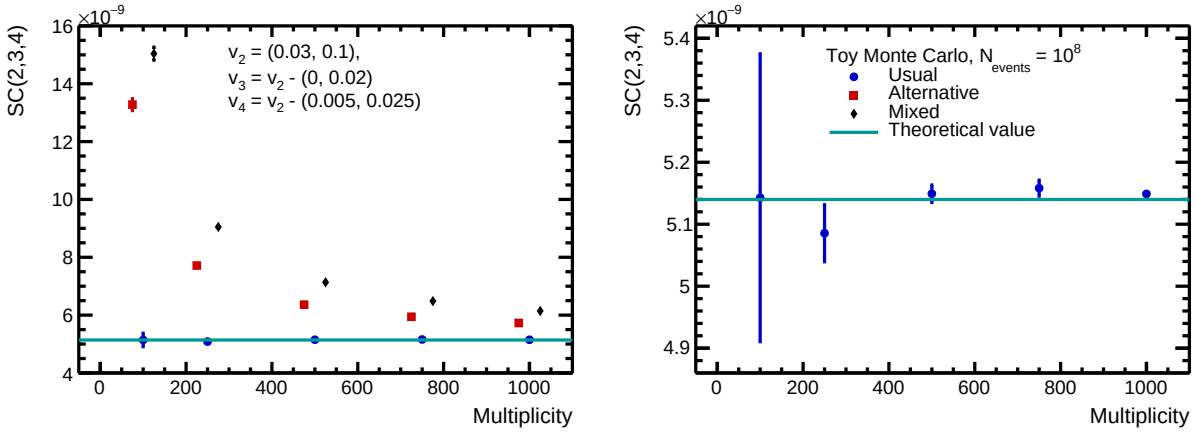

Figure 4.3: Multiplicity dependence of $\mathrm{SC}(2,3,4)$ for Eqs. (4.11)–(4.13) (*left*) and for the usual expression only (*right*) when the three flow amplitudes are genuinely correlated. The notation (M_{min}, M_{max}) indicates the range for the uniform event-by-event sampling [117].

for Eq. (4.11). The definitions involving products of two- and four-particle correlations inside the all-event averages show a strong deviation for low numbers of events. This divergence can thus be explained mathematically, as presented in Section 4.1.3.

Choice of the event weights

All the multiparticle correlators involved in the evaluation of the SCs are in terms of all-event averages. Moreover, the transition from the single-event to the all-event average depends on the choice of event weights, which will impact both the statistical and systematic uncertainties of the final SCs (Eq. (2.29)). The following setup is used to investigate the impact of the event weights. The number of simulated events is kept to $N_{events} = 10^8$. The flow amplitudes are set to the constant values $v_2 = 0.09, v_3 = 0.07, v_4 = 0.05$. As fluctuations are absent, the final result for $\mathrm{SC}(2,3,4)$ must be zero. Finally, the multiplicity is uniformly sampled event-by-event in the interval $M = (50, 500)$, which is a good approximation of the number of particles detected by ALICE in the Pb–Pb collisions at $\sqrt{s_{\mathrm{NN}}} = 2.76$ TeV. The different event weights under consideration are the unit weight, the multiplicity of the current event and the number of combinations [121] that can be obtained from k particles out of M. The final results for these weights are presented in Fig. 4.4. The comparison between the three different event weights shows that the "number of combinations" leads to the smallest statistical error in the final SC, with a result compatible with the expected zero. The "multiplicity" weight still returns $\mathrm{SC}(2,3,4) = 0$, but the statistical spread is more important. Finally, the unit event weight introduces the largest statistical error, but also a non-negligible bias in the obtained cumulant. One additional remark is that this conclusion is in agreement with the standard choice of event weights in flow analyses.

4.1.3 Explanation of the disagreement of the alternative expression

The comparison of the three expressions for the SC observable in the various TMC studies above highlights an ambiguity in the alternative and mixed definitions (Eqs. (4.12) and (4.13)). At first look, they both seem to be equal to Eq. (4.1) through the relation given in Eq. (2.12), in the same way as Eq. (4.11). However, the results from the TMC simulations show a clear disagreement at low multiplicities, while the usual expression always agrees with the predictions.

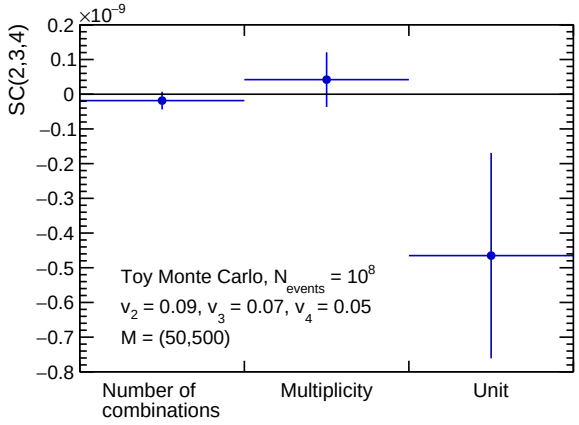

Figure 4.4: Comparison of the values for $\mathrm{SC}(2,3,4)$ for three different event weights: the number of combinations, the event multiplicity and the unit weight. The multiplicity is sampled uniformly event-by-event in the range $(50, 500)$. The expected value is zero as the three flow amplitudes are kept constant [117].

This deviation can be explained analytically. Due to the complexity and number of terms involved, the derivation is not done for three different flow harmonics, but in the simpler case of the well-known lower order SCs. Its conclusion is then illustrated with TMC studies based on the setup described above.

For two harmonics m, n with $m \neq n$, the corresponding SC is defined in terms of flow amplitudes in Eq. (2.62). Similarly as for $\mathrm{SC}(k,l,m)$, the *usual* expression of $\mathrm{SC}(m,n)$ is given by Eq. (2.61) and recalled here,

$$\mathrm{SC}(m,n)_{usual} = \left\langle\left\langle e^{i(m\varphi_1+n\varphi_2-m\varphi_3-n\varphi_4)}\right\rangle\right\rangle - \left\langle\left\langle e^{i(m\varphi_1-m\varphi_2)}\right\rangle\right\rangle\left\langle\left\langle e^{i(n\varphi_1-n\varphi_2)}\right\rangle\right\rangle. \tag{4.16}$$

Taking into account the analytic relation between the azimuthal angles and the flow degrees of freedom (Eq. (2.12)), Eq. (2.62) can be *a priori* expressed with another combination of correlators,

$$\mathrm{SC}(m,n)_{alternative} = \left\langle\left\langle e^{i(m\varphi_1-m\varphi_2)}\right\rangle\left\langle e^{i(n\varphi_1-n\varphi_2)}\right\rangle\right\rangle - \left\langle\left\langle e^{i(m\varphi_1-m\varphi_2)}\right\rangle\right\rangle\left\langle\left\langle e^{i(n\varphi_1-n\varphi_2)}\right\rangle\right\rangle. \tag{4.17}$$

Since the four-particle correlator in the first term of the usual expression is replaced with the product of two two-particle correlators as in Eq. (4.12), Eq. (4.17) is called the *alternative* form of $\mathrm{SC}(m,n)$. Furthermore, as Eqs. (4.16) and (4.17) only differ by their first term, it suffices to show the inequality between these two averages to prove the one between the two expressions themselves.

For an event with multiplicity M and three flow harmonics m, n and o with the unique condition that $m+n+o=0$, the single-event two-, three- and four-particle correlations are respectively given by

$$\begin{aligned}\left\langle e^{i(m\varphi_1-m\varphi_2)}\right\rangle &= \frac{\sum_{\substack{h,j=1\\h\neq j}}^{M} e^{i(m\varphi_h-m\varphi_j)}}{\sum_{\substack{h,j=1\\h\neq j}}^{M} 1} \\ &= \frac{1}{M(M-1)}\sum_{\substack{h,j=1\\h\neq j}}^{M} e^{i(m\varphi_h-m\varphi_j)},\end{aligned} \tag{4.18}$$

$$\begin{aligned}\left\langle \mathrm{e}^{i(m\varphi_1+n\varphi_2+o\varphi_3)}\right\rangle &= \frac{\sum_{\substack{h,j,k=1\\h\neq j\neq k}}^{M} \mathrm{e}^{i(m\varphi_h+n\varphi_j+o\varphi_k)}}{\sum_{\substack{h,j,k=1\\h\neq j\neq k}}^{M} 1} \\ &= \frac{1}{M(M-1)(M-2)} \sum_{\substack{h,j,k=1\\h\neq j\neq k}}^{M} \mathrm{e}^{i(m\varphi_h+n\varphi_j+o\varphi_k)}\end{aligned} \tag{4.19}$$

$$\begin{aligned}\left\langle \mathrm{e}^{i(m\varphi_1+n\varphi_2-m\varphi_3-n\varphi_4)}\right\rangle &= \frac{\sum_{\substack{h,j,k,l=1\\h\neq j\neq k\neq l}}^{M} \mathrm{e}^{i(m\varphi_h-m\varphi_j+n\varphi_k-n\varphi_l)}}{\sum_{\substack{h,j,k,l=1\\h\neq j\neq k\neq l}}^{M} 1} \\ &= \frac{1}{M(M-1)(M-2)(M-3)} \sum_{\substack{h,j,k,l=1\\h\neq j\neq k\neq l}}^{M} \mathrm{e}^{i(m\varphi_h-m\varphi_j+n\varphi_k-n\varphi_l)}.\end{aligned} \tag{4.20}$$

Using Eq. (4.18), the product of two two-particle correlators for the harmonics m and n goes as follows:

$$\begin{aligned}\left\langle \mathrm{e}^{i(m\varphi_1-m\varphi_2)}\right\rangle \left\langle \mathrm{e}^{i(n\varphi_1-n\varphi_2)}\right\rangle &= \frac{1}{M^2(M-1)^2} \left[\sum_{\substack{h,j=1\\h\neq j}}^{M} \mathrm{e}^{i(m\varphi_h-m\varphi_j)}\right] \cdot \left[\sum_{\substack{k,l=1\\k\neq l}}^{M} \mathrm{e}^{i(n\varphi_k-n\varphi_l)}\right] \\ &= \frac{1}{M^2(M-1)^2} \left[\sum_{\substack{h,j,k,l=1\\h\neq j\\k\neq l}}^{M} \mathrm{e}^{i(m\varphi_h-m\varphi_j+n\varphi_k-n\varphi_l)}\right].\end{aligned} \tag{4.21}$$

The conditions $h \neq j$ and $k \neq l$ on the sum $\sum_{h,j,k,l=1}^{M}$ mean that only the following combinations of harmonics are possible:

- $h \neq j \neq k \neq l$,
- $h \neq j$, $h = k$ and $j = l$,
- $h \neq j$, $h = k$ but $j \neq l$,
- $h \neq j$, $h \neq k$ and $j = l$,
- $h \neq j$, $h = l$ and $j = k$,
- $h \neq j$, $h = l$ but $j \neq k$, and
- $h \neq j$, $h \neq l$ but $j = k$.

This implies that Eq. (4.21) can be expressed with

$$\begin{aligned}\left\langle \mathrm{e}^{i(m\varphi_1 - m\varphi_2)} \right\rangle \left\langle \mathrm{e}^{i(n\varphi_1 - n\varphi_2)} \right\rangle = \frac{1}{M^2(M-1)^2} \Bigg[& \sum_{\substack{h,j,k,l=1 \\ h\neq j\neq k\neq l}}^{M} \mathrm{e}^{i(m\varphi_h - m\varphi_j + n\varphi_k - n\varphi_l)} \\ & + \sum_{\substack{h,j,k,l=1 \\ h=k \\ j=l \\ h\neq j}}^{M} \mathrm{e}^{i(m\varphi_h - m\varphi_j + n\varphi_h - n\varphi_j)} + \sum_{\substack{h,j,k,l=1 \\ h=k \\ h\neq j\neq l}}^{M} \mathrm{e}^{i(m\varphi_h - m\varphi_j + n\varphi_h - n\varphi_l)} \\ & + \sum_{\substack{h,j,k,l=1 \\ j=l \\ h\neq j\neq k}}^{M} \mathrm{e}^{i(m\varphi_h - m\varphi_j + n\varphi_k - n\varphi_j)} + \sum_{\substack{h,j,k,l=1 \\ h=l \\ j=k \\ h\neq j}}^{M} \mathrm{e}^{i(m\varphi_h - m\varphi_j + n\varphi_j - n\varphi_h)} \\ & + \sum_{\substack{h,j,k,l=1 \\ h=l \\ h\neq j\neq k}}^{M} \mathrm{e}^{i(m\varphi_h - m\varphi_j + n\varphi_k - n\varphi_h)} + \sum_{\substack{h,j,k,l=1 \\ j=k \\ h\neq j\neq l}}^{M} \mathrm{e}^{i(m\varphi_h - m\varphi_j + n\varphi_j - n\varphi_l)} \Bigg] .\end{aligned} \tag{4.22}$$

Equations (4.18)–(4.20) are inserted in Eq. (4.22), leading to

$$\begin{aligned}\left\langle \mathrm{e}^{i(m\varphi_1 - m\varphi_2)} \right\rangle \left\langle \mathrm{e}^{i(n\varphi_1 - n\varphi_2)} \right\rangle = \frac{1}{M^2(M-1)^2} \Big[& M(M-1)(M-2)(M-3) \left\langle \mathrm{e}^{i(m\varphi_1 + n\varphi_2 - m\varphi_3 - n\varphi_4)} \right\rangle \\ & + M(M-1) \left\{ \left\langle \mathrm{e}^{i((m+n)\varphi_1 - (m+n)\varphi_2)} \right\rangle + \left\langle \mathrm{e}^{i((m-n)\varphi_1 - (m-n)\varphi_2)} \right\rangle \right\} \\ & + M(M-1)(M-2) \left\{ \left\langle \mathrm{e}^{i((m+n)\varphi_1 - m\varphi_2 - n\varphi_3)} \right\rangle + \left\langle \mathrm{e}^{i((m-n)\varphi_1 - m\varphi_2 + n\varphi_3)} \right\rangle \right. \\ & \left. + \left\langle \mathrm{e}^{i(m\varphi_1 + (n-m)\varphi_2 - n\varphi_3)} \right\rangle + \left\langle \mathrm{e}^{i(m\varphi_1 - (m+n)\varphi_2 + n\varphi_3)} \right\rangle \right\} \Big] .\end{aligned} \tag{4.23}$$

Finally, the all-event average is given by

$$\begin{aligned}\left\langle \left\langle \mathrm{e}^{i(m\varphi_1 - m\varphi_2)} \right\rangle \left\langle \mathrm{e}^{i(n\varphi_1 - n\varphi_2)} \right\rangle \right\rangle = \frac{1}{M(M-1)} \Big[& (M-2)(M-3) \left\langle \left\langle \mathrm{e}^{i(m\varphi_1 + n\varphi_2 - m\varphi_3 - n\varphi_4)} \right\rangle \right\rangle \\ & + \left\langle \left\langle \mathrm{e}^{i((m+n)\varphi_1 - (m+n)_2)} \right\rangle \right\rangle + \left\langle \left\langle \mathrm{e}^{i((m-n)\varphi_1 - (m-n)\varphi_2)} \right\rangle \right\rangle \\ & + (M-2) \left\{ \left\langle \left\langle \mathrm{e}^{i((m+n)\varphi_1 - m\varphi_2 - n\varphi_3)} \right\rangle \right\rangle + \left\langle \left\langle \mathrm{e}^{i((m-n)\varphi_1 - m\varphi_2 + n\varphi_3)} \right\rangle \right\rangle \right. \\ & \left. + \left\langle \left\langle \mathrm{e}^{i(m\varphi_1 + (n-m)\varphi_2 - n\varphi_3)} \right\rangle \right\rangle + \left\langle \left\langle \mathrm{e}^{i(m\varphi_1 - (m+n)\varphi_2 + n\varphi_3)} \right\rangle \right\rangle \right\} \Big] .\end{aligned} \tag{4.24}$$

The first term is the four-particle correlators present in the usual expression in Eq. (4.16). However, while the autocorrelations are removed in the expression of a single two-particle correlator, it is not the case in their products. All the additional terms in Eq. (4.24) come from the remaining self-correlations introduced by the product itself.

Using the TMC setup described in the previous subsection, simulated results are obtained to illustrate the difference between the usual and alternative expressions of $\mathrm{SC}(m,n)$ and the impact of the additional terms coming from the partial removal of the autocorrelations in the latter. The flow magnitudes are set constant to $v_2 = 0.15$ and $v_4 = 0.1$ for each of the $N_{events} = 10^6$ events. The results for the first term of the two expressions are shown in Fig. 4.5, along with

their theoretical prediction. The four-particle correlator $\left\langle\left\langle e^{i(m\varphi_1+n\varphi_2-m\varphi_3-n\varphi_4)}\right\rangle\right\rangle$ is in good agreement with the expected value, while the all-event average of the product of the two-particle shows the same multiplicity dependence as observed before. Figure 4.5 shows with the open

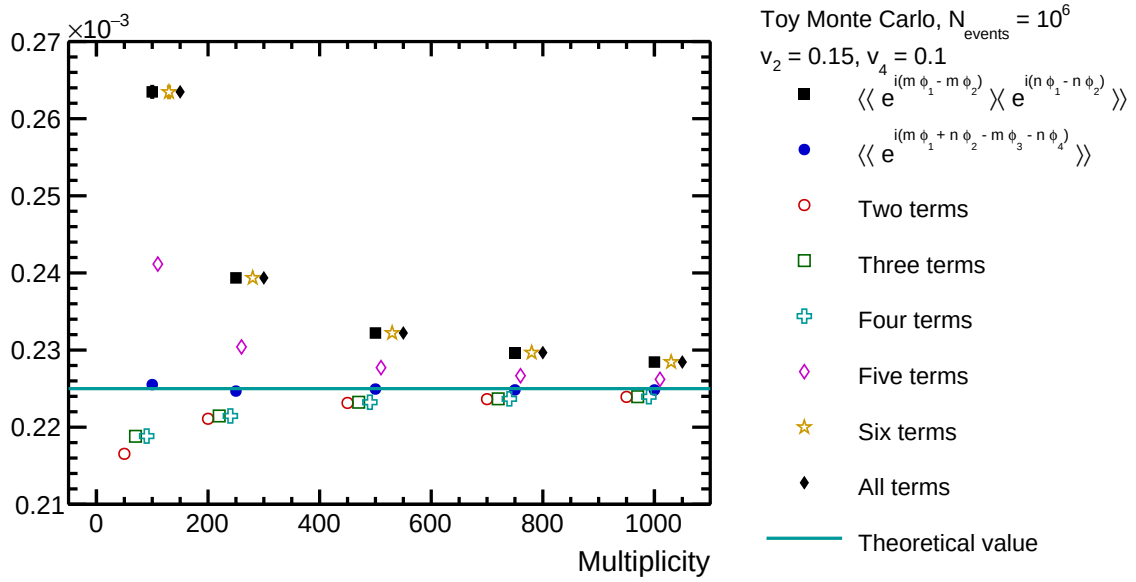

Figure 4.5: Comparison between the first terms of the usual and alternative expressions of $\mathrm{SC}(m,n)$ as a function of the multiplicity. The addition of each successive term in Eq. (4.24) tends to the results of $\left\langle\left\langle e^{i(m\varphi_1-m\varphi_2)}\right\rangle\left\langle e^{i(n\varphi_1-n\varphi_2)}\right\rangle\right\rangle$.

markers also the convergence of the sum of terms from Eq. (4.24). The open red circles are the sum of the two first terms of Eq. (4.24), the open black squares the sum of the three first terms, and so on until the full sum represented with the closed black diamonds. As the latter is is perfect agreement with $\left\langle\left\langle e^{i(m\varphi_1-m\varphi_2)}\right\rangle\left\langle e^{i(n\varphi_1-n\varphi_2)}\right\rangle\right\rangle$, proving the mathematical derivation made above.

A similar proof can be done to show this effect in the alternative and mixed expressions of $\mathrm{SC}(k,l,m)$, their multiplicity dependence can still be explained by the introduction of self-correlations from the product of single-event multiparticle correlations. Furthermore, as the usual expression uses the largest multiparticle correlator for each event-by-event average, it removes all autocorrelations by definition.

4.1.4 Comparison between the traditional and new approaches

The studies above have proved the validity of the new approach in the generalisation of $\mathrm{SC}(m,n)$ to three and more harmonics. The genuine correlations between the j flow amplitudes $v_{n_1}^2$, $v_{n_2}^2$ to $v_{n_j}^2$ can be estimated by identifying them in the expansion of the j-th order cumulant $\kappa_{1,\ldots,1}$. Their experimental evaluation is obtained with the use of the analytical relation between the azimuthal angles and the flow degrees of freedom (Eq. (2.12)). The necessity of introducing a new approach is now analysed by looking at the application of the traditional approach to generalise the SCs and the comparison of the results.

In the traditional approach, the expressions for a flow observable are obtained by performing the cumulant expansion directly with the azimuthal angles as stochastic variables. In the case of the 3-harmonic SCs, six particles are needed in the largest correlator and thus, the starting

cumulant is $\kappa_{1,1,1,1,1,1}$. Using the usual identification $X_1 = \mathrm{e}^{ik\varphi_1}$, $X_2 = \mathrm{e}^{il\varphi_2}$, $X_3 = \mathrm{e}^{im\varphi_3}$, $X_4 = \mathrm{e}^{-ik\varphi_4}$, $X_5 = \mathrm{e}^{-il\varphi_5}$ and $X_6 = \mathrm{e}^{-im\varphi_6}$, the all-event average is given by

$$\begin{aligned}
\kappa_{1,1,1,1,1,1} = &-\left\langle\left\langle \mathrm{e}^{i(l\varphi_2+m\varphi_3-k\varphi_4)}\right\rangle\right\rangle\left\langle\left\langle \mathrm{e}^{i(k\varphi_1-l\varphi_5-m\varphi_6)}\right\rangle\right\rangle \\
&+2\left\langle\left\langle \mathrm{e}^{i(m\varphi_3-m\varphi_6)}\right\rangle\right\rangle\left\langle\left\langle \mathrm{e}^{i(l\varphi_2-l\varphi_5)}\right\rangle\right\rangle\left\langle\left\langle \mathrm{e}^{i(k\varphi_1-k\varphi_4)}\right\rangle\right\rangle \\
&-\left\langle\left\langle \mathrm{e}^{i(l\varphi_2+m\varphi_3-l\varphi_5-m\varphi_6)}\right\rangle\right\rangle\left\langle\left\langle \mathrm{e}^{i(k\varphi_1-k\varphi_4)}\right\rangle\right\rangle \\
&-\left\langle\left\langle \mathrm{e}^{i(l\varphi_2-k\varphi_4-m\varphi_6)}\right\rangle\right\rangle\left\langle\left\langle \mathrm{e}^{i(k\varphi_1+m\varphi_3-l\varphi_5)}\right\rangle\right\rangle \\
&-\left\langle\left\langle \mathrm{e}^{i(l\varphi_2-l\varphi_5)}\right\rangle\right\rangle\left\langle\left\langle \mathrm{e}^{i(k\varphi_1+m\varphi_3-k\varphi_4-m\varphi_6)}\right\rangle\right\rangle \\
&-\left\langle\left\langle \mathrm{e}^{i(m\varphi_3-k\varphi_4-l\varphi_5)}\right\rangle\right\rangle\left\langle\left\langle \mathrm{e}^{i(k\varphi_1+l\varphi_2-m\varphi_6)}\right\rangle\right\rangle \\
&-\left\langle\left\langle \mathrm{e}^{i(m\varphi_3-m\varphi_6)}\right\rangle\right\rangle\left\langle\left\langle \mathrm{e}^{i(k\varphi_1+l\varphi_2-k\varphi_4-l\varphi_5)}\right\rangle\right\rangle \\
&+\left\langle\left\langle \mathrm{e}^{i(k\varphi_1+l\varphi_2+m\varphi_3-k\varphi_4-l\varphi_5-m\varphi_6)}\right\rangle\right\rangle .
\end{aligned} \tag{4.25}$$

It has to be noted that all terms where isotropy could not be achieved with any combination of harmonics have been removed in the expression above. Two different cases are now treated as examples.

The first example is obtained by setting $k = 4n$, $l = 3n$ and $m = 2n$, for any n a non-zero harmonic, into Eq. (4.25). This leads to an expression of the corresponding "SC" observable in the traditional approach:

$$\begin{aligned}
\mathrm{SC}(2n,3n,4n)_{old} = &\,2\left\langle\left\langle \mathrm{e}^{2in(\varphi_3-\varphi_6)}\right\rangle\right\rangle\left\langle\left\langle \mathrm{e}^{3in(\varphi_2-\varphi_5)}\right\rangle\right\rangle\left\langle\left\langle \mathrm{e}^{4in(\varphi_1-\varphi_4)}\right\rangle\right\rangle \\
&-\left\langle\left\langle \mathrm{e}^{in(3\varphi_2+2\varphi_3-3\varphi_5-2\varphi_6)}\right\rangle\right\rangle\left\langle\left\langle \mathrm{e}^{4in(\varphi_1-\varphi_4)}\right\rangle\right\rangle \\
&-\left\langle\left\langle \mathrm{e}^{in(4\varphi_1+2\varphi_3-4\varphi_4-2\varphi_6)}\right\rangle\right\rangle\left\langle\left\langle \mathrm{e}^{3in(\varphi_2-\varphi_5)}\right\rangle\right\rangle \\
&-\left\langle\left\langle \mathrm{e}^{in(4\varphi_1+3\varphi_2-4\varphi_4-3\varphi_5)}\right\rangle\right\rangle\left\langle\left\langle \mathrm{e}^{2in(\varphi_3-\varphi_6)}\right\rangle\right\rangle \\
&+\left\langle\left\langle \mathrm{e}^{in(4\varphi_1+3\varphi_2+2\varphi_3-4\varphi_4-3\varphi_5-2\varphi_6)}\right\rangle\right\rangle ,
\end{aligned} \tag{4.26}$$

where the isotropy condition has already been applied. Using Eq. (2.12) returns the following equation in terms of the flow degrees of freedom:

$$\begin{aligned}
\mathrm{SC}(2n,3n,4n)_{old} = &\,2\left\langle v_{2n}^2\right\rangle\left\langle v_{3n}^2\right\rangle\left\langle v_{4n}^2\right\rangle - \left\langle v_{2n}^2 v_{3n}^2\right\rangle\left\langle v_{4n}^2\right\rangle - \left\langle v_{2n}^2 v_{4n}^2\right\rangle\left\langle v_{3n}^2\right\rangle \\
&-\left\langle v_{3n}^2 v_{4n}^2\right\rangle\left\langle v_{2n}^2\right\rangle + \left\langle v_{2n}^2 v_{3n}^2 v_{4n}^2\right\rangle .
\end{aligned} \tag{4.27}$$

This corresponds to the definition of $\mathrm{SC}(k,l,m)$ in terms of flow amplitudes presented in Eq. (4.1). This means that both the new and the traditional approaches converge for this specific choice of harmonics.

In the second example, the harmonics are set to $k = 3n$, $l = 2n$ and $m = n$ for any strictly

positive integer n. Equation (4.25) transforms into

$$\begin{aligned}\mathrm{SC}(n,2n,3n)_{old} = &-\left\langle\left\langle \mathrm{e}^{in(2\varphi_2+\varphi_3-3\varphi_4)}\right\rangle\right\rangle\left\langle\left\langle \mathrm{e}^{in(3\varphi_1-2\varphi_5-\varphi_6)}\right\rangle\right\rangle \\ &+2\left\langle\left\langle \mathrm{e}^{in(\varphi_3-\varphi_6)}\right\rangle\right\rangle\left\langle\left\langle \mathrm{e}^{2in(\varphi_2-\varphi_5)}\right\rangle\right\rangle\left\langle\left\langle \mathrm{e}^{3in(\varphi_1-\varphi_4)}\right\rangle\right\rangle \\ &-\left\langle\left\langle \mathrm{e}^{in(2\varphi_2+\varphi_3-2\varphi_5-\varphi_6)}\right\rangle\right\rangle\left\langle\left\langle \mathrm{e}^{3in(\varphi_1-\varphi_4)}\right\rangle\right\rangle \\ &-\left\langle\left\langle \mathrm{e}^{in(3\varphi_1+\varphi_3-3\varphi_4-\varphi_6)}\right\rangle\right\rangle\left\langle\left\langle \mathrm{e}^{2in(\varphi_2-\varphi_5)}\right\rangle\right\rangle \\ &-\left\langle\left\langle \mathrm{e}^{in(3\varphi_1+2\varphi_2-3\varphi_4-2\varphi_5)}\right\rangle\right\rangle\left\langle\left\langle \mathrm{e}^{in(\varphi_3-\varphi_6)}\right\rangle\right\rangle \\ &+\left\langle\left\langle \mathrm{e}^{in(3\varphi_1+2\varphi_2+\varphi_3-3\varphi_4-2\varphi_5-\varphi_6)}\right\rangle\right\rangle .\end{aligned} \tag{4.28}$$

This becomes in terms of flow amplitudes and symmetry planes

$$\begin{aligned}\mathrm{SC}(n,2n,3n)_{old} = &-\left\langle v_n v_{2n} v_{3n}\cos\left[in(2\Psi_{2n}+\Psi_n-3\Psi_{3n})\right]\right\rangle^2 \\ &+2\left\langle v_n^2\right\rangle\left\langle v_{2n}^2\right\rangle\left\langle v_{3n}^2\right\rangle-\left\langle v_n^2 v_{2n}^2\right\rangle\left\langle v_{3n}^2\right\rangle-\left\langle v_n^2 v_{3n}^2\right\rangle\left\langle v_{2n}^2\right\rangle \\ &-\left\langle v_{2n}^2 v_{3n}^2\right\rangle\left\langle v_n^2\right\rangle+\left\langle v_n^2 v_{2n}^2 v_{3n}^2\right\rangle .\end{aligned} \tag{4.29}$$

In opposition to the previous example, this equation diverges with the expression obtained in the new approach. Furthermore, this is not a valid cumulant of the flow amplitudes due to the first term containing a contribution from the symmetry planes themselves. This, for example, means that this equation does not return zero when the three flow magnitudes v_n, v_{2n} and v_{3n} are not all genuinely correlated.

Based on this observation, comparisons between the two approaches using MC studies are now provided. The observable that is used as a concrete example is $\mathrm{SC}(1,2,3)$. Its expression in the new formalism, denoted by $\mathrm{SC}(1,2,3)_{new}$, is given by Eq. (4.11) where $k=1$, $l=2$ and $m=3$. The traditional definition ($\mathrm{SC}(1,2,3)_{old}$) is obtained by setting $n=1$ in Eq. (4.29) given above.

The first study is done with another TMC setup than the one described in Section 4.1.2. Its particularities are shown below. The total number of events is $N_{events}=10000$. The flow magnitudes are uniformly and independently sampled event-by-event in the ranges $v_1=(0.03,0.1)$, $v_2=(0.04,0.1)$ and $v_3=(0.05,0.1)$. Furthermore, their corresponding symmetry planes are sampled for each event in the uniform ranges $\Psi_1,\Psi_2=(0,2\pi)$ and $\Psi_3=\frac{1}{3}\left(\frac{\pi}{4}+2\Psi_2+\Psi_1\right)$. The amplitudes and planes are then directly used to compute the terms of the two cumulant expressions. The final observables are presented in Fig. 4.6. As the flow amplitudes are all sampled independently event-by-event, the measure of their genuine correlations must be equal to zero. This is the case for $\mathrm{SC}(1,2,3)_{new}$ obtained with the new approach. However, due to the presence of the term with symmetry planes in its expression, $\mathrm{SC}(1,2,3)_{old}$ is non-zero. This shows that only the new formalism presented above preserves the properties of the cumulants for the flow amplitudes.

This influence of the symmetry planes is visible also in predictions from real MC models, for example, iEBE-VISHNU (see Section 6.1.4 for a description of iEBE-VISHNU and its setup for this work). Figure 4.7 shows in the left panel the centrality dependence of $\mathrm{SC}(1,2,3)$ obtained through the two approaches using iEBE-VISHNU and in the right panel the centrality dependence of their difference. The predicted results show clear differences in their trend for collisions with a centrality percentile higher or equal to 25%. Furthermore, their difference presents a non-negligible systematic bias, again due to the impact from the term with the symmetry planes in the traditional formalism.

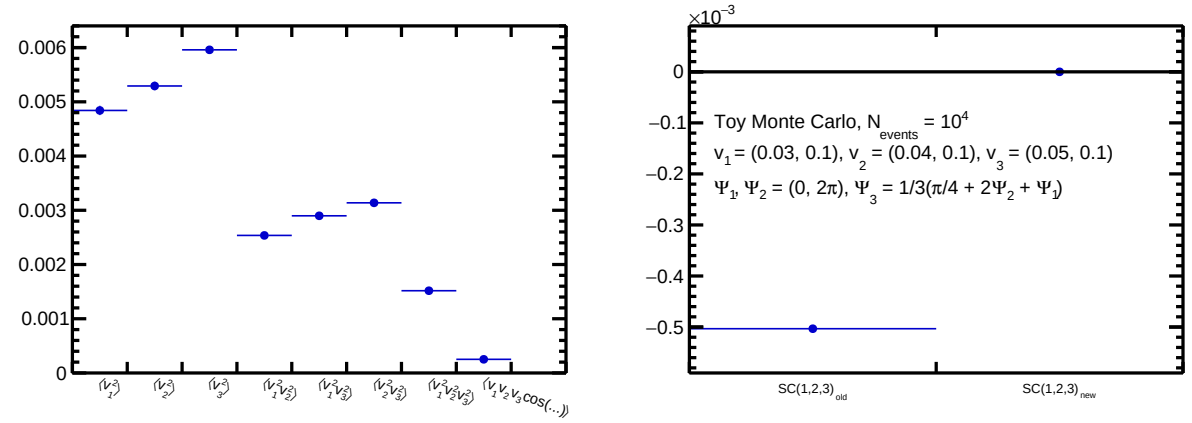

Figure 4.6: (*Left*) All-event averages involved in the traditional (old) and new approaches of $\mathrm{SC}(1,2,3)$ for the TMC described in the text and (*right*) final corresponding final expressions for the traditional $\mathrm{SC}(1,2,3)_{old}$ and new $\mathrm{SC}(1,2,3)_{new}$ approaches. Results courtesy of A. Bilandzic [117].

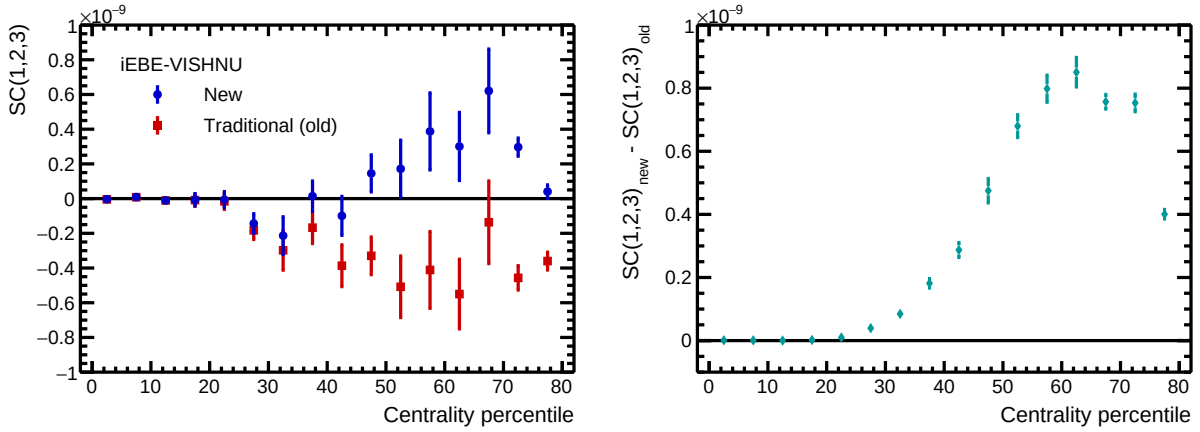

Figure 4.7: Centrality dependence of $\mathrm{SC}(1,2,3)$ in the two different approaches (*left*) and of their difference (*right*) in iEBE-VISHNU. Results courtesy of S.F. Taghavi [117].

4.1.5 Robustness against nonflow correlations

Another criterion for the generalisation of the SCs is their robustness against nonflow correlations. Nonflow is not a collective effect and thus, it is a systematic bias in any flow analysis. Two different studies are conducted to probe the nonflow effects in the proposed novel observables: the nonflow scaling through TMC simulations and their sensitivity to nonflow with the realistic model HIJING [72, 73].

Nonflow scaling with TMC studies

The nonflow scaling of a compound observable is based on the scaling of each one of its k-particle correlators given by Eq. (2.32). From the number of particles in each term of Eq. (4.11),

the final scaling of $\mathrm{SC}(k,l,m)$ is expressed as

$$\delta_3^{\mathrm{SC}} \sim \delta_6 + \delta_4 \cdot \delta_2 + (\delta_2)^3 = \frac{\alpha}{M^5} + \frac{\beta}{M^4} + \frac{\gamma}{M^3}, \tag{4.30}$$

where α, β and γ are three constants used to quantify the different sources that contribute to nonflow. They are obtained by fitting the multiplicity dependence of a SC observable. This is achieved with the following configuration of the TMC setup from Section 4.1.2. For $N_{events} = 10^8$ events, all flow magnitudes are set to zero, removing all contributions from collective flow. Strong two-particle correlations are introduced by first sampling the azimuthal angles over $M_{initial}$ before doubling all particles. The final multiplicity M_{final} is thus $M_{final} = 2M_{initial}$. This case can be seen as an example of extreme track splitting where each particle is counted twice in the detector. Finally, the multiplicity dependence of the obtained SC (Fig. 4.8) is fit with the

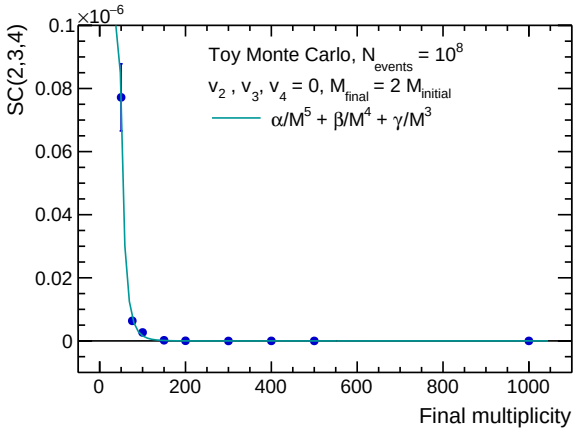

Figure 4.8: Multiplicity dependence of $\mathrm{SC}(2,3,4)$ for strong two-particle correlations. The cyan line shows the fit of the nonflow scaling expected for $\mathrm{SC}(k,l,m)$ [117].

scaling from Eq. (4.30). The fit parameters are found to be

$$\begin{aligned}
\alpha &= 27.011 \pm 9.787, \\
\beta &= -0.0947 \pm 0.1743, \\
\gamma &= (-1.383 \pm 5.876) \times 10^{-4},
\end{aligned}$$

with a fit goodness $\chi^2/ndf = 0.7$. This means that the proposed fit is a good description of the results. Furthermore, both β and γ are consistent with zero, which implies that the dominant contribution to nonflow originates from the six-particle correlator.

Nonflow estimations in HIJING

Until now, the studies of the properties of the experimental expression of $\mathrm{SC}(k,l,m)$ have been established either in a fully controlled environment or in a realistic model, iEBE-VISHNU. While the TMC setup is a good and necessary passage to ensure everything goes as expected — the output can be completely predicted from the input parameters — it is not a true representation of the collisions between heavy ions. In addition, iEBE-VISHNU contains both flow and nonflow, making it impossible to estimate reliably the influence of the latter in the SCs measurements. In that context, the next natural step is to study the predictions of the SCs observables with the help of realistic MC models containing only nonflow.

HIJING is such a MC generator, which describes phenomena involving correlations between few particles only, without any contribution from collective effects. Therefore, it is widely used in flow analyses to test the sensitivity to nonflow of a multiparticle azimuthal correlator or a compound observable like the SCs. If its predictions in HIJING are compatible with zero within statistical uncertainties, the corresponding variable is a reliable estimator of the properties of the anisotropic flow. A more complete discussion about HIJING is presented in Section 6.1.1.

The data sample used here corresponds to Pb–Pb collisions obtained at $\sqrt{s_{\mathrm{NN}}} = 2.76$ TeV in the same conditions as the measurements done with the ALICE detector in 2010. The details about the simulations and the selection criteria applied to the data can be found in Chapter 5. It has to be noted that the analysed data have been obtained at reconstruction level and no particle weight has been applied. The predictions from HIJING for various combinations of harmonics are shown in Fig. 4.9 for SC$(2,3,4)$, Fig. 4.10 for SC$(2,3,5)$, Fig. 4.11 for SC$(2,4,6)$ and Fig. 4.12 for SC$(3,4,5)$. These combinations have been chosen as their experimental counterparts are studied in Chapter 6. Moreover, all figures are organised as follows: the centrality dependence of each term of the expression of SC(k,l,m) is presented in the left panel, while the right panel demonstrates the centrality dependence of the SC itself.

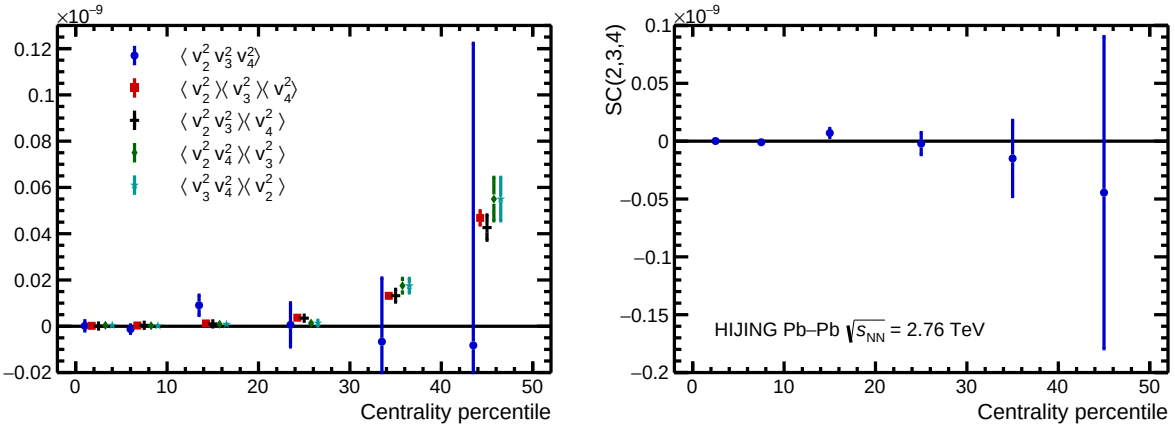

Figure 4.9: Centrality dependence of each individual term in the expression of SC$(2,3,4)$ (*left*) and of the final SC$(2,3,4)$ itself (*right*) with the HIJING model.

In the left panels, the individual terms are not all in agreement with zero. They exhibit a centrality dependence that the statistical fluctuations cannot explain. The figures in the right panels present values that are compatible with zero for all centrality bins. This leads to the conclusion that the presented combinations are not sensitive to nonflow correlations than each of the correlators in their definition taken individually.

4.2 Asymmetric Cumulants

The alternative approach introduced for the generalisation of the two-harmonic SCs to three and more flow amplitudes has been shown to lead to observables with all the properties needed for flow analyses. Examples of such properties are the accurate evaluation of the correlations both with the flow amplitudes and with the azimuthal angles, or their robustness against few-particle nonflow correlations. Nevertheless, these SCs represent only a subset of the cumulants of the flow amplitudes squared. To determine the full p.d.f., the information relative to distinct orders and moments of the flow amplitudes are needed. The aim of this section is thus to expand

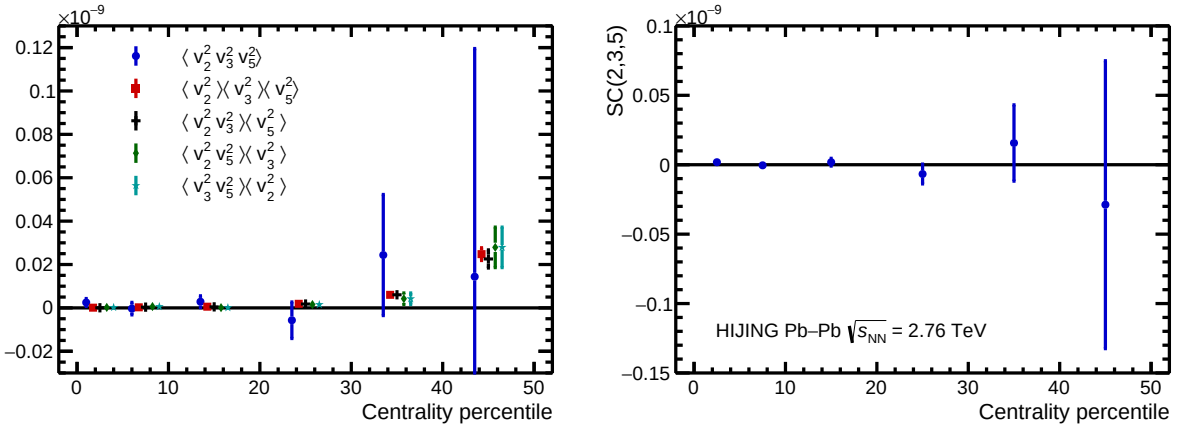

Figure 4.10: Centrality dependence of each individual term in the expression of $\mathrm{SC}(2,3,5)$ (*left*) and of the final $\mathrm{SC}(2,3,5)$ itself (*right*) with the HIJING model.

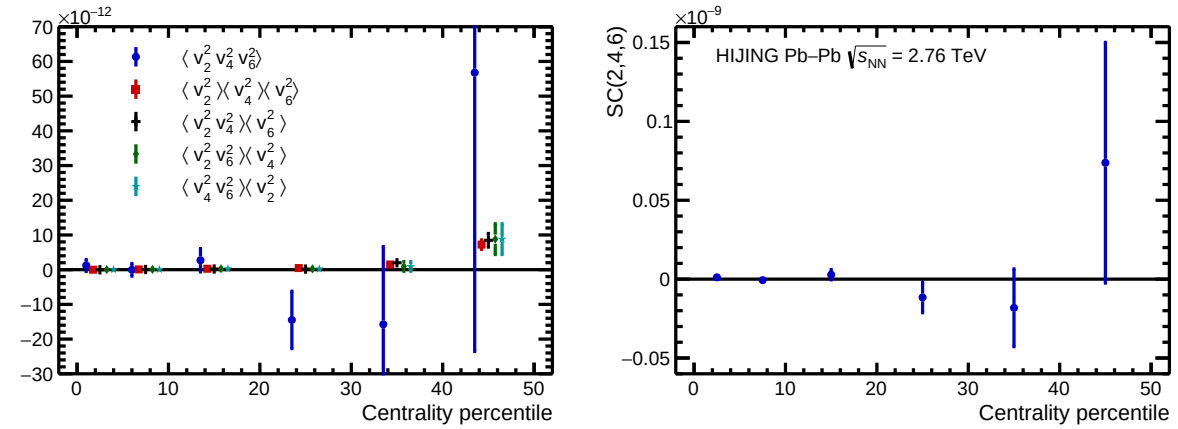

Figure 4.11: Centrality dependence of each individual term in the expression of $\mathrm{SC}(2,4,6)$ (*left*) and of the final $\mathrm{SC}(2,4,6)$ itself (*right*) with the HIJING model.

the new approach for cumulants to design observables, the ACs, that can be reliably used to study the genuine correlations between these different moments of the flow magnitudes.

4.2.1 Lowest order Asymmetric Cumulant

The first combination of moments that will be investigated here is the two-harmonic AC denoted by $\mathrm{AC}_{2,1}(m,n)$. In opposition to the SCs where the order of the cumulant is identical to its number of harmonics, the order of an AC is at least equal to the number of concerned flow amplitudes plus one. This means that the lowest order AC which can be defined is of third order, as it cannot involve less than two harmonics:

$$\mathrm{AC}_{2,1}(m,n) \equiv \left\langle (v_m^2)^2 v_n^2 \right\rangle_c \equiv \left\langle v_m^4 v_n^2 \right\rangle_c . \tag{4.31}$$

Before going further, a comment has to be made on the notation chosen for these novel observables. While it seems complicated, it allows knowing directly which flow amplitudes and which moments are used in the cumulant expansion. Furthermore, it can easily be generalised

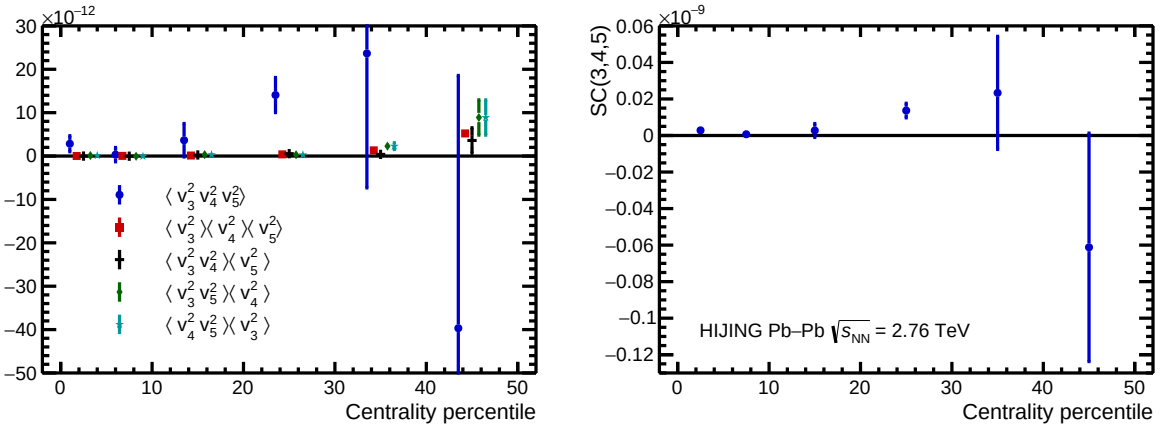

Figure 4.12: Centrality dependence of each individual term in the expression of $\mathrm{SC}(3,4,5)$ (*left*) and of the final $\mathrm{SC}(3,4,5)$ itself (*right*) with the HIJING model.

to any number of amplitudes and any moment and thus, to any future new AC observable. As for the higher order SCs, two expressions are needed for the ACs: the general one in terms of the flow amplitudes which can be straightforwardly used to get theoretical predictions, and the one with the azimuthal angles to analyse the experimental data. The observable $\mathrm{AC}_{2,1}(m,n)$ is based on the cumulant expansion of $\kappa_{2,1}$ (Eq. (2.43)) as indicated by its indices. The new approach states that the theoretical expression of any two-harmonic cumulant can be obtained with the identification of $X_1 = v_m^2$ and $X_2 = v_n^2$ in its cumulant expansion. The expression for $\mathrm{AC}_{2,1}(m,n)$ is then

$$\mathrm{AC}_{2,1}(m,n) = \left\langle v_m^4 v_n^2 \right\rangle - \left\langle v_m^4 \right\rangle \left\langle v_n^2 \right\rangle - 2\left\langle v_m^2 v_n^2 \right\rangle \left\langle v_m^2 \right\rangle + 2\left\langle v_m^2 \right\rangle^2 \left\langle v_n^2 \right\rangle . \tag{4.32}$$

In a way similar to what has been done in Section 4.1, the proof is now given that $\mathrm{AC}_{2,1}(m,n)$ is also a valid cumulant of the flow amplitudes squared and hence, that the new method can be successfully extended to the measurements of the genuine correlations between different moments of the flow amplitudes.

Statistical independence. The fluctuations of v_m^2 and v_n^2 are considered being completely uncorrelated. Equation (4.32)) simplifies into

$$\mathrm{AC}_{2,1}(m,n) = \left\langle v_m^4 \right\rangle \left\langle v_n^2 \right\rangle - \left\langle v_m^4 \right\rangle \left\langle v_n^2 \right\rangle - 2\left\langle v_m^2 \right\rangle \left\langle v_n^2 \right\rangle \left\langle v_m^2 \right\rangle + 2\left\langle v_m^2 \right\rangle^2 \left\langle v_n^2 \right\rangle = 0, \quad \square \tag{4.33}$$

as expected for a cumulant.

Reduction. The flow magnitudes are set equal, i.e. $v_m^2 = v_n^2 \equiv v^2$, leading to

$$\begin{aligned} \mathrm{AC}_{2,1}(m,n) &= \left\langle v^6 \right\rangle - \left\langle v^4 \right\rangle \left\langle v^2 \right\rangle - 2\left\langle v^4 \right\rangle \left\langle v^2 \right\rangle + 2\left\langle v^2 \right\rangle^2 \left\langle v^2 \right\rangle \\ &= \left\langle v^6 \right\rangle - 3\left\langle v^4 \right\rangle \left\langle v^2 \right\rangle + 2\left\langle v^2 \right\rangle^3 . \quad \square \end{aligned} \tag{4.34}$$

Exactly as for $\mathrm{SC}(k,l,m)$, this is the expansion for κ_3 with v^2 as the fundamental stochastic variable, and thus a cumulant.

Semi-invariance. Let c_m and c_n be two constants. The semi-invariance requirement is demonstrated with

$$\begin{aligned}
\left\langle (v_m^2 + c_m)^2 (v_n^2 + c_n) \right\rangle_c &= \left\langle (v_m^2 + c_m)^2 (v_n^2 + c_n) \right\rangle - \left\langle (v_m^2 + c_m)^2 \right\rangle \left\langle v_n^2 + c_n \right\rangle \\
&\quad - 2 \left\langle (v_m^2 + c_m)(v_n^2 + c_n) \right\rangle \left\langle v_m^2 + c_m \right\rangle \\
&\quad + 2 \left\langle v_m^2 + c_m \right\rangle^2 \left\langle v_n^2 + c_n \right\rangle \\
&= \left\langle (v_m^4 + 2c_m v_m^2 + c_m^2)(v_n^2 + c_n) \right\rangle \\
&\quad - \left\langle v_m^4 + 2c_m v_m^2 + c_m^2 \right\rangle \left\langle v_n^2 + c_n \right\rangle \\
&\quad - 2 \left(\left\langle v_m^2 v_n^2 + c_m v_n^2 + c_n v_m^2 + c_m c_n \right\rangle \left\langle v_m^2 + c_m \right\rangle \right) \\
&\quad + 2 \left((\left\langle v_m^2 \right\rangle^2 + 2c_m \left\langle v_m^2 \right\rangle + c_m) \left\langle v_n^2 + c_n \right\rangle \right) \\
&= \mathrm{AC}_{2,1}(m,n) \\
&\quad + 2c_m \left(\left\langle v_m^2 v_n^2 \right\rangle - 2 \left\langle v_m^2 \right\rangle \left\langle v_n^2 \right\rangle - \left\langle v_m^2 v_n^2 \right\rangle + 2 \left\langle v_m^2 \right\rangle \left\langle v_n^2 \right\rangle \right) \\
&\quad + c_n \left(\left\langle v_m^4 \right\rangle - \left\langle v_m^4 \right\rangle + 2 \left\langle v_m^2 \right\rangle^2 - 2 \left\langle v_m^2 \right\rangle^2 \right) \\
&\quad + c_m^2 \left(3 \left\langle v_n^2 \right\rangle - 3 \left\langle v_n^2 \right\rangle \right) + 2c_m c_n \left(3 \left\langle v_m^2 \right\rangle - 3 \left\langle v_m^2 \right\rangle \right) \\
&\quad + c_m^2 c_n (3 - 3) \\
&= \mathrm{AC}_{2,1}(m,n). \qquad \square
\end{aligned} \tag{4.35}$$

Homogeneity. Let c_m and c_n be two constants again. The proof goes as follows

$$\begin{aligned}
\left\langle (c_m v_m^2)^2 (c_n v_n^2) \right\rangle_c &= \left\langle c_m^2 v_m^4 c_n v_n^2 \right\rangle - \left\langle c_m^2 v_m^4 \right\rangle \left\langle c_n v_n^2 \right\rangle \\
&\quad - 2 \left\langle c_m v_m^2 c_n v_n^2 \right\rangle \left\langle c_m v_m^2 \right\rangle + 2 \left\langle c_m v_m^2 \right\rangle^2 \left\langle c_n v_n^2 \right\rangle \\
&= c_m^2 c_n \mathrm{AC}_{2,1}(m,n). \qquad \square
\end{aligned} \tag{4.36}$$

Multilinearity. Consider the three different flow amplitudes v_m^2, v_n^2 and v_k^2, then

$$\begin{aligned}
\mathrm{AC}_{2,1}(m, n+k) &= \left\langle v_m^4 (v_n^2 + v_k^2) \right\rangle - \left\langle v_m^4 \right\rangle \left\langle v_n^2 + v_k^2 \right\rangle \\
&\quad - 2 \left\langle v_m^2 (v_n^2 + v_k^2) \right\rangle \left\langle v_m^2 \right\rangle + 2 \left\langle v_m^2 \right\rangle^2 \left\langle v_n^2 + v_k^2 \right\rangle \\
&= \mathrm{AC}_{2,1}(m,n) + \mathrm{AC}_{2,1}(m,k). \qquad \square
\end{aligned} \tag{4.37}$$

The definition of $\mathrm{AC}_{2,1}(m,n)$ as given by Eq. (4.32) passed all the requirements for an observable to be called a valid multivariate cumulant. Furthermore, as it was done for the SCs themselves, it is possible to replace the flow amplitudes by the corresponding eccentricities and measure the ACs in the initial state. This means that one can also define the normalised ACs based on the standard method for normalisation (see Ref. [159]), i.e.

$$\mathrm{NAC}_{2,1}(m,n) \equiv \frac{\mathrm{AC}_{2,1}(m,n)}{\langle v_m^2 \rangle^2 \langle v_n^2 \rangle}. \tag{4.38}$$

The next step is now to determine the combination of azimuthal multiparticle correlators that represents $\mathrm{AC}_{2,1}(m,n)$. Since the ACs share the same approach developed for the generalisation of the SCs to the higher orders, the knowledge obtained from the TMC studies in Section 4.1.2 is employed here. The passage from the theoretical expression with the flow magnitudes to a definition which can be used with experimental data is governed with the analytical relation of Eq. (2.12). The ambiguity encountered for $\mathrm{SC}(k,l,m)$ (see Section 4.1.3) is avoided by maximising in each term the number of particles needed for each azimuthal correlations, while including the isotropy requirement for the concerned harmonics. Taking all these points into account, this leads to the final azimuthal expression

$$\begin{aligned}\mathrm{AC}_{2,1}(m,n) = &\left\langle\left\langle \mathrm{e}^{i(m\varphi_1+m\varphi_2+n\varphi_3-m\varphi_4-m\varphi_5-n\varphi_6)}\right\rangle\right\rangle \\ &- \left\langle\left\langle \mathrm{e}^{i(m\varphi_1+m\varphi_2-m\varphi_3-m\varphi_4)}\right\rangle\right\rangle\left\langle\left\langle \mathrm{e}^{i(n\varphi_1-n\varphi_2)}\right\rangle\right\rangle \\ &- 2\left\langle\left\langle \mathrm{e}^{i(m\varphi_1+n\varphi_2-m\varphi_3-n\varphi_4)}\right\rangle\right\rangle\left\langle\left\langle \mathrm{e}^{i(m\varphi_1-m\varphi_2)}\right\rangle\right\rangle \\ &+ 2\left\langle\left\langle \mathrm{e}^{i(m\varphi_1-m\varphi_2)}\right\rangle\right\rangle^2\left\langle\left\langle \mathrm{e}^{i(n\varphi_1-n\varphi_2)}\right\rangle\right\rangle .\end{aligned} \tag{4.39}$$

Correlations between different moments of the flow amplitudes have also been presented with the traditional approach in Ref. [160]. Among the observables that are proposed, the counterpart of $\mathrm{AC}_{2,1}(m,n)$, namely $MHC(v_m^4, v_n^2)$, is presented. Its expression in terms of the flow amplitudes v_m and v_n is given by

$$MHC(v_m^4, v_n^2) = \left\langle v_m^4 v_n^2\right\rangle - \left\langle v_m^4\right\rangle\left\langle v_n^2\right\rangle - 4\left\langle v_m^2 v_n^2\right\rangle\left\langle v_m^2\right\rangle + 4\left\langle v_m^2\right\rangle^2\left\langle v_n^2\right\rangle . \tag{4.40}$$

This equation is based on the same averages as the ones in Eq. (4.32). However, it has to be noted that the two last terms differ by a factor two when compared to the result of the new approach. This implies that Eq. (4.40) is not a valid cumulant of v_n or v_n^2 and therefore, it cannot be used to estimate reliably the genuine correlations between only the flow amplitudes. Moreover, this difference of factors is not surprising as it is present also, for example, between the known four-particle cumulant of v_n, i.e. $v_n\{4\} \equiv \langle v_n^4\rangle - 2\langle v_n^2\rangle^2$ and the variance of v_n^2 ($\langle v_n^4\rangle - \langle v_n^2\rangle^2$) which is obtained through the new method. One of the goals of the TMC studies presented in Section 4.2.3 will be to compare the nonflow scaling of the two approaches in the case of ACs.

4.2.2 Generalisation to higher order cumulant expansions

In a similar way as for the generalisation of $\mathrm{SC}(m,n)$ to more than two harmonics, $\mathrm{AC}_{2,1}(m,n)$ can be extended. Although, this generalisation cannot only be done on the number of harmonics, but also on the order of the ACs for a fixed number of harmonics. Therefore, in addition to $\mathrm{AC}_{2,1}(m,n)$ presented above, three other ACs are investigated:

$$\begin{aligned}\mathrm{AC}_{3,1}(m,n) &\equiv \left\langle (v_m^2)^3 v_n^2\right\rangle_c \equiv \left\langle v_m^6 v_n^2\right\rangle_c , \\ \mathrm{AC}_{4,1}(m,n) &\equiv \left\langle (v_m^2)^4 v_n^2\right\rangle_c \equiv \left\langle v_m^8 v_n^2\right\rangle_c , \\ \mathrm{AC}_{2,1,1}(k,l,m) &\equiv \left\langle (v_k^2)^2 v_l^2 v_m^2\right\rangle_c \equiv \left\langle v_k^4 v_l^2 v_m^2\right\rangle_c .\end{aligned}$$

Comparing the first two observables with the ones from $\mathrm{AC}_{2,1}(m,n)$ allow to see how the genuine correlations between two given flow amplitudes differ with the considered moments. The last variable, $\mathrm{AC}_{2,1,1}(k,l,m)$ can bring complementary information with respect to the usual three-harmonic SCs in a way similar to the previous case.

The technical expressions for these additional two-harmonic ACs are based on the cumulant expansion of $\kappa_{3,1}$ for $\mathrm{AC}_{3,1}(m,n)$ and $\kappa_{4,1}$ for $\mathrm{AC}_{4,1}(m,n)$. These are given here for the sake of completeness:

$$\begin{aligned}\kappa_{3,1} \equiv & -6\mu_{0,1}{\mu_{1,0}}^3 + 6\mu_{1,1}{\mu_{1,0}}^2 + 6\mu_{0,1}\mu_{2,0}\mu_{1,0} \\ & - 3\mu_{2,1}\mu_{1,0} - 3\mu_{1,1}\mu_{2,0} - \mu_{0,1}\mu_{3,0} + \mu_{3,1}\end{aligned} \tag{4.41}$$

and

$$\begin{aligned}\kappa_{4,1} \equiv & 24\mu_{0,1}{\mu_{1,0}}^4 - 24\mu_{1,1}{\mu_{1,0}}^3 - 36\mu_{0,1}\mu_{2,0}{\mu_{1,0}}^2 + 12\mu_{2,1}{\mu_{1,0}}^2 \\ & + 24\mu_{1,1}\mu_{2,0}\mu_{1,0} + 8\mu_{0,1}\mu_{3,0}\mu_{1,0} - 4\mu_{3,1}\mu_{1,0} + 6\mu_{0,1}{\mu_{2,0}}^2 \\ & - 6\mu_{2,0}\mu_{2,1} - 4\mu_{1,1}\mu_{3,0} - \mu_{0,1}\mu_{4,0} + \mu_{4,1}.\end{aligned} \tag{4.42}$$

The substitution $X_1 = v_m^2$ and $X_2 = v_n^2$ used in the new cumulant approach gives the following expressions:

$$\begin{aligned}\mathrm{AC}_{3,1}(m,n) = & \left\langle v_m^6 v_n^2 \right\rangle - \left\langle v_m^6 \right\rangle \left\langle v_n^2 \right\rangle - 3\left\langle v_m^2 v_n^2 \right\rangle \left\langle v_m^4 \right\rangle - 3\left\langle v_m^4 v_n^2 \right\rangle \left\langle v_m^2 \right\rangle \\ & + 6\left\langle v_m^4 \right\rangle \left\langle v_m^2 \right\rangle \left\langle v_n^2 \right\rangle + 6\left\langle v_m^2 v_n^2 \right\rangle \left\langle v_m^2 \right\rangle^2 - 6\left\langle v_m^2 \right\rangle^3 \left\langle v_n^2 \right\rangle,\end{aligned} \tag{4.43}$$

and

$$\begin{aligned}\mathrm{AC}_{4,1}(m,n) = & \left\langle v_m^8 v_n^2 \right\rangle - \left\langle v_m^8 \right\rangle \left\langle v_n^2 \right\rangle - 4\left\langle v_m^2 v_n^2 \right\rangle \left\langle v_m^6 \right\rangle - 6\left\langle v_m^4 v_n^2 \right\rangle \left\langle v_m^4 \right\rangle \\ & + 6\left\langle v_m^4 \right\rangle^2 \left\langle v_n^2 \right\rangle - 4\left\langle v_m^6 v_n^2 \right\rangle \left\langle v_m^2 \right\rangle + 8\left\langle v_m^6 \right\rangle \left\langle v_m^2 \right\rangle \left\langle v_n^2 \right\rangle \\ & + 24\left\langle v_m^2 v_n^2 \right\rangle \left\langle v_m^4 \right\rangle \left\langle v_m^2 \right\rangle + 12\left\langle v_m^4 v_n^2 \right\rangle \left\langle v_m^2 \right\rangle^2 \\ & - 36\left\langle v_m^4 \right\rangle \left\langle v_m^2 \right\rangle^2 \left\langle v_n^2 \right\rangle - 24\left\langle v_m^2 v_n^2 \right\rangle \left\langle v_m^2 \right\rangle^3 + 24\left\langle v_m^2 \right\rangle^4 \left\langle v_n^2 \right\rangle.\end{aligned} \tag{4.44}$$

In the case of the three-harmonic AC, the initial cumulant is the fourth-order three-variable $\kappa_{2,1,1}$ defined as

$$\begin{aligned}\kappa_{2,1,1} \equiv & -6\mu_{0,0,1}\mu_{0,1,0}{\mu_{1,0,0}}^2 + 2\mu_{0,1,1}{\mu_{1,0,0}}^2 + 4\mu_{0,1,0}\mu_{1,0,1}\mu_{1,0,0} \\ & + 4\mu_{0,0,1}\mu_{1,1,0}\mu_{1,0,0} - 2\mu_{1,1,1}\mu_{1,0,0} - 2\mu_{1,0,1}\mu_{1,1,0} + 2\mu_{0,0,1}\mu_{0,1,0}\mu_{2,0,0} \\ & - \mu_{0,1,1}\mu_{2,0,0} - \mu_{0,1,0}\mu_{2,0,1} - \mu_{0,0,1}\mu_{2,1,0} + \mu_{2,1,1}.\end{aligned} \tag{4.45}$$

With the usual identification $X_1 = v_k^2$, $X_2 = v_l^2$ and $X_3 = v_m^2$, this leads to an expression of $\mathrm{AC}_{2,1,1}(k,l,m)$ with

$$\begin{aligned}\mathrm{AC}_{2,1,1}(k,l,m) = & \left\langle v_k^4 v_l^2 v_m^2 \right\rangle - \left\langle v_k^4 v_l^2 \right\rangle \left\langle v_m^2 \right\rangle - \left\langle v_k^4 v_m^2 \right\rangle \left\langle v_l^2 \right\rangle - \left\langle v_k^4 \right\rangle \left\langle v_l^2 v_m^2 \right\rangle \\ & + 2\left\langle v_k^4 \right\rangle \left\langle v_l^2 \right\rangle \left\langle v_m^2 \right\rangle - 2\left\langle v_k^2 v_l^2 \right\rangle \left\langle v_k^2 v_m^2 \right\rangle - 2\left\langle v_k^2 v_l^2 v_m^2 \right\rangle \left\langle v_k^2 \right\rangle \\ & + 4\left\langle v_k^2 v_l^2 \right\rangle \left\langle v_k^2 \right\rangle \left\langle v_m^2 \right\rangle + 4\left\langle v_k^2 v_m^2 \right\rangle \left\langle v_k^2 \right\rangle \left\langle v_l^2 \right\rangle \\ & + 2\left\langle v_k^2 \right\rangle^2 \left\langle v_l^2 v_m^2 \right\rangle - 6\left\langle v_k^2 \right\rangle^2 \left\langle v_l^2 \right\rangle \left\langle v_m^2 \right\rangle.\end{aligned} \tag{4.46}$$

All these observables are cumulants of the flow amplitudes squared. Their demonstrations are similar to the ones done for $\mathrm{AC}_{2,1}(m,n)$ and the SC observables. Furthermore, like these latter variables, the dependence on the fluctuations of the flow amplitudes themselves and the transverse momentum is removed by normalising these expressions. This leads to the following

three new definitions:

$$\mathrm{NAC}_{3,1}(m,n) \equiv \frac{\mathrm{AC}_{3,1}(m,n)}{\langle v_m^2\rangle^3 \langle v_n^2\rangle} \tag{4.47}$$

$$\mathrm{NAC}_{4,1}(m,n) \equiv \frac{\mathrm{AC}_{4,1}(m,n)}{\langle v_m^2\rangle^4 \langle v_n^2\rangle} \tag{4.48}$$

$$\mathrm{NAC}_{2,1,1}(k,l,m) \equiv \frac{\mathrm{AC}_{2,1,1}(k,l,m)}{\langle v_k^2\rangle^2 \langle v_l^2\rangle \langle v_m^2\rangle} \tag{4.49}$$

Moreover, the definitions of these ACs in the initial state are obtained by replacing the flow amplitudes by the corresponding eccentricities. Finally, the equations in terms of the azimuthal angles are then obtained following the same strategy as in Section 4.2.1, leading to

$$\begin{aligned}
\mathrm{AC}_{3,1}(m,n) = &\left\langle\left\langle e^{i(m\varphi_1+m\varphi_2+m\varphi_3+n\varphi_4-m\varphi_5-m\varphi_6-m\varphi_7-n\varphi_8)}\right\rangle\right\rangle \\
&- \left\langle\left\langle e^{i(m\varphi_1+m\varphi_2+m\varphi_3-m\varphi_4-m\varphi_5-m\varphi_6)}\right\rangle\right\rangle \left\langle\left\langle e^{i(n\varphi_1-n\varphi_2)}\right\rangle\right\rangle \\
&- 3\left\langle\left\langle e^{i(m\varphi_1+m\varphi_2-m\varphi_3-m\varphi_4)}\right\rangle\right\rangle \left\langle\left\langle e^{i(m\varphi_1+n\varphi_2-m\varphi_3-n\varphi_4)}\right\rangle\right\rangle \\
&- 3\left\langle\left\langle e^{i(m\varphi_1+m\varphi_2+n\varphi_3-m\varphi_4-m\varphi_5-n\varphi_6)}\right\rangle\right\rangle \left\langle\left\langle e^{i(m\varphi_1-m\varphi_2)}\right\rangle\right\rangle \\
&+ 6\left\langle\left\langle e^{i(m\varphi_1+m\varphi_2-m\varphi_3-m\varphi_4)}\right\rangle\right\rangle \left\langle\left\langle e^{i(m\varphi_1-m\varphi_2)}\right\rangle\right\rangle \left\langle\left\langle e^{i(n\varphi_1-n\varphi_2)}\right\rangle\right\rangle \\
&+ 6\left\langle\left\langle e^{i(m\varphi_1+n\varphi_2-m\varphi_3-n\varphi_4)}\right\rangle\right\rangle \left\langle\left\langle e^{i(m\varphi_1-m\varphi_2)}\right\rangle\right\rangle^2 \\
&- 6\left\langle\left\langle e^{i(m\varphi_1-m\varphi_2)}\right\rangle\right\rangle^3 \left\langle\left\langle e^{i(n\varphi_1-n\varphi_2)}\right\rangle\right\rangle,
\end{aligned} \tag{4.50}$$

$$\begin{aligned}
\mathrm{AC}_{4,1}(m,n) = &\left\langle\left\langle e^{i(m\varphi_1+m\varphi_2+m\varphi_3+m\varphi_4+n\varphi_5-m\varphi_6-m\varphi_7-m\varphi_8-m\varphi_9-n\varphi_{10})}\right\rangle\right\rangle \\
&- \left\langle\left\langle e^{i(m\varphi_1+m\varphi_2+m\varphi_3+m\varphi_4-m\varphi_5-m\varphi_6-m\varphi_7-m\varphi_8)}\right\rangle\right\rangle \left\langle\left\langle e^{i(n\varphi_1-n\varphi_2)}\right\rangle\right\rangle \\
&- 4\left\langle\left\langle e^{i(m\varphi_1+n\varphi_2-m\varphi_3-n\varphi_4)}\right\rangle\right\rangle \left\langle\left\langle e^{i(m\varphi_1+m\varphi_2+m\varphi_3-m\varphi_4-m\varphi_5-m\varphi_6)}\right\rangle\right\rangle \\
&- 6\left\langle\left\langle e^{i(m\varphi_1+m\varphi_2+n\varphi_3-m\varphi_4-m\varphi_5-n\varphi_6)}\right\rangle\right\rangle \left\langle\left\langle e^{i(m\varphi_1+m\varphi_2-m\varphi_3-m\varphi_4)}\right\rangle\right\rangle \\
&+ 6\left\langle\left\langle e^{i(m\varphi_1+m\varphi_2-m\varphi_3-m\varphi_4)}\right\rangle\right\rangle^2 \left\langle\left\langle e^{i(n\varphi_1-n\varphi_2)}\right\rangle\right\rangle \\
&- 4\left\langle\left\langle e^{i(m\varphi_1+m\varphi_2+m\varphi_3+n\varphi_4-m\varphi_5-m\varphi_6-m\varphi_7-n\varphi_8)}\right\rangle\right\rangle \left\langle\left\langle e^{i(m\varphi_1-m\varphi_2)}\right\rangle\right\rangle \\
&+ 8\left\langle\left\langle e^{i(m\varphi_1+m\varphi_2+m\varphi_3-m\varphi_4-m\varphi_5-m\varphi_6)}\right\rangle\right\rangle \left\langle\left\langle e^{i(m\varphi_1-m\varphi_2)}\right\rangle\right\rangle \left\langle\left\langle e^{i(n\varphi_1-n\varphi_2)}\right\rangle\right\rangle \\
&+ 24\left\langle\left\langle e^{i(m\varphi_1+n\varphi_2-m\varphi_3-n\varphi_4)}\right\rangle\right\rangle \left\langle\left\langle e^{i(m\varphi_1+m\varphi_2-m\varphi_3-m\varphi_4)}\right\rangle\right\rangle \left\langle\left\langle e^{i(m\varphi_1-m\varphi_2)}\right\rangle\right\rangle \\
&+ 12\left\langle\left\langle e^{i(m\varphi_1+m\varphi_2+n\varphi_3-m\varphi_4-m\varphi_5-n\varphi_6)}\right\rangle\right\rangle \left\langle\left\langle e^{i(m\varphi_1-m\varphi_2)}\right\rangle\right\rangle^2 \\
&- 36\left\langle\left\langle e^{i(m\varphi_1+m\varphi_2-m\varphi_3-m\varphi_4)}\right\rangle\right\rangle \left\langle\left\langle e^{i(m\varphi_1-m\varphi_2)}\right\rangle\right\rangle^2 \left\langle\left\langle e^{i(n\varphi_1-n\varphi_2)}\right\rangle\right\rangle \\
&- 24\left\langle\left\langle e^{i(m\varphi_1+n\varphi_2-m\varphi_3-n\varphi_4)}\right\rangle\right\rangle \left\langle\left\langle e^{i(m\varphi_1-m\varphi_2)}\right\rangle\right\rangle^3 \\
&+ 24\left\langle\left\langle e^{i(m\varphi_1-m\varphi_2)}\right\rangle\right\rangle^4 \left\langle\left\langle e^{i(n\varphi_1-n\varphi_2)}\right\rangle\right\rangle,
\end{aligned} \tag{4.51}$$

and finally,

$$\begin{aligned}
\mathrm{AC}_{2,1,1}(k,l,m) = &\left\langle\left\langle \mathrm{e}^{i(k\varphi_1+k\varphi_2+l\varphi_3+m\varphi_4-k\varphi_5-k\varphi_6-l\varphi_7-m\varphi_8)}\right\rangle\right\rangle \\
&- \left\langle\left\langle \mathrm{e}^{i(k\varphi_1+k\varphi_2+l\varphi_3-k\varphi_4-k\varphi_5-l\varphi_6)}\right\rangle\right\rangle \left\langle\left\langle \mathrm{e}^{i(m\varphi_1-m\varphi_2)}\right\rangle\right\rangle \\
&- \left\langle\left\langle \mathrm{e}^{i(k\varphi_1+k\varphi_2+m\varphi_3-k\varphi_4-k\varphi_5-m\varphi_6)}\right\rangle\right\rangle \left\langle\left\langle \mathrm{e}^{i(l\varphi_1-l\varphi_2)}\right\rangle\right\rangle \\
&- \left\langle\left\langle \mathrm{e}^{i(k\varphi_1+k\varphi_2-k\varphi_3-k\varphi_4)}\right\rangle\right\rangle \left\langle\left\langle \mathrm{e}^{i(l\varphi_1+m\varphi_2-l\varphi_3-m\varphi_4)}\right\rangle\right\rangle \\
&+ 2\left\langle\left\langle \mathrm{e}^{i(k\varphi_1+k\varphi_2-k\varphi_3-k\varphi_4)}\right\rangle\right\rangle \left\langle\left\langle \mathrm{e}^{i(l\varphi_1-l\varphi_2)}\right\rangle\right\rangle \left\langle\left\langle \mathrm{e}^{i(m\varphi_1-m\varphi_2)}\right\rangle\right\rangle \\
&- 2\left\langle\left\langle \mathrm{e}^{i(k\varphi_1+l\varphi_2-k\varphi_3-l\varphi_4)}\right\rangle\right\rangle \left\langle\left\langle \mathrm{e}^{i(k\varphi_1+m\varphi_2-k\varphi_3-m\varphi_4)}\right\rangle\right\rangle \\
&- 2\left\langle\left\langle \mathrm{e}^{i(k\varphi_1+l\varphi_2+m\varphi_3-k\varphi_4-l\varphi_5-m\varphi_6)}\right\rangle\right\rangle \left\langle\left\langle \mathrm{e}^{i(k\varphi_1-k\varphi_2)}\right\rangle\right\rangle \\
&+ 4\left\langle\left\langle \mathrm{e}^{i(k\varphi_1+l\varphi_2-k\varphi_3-l\varphi_4)}\right\rangle\right\rangle \left\langle\left\langle \mathrm{e}^{i(k\varphi_1-k\varphi_2)}\right\rangle\right\rangle \left\langle\left\langle \mathrm{e}^{i(m\varphi_1-m\varphi_2)}\right\rangle\right\rangle \\
&+ 4\left\langle\left\langle \mathrm{e}^{i(k\varphi_1+m\varphi_2-k\varphi_3-m\varphi_4)}\right\rangle\right\rangle \left\langle\left\langle \mathrm{e}^{i(k\varphi_1-k\varphi_2)}\right\rangle\right\rangle \left\langle\left\langle \mathrm{e}^{i(l\varphi_1-l\varphi_2)}\right\rangle\right\rangle \\
&+ 2\left\langle\left\langle \mathrm{e}^{i(k\varphi_1-k\varphi_2)}\right\rangle\right\rangle^2 \left\langle\left\langle \mathrm{e}^{i(l\varphi_1+m\varphi_2-l\varphi_3-m\varphi_4)}\right\rangle\right\rangle \\
&- 6\left\langle\left\langle \mathrm{e}^{i(k\varphi_1-k\varphi_2)}\right\rangle\right\rangle^2 \left\langle\left\langle \mathrm{e}^{i(l\varphi_1-l\varphi_2)}\right\rangle\right\rangle \left\langle\left\langle \mathrm{e}^{i(m\varphi_1-m\varphi_2)}\right\rangle\right\rangle .
\end{aligned} \tag{4.52}$$

4.2.3 Cumulant properties with toy Monte Carlo studies

In the same fashion as for the SCs, TMC simulations are established to check the properties of the expressions above. The setup used in this section is slightly modified with respect to the one employed in Section 4.1.2. Non-zero symmetry planes are introduced in the implementation of the Fourier series, leading to

$$f(\varphi) = \frac{1}{2\pi}\left[1 + 2v_1\cos(\varphi - \Psi_1) + 2v_2\cos(2(\varphi - \Psi_2)) + 2v_3\cos(3(\varphi - \Psi_3))\right]. \tag{4.53}$$

This equation has six independent parameters: the three flow amplitudes v_1, v_2 and v_3 and the three symmetry planes angles Ψ_1, Ψ_2 and Ψ_3. The simulations are obtained for $N_{events} = 10^8$ events in total, with Ψ_1, Ψ_2 and Ψ_3 uniformly sampled event-by-event in the interval $(0, 2\pi)$. Unless stated otherwise, the multiplicities are kept constant to the initial values $M = 50, 100, 250, 500$ and 750. Ten particles per events ($M = 10$) has been considered to investigate the results at low multiplicities. However, as the terms appearing in the ACs involve six-, eight- and even ten-particle correlations, such results will show severe biases and errors, and therefore, $M = 10$ has not been used.

The various checks studied with this TMC setup come from the ones realised for $\mathrm{SC}(k,l,m)$, their differences will be discussed later. This section concerns the subject of the cumulant properties, while a deeper look at the nonflow scaling using strong few-particle correlations is given in Section 4.2.4. The analyses of the cumulant properties of the azimuthal expressions of the ACs are made with four simulations: the amplitudes are kept constant or uncorrelated, only two of them present genuine correlations, and the three magnitudes are genuinely correlated. Moreover, all the results are organised in a similar way: the top left panel shows the results for $\mathrm{AC}_{2,1}(m,n)$, the top right panel for $\mathrm{AC}_{3,1}(m,n)$, the bottom left panel for $\mathrm{AC}_{4,1}(m,n)$ and finally, the bottom right panel for $\mathrm{AC}_{2,1,1}(k,l,m)$.

Figure 4.13 shows the results for three constant flow amplitudes set to $v_1 = 0.1$, $v_2 = 0.08$ and $v_3 = 0.06$ respectively. In Fig. 4.14, the magnitudes are uncorrelated event-by-event and fluctuate in the interval $v_1, v_2, v_3 = (0.05, 0.1)$. For multiplicities comparable to the ones

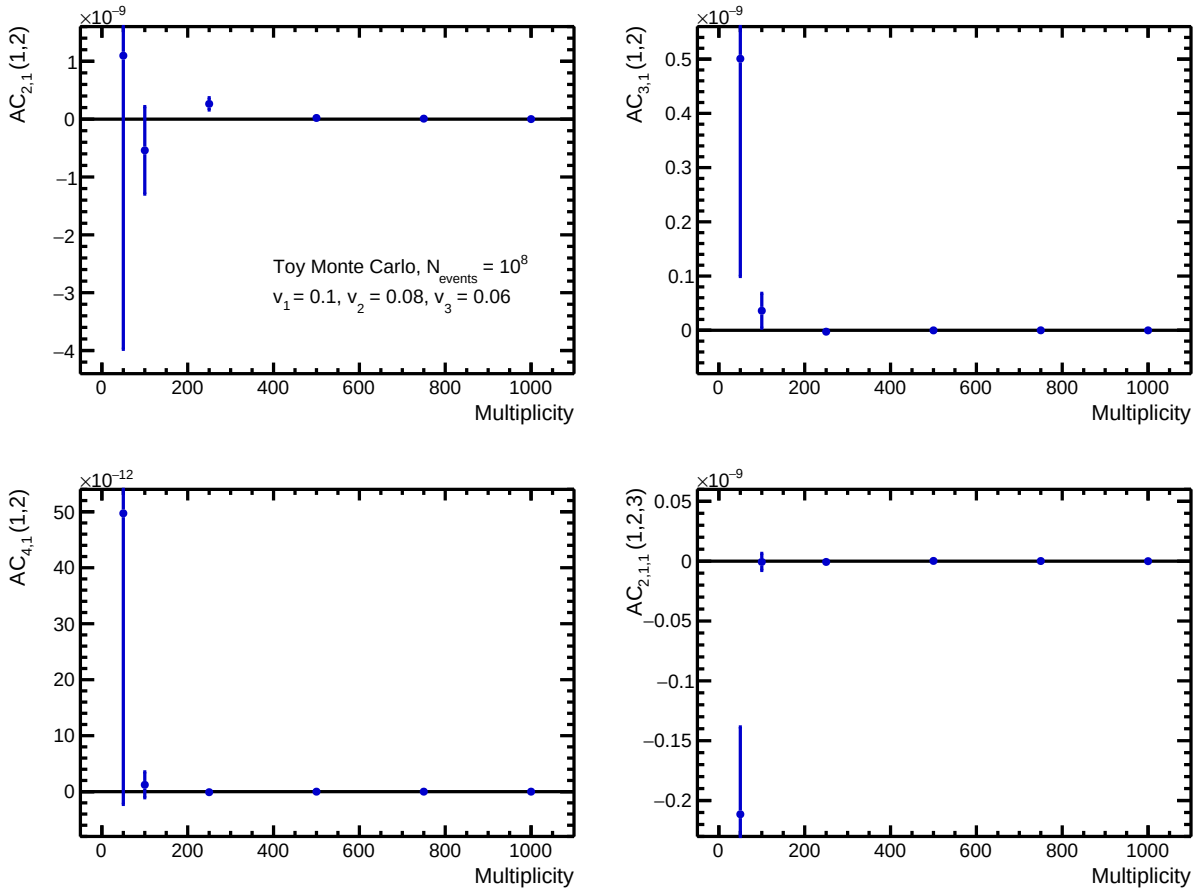

Figure 4.13: Multiplicity dependence for all the ACs for three constant flow amplitudes set to $v_1 = 0.1, v_2 = 0.08$ and $v_3 = 0.06$ respectively [157].

in central and mid-central heavy-ion collisions, the ACs are in agreement within statistical uncertainties with zero as expected. Important variations are observed for $M = 50$ particles per event. They are not surprising, since multiparticle correlations as used in the current studies are precision techniques only in environments with large numbers of events and multiplicities like the ones found in heavy-ion collisions.

The next test concerns the situation of two genuinely correlated harmonics. Therefore, the flow amplitudes are fixed to $v_1, v_3 = (0.05, 0.1), v_2 = v_1 - (0.005, 0.025)$. Like for the SCs, the theoretical values expected for the final ACs are computed for a box p.d.f. using Mathematica [158] and compared to the results from the simulations. Figure 4.15 presents the comparisons for all observables. $\mathrm{AC}_{2,1,1}(1,2,3) = 0$ as only a subset of harmonics are genuinely correlated. For the two-harmonic ACs, the simulations are in good agreement with the predictions from Mathematica.

Finally, the three non-zero harmonics are all correlated with $v_1 = (0.05, 0.1), v_2 = v_1 - (0., 0.02), v_3 = v_1 - (0.005, 0.025)$. In this case, $\mathrm{AC}_{a,1}(1,2), a = 2,3,4$ are expected to be still in good agreement with the predictions from Mathematica with the box distribution, but with values different to the previous test — the initial distribution has changed —, while $\mathrm{AC}_{2,1,1}(1,2,3)$ must agree to its own non-zero prediction. The results, visible in Fig. 4.16, confirm these expectations with a good compatibility between theory and TMC simulations.

From all these TMC studies, it can be deduced that the expressions proposed for all the

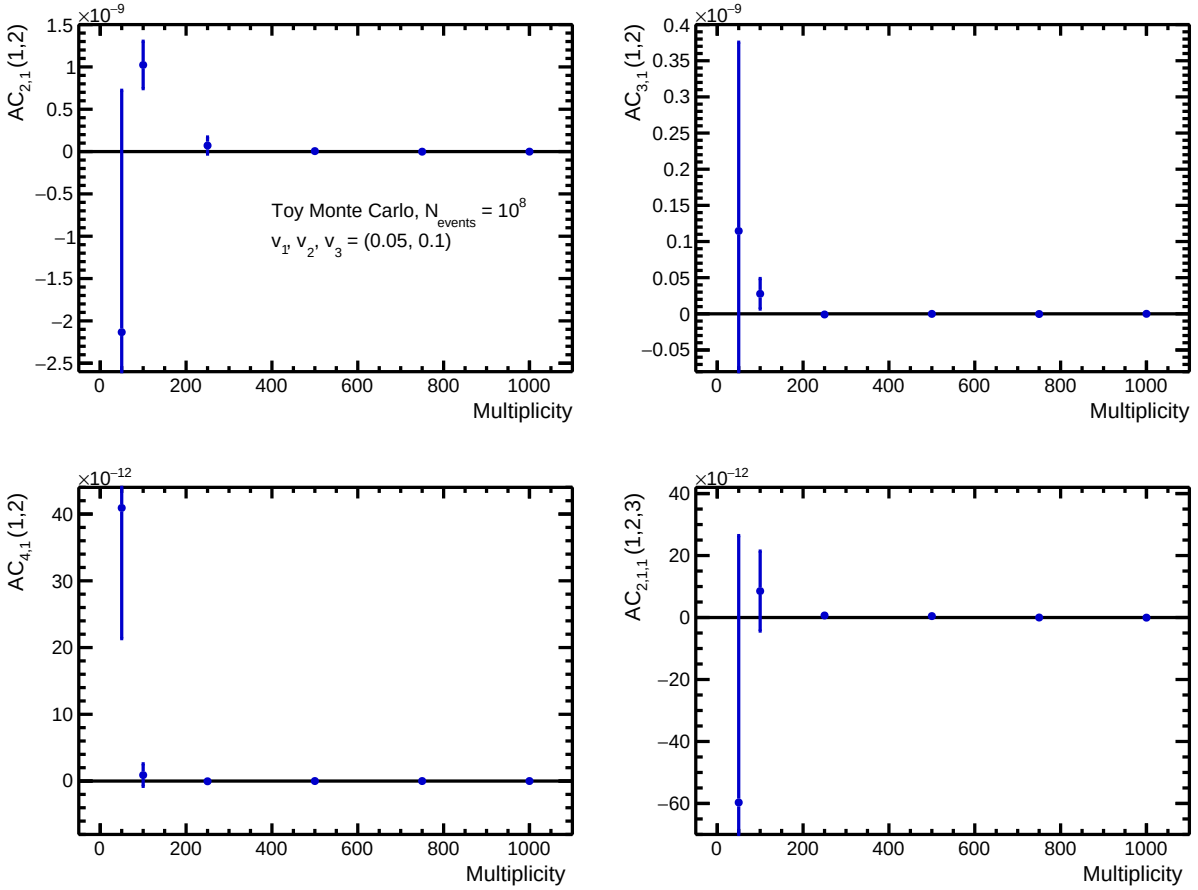

Figure 4.14: Multiplicity dependence for all the ACs for three uncorrelated flow amplitudes fluctuating in the interval $v_1, v_2, v_3 = (0.05, 0.1)$ [157].

ACs have all the properties to be called cumulants of the flow amplitudes squared: they are non-zero if and only if the number of flow magnitudes that are genuinely correlated is equal to the number of harmonics involved in a considered AC.

In addition to the checks of the cumulant properties and the nonflow scaling (see next section), several additional checks have been done for the SCs but they are deemed unnecessary this time based on the knowledge collected previously. These include the following list:

Flow harmonics set to zero. The output of this check is redundant with the one for non-zero constant harmonics, as they both need to return null ACs. This simulation would have been done only if the latter had returned non-zero ACs, to ensure the absence of built-in correlations which may have biased the final results.

Uniqueness of the experimental expression. As discussed above, this study in the context of SC(m, n) and SC(k, l, m) has shown that it is not possible to use the all-event average of the product of two-particle correlators and that each correlation must be defined with the higher number of involved particles, e.g. $v_2^4 v_l^2 v_m^2$ must be a six-particle correlator. This conclusion has already been used to derive the expressions of the ACs in terms of multiparticle azimuthal angles.

Choice of the event weight. The analyses for SC(k, l) demonstrated that the event weights to use is the "number of combinations" and this was confirmed with the TMC done for SC(k, l, m). As the ACs are an extension of the SC observables and also use the Generic

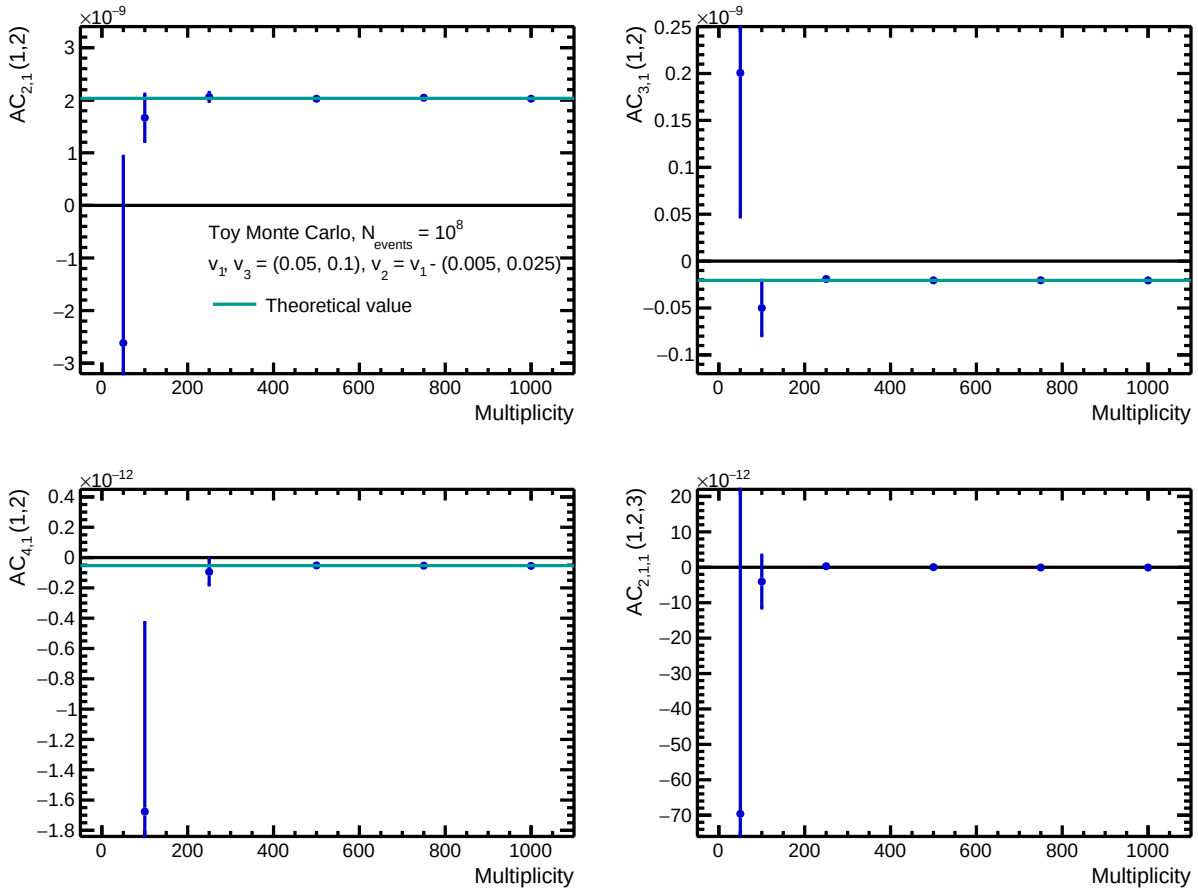

Figure 4.15: Multiplicity dependence for all the ACs in the case of two genuinely correlated flow amplitudes with $v_1, v_3 = (0.05, 0.1), v_2 = v_1 - (0.005, 0.025)$ [157].

Framework [110], their event weights must also be the number of combinations.

4.2.4 Robustness against nonflow correlations

Nonflow scaling with strong multiparticle correlations

The same configuration as in Section 4.1.2 is now implemented for the TMC setup described in Section 4.2.3. All contributions from collective flow are removed by setting the magnitudes to $v_1, v_2, v_3 = 0$, while the corresponding symmetry planes are still uniformly sampled in $(0, 2\pi)$. It has to be noted that setting the planes to zero change nothing in the definition of the Fourier series given by Eq.(4.53). The nonflow scaling of each order of ACs is again determined by using the scaling for a single multiparticle azimuthal correlator given by Eq. (2.32). This leads to

$$\mathrm{AC}_{2,1}(m,n) \simeq \frac{\alpha}{M^5} + \frac{\beta}{M^4} + \frac{\gamma}{M^3}, \tag{4.54}$$

$$\mathrm{AC}_{3,1}(m,n) \simeq \frac{\alpha}{M^7} + \frac{\beta}{M^6} + \frac{\gamma}{M^5} + \frac{\delta}{M^4}, \tag{4.55}$$

$$\mathrm{AC}_{4,1}(m,n) \simeq \frac{\alpha}{M^9} + \frac{\beta}{M^8} + \frac{\gamma}{M^7} + \frac{\delta}{M^6} + \frac{\epsilon}{M^5}, \tag{4.56}$$

$$\mathrm{AC}_{2,1,1}(k,l,m) \simeq \frac{\alpha}{M^7} + \frac{\beta}{M^6} + \frac{\gamma}{M^5} + \frac{\delta}{M^4}, \tag{4.57}$$

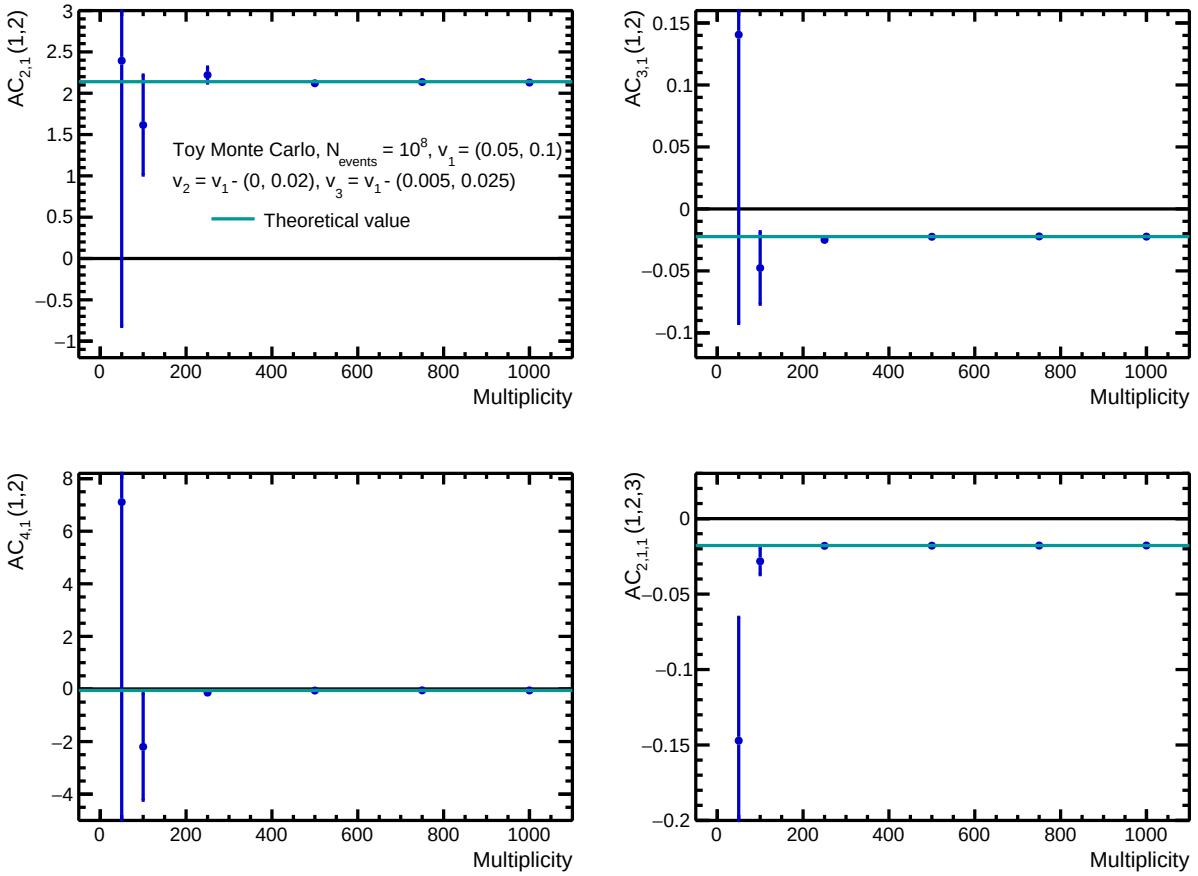

Figure 4.16: Multiplicity dependence for all the ACs for three genuinely correlated flow amplitudes with $v_1 = (0.05, 0.1), v_2 = v_1 - (0., 0.02), v_3 = v_1 - (0.005, 0.025)$ [157].

with $\alpha, \beta, \gamma, \delta, \epsilon$ the fit parameters.

Strong multiparticle correlations are introduced by taking multiple times the same set of azimuthal angles, reproducing the effect that all tracks are split in the detector. Three different cases of track splitting are going to be investigated here: two, three and four particles. The tested multiplicities in every case are set initially to

$$M_{initial,2p} = 10, 18, 25, 38, 50, 75, 100, 150, 200, 250, 500,$$
$$M_{initial,3p} = 7, 12, 15, 25, 33, 50, 66, 100, 133, 166, 333,$$
$$M_{initial,4p} = 5, 9, 12, 20, 25, 40, 50, 75, 100, 125, 250$$

and the final multiplicities are respectively $M_{final,2p} = 2M_{initial,2p}$, $M_{final,3p} = 3M_{initial,3p}$ and $M_{final,3p} = 3M_{initial,3p}$. Figure 4.17 presents the results for all track splitting for each AC up to $M_{final} = 120$ for clarity purposes. A version going to $M_{final} = 550$ is visible in Appendix C. The obtained fit parameters are gathered in Tables 4.1 for $\mathrm{AC}_{2,1}(1,2)$, 4.2 for $\mathrm{AC}_{3,1}(1,2)$, 4.3 for $\mathrm{AC}_{4,1}(1,2)$ and 4.4 for $\mathrm{AC}_{2,1,1}(1,2,3)$. Figure 4.17 shows that the results of the TMC simulations converge to zero with the multiplicity for the three cases of strong few-particle correlations. This convergence gets faster with the order of the observable. Furthermore, all observables follow with a good agreement their corresponding nonflow scaling (Eqs. (4.54)–(4.57)).

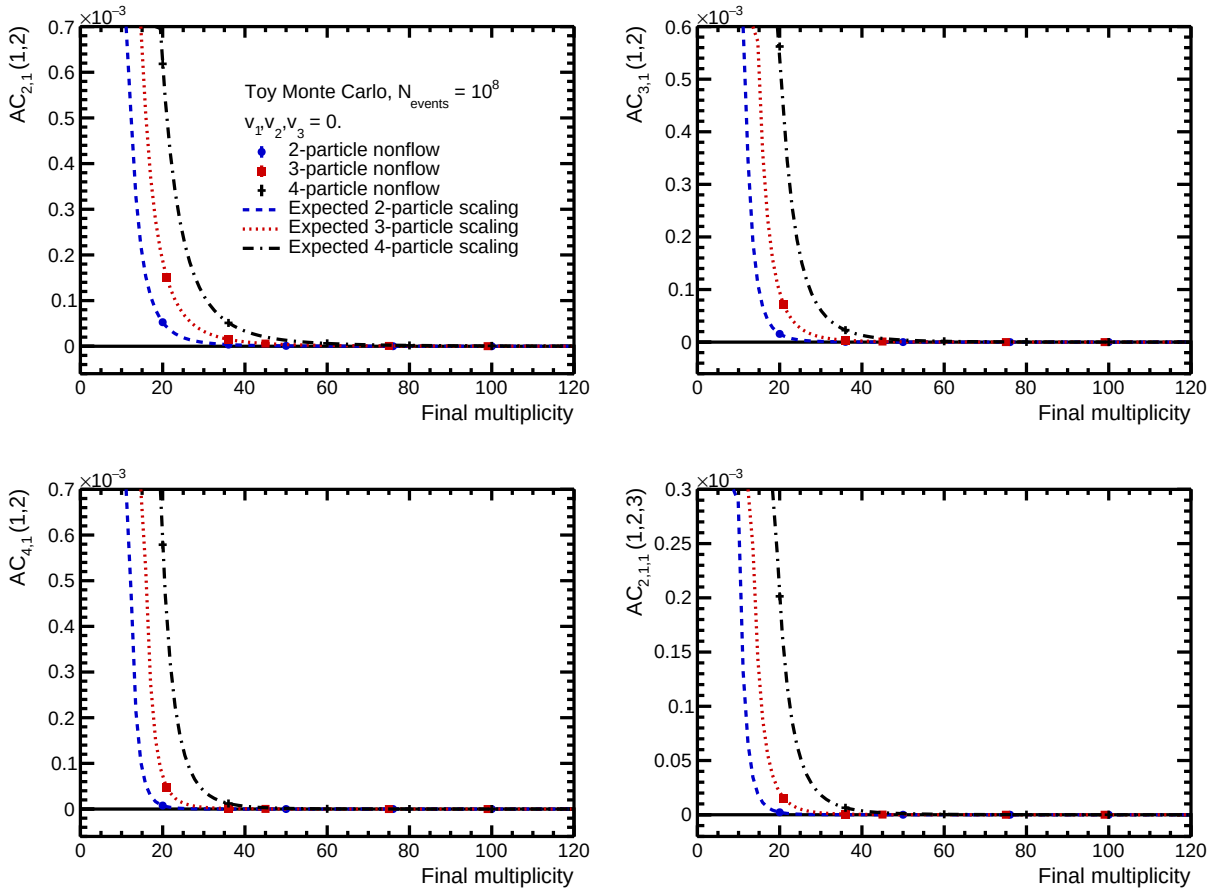

Figure 4.17: Multiplicity dependence of the various ACs for strong few-particle correlations with the fit of the corresponding nonflow scaling [157].

Table 4.1: Fit parameters for $\mathrm{AC}_{2,1}(1,2)$ for the strong two-, three- and four-particle scaling illustrated in Fig. 4.17.

	2-particle	**3-particle**	**4-particle**
α	101.82 ± 2.45	198.41 ± 10.60	533.48 ± 25.96
β	$(33.00 \pm 1.16) \times 10^{-1}$	19.75 ± 0.49	72.41 ± 1.18
γ	$(12.24 \pm 7.30) \times 10^{-4}$	$(3.44 \pm 2.99) \times 10^{-3}$	$(-17.54 \pm 8.45) \times 10^{-3}$
χ^2/NDF	1.13	1.06	2.90

The cumulant $\mathrm{AC}_{2,1}(m,n)$ is compared with its counterpart in the traditional approach $\mathrm{MHC}(v_m^4, v_n^2)$ given by Eq. (4.40), but also with the alternative expressions $\mathrm{Alt}_1(m,n)$ and $\mathrm{Alt}_3(m,n)$, where

$$\mathrm{Alt}_j(m,n) \equiv \left\langle v_m^4 v_n^2 \right\rangle - \left\langle v_m^4 \right\rangle \left\langle v_n^2 \right\rangle - j \left\langle v_m^2 v_n^2 \right\rangle \left\langle v_m^2 \right\rangle + j \left\langle v_m^2 \right\rangle^2 \left\langle v_n^2 \right\rangle . \tag{4.58}$$

In this notation, $\mathrm{AC}_{2,1}(m,n)$ corresponds to $\mathrm{Alt}_2(m,n)$ and $\mathrm{MHC}(v_m^4, v_n^2)$ to $\mathrm{Alt}_4(m,n)$. Thus, all these definitions share the same combinations of all-event averages of flow amplitudes squared. Figure 4.18 presents the nonflow scaling of these observables for $m = 1$ and $n = 2$ and the strong two-, three- and four-particle correlations. For multiplicities comparable to the ones measured in heavy-ion collisions ($M > 150$), all tested expressions present no sensitivity to nonflow.

Table 4.2: Fit parameters for $AC_{3,1}(1,2)$ for the strong two-, three- and four-particle scaling illustrated in Fig. 4.17.

	2-particle	**3-particle**	**4-particle**
α	$(9.11 \pm 2.49) \times 10^3$	$(3.19 \pm 1.36) \times 10^4$	$(9.70 \pm 4.00) \times 10^4$
β	329.45 ± 179.71	1217.08 ± 929.56	$(11.27 \pm 2.87) \times 10^3$
γ	10.63 ± 3.06	159.76 ± 15.49	998.01 ± 49.34
δ	$(4.02 \pm 9.22) \times 10^{-3}$	$(6.83 \pm 46.98) \times 10^{-3}$	$(-2.56 \pm 1.79) \times 10^{-1}$
χ^2/NDF	0.80	1.22	3.60

Table 4.3: Fit parameters for $AC_{4,1}(1,2)$ for the strong two-, three- and four-particle scaling illustrated in Fig. 4.17.

	2-particle	**3-particle**	**4-particle**
α	$(3.00 \pm 3.18) \times 10^6$	$(8.89 \pm 4.42) \times 10^7$	$(136.32 \pm 5.96) \times 10^6$
β	$(-5.01 \pm 28.16) \times 10^4$	$(-6.66 \pm 3.81) \times 10^6$	$(-119.54 \pm 3.49) \times 10^5$
γ	$(4.30 \pm 7.49) \times 10^3$	$(19.41 \pm 9.83) \times 10^4$	$(77.28 \pm 1.73) \times 10^4$
δ	25.78 ± 68.13	355.05 ± 846.48	$(111.48 \pm 4.38) \times 10^2$
ϵ	$(1.73 \pm 1.42) \times 10^{-2}$	1.29 ± 1.86	5.06 ± 3.15
χ^2/NDF	1.04	0.39	3.50

Table 4.4: Fit parameters for $AC_{2,1,1}(1,2,3)$ for the strong two-, three- and four-particle scaling illustrated in Fig. 4.17.

	2-particle	**3-particle**	**4-particle**
α	2377.30 ± 530.95	$(10.30 \pm 3.54) \times 10^3$	$(11.85 \pm 1.28) \times 10^4$
β	49.59 ± 36.84	559.63 ± 248.22	$(21.20 \pm 9.12) \times 10^2$
γ	-1.37 ± 0.60	12.44 ± 4.44	243.71 ± 15.83
δ	$(7.64 \pm 2.05) \times 10^{-3}$	$(3.52 \pm 15.94) \times 10^{-3}$	$(-7.97 \pm 5.47) \times 10^{-2}$
χ^2/NDF	1.11	0.11	1.02

Therefore, the new approach developed with SCs is as valid as the traditional approach to design observables robust against few-particle correlations.

Sensitivity to nonflow with HIJING

Now that it is ensured that the ACs behave as expected, their sensitivity to nonflow correlations is estimated with the HIJING generator. The characteristics of the data sample are the same as for the SCs studied above. This means the data correspond to Pb–Pb events at $\sqrt{s_{\rm NN}} = 2.76$ TeV, taken with the same detector configuration as in the measurements of 2010 with ALICE.

Figures 4.19 and 4.20 show the predictions in HIJING as a function of the centrality for the two-harmonic $AC_{a,1}(2,3)$ and $AC_{a,1}(2,4)$, with $a = 2,3,4$ respectively. The top left panel of each figure shows that each term taken individually presents a centrality dependence due to nonflow. However, when combined according to the expressions for the various two-harmonic ACs, the final results are in agreement with zero, meaning the proposed observables are robust against nonflow correlations. In the case of the third order two-harmonic AC, $AC_{2,1}(m,n)$, the comparison with its counterpart in the traditional azimuthal approach, $MHC(v_m^4, v_n^2)$, shows that both methods lead to similar sensitivity to few-particle nonflow correlations. Finally, Fig. 4.21 illustrates the case of $AC_{2,1,1}(2,3,4)$. This observable is also compatible with zero as a function of the centrality, meaning it is robust against nonflow as well. Furthermore, $AC_{2,1,1}(k,l,m)$ is

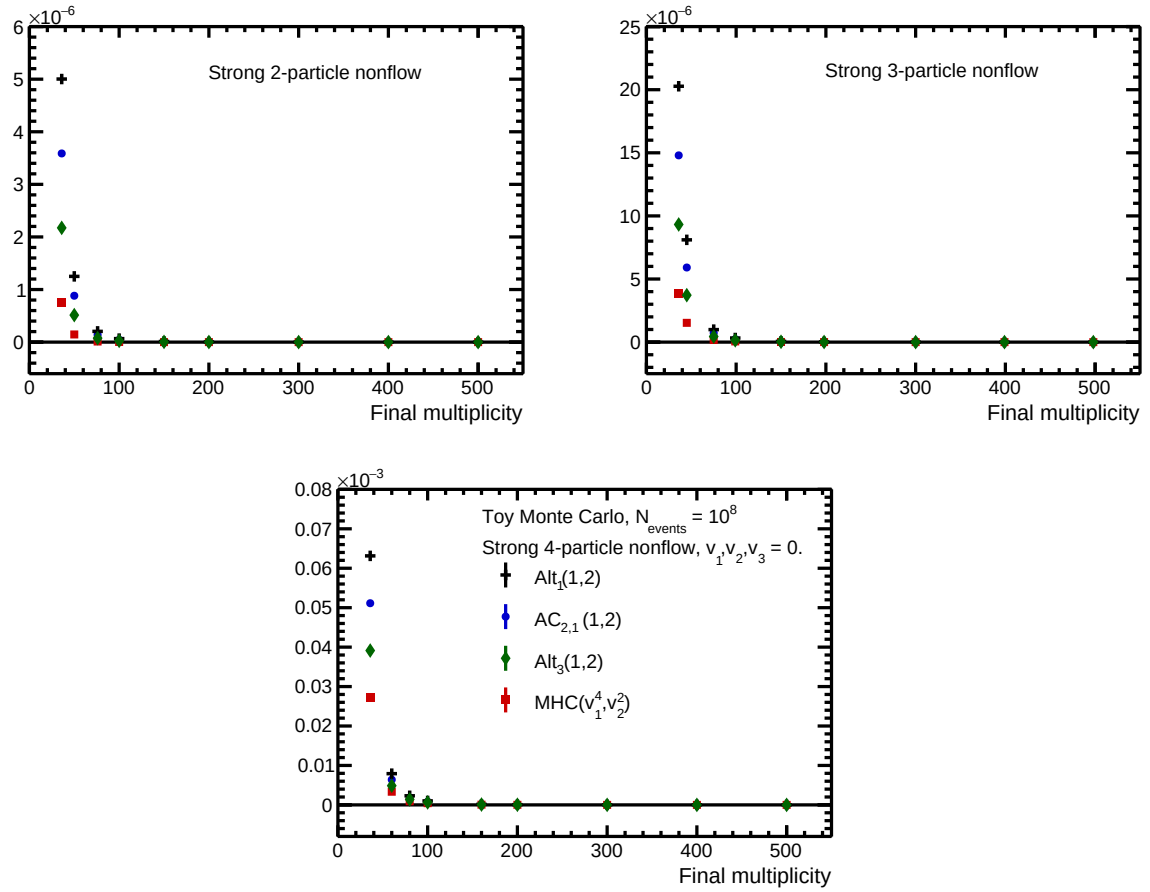

Figure 4.18: Multiplicity dependence of different combinations of correlators with strong two- (*top left*), three- (*top right*) and four-particle (*bottom*) nonflow correlations [157].

symmetric under the permutation $l \leftrightarrow m$, i.e. $\mathrm{AC}_{2,1,1}(k,l,m) = \mathrm{AC}_{2,1,1}(k,m,l)$.

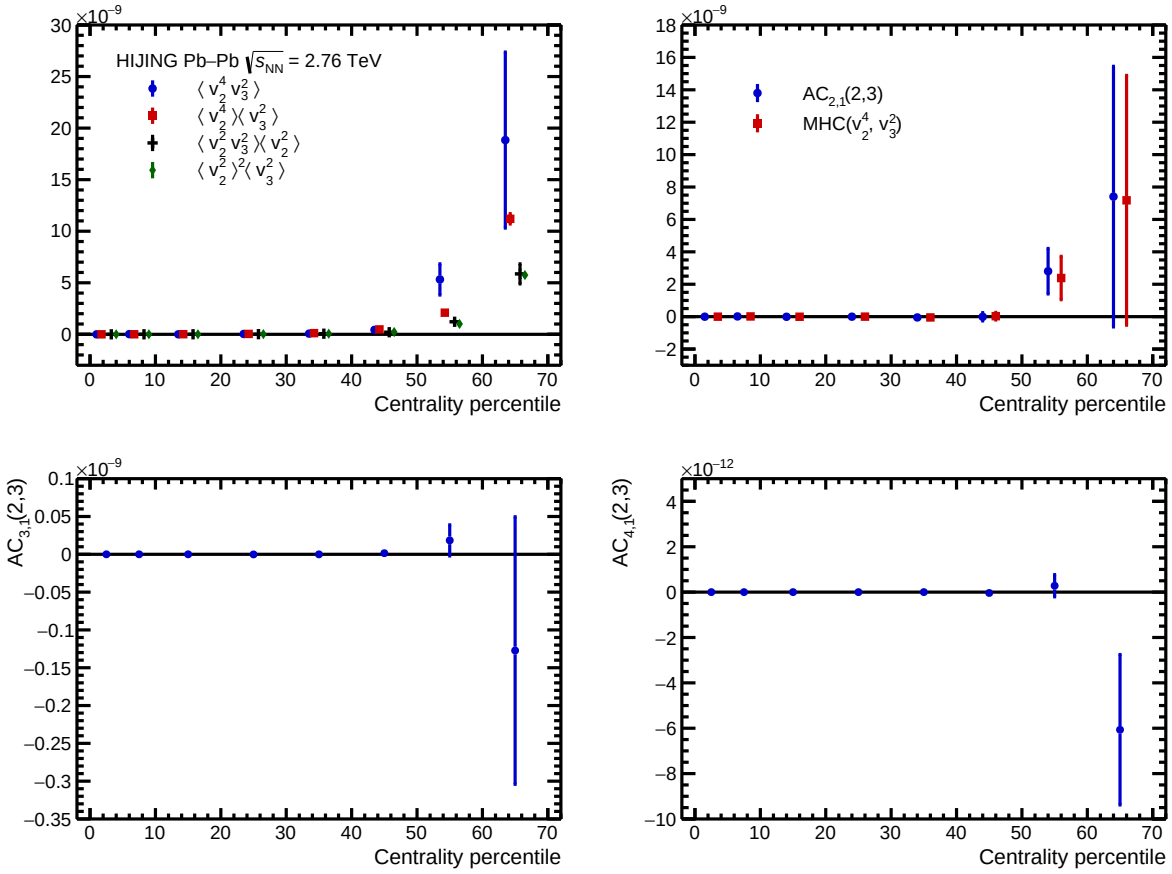

Figure 4.19: Centrality dependence of the terms in $\mathrm{AC}_{2,1}(2,3)$ (*top left*), $\mathrm{AC}_{2,1}(2,3)$ (*top right*), $\mathrm{AC}_{3,1}(2,3)$ (*bottom left*) and $\mathrm{AC}_{4,1}(2,3)$ (*bottom right*) in HIJING [157].

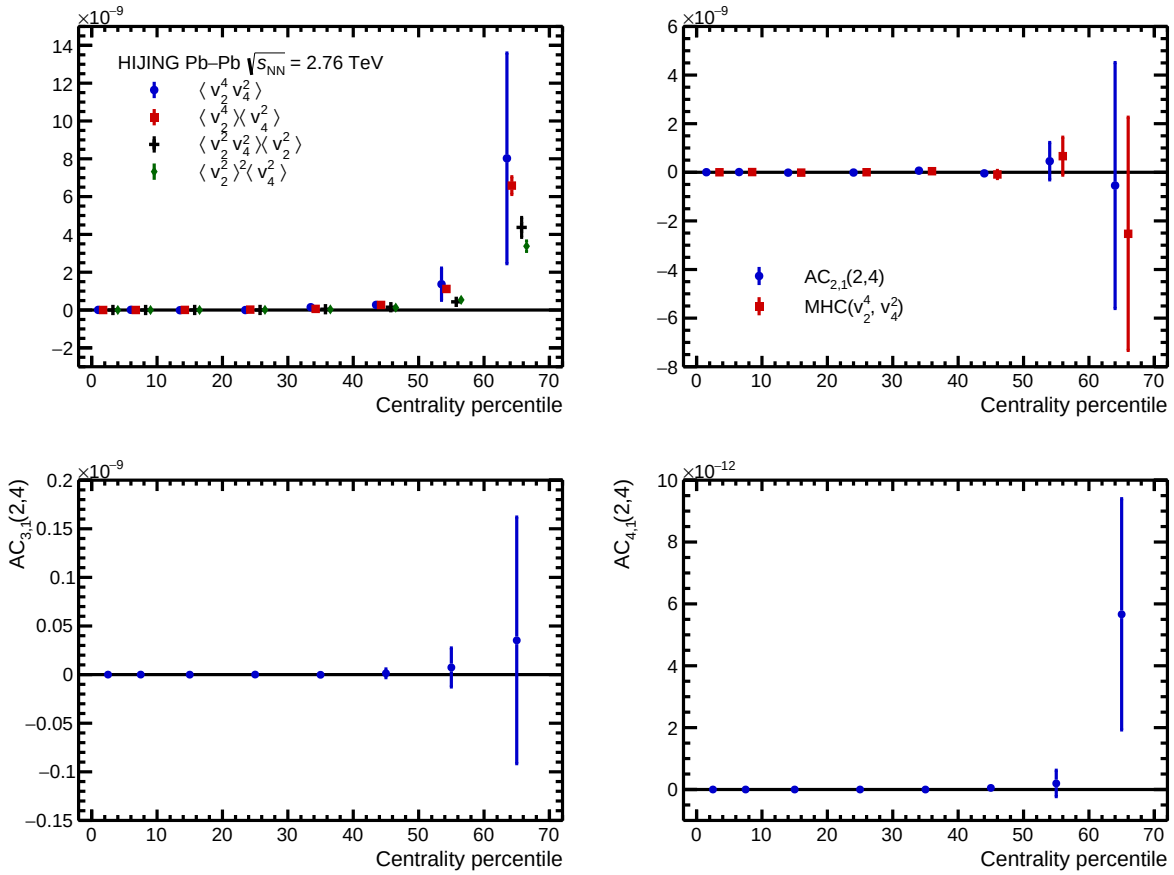

Figure 4.20: Centrality dependence of the terms in $\mathrm{AC}_{2,1}(2,4)$ (*top left*), $\mathrm{AC}_{2,1}(2,4)$ (*top right*), $\mathrm{AC}_{3,1}(2,4)$ (*bottom left*) and $\mathrm{AC}_{4,1}(2,4)$ (*bottom right*) in HIJING [125].

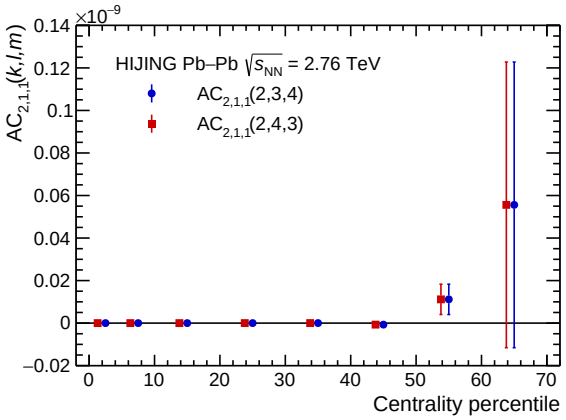

Figure 4.21: Centrality dependence of $\mathrm{AC}_{2,1,1}(2,3,4)$ in HIJING [157].

Chapter 5

Data Analysis

This chapter presents the details for the experimental analysis of the higher order SCs. The distinct steps required to select the final data sample are described in Sections 5.1 and 5.2. Section 5.3 explains the procedure to obtain the particle weights needed to correct for various detector inefficiencies. Once the tracks are selected and the corrections applied, the quality of the final data sample must be ensured at different levels, as illustrated in Section 5.4. Finally, the methods employed to calculate the statistical and systematic uncertainties are explained in Sections 5.5 and 5.6 respectively.

The analysis is carried on the Pb–Pb sample at $\sqrt{s_{\mathrm{NN}}} = 2.76$ TeV collected by ALICE in 2010 during the LHC Run 1. The work uses AOD files, as a large quantity of events and tracks deemed not usable for physics analyses are removed with the filtering from ESD samples (see Section 3.2.4). Technical details about the software and runs can be found in Appendix D.

5.1 Event selection

While the applied filtering of the data is a prerequisite to remove bad events, several additional criteria must be introduced to guarantee that the selected tracks are suitable for flow analyses. The experimental results presented in Chapter 6 are the generalisation of the formalism of the SCs. This means that the event and track selections are based on the ones established in the studies of the lower order observables, also with the 2010 Pb–Pb data from ALICE and published in Refs. [114,116]. The main points in the default event selection are listed in Table 5.1.

Table 5.1: Summary of the default event selection criteria employed in this analysis. M_{TPC} (M_{gl}) stands for the multiplicity of TPC-standalone (global hybrid) tracks after the selection of the primary vertices.

Selection criterion	**Value**
Trigger	Minimum bias (kMB)
Centrality estimator	SPD clusters ($CL1$)
Primary vertex along the beam axis (PV_z)	$< \|10\|$ cm
Minimum boundary for the high multiplicity outliers	$M_{TPC} > 1.54 M_{gl} - 65.00$
Maximum boundary for the high multiplicity outliers	$M_{TPC} < 2.30 M_{gl} + 90.00$
Minimum event multiplicity	≥ 6

The initial data sample has been collected with the minimum bias interaction trigger kMB. An event is accepted if hits have been seen simultaneously in both the V0A and the V0C (Section 3.2.3). The centrality of the triggered events must then be estimated. Many detectors in ALICE can be employed for this task, using different working principles and measured quantities [161, 162]. The resolution of the most commonly used estimators is showed in the performance figure in Fig. 5.1. The V0M estimator comes from the combination of the A and C sides

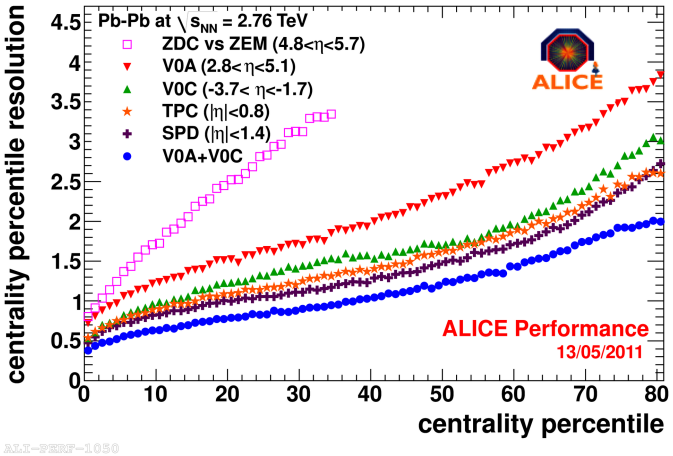

Figure 5.1: Centrality resolutions of the main estimators in ALICE. Performance figure from [161, 162].

of the V0 detector itself. It is the main centrality estimator for ALICE analyses as it presents the best resolution of all estimators due to its wide pseudorapidity acceptance. However, because of issues with high multiplicity outliers (HMOs), the default estimator for this study uses the clusters found in the SPD ($CL1$), while V0M is kept as a trial for the determination of the systematic uncertainties (Section 5.6.2). From Fig. 5.1, the resolution of the SPD goes from 1% to 3% with the centrality. This is slightly worse than for V0M, which is in the 0.5–2% range, but still perfectly acceptable. More information about the HMOs is provided later in this section.

The last criterion in this list, the minimum multiplicity of an event, is applied after the track selection itself, i.e. at the end of the full selection and before the computation of the averages appearing in the expression of $\mathrm{SC}(k, l, m)$. In opposition to the other criteria whose applications have physics origins, the requirement that an event must have at least six tracks to be taken into account in the final sample is introduced to prevent problems in the calculations of the multiparticle correlators themselves. In the case of the three-harmonic SCs, six particles are involved in the computation of the largest correlator. As these particles must be distinct to avoid autocorrelations, an event with five or fewer tracks cannot be kept for the analysis.

5.1.1 Primary vertex

The position of the primary vertex of an event is reconstructed with the information from the ITS (Section 3.2.1). As previously seen, it is possible to relate the multiplicity of an event to its centrality. For example, a head-on collision will have a higher number of participating nucleons and therefore, the number of produced particles that are detected must increase as well. However, if such a collision happens too far from the nominal interaction point, the probability that a large number of these particles escape the central barrel of ALICE without being detected becomes non-negligible. This leads to a lower multiplicity of the event and consecutively, its misidentification as a peripheral event.

In order to prevent this scenario, the condition that the primary vertex in the z-direction (PV_z) must be at most at ± 10 cm from the nominal interaction point is imposed. This guarantees a full geometrical acceptance in the ITS and a complete acceptance in the pseudorapidity range $|\eta| < 0.9$ in the TPC. Figure 5.2 shows the distribution of the primary vertex along the three Cartesian coordinates. It has to be noted that no selection needs to be imposed on the position of the primary vertex in the transverse plane xy.

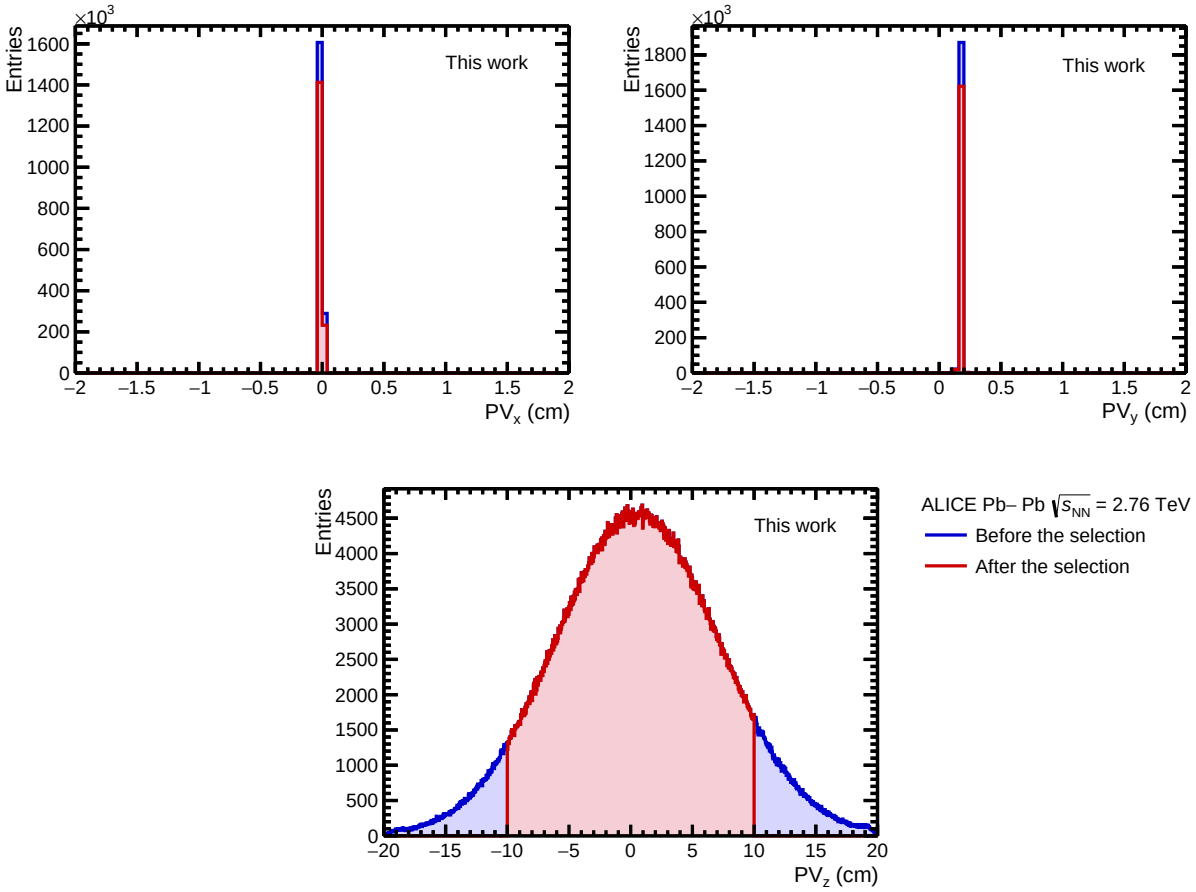

Figure 5.2: Position of the primary vertex along the x- (*top left*), the y- (*top right*) and the z-direction (*bottom*) for the centrality range 10–20% before and after the application of the physics event selection.

5.1.2 High multiplicity outliers

Another set of requirements concerns the removal of the HMOs. For a given centrality range and centre of mass energy, the number of produced tracks per event is expected to be in a certain interval. Furthermore, the more central the collision is, the higher the multiplicity must be. Figure 5.3 is provided as an example for the Run 1 energies. The distribution of the number of tracks after the full selection without the rejection of the HMOs is shown for the centrality range 10–20% in the left panel and for 40–50% in the right panel. Some events show a final multiplicity above 1000 in the range 40–50%. This is about one order of magnitude higher than the expected number of tracks for this centrality, as the peak lies between 200 and 700 tracks per event. These unphysical events are present at the per mille level. However, their contribution is dominant in the computation of the multiparticle correlators, and more so for

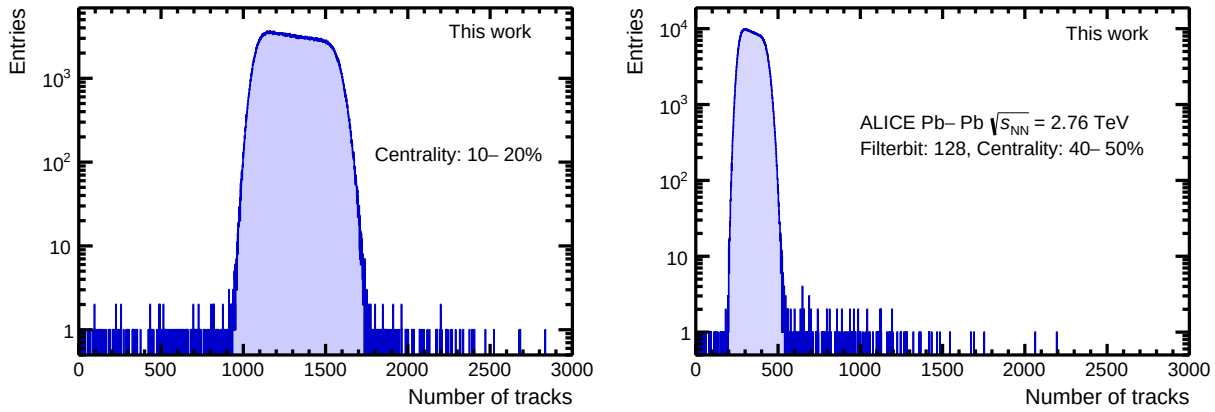

Figure 5.3: Final distribution of the number of tracks for the centrality ranges 10–20% (*left*) and 40–50% (*right*) after application of the default selection without the requirement on the HMOs.

the higher order correlators. This is due to the fact that the weight of an event is proportional to the multiplicity of said event raised to the number of particles involved in the correlator. This effect results in a bias in the final SCs, as it can be seen in Fig. 5.4. The comparison between

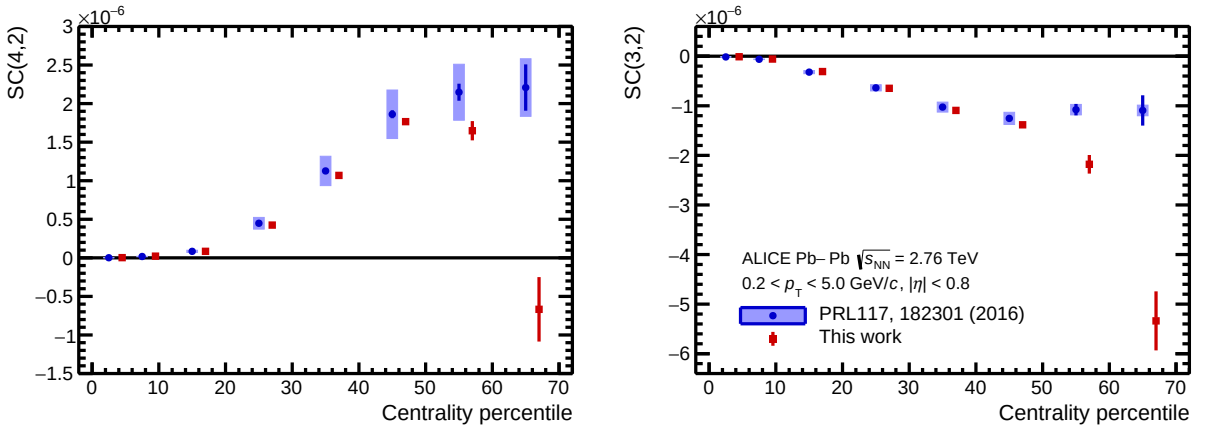

Figure 5.4: Centrality dependence of SC(4, 2) (*left*) and SC(3, 2) (*right*) in presence of the HMOs, compared to the results published in Ref. [114]. The effects of the HMOs become dominant as the collisions get more peripheral.

the published measurements for SC(4, 2) and SC(3, 2) [114] and the results obtained with the default selection without the removal of the HMOs, shows that the contribution of the HMOs become non-negligible for the semicentral and peripheral collisions.

The determination of the criteria to remove these HMOs is done with the help of a two-dimensional correlation histogram between the multiplicities of two different filterbits. Figure 5.5 shows the correlations between the multiplicity of TPC-only tracks and global hybrid tracks after the application of the selection on the primary vertices for the full centrality range 0–80%. These correspond respectively to the filterbit 128 and 256 for the AOD160 filtering of the LHC10h dataset. This correlation histogram can be decomposed into two main components: the central triangle containing the "healthy" events and the HMOs outside of it, along the y-axis. These outliers can be removed by parametrising the sides of the main triangle, as shown in the right

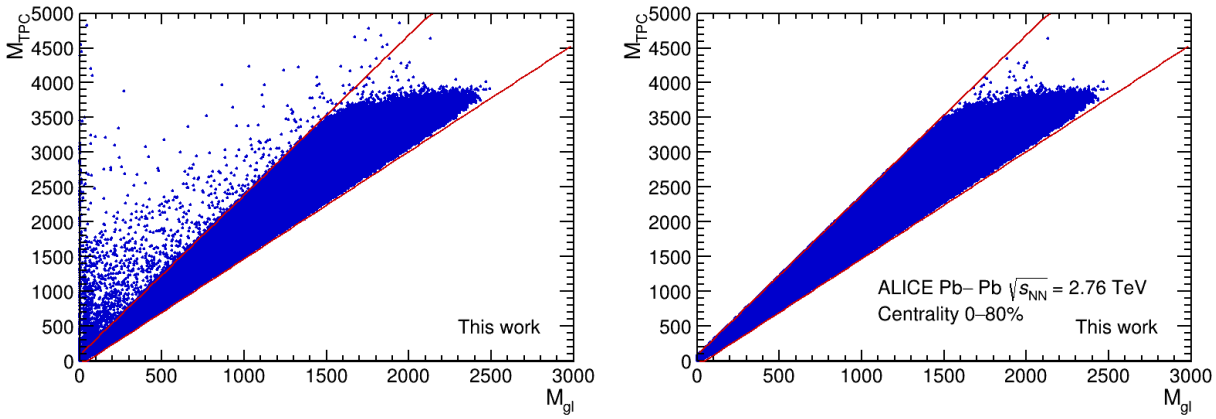

Figure 5.5: Correlation histogram for the multiplicity of TPC-only tracks (filterbit 128, M_{TPC}) and global hybrid tracks (filterbit 256, M_{gl}) for the full centrality range 0–80% before (*left*) and after (*right*) the rejection of the HMOs with the parametrised criteria shown in red.

panel.

However, these criteria on the two-dimensional correlation histogram are not sufficient. Figure 5.6 shows the correlation histogram after removal of the HMOs in the case of hybrid tracks with the filterbit 768[1] and the global hybrid tracks already mentioned above, for the centrality 40–50% estimated with SPD clusters (left panel) and V0M (right panel). While all

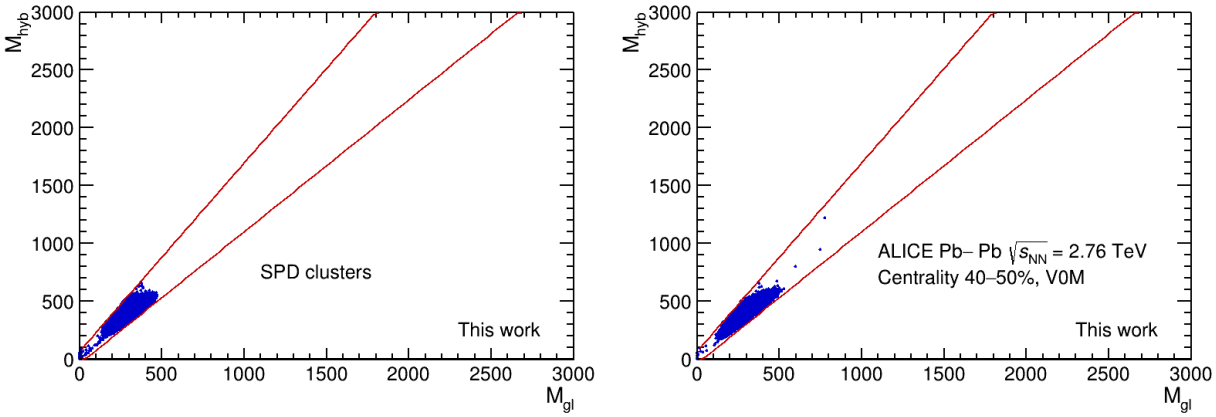

Figure 5.6: Correlation histogram for the multiplicity of the hybrid tracks (filterbit 768, M_{hyb}) and global hybrid tracks (filterbit 256, M_{gl}) after the selection on PV_z for the centrality range 40–50% estimated with the SPD clusters (*left*) and with the V0M (*right*). The red line indicates the parametrisations used to remove the HMOs.

outliers for the SPD clusters are removed with the introduced criteria, this is not the case for the V0M estimator. Some points can still be seen inside the range allowed by the HMOs selection. They cannot be removed with the method described above, as they lie inside the main triangle for the full range 0–80%. This leads to the SPD clusters being used as the default centrality estimator in the analysis.

[1]The criteria to remove the HMOs depend on the main filterbit used in the analysis. The ones for hybrid tracks 768 are given in Section 5.6.

Figure 5.7 shows the final multiplicity distribution in the ranges 10–20% (left) and 40–50% (right) after application of the full event and track selection with the removal of the HMOs. All outliers are removed with the application of the parametrised lines from Table 5.1.

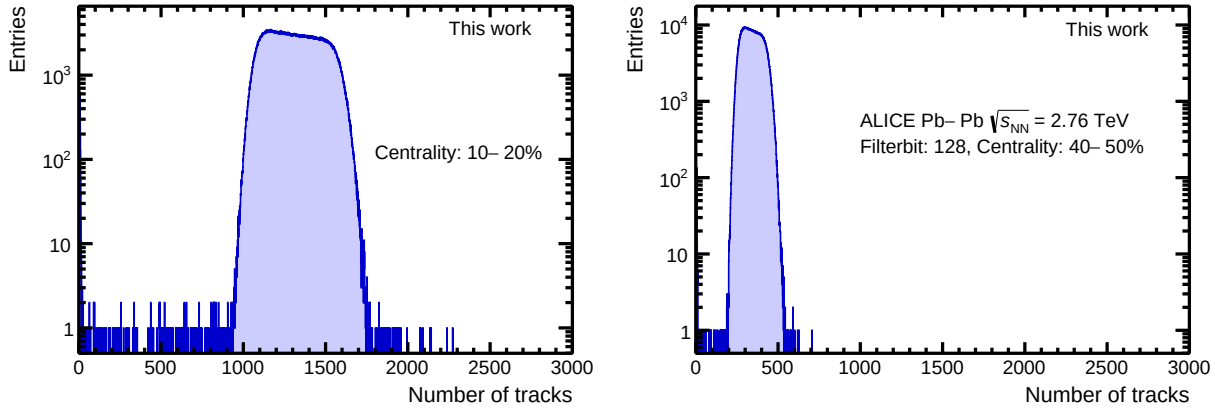

Figure 5.7: Final distribution of the number of tracks for the ranges 10–20% (*left*) and 40–50% (*right*) in the case where the requirements on the HMOs are applied.

5.2 Track selection

The experimental results obtained in this work are for all included charged particles. Therefore, the goal of this second part of the selection is to remove poorly reconstructed or misreconstructed tracks from the final data sample. The default track selection is listed in Table 5.2. While TPC-only tracks have been obtained by the application of requirements on some of these

Table 5.2: Summary of the default track selection criteria employed in this analysis.

Selection criterion	**Value**
Type of tracks (Filterbit)	TPC-only (128)
Transverse momentum (p_{T})	$[0.2, 5.0]$ GeV/c
Pseudorapidity (η)	$[-0.8, 0.8]$
Number of TPC clusters (N_{TPC})	> 70
χ^2 per TPC cluster	$[0.1, 4.0]$
Distance of closest approach in xy-plane (DCA_{xy})	< 2.4 cm
Distance of closest approach in z-direction (DCA_{z})	< 3.2 cm
Non-uniform efficiency (NUE) corrections	p_{T}-weights from HIJING
Non-uniform acceptance (NUA) corrections	None

quantities in the passage from ESD to AOD files, these criteria are applied nonetheless to ensure the proper application of the filtering or to tighten it.

Figure 5.8 shows the distribution of the transverse momentum (p_{T}) of the tracks directly after the application of the selection on PV_z and on the HMOs. The reconstruction of the transverse momentum and its quality depend on the combination of the information from the various tracking detectors, according to the type of tracks used in the analysis. This means, for example, that if a charged particle has a too low momentum, it will not reach the TPC due to its bending in the magnetic field. This efficiency of the reconstruction depends on the transverse

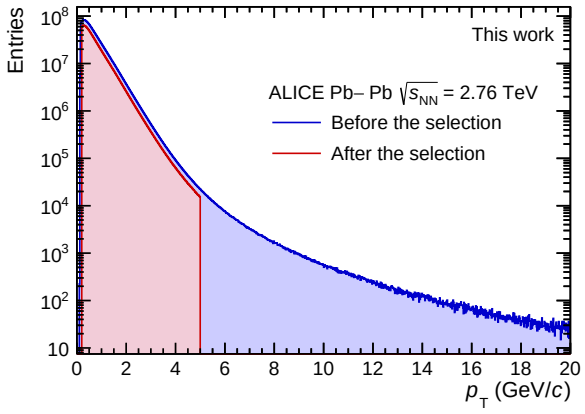

Figure 5.8: Transverse momentum spectrum of the TPC-only tracks for the centrality range 10–20% before and after the application of the full track selection.

momentum itself and is smaller at lower p_T. To remove the bias these tracks would have brought in the analysis, a minimum requirement of $p_T > 0.2$ GeV is made. Furthermore, jets are more predominant at higher momenta. A jet can be classified as a phenomenon that correlates only some of the produced particles. Therefore, they represent a bias in flow analyses and need to be removed. This is achieved by the maximum criterion $p_T < 5.0$ GeV introduced in the selection.

As seen in Section 3.2, the central barrel has a pseudorapidity coverage of $|\eta| < 0.9$. The requirement is set to $|\eta| < 0.8$ to reject edge effect (Fig. 5.9).

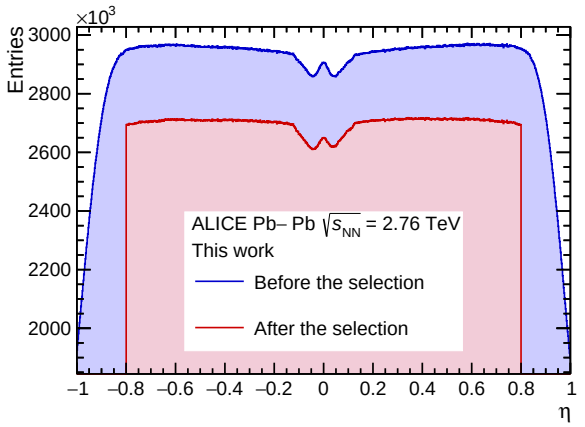

Figure 5.9: Pseudorapidity distribution of the TPC-only tracks for the centrality range 10–20% before and after the application of the full track selection.

The TPC is the main tracking detector in ALICE and this analysis used TPC-only tracks. The 2010 Pb–Pb dataset is known for its particularly good detector conditions. The space-charge distortions (deformations of the drift electric field due to accumulation of ions from the passage of the produced particles) and the pile-up were negligible. No requirements are added to the selection with respect to these points.

To ensure the quality of the tracks, two criteria concerning the TPC clusters are included in the track selection: the number of TPC clusters and the goodness of fit χ^2/ndf per TPC cluster.

Their distributions are shown in Fig. 5.10. A track passing through the TPC can have up to

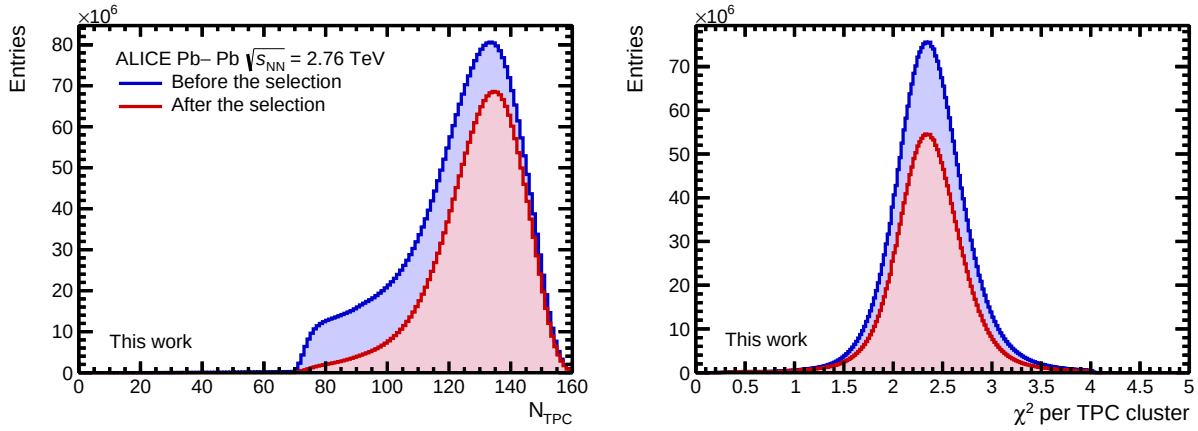

Figure 5.10: Distributions of the number of TPC clusters (*left*) and χ^2 per TPC cluster(*right*) of the TPC-only tracks for the centrality range 10–20% before and after the application of the full track selection.

159 space points (or TPC clusters) usable for its reconstruction. The number depends on the physics properties of the track, like its momentum, and of the conditions inside the detector, like the drift field. For example, a high-momentum track will have a straight trajectory inside the chamber and thus a higher number of space points. Furthermore, tracks with higher numbers of space points are generally better reconstructed. In this analysis, the selected tracks need to be reconstructed with at least 70 space points. Concerning the χ^2/ndf, the value of a given track is required to be in the range $[0.1, 4.0]$.

The DCA measures the distance between the position of the track closest to the primary vertex and the vertex itself (see Fig. 5.11). Cosmic tracks and secondary particles originating from weak decays of long-lived primaries or from conversion in the material of the detector are characterised by large values of the DCA. The contribution from these particles is then reduced by introducing criteria on the DCA in the transverse plane (DCA_{xy}) and along the beam direction (DCA_z). Figure 5.12 shows the distribution of DCA_{xy} in the left panel and DCA_z in the right panel. These distributions are quite wide, reaching the centimetre level. This comes from the fact that the only used information is from the TPC, which is not the detector closest to the primary vertex. As a consequence, the criteria related to the DCA added to the track selection are $|DCA_{xy}| < 2.4$ cm and $|DCA_z| < 3.2$ cm. These are directly inherited from the values used in the filtering for TPC-only tracks.

5.3 Particle weights

Amongst the systematic biases present in analyses, some originate from the presence of detector inefficiencies. An example of such effects is the presence of dead or defective sectors in a detector. In these regions, some, if not all, particles would not be detected and the corresponding distributions would be biased. These inefficiencies can further be divided into two main types, the NUA and NUE, which need to be corrected with the use of particle weights. In this section, the effects of two different corrections are investigated: the NUE of the transverse momentum and the NUA of the azimuthal angles.

The procedure to get the particle weights is established with the help of realistic MC sim-

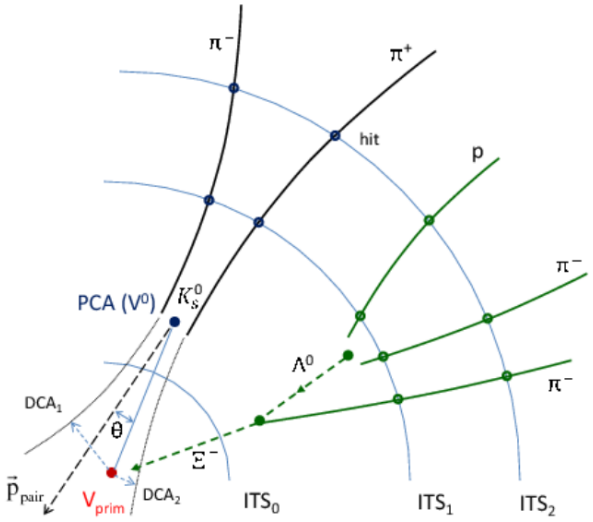

Figure 5.11: Definition of the DCA and principle of the reconstruction of secondary vertex using K^0 and ξ as examples [163]. The reconstructed tracks are shown with the solid lines, the extrapolation to the primary vertex with the dashed ones.

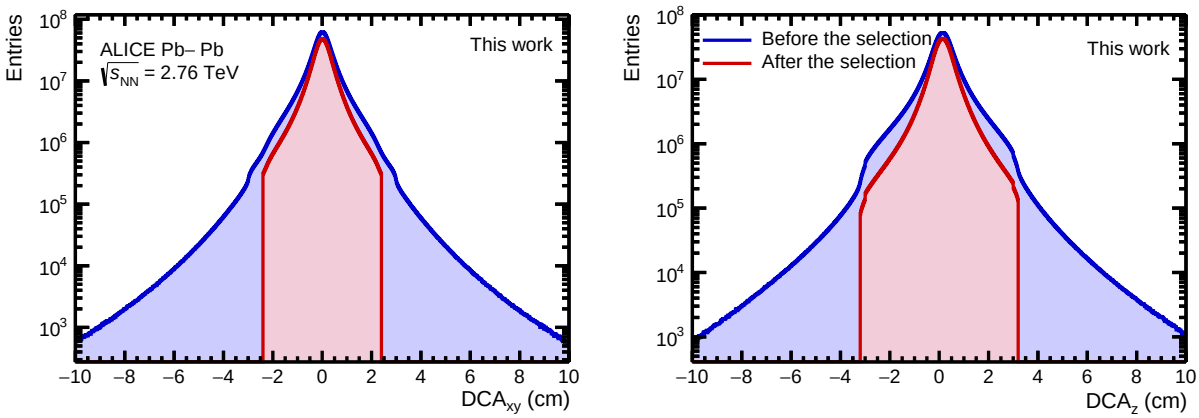

Figure 5.12: Distance of closest approach in the transverse plane (*left*) and along the beam (*right*) of the TPC-only tracks for the centrality range 10–20% before and after the application of the full track selection.

ulations anchored to experimental data. Simulated events are used since they contain both the descriptions of the particles at the kinematics and the reconstruction levels (see Section 3.2.4). The comparison between what would be measured in the ideal case (kinematics) and what is measured in reality with ALICE (reconstruction) allows to get good estimations of the detector effects like the particle absorption or the smearing of the transverse momentum in the detector. The corrections of these effects are done in this work with the use of particle weights. In the rest of this section, the kinematics and reconstruction levels will be respectively abbreviated as *kine* and *reco*.

For a given MC production, in this case the HIJING simulations anchored to the 2010 Pb–Pb dataset, the starting point to obtain the corrections for the data is the measurement of the distributions of the transverse momenta and azimuthal angles at the kine and reco levels.

Two major points need to be stressed out concerning this step. First, the selection criteria applied to the reconstructed MC events and tracks must be identical as the one used for the counterpart experimental analysis. For the kine information, only the kinetic criteria (p_{T} and η) and global event observables (PV_z in this case) must be applied. Secondly, the distributions must be obtained for each run in the data period individually. This comes from the presence of run-by-run variations in the detector conditions. The final p_{T}- and φ-weights are then obtained

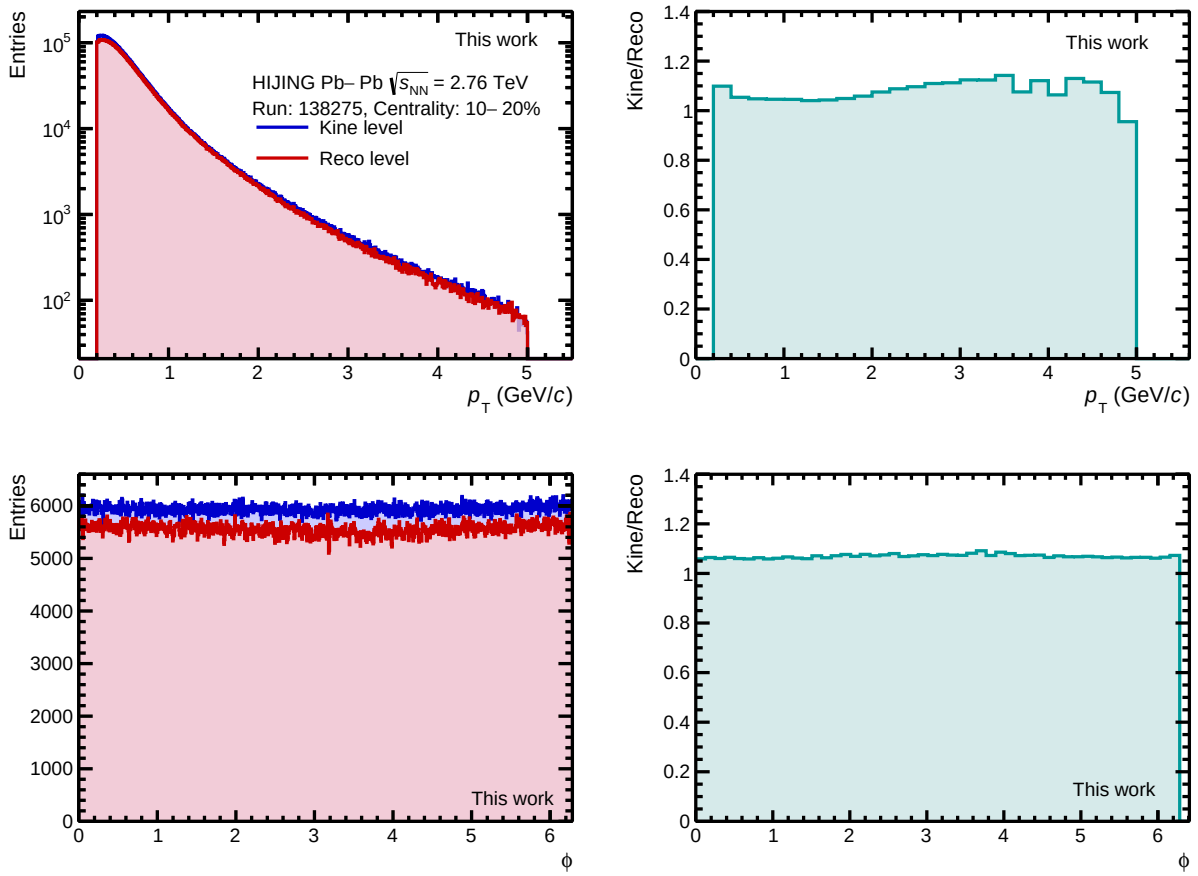

Figure 5.13: Distribution of the transverse momentum (*top left*) and the azimuthal angles (*bottom left*) in HIJING for the run 138275 in the centrality range 10–20% and corresponding p_{T}-weights (*top right*) and φ-weights (*bottom right*).

by taking the ratio of the concerned distribution at kine level over the same distribution at reco level. An example of distributions and corresponding particle weights for the run 138275 in the centrality range 10–20% is presented in Fig. 5.13. Finally, once the particle weights are obtained for each run and centrality, they can easily be applied to the experimental data. As seen in Section 2.1, the Q-vectors can be expressed in terms of the azimuthal angles and the particle weights themselves (Eq. (2.16)). Furthermore, if the corrections come from different sources (e.g. p_{T}- and φ-weights together), the resulting weight is the product of the individual weights.

In order to determine the necessity to include particle weights in the default track selection or as part of the systematic trials, the previously published SC(4, 2) and SC(3, 2) are measured without any correction applied, with p_{T}-weights for NUE effects, and with φ-weights for NUA effects (Fig. 5.14). The comparison of the results without particle weights to the results with the correction from φ-weights show that the latter have no effect on the final SCs. This outcome

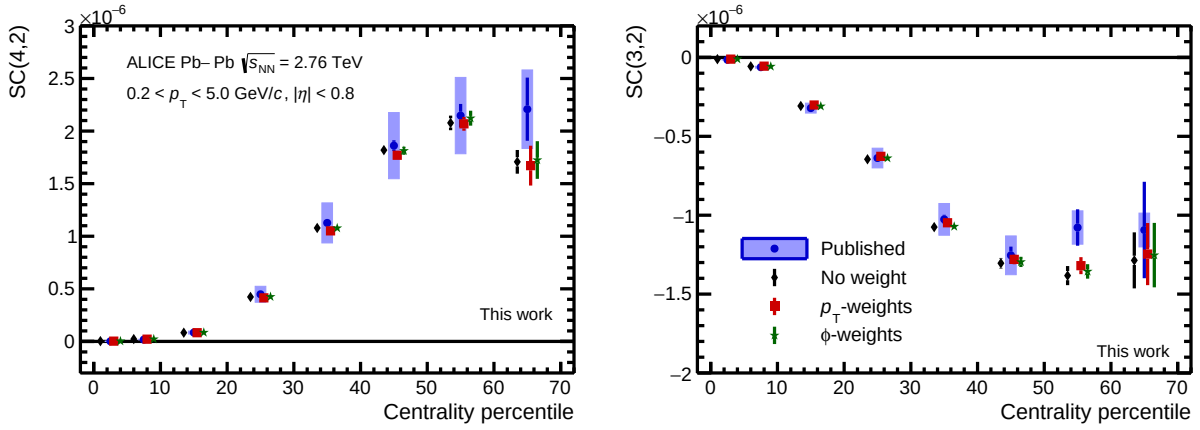

Figure 5.14: Centrality dependence of SC(4, 2) (*left*) and SC(3, 2) (*right*) measured without particle weights, with p_{T}-weights and with φ-weights, compared with the results from Ref. [114].

is expected as the 2010 Pb–Pb data period is known to have a particularly flat distribution of the azimuthal angles for the TPC-only tracks (see for example Fig. 5.16 (right)). However, one has to be careful with the interpretation of the results without and with the p_{T}-weights. The published results shown with the blue circles have been obtained without the use of any weight (they have been included in the systematic uncertainties). This explains why the current results without weights are in good agreement with the published ones. However, the presence of detector effects is known, as well as the technology to correct for them. The decision is thus made to include the NUE corrections in the default track selection (Table 5.2).

5.4 Final quality assurance of the data

The data selection summarised in Tables 5.1 and 5.2 is introduced to reject bad events and tracks. However, the variables and values are based on the characteristics of the various detectors in ALICE and the knowledge from previous studies (physics analyses, but also studies about the quality of the data themselves). It is thus needed to ensure that the selected tracks have the quality required for the analysis.

The first step is the comparison of the runs with each other (Section 5.4.1). Runs with values that are systematically off are excluded from such final data sample. After the run-by-run trending, the quality of the resulting dataset is checked as well (Section 5.4.2). This is established with the help of some known distributions, e.g. the pseudorapidity (Fig. 5.9) or the azimuthal angles, and with the comparisons to some previous results from the ALICE Collaboration.

5.4.1 Run-by-run trending

The values for a set of quantities are extracted for each run and compared between each other. While some fluctuations are tolerated for a given observable (for example due to fewer events recorded in a run), a run that is systematically off in multiple observables is a clear indication of an underlying problem. In this case, the corresponding run needs to be excluded from the final data sample. Figure 5.15 shows the spread of the average multiplicity $\langle M \rangle$ and of two two-particle correlators, $\langle 2 \rangle_{1,-1}$ and $\langle 2 \rangle_{2,-2}$ for the centrality range 10–20%. As all the

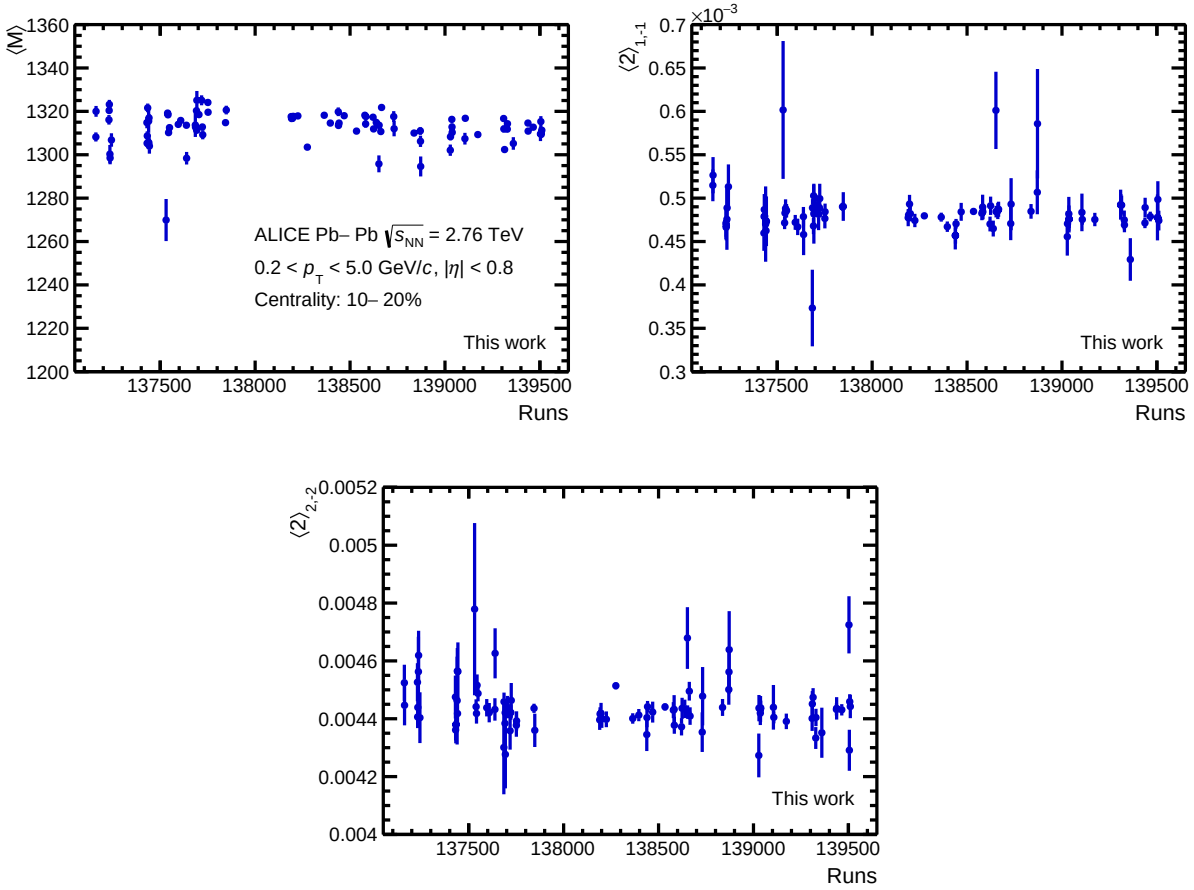

Figure 5.15: Spread as a function of the runs of the average multiplicity $\langle M \rangle$ (*left top*), the two-particle correlator $\langle 2 \rangle_{1,-1}$ (*top right*) and the two-particle correlator $\langle 2 \rangle_{2,-2}$ (*bottom*) for the centrality range 10–20%.

runs are consistent with the others, all 88 of them are included in the final analysis. The gap in the numbering of the runs comes from the way they are defined by the electronic system in ALICE and correspond to non-physics runs.

5.4.2 Quality assurance of the full dataset

The final sample of data obtained from all the runs that passed the trending is controlled as well. The aim is to confirm that the applied selection does not include poorly reconstructed events due to detector issues or HMOs for instance. Figure 5.16 (left) shows the number of events after the full default selection per centrality bin defined in the analysis. This distribution is flat per bin of 10% as needed for the analysis. A non-flat distribution would indicate the presence of misreconstructed or undetected escaping particles leading to a misidentification of the centrality of these events. Another histogram used to check the quality of the dataset is the distribution of the azimuthal angles (right panel in Fig. 5.16). This distribution is known to be perfectly uniform for TPC-only tracks in LHC10h. If an issue arises during the selection of the data, this will have an impact of this distribution, with the apparition of holes or peaks. The two distributions correspond to their expected profiles, meaning that both the dataset and selection can be used for analysis.

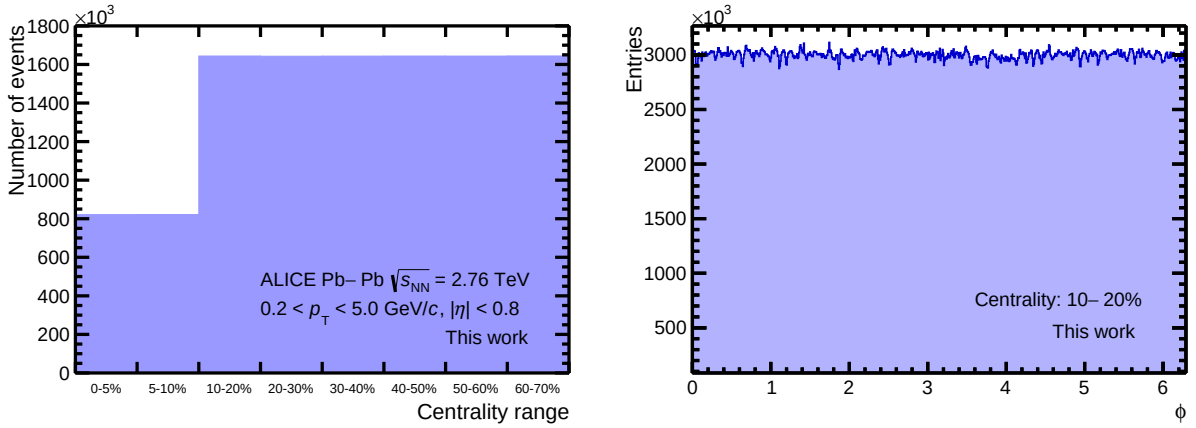

Figure 5.16: (*Left*) Number of events per centrality bin for the full LHC10h data sample and (*right*) distribution of the azimuthal angles for the centrality range 10–20%, both after the default selection.

The last checks to perform are the comparisons to previously published flow observables with similar selections and energies, with the same results obtained with the current work. For this, two sets of measurements are reproduced: the two-harmonic SCs, $SC(4,2)$ and $SC(3,2)$, published in Ref. [114], and the elliptic flow amplitudes measured with the two- and a four-particle cumulants ($v_2\{2\}$ and $v_2\{4\}$ respectively) published in Ref. [126]. The comparisons for the SCs can be seen in Fig. 5.14. Figure 5.17 presents the measurements of the elliptic flow coefficient. In all cases, the results obtained with the default selection described in Sections 5.1

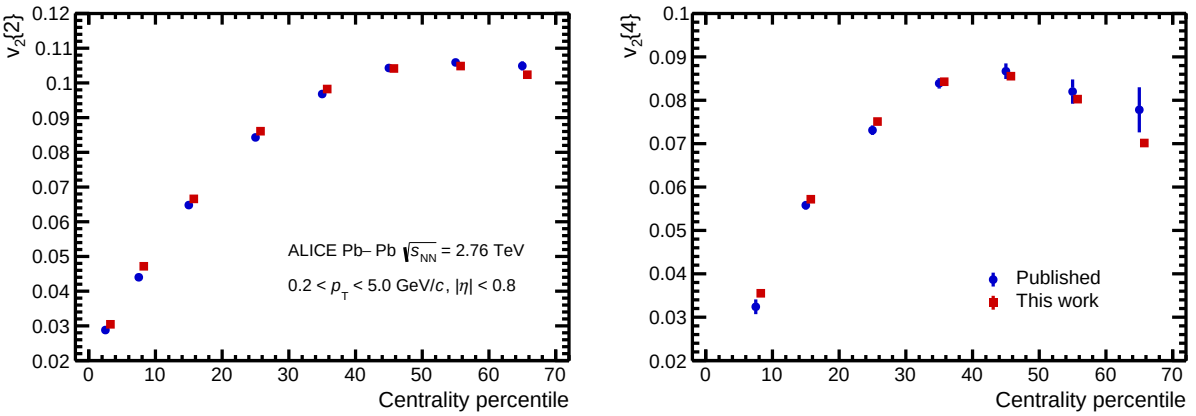

Figure 5.17: Centrality dependence of $v_2\{2\}$ (*left*) and $v_2\{4\}$ (*right*) for the results published in Ref. [126] and the selection used in this work.

to 5.3 are in good agreement with the published ones. Furthermore, it has to be noted that the previous analyses have been conducted without p_{T}-weights in the default selection, but added them as a systematic effect in the overall uncertainties. This explains why the results without particle weights or with φ-weights are generally closer to the published measurements. For the 2010 measurements of $v_2\{2\}$ and $v_2\{4\}$, the published analysis was performed on only 45×10^3 events, which corresponds to only a small part of the full dataset. As a comparison, the LHC10h data sample used here contains about 10.9×10^6 events after full selection in the same centrality

range 0–70%.

5.5 Statistical uncertainties

The SCs as defined as in Eq. (4.1) in terms of the flow amplitudes or Eq. (4.11) for the azimuthal angles are compound observables. This means that the statistical errors cannot be trivially obtained from the profiles filled with the values of each correlator. Furthermore, due to the complexity of its expression and the number of covariance terms involved, the error propagation like it was done for $\mathrm{SC}(m,n)$ in Ref. [114] is not feasible in practice. The technique used in this work is the *bootstrap method* or *bootstrapping*.

The idea behind the bootstrap method is the following. The initial sample, here the LHC10h dataset, is divided into S subsamples with approximately the same statistics N_{avg},

$$N_{\mathrm{avg}} \equiv \frac{N_{\mathrm{Total}}}{S}, \tag{5.1}$$

with N_{Total} the total statistics of a given quantity in the initial sample. In the rest of this chapter, the term "statistics" is chosen to refer to the number of events in the centrality range 10–20% after the application of all the selection criteria given in Tables 5.1 and 5.2. Moreover, it can be shown with the help of the central limit theorem that a good estimation of the statistical errors can be achieved with already ten subsamples. Therefore, this number is set to $S = 10$ in the analysis.

Conditions on the minimum and maximum numbers of events are then applied such that each subset has a number of events in the range $[N_{\mathrm{avg}} - x, N_{\mathrm{avg}} + x]$. This additional requirement ensures that all subsets have about the same size. The width of the acceptance band is chosen depending on the statistics of the initial sample. As it is made out of indivisible datasets with fixed sizes, the runs, the smaller the initial sample is, the larger the acceptance band must be. In the case of LHC10h with the 88 runs listed in Appendix D, the half-width of the band is fixed to $x = 10\%$ of N_{avg}.

Once the subsamples are formed, the observable of interest x_i is calculated for each subset $i = 1, \ldots, S$. If x denotes the compound observable estimated for the initial sample (x can therefore be a $\mathrm{SC}(k,l,m)$ or a $\mathrm{NSC}(k,l,m)$ for example), the unbiased estimator for the variance V can be computed with

$$V \equiv \frac{1}{S-1} \sum_{i=1}^{S} (x - x_i)^2. \tag{5.2}$$

The final statistical error σ_x to attribute to the observable x is then calculated using

$$\sigma_x \equiv \sqrt{V/S}. \tag{5.3}$$

The validity of the bootstrapping is proved with its comparison to the traditional error propagation used for the observables $\mathrm{SC}(3,2)$ and $\mathrm{SC}(4,2)$. The results obtained with the data selection described above are presented with the ones from Ref. [114] in Fig. 5.18. The statistical errors on the results obtained with the default selection and the bootstrap method (blue squares) described above are of the same order of magnitude with the errors obtained with the usual error propagation (red circles). It has to be noted that the differences between the values themselves originate from the changes in their selection. The measurements published in Ref. [114] have been obtained with ESD global tracks and tighter criteria on the DCA.

Figure 5.18 shows also the effects of the absence of the acceptance band in the bootstrap method with the black cross markers. In this version of the bootstrap, said band is replaced with

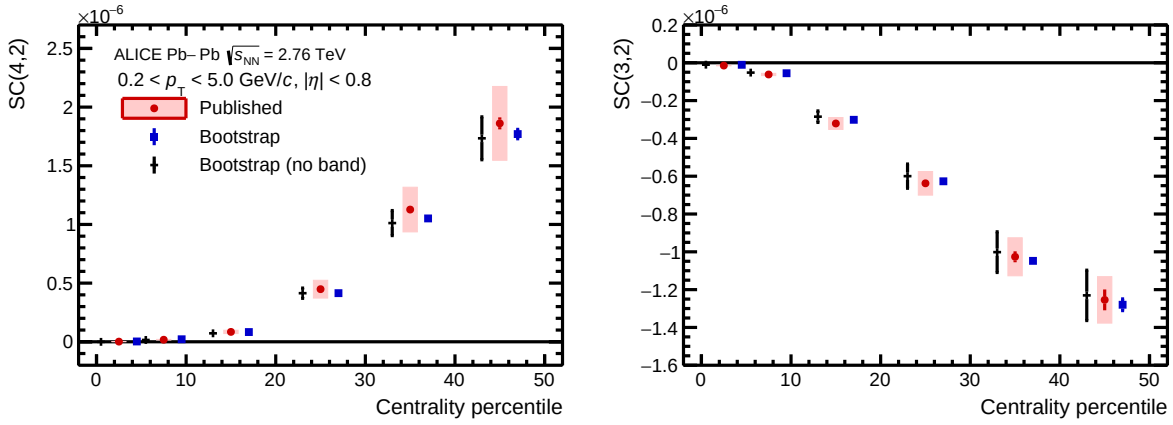

Figure 5.18: Centrality dependence of SC(4, 2) (*left*) and SC(3, 2) (*right*) for the LHC10h. The first published results with error propagation [114] are shown with the red circles, the results with the default selection and the bootstrap with the blue squares and the results with the bootstrap without the acceptance band with the black crosses.

a condition on the minimum number of events a subset must have. However, no requirement is made on their maximum, meaning it is possible — and even probable — to have one or many subsamples with a size more important than the others. This leads to larger final statistical errors than the ones from error propagation or bootstrap with the acceptance band and shows the importance of imposing a limit on the maximal size of the samples. Furthermore, it has to be noted that the difference between the black points and the others can again be explained with variations in the default track selection. In this case, the measurements have been obtained with the first version of the selection used for the preliminary results approved for the "Quark Matter 2019" conference and "inverted" (wrong) p_{T} corrections.

5.6 Systematic uncertainties

The systematic uncertainties are here estimated with the use of a Barlow test [164, 165]. The method employed in this analysis is presented in Section 5.6.1. The errors obtained for SC(2, 3, 4) with the 2010 Pb–Pb data sample are listed as an example in Section 5.6.2. It has to be noted that the conventions introduced below are specific to this section.

5.6.1 Explanations of the Barlow test

The value of one criterion in the default selection is slightly changed and the observables of interest, in this case the SCs and NSCs, are measured with this new selection. From now on, a criterion which is not set to its default value is called a *trial*, and the results obtained with the default (varied) selection are indicated with the index *def* (*var*). Furthermore, the variable "SC" represents any combination of SC(k, l, m), but also of NSC(k, l, m).

From the results measured with the default and the trial selection, their absolute variation or *difference* is defined as

$$\mathrm{Diff} \equiv \mathrm{SC}_{var} - \mathrm{SC}_{def}. \tag{5.4}$$

Furthermore, the default and varied datasets are correlated. This means that if the selection for the given trial is tightened, the resulting sample will contain less of the data from the default

sample. On the other hand, if the selection is loosened, the inverse holds true and the final sample will contain more data than the one for the default selection. This effect is acknowledged in the computation of the *error on the difference*

$$\text{Error} \equiv \sqrt{|\sigma_{var}^2 - \sigma_{def}^2|}, \tag{5.5}$$

where σ_x represents the statistical error on SC_x obtained via the bootstrap method described in Section 5.5, where $x = def, var$. It has to be noted that if the two initial data samples are fully uncorrelated, the quadratic sum must be taken instead in the expression of the error (Eq. (5.5)). This case is not present in the trials studied here.

The *Barlow* σ can then be used to estimate how statistically significant the observed deviations are. It is defined as

$$\sigma_{\text{Barlow}} \equiv \frac{\text{Diff}}{\text{Error}}. \tag{5.6}$$

A value of σ_{Barlow} larger than a certain chosen value is then interpreted as a sign of systematic deviation and the corresponding trial is included in the calculation of the final systematic error. In this analysis, the number of required σ_{Barlow} is set to one, which is the most commonly used value in ALICE.

The error to attribute is obtained with this last variable, the *relative variation* between the results with the default and the varied selections,

$$\text{Relative Var} \equiv \frac{\text{Diff}}{\text{SC}_{def}}. \tag{5.7}$$

This value can then be taken as a percentage of error on the value of SC_{def} itself. Once all the individual contributions to the systematic errors are gathered, the final overall uncertainty is obtained by taking their quadratic sum.

All the variables listed above are measured for each centrality range individually. Furthermore, as visible in the experimental results presented in Section 6.2, the statistical errors are dominant in the analysis. This fact can lead to difficulties in the determination of if a trial has a systematic effect or not. More precisely, SC_{var} may be in agreement with SC_{def} within statistical uncertainties, and thus the resulting σ_{Barlow} is artificially below one. To palliate for this issue, the differential representation is supported with the integrated versions of the variables from Eqs. (5.4)–(5.7). To compute them, the results for the SC must first be rebinned for the analysed centrality range, with the help of the method presented in Ref. [166]. This rebinning allows to increase the total statistics of the sample and therefore to reduce the width of the statistical uncertainties. Using the same notation introduced in the first part of this section, the weight average, or *integrated result* for a given SC is defined as

$$\widehat{\text{SC}}_i = \frac{\sum_{j=1}^{N} \text{SC}_{i,j}/\sigma_{\text{i,j}}^2}{\sum_{j=1}^{N} 1/\sigma_{\text{i,j}}^2}, \qquad i = def, var, \tag{5.8}$$

where N is the number of centrality bins included in the rebinning, i.e. the number of points in the differential representation of the Barlow test. The variance on $\widehat{\text{SC}}_i$ is calculated with

$$\widehat{\text{Var}}_i = \frac{1}{\sum_{j=1}^{N} 1/\sigma_{\text{i,j}}^2}, \qquad i = def, var. \tag{5.9}$$

This leads to an estimation of the rebinned statistical error given by

$$\widehat{\sigma}_i = \sqrt{\widehat{\text{Var}}_i / N}, \qquad i = def, var. \tag{5.10}$$

The attribution of the systematic uncertainty for a trial is done in the following way. The integrated Barlow variables are used as the key element to determine if a trial needs to be included in the final systematic uncertainties. The individual errors are obtained from the differential representation. Two effects need to be taken into account. Firstly, the final measurements for a given SC(k, l, m) are spread on several orders of magnitude. Secondly, the values and errors in the central collisions are small, leading to an increased probability to present artifacts for the σ_{Barlow} and the relative variation. Based on these, two different estimations are used. For the measurements in the central ranges 0–5%, 5–10% and 10–20%, the absolute variation is taken as the raw systematic error for the trial. For the semicentral results (20–50%), the smoothed relative variation (i.e. the arithmetic average between the data points[2]) is used instead. As the measurements of SC$(2, 4, 6)$ and SC$(3, 4, 5)$ cover the centrality range 0–30%, the absolute variation is also used in the centrality bin 20–30% for these two observables.

5.6.2 Example of systematic analysis: SC$(2, 3, 4)$

This section gathers the outcomes of each trial for the observable SC$(2, 3, 4)$ as an example of the method described above. The corresponding attributed errors are summarised in Table 5.3. The tables for the other observables can be found in Appendix E. The corresponding figures can be found in the ALICE internal analysis notes in Ref. [167].

Table 5.3: Summary of the systematic uncertainties for each trial for the observable SC$(2, 3, 4)$. The columns 0–5%, 5–10% and 10–20% summarise the absolute variations, while 20–50% contains the relative variations (see text). An en-dash "—" indicate a trial without a statistically significant deviation.

Trial	**0–5%**	**5–10%**	**10–20%**	**20–50%**	**Figures**
Centrality	1.61×10^{-13}	-4.82×10^{-13}	1.86×10^{-12}	15.3%	5.19
PV_z	-2.58×10^{-13}	-3.21×10^{-13}	-7.15×10^{-13}	3.3%	5.20
N_{TPC}	-2.87×10^{-13}	-7.50×10^{-13}	-1.18×10^{-12}	5.0%	5.21
χ^2/NDF	—	—	—	—	5.22
DCA_{xy}	-1.17×10^{-13}	-9.65×10^{-14}	5.02×10^{-13}	19.7%	5.23
DCA_z	—	—	—	—	5.24
++/- -	—	—	—	—	5.25
Filter	5.65×10^{-13}	9.69×10^{-14}	2.61×10^{-12}	3.8%	5.27
Overall	7.13×10^{-13}	9.57×10^{-13}	3.53×10^{-12}	25.9%	

Centrality

The default centrality estimation in this work is done with the SPD clusters $CL1$. The trial is thus established by changing the centrality estimator in Table 5.1 to a second estimator, the V0M. No other modifications are needed as the "triangle" employed to parametrise the criteria for the rejection of the HMOs present the same shape and inclination with the two estimators (Fig. 5.5). Figure 5.19 summarises the outcome of the Barlow test in this case. The number of σ_{Barlow} for the integrated results is $\sigma_{\text{Barlow}} \sim 2$. Combined to the σ_{Barlow} oscillating between -2 and 2 in the differential view, this means this trial must be included in the systematic uncertainties.

[2] If a centrality presents a relative variation highly different from the others due to artifacts, it is excluded from the averaging.

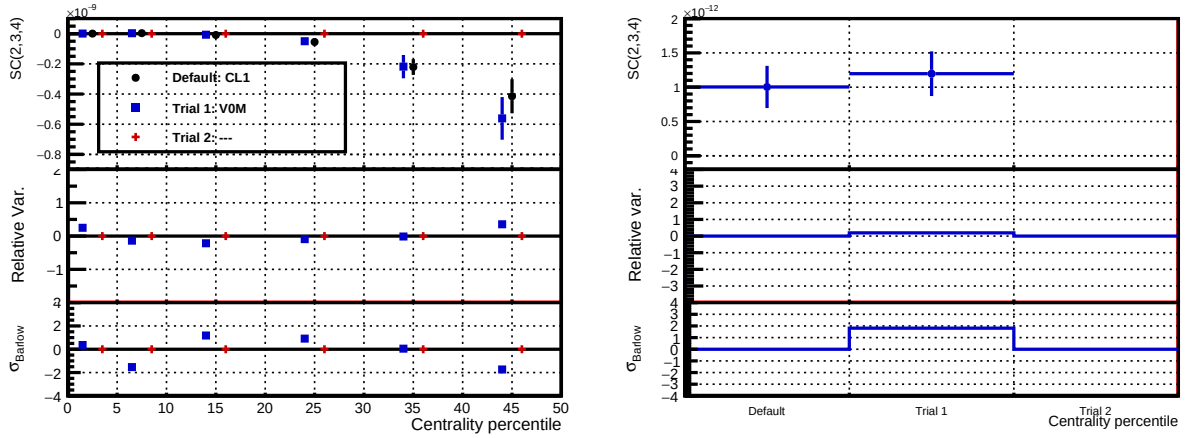

Figure 5.19: Differential (*left*) and integrated (*right*) Barlow test for SC(2,3,4) for the centrality estimation.

Primary vertex

The systematic trials considered here are $|PV_z| < 6$ cm and $|PV_z| < 12$ cm, compared to the default $|PV_z| < 10$ cm. The results are shown in Fig. 5.20. The integrated view shows a σ_{Barlow}

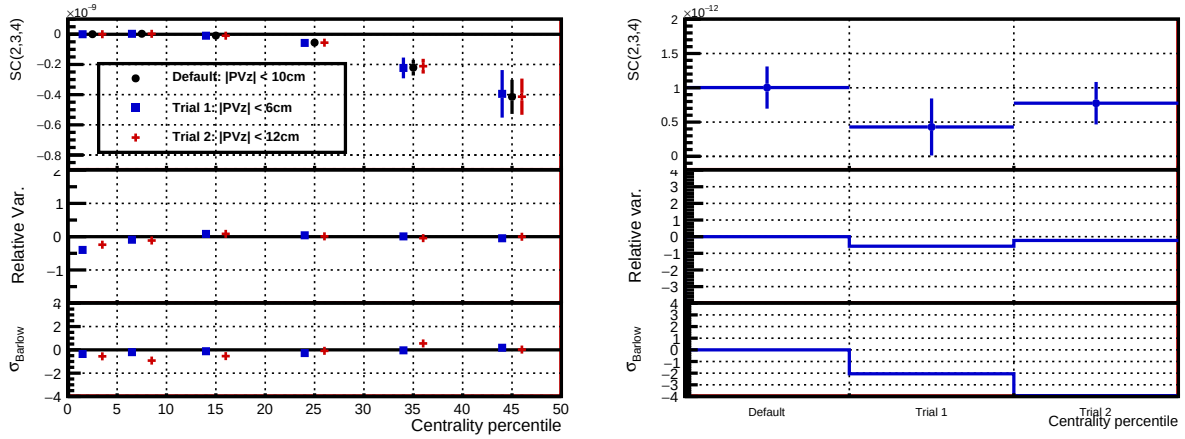

Figure 5.20: Differential (*left*) and integrated (*right*) Barlow test for SC(2,3,4) for the primary vertex.

higher than one for the two trials. Furthermore, the relative variations in the differential representation present values which can reach nearly 50% in central collisions. It has been therefore decided to add the second trial into the list of contributions to the systematic uncertainties.

Number of TPC clusters and χ^2/ndf

The decision on the minimum number of space points in the TPC needed for a track to be acceptable can be seen as a compromise between two factors. As stated in Section 5.2, the more points a track possesses, the better it can be reconstructed. However, setting the minimum requirement with a higher value will bias the selection towards the high-momentum straight tracks. In this analysis, the default selection is generally fixed to 70, which is a commonly accepted value in ALICE. The systematic trials are then obtained by relaxing this value to 50 and tightening to 100 (Fig. 5.21). It has to be noted that 50 is the minimum requirement set

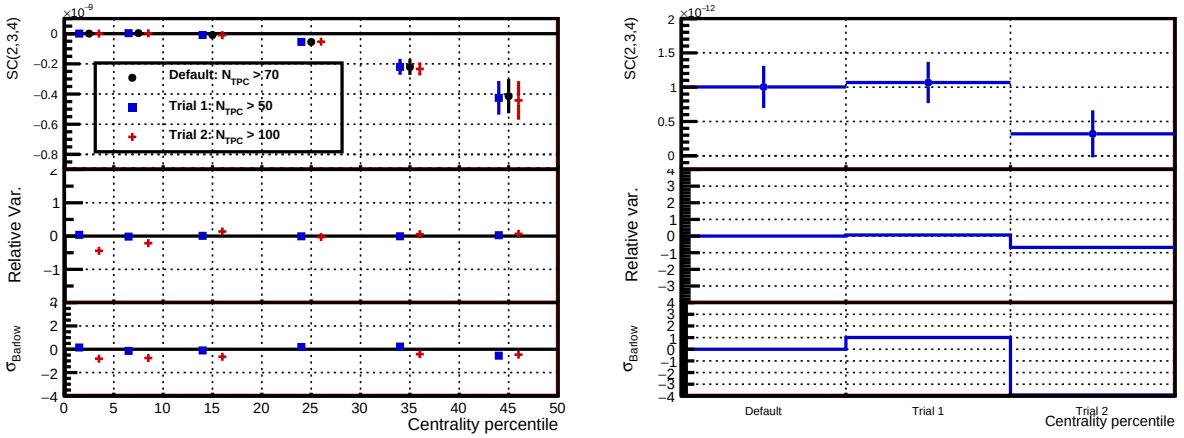

Figure 5.21: Differential (*left*) and integrated (*right*) Barlow test for SC(2,3,4) for the number of TPC clusters.

during the filtering of the TPC-only tracks. It has been decided to include the second trial into the contributions to the overall systematic error, as its has a σ_{Barlow} larger than 1 for the integrated view, and systematically negative in the differential one.

Concerning the χ^2/ndf, the default range $[0.1, 4.0]$ is varied to $[0.3, 4.0]$ as a first trial, and to $[0.1, 3.5]$ as a second trial. Both trials present extremely small σ_{Barlow} for all centralities in Fig. 5.22, therefore this check is not included in the list.

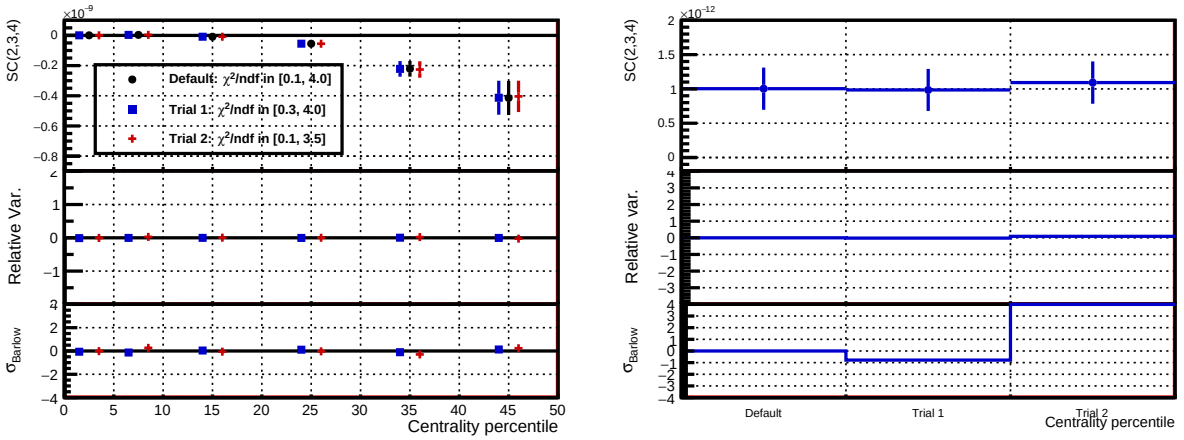

Figure 5.22: Differential (*left*) and integrated (*right*) Barlow test for SC(2,3,4) for χ^2/ndf.

Distance of closest approach

The variations of the criteria on the distance of closest approach has an effect on the rejection of tracks whose origin is too far from the primary vertex, and thus, it directly affects the contribution from the secondary particles from weak decays for example. Figure 5.23 summarises the results of tightening the default criterion $|DCA_{xy}| < 2.4$ cm to 1 and 2 cm, while Fig. 5.24 does the same for the variation from $|DCA_z| < 3.2$ cm to 2.1 cm. A statistically significant deviation is observed only for DCA_{xy}.

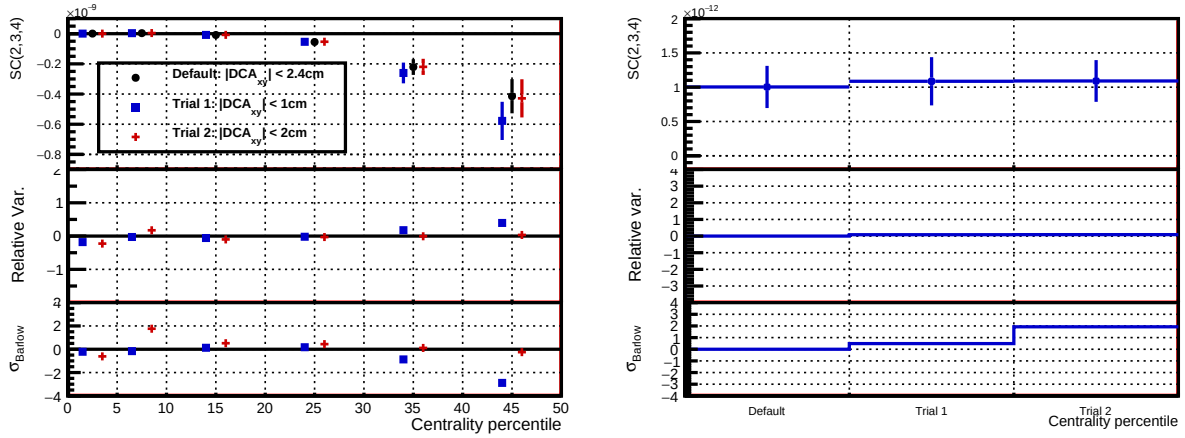

Figure 5.23: Differential (*left*) and integrated (*right*) Barlow test for SC(2,3,4) for the DCA in the transverse plane.

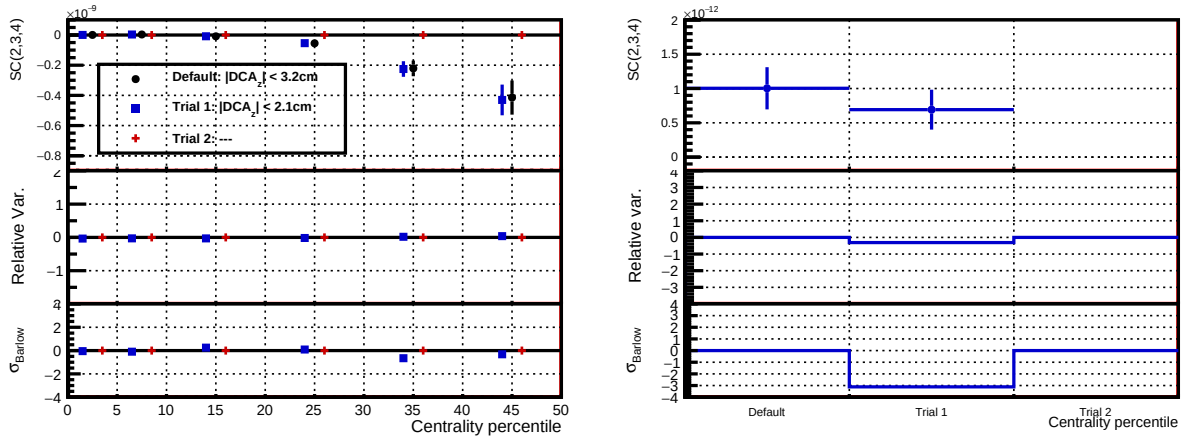

Figure 5.24: Differential (*left*) and integrated (*right*) Barlow test for SC(2,3,4) for the DCA along the beamline.

Magnetic field

The two configurations of the solenoid magnet in ALICE are included in the default analysis. As a systematic check, the 88 good runs of the data sample are divided between the ones measured with the polarity of the magnet "++" and the ones with the polarity "- -". The results are obtained for each one of these subsamples and compared to the default study in Fig. 5.25. Despite the large relative variations, no systematic trend can be seen. Therefore, no systematic variation has been attributed to this observable.

Filterbit

The last systematic observable that is considered here is the choice of filtering conditions that are applied in the transition from ESD to AOD files. As stated in Table 5.2, the results are obtained by default with TPC-only tracks. To determine the effects coming from the filtering, a trial is conducted using hybrid tracks with the filterbit 768. This filter is the combination of two different filters: the global hybrid tracks (filterbit 256) and the complementary hybrid tracks (filterbit 512). These filters combine the information from the ITS and the TPC, but

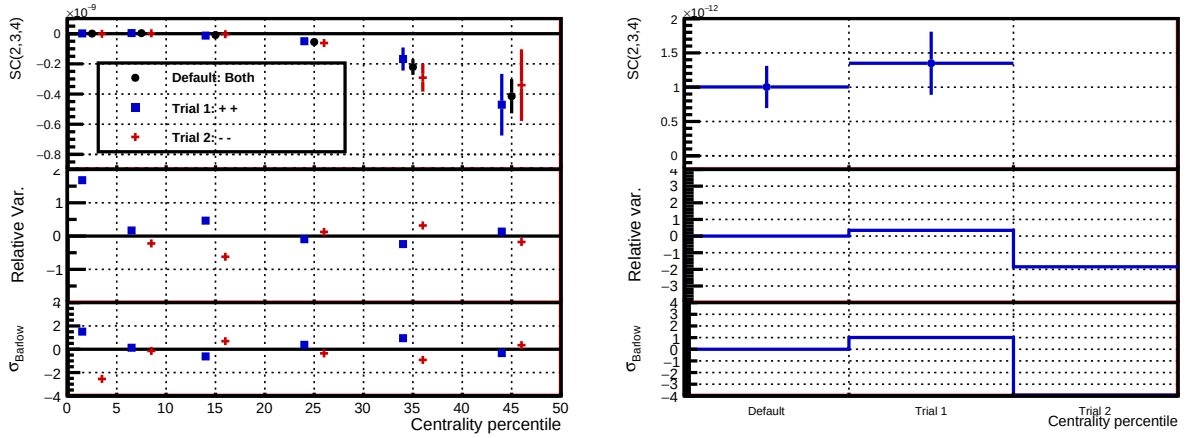

Figure 5.25: Differential (*left*) and integrated (*right*) Barlow test for SC(2,3,4) for the polarity of the solenoid magnet.

lead to a severely non-uniform azimuthal distribution. To palliate some of this effect, the hybrid filter 768 has been designed. Furthermore, the addition of the ITS allows the removal of a more important portion of the secondary tracks.

However, as the filter used in the analysis is also used in this case to reject the HMOs, these latter criteria have to be adapted. As shown in the left panel of Fig. 5.26, the parametrised lines defined for TPC-standalone tracks reject an important part of the healthy events originating from the two-dimensional correlations between hybrids and global hybrids. The parametrisation

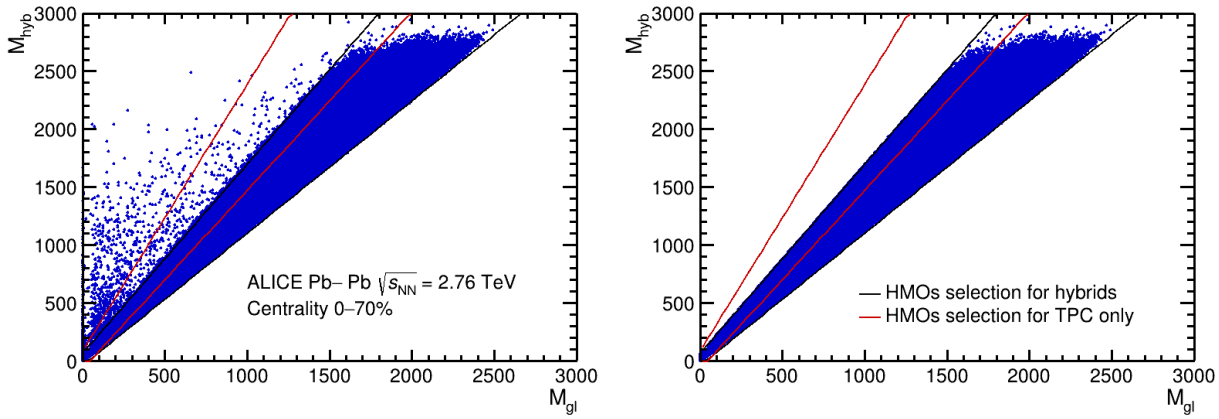

Figure 5.26: Correlation histogram for the multiplicity of the hybrid tracks (filterbit 768, M_{hyb}) and the global hybrid tracks (filterbit 256, M_{gl}) after the selection on PV_z before (*left*) and after (*right*) application of the criteria to reject the HMOs. The black (red) lines show the criteria obtained for hybrid (TPC-only) tracks.

is therefore changed to the following selection criteria:

$$\text{Minimum boundary for the high multiplicity outliers}: M_{hyb} \geq 1.14 M_{gl} - 35.00,$$
$$\text{Maximum boundary for the high multiplicity outliers}: M_{hyb} \leq 1.63 M_{gl} + 70.00,$$

where M_{hyb} (M_{gl}) is the multiplicity of (global) hybrid tracks in a certain event.

The results of the systematic trial for the hybrid tracks is shown in Fig. 5.27. A significant variation can be observed, meaning this trial is included in the overall uncertainty on SC(2, 3, 4).

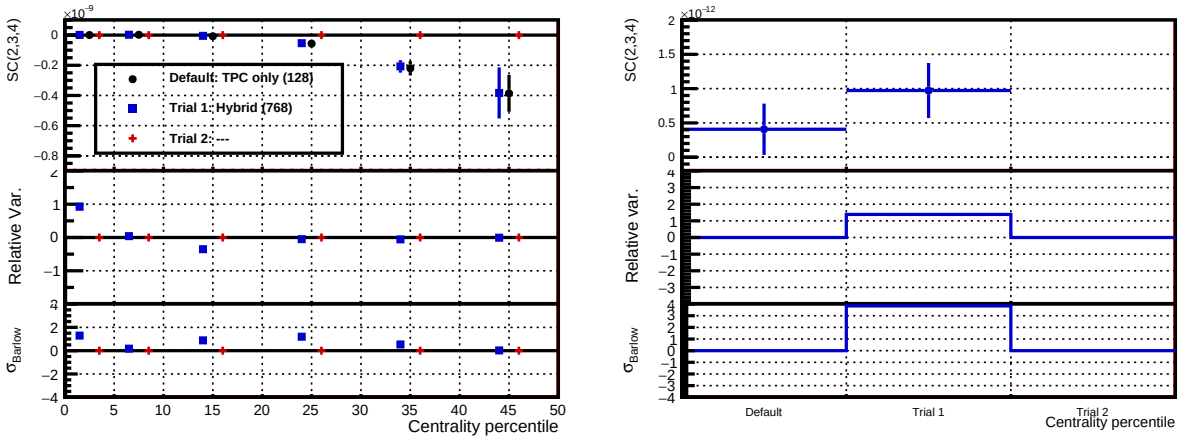

Figure 5.27: Differential (*left*) and integrated (*right*) Barlow test for SC(2,3,4) for the filterbit.

Chapter 6

Experimental Results and Theoretical Calculations

This last chapter is divided into three main parts. The first one, Section 6.1, describes the theoretical models used in this work. Section 6.2 shows the experimental results for the three-harmonic SCs measured with ALICE and compared to theoretical calculations from EKRT and iEBE-VISHNU. Finally, the first predictions for the ACs are presented in Section 6.3. Furthermore, if not stated otherwise, the errors bars represent the statistical uncertainties of the measurements and the coloured boxes their systematic uncertainties.

6.1 Theoretical models

This section summarises the details about the theoretical models used through this work, either to check properties of the proposed observables, either to get predictions at initial and final states. In the latter case, the comparisons of these predictions to the experimental results allow a better fine-tuning of the input parameters of the models or the development of brand new ones.

6.1.1 HIJING

One of the principal models widely used in this analysis is HIJING [72, 73], already mentioned in Section 1.4 and in Chapters 4 and 5. HIJING is a MC event generator designed for the studies of the jet and multiparticle production in high energy nuclear collisions (pp, p–A, A–A) and the exploration of various ranges of initial conditions which may happen in high energy nuclear collisions. It contains descriptions of mechanisms like soft beamjets, multiple minijet production, a model for jet quenching, and a parton structure dependent on the impact parameter of the collision for nuclear shadowing studies. Additionally, the dependence on the inelastic processes number on the impact parameter is expressed based on the geometry of the nuclei. These features are formulated based on various models like the Lund FRITIOF and the dual parton model for the description of nuclear collisions at centre of mass energy $\sqrt{s_{\mathrm{NN}}} \leq 20$ GeV/u, and pQCD in PYTHIA for the hadronic interactions. This combination of pQCD to nuclear effects and jet-related processes gave to HIJING a major role in nuclear collisions studies, as semihard phenomena were expected to become central at the RHIC and LHC energies. Furthermore, HIJING makes also a link between the physics at the SPS, dominated by non-perturbative fragmentation, and the pQCD found in the higher energies colliders.

While all these points above show the use of HIJING as a prediction and analysis tool for jet

and more widely nuclear physics, its role in flow analysis is slightly different. All the mechanisms described in HIJING introduce correlations between only a few particles in the system. As flow, as a collective effect between all the produced particles, is not present in HIJING, this generator can be used to test the robustness of newly designed flow observables against nonflow, like the SCs (Section 4.1.5) and the ACs (Section 4.2.4). Moreover, its second role in this work has the estimation of the p_{T}-weights for the NUE corrections as described in Section 5.3.

The HIJING simulations used here are the LHC11a10a_bis ALICE production anchored to the LHC10h Pb–Pb data at $\sqrt{s_{\mathrm{NN}}} = 2.76$ TeV, as mentioned in Section 3.2.4. For the AOD 162 filtering, the list of runs selected for the analysis is the same as the one for the experimental data (see Appendix D). The details of the event and track selections applied at reconstruction level for the robustness against nonflow of the SCs and ACs can be found in Tables 5.1 and 5.2.

6.1.2 EKRT

One of the models used to get theoretical predictions of the higher-order SCs is the event-by-event Eskola-Kajantie-Ruuskanen-Tuominen (EKRT) model [118, 168]. The initial conditions, for example the initial energy density profiles, are computed using an event-by-event next-to-leading-order (NLO) combination of pQCD and saturation model for the gluon production. Elliptic flow has been originally described using (2+1)D ideal fluid dynamics. The NLO-extension introduced viscous hydrodynamics descriptions among other elements. This state-of-the-art model is well known for its various parametrisations of the temperature dependence of the η/s, tuned to reproduce measurements of v_n for the full centrality range in heavy-ion collisions (see bottom panels of Fig. 1.19). It is also able to predict with good agreement the charged hadron multiplicity and spectra in the low-p_{T} region at RHIC and LHC energies. More examples of predictions with the different parametrisations of the NLO-extension of EKRT can be found in Ref. [118].

The theoretical predictions for the three-harmonic SCs have been obtained with a sample of 40k events for the centrality range 0–100%. Two different parametrisations of $\eta/s(T)$ have been initially studied: $\eta/s(T) = 0.2$ and $\eta/s(T) =$ "param1" (Fig. 1.19). This latter tuning is characterised by a lower temperature of about 150 MeV of the transition from the hadronic to the QGP phase [118, 169]. The slope is linearly decreasing in the hadronic phase, while the opposite behaviour is seen above the phase transition. These two parametrisations have been chosen as they are the ones with the best predictions of the lower order SCs. This can be seen, for instance, in Fig. 2 of Refs. [114, 116], also visible in Section 1.5. As they gave similar descriptions of all the studied combinations of SCs and NSCs, only the predictions obtained for the "param1" tuning are presented in the experimental part of the analysis (Section 6.2).

6.1.3 $\mathrm{T_R}$ENTo

The Reduced Thickness Event-by-event Nuclear Topology ($\mathrm{T_R}$ENTo) model [170] is one of the two models used for the initial conditions of the hydrodynamic model iEBE-VISHNU (see Section 6.1.4). It has been introduced for the study and constraint of the initial state of high-energy pp, p–A and A–A collisions. Its name comes from its key concept: the participant thickness of each projectile involved in the collision. The supposition is then made that there is a scalar field, dependent on the thickness of the two projectiles, which proportionally relate them to the entropy production. $\mathrm{T_R}$ENTo is, therefore, an effective model for the generation of realistic MC entropy profiles for the initial conditions. It also contains no assumption on the physical mechanisms that intervene in the entropy production, the pre-equilibrium dynamics or the thermalisation phase.

It has to be noted that $\mathrm{T_R}$ENTo depends on a dimensionless parameter p, which can take

any real value. According to this value of p, different physical mechanisms governing the entropy production can be described. For example, $p = 1$ reduces T$_\mathrm{R}$ENTo to a MC-Glauber model with wounded nucleons, or if p is negative, the deposition of entropy is completely suppressed in the direction of the impact parameter. In the simulations used in this work, this parameter is set to $p = 0.007$, as this tuning has been shown to reproduce with good agreement previous experimental measurements.

6.1.4 iEBE-VISHNU

The second theoretical model used for predictions of the SCs is iEBE-VISHNU [171]. This MC event generator simulates the hydrodynamic evolution of the heavy-ion collision. As seen in Section 1.4, models based on hydrodynamics computations need initial conditions as an input. iEBE-VISHNU calculates then the initial energy density evolution using a combination of 2+1 causal hydrodynamics and an equation of state itself a union of lattice QCD and hadronic resonance gas model [172]. The final distributions of fluid are then converted into distributions of hadrons through the application of the Cooper-Frye formula [173]. It has to be noted that iEBE-VISHNU directly returns as its output the flow amplitudes and symmetry planes in each event, meaning they don't need to be estimated afterwards with correlations techniques.

The first theoretical predictions obtained for the three-harmonic SCs have been obtained using MC-Glauber as initial conditions for iEBE-VISHNU. The final state results have then been obtained with the output of the hadronisation phase. More details about the tuning and the obtained results can be found in Ref. [117]. However, a distinct set of predictions has been used for the results published in Ref. [169] and presented in this thesis. There, the initial energy density comes from the T$_\mathrm{R}$ENTo model described above. This distribution is then connected to iEBE-VISHNU and the hadron distributions obtained at the end of this procedure are let evolved through the UrQMD model [174, 175]. Finally, a global Bayesian analysis is employed to extract the initial conditions and free parameters of the full model. It has to be further noted that, in the case of the ACs, predictions for the two configurations of iEBE-VISHNU have been employed.

6.1.5 *MuPa Monte Carlo Glauber* model

The last model presented here is the *MuPa MC-Glauber* model. This version of the MC-Glauber model presented in Section 1.3 has been developed locally, mainly based on Ref. [60]. The main conception steps about the implementation of this model can be found in Ref. [176]. However, the current work employed an updated version of the model, with the following changes compared to the implementation described in said reference. First, the minimal distance previously set to 0.8 fm has been changed to 0.4 fm according to Ref. [177]. Furthermore, the impact parameter is now randomly selected following a linear distribution in the range 0–20 fm. Finally, the output of the simulations is saved event-by-event and the needed all-event averages can be computed in the post-processing step of the analysis.

The simulated data used in this work have been obtained with the following configuration of the parameters. The lead ions are simulated with a radius $R_A = 6.67$ fm and a surface width parameter $\xi = 0.44$ fm. The centre of mass energy is set to $\sqrt{s_{\mathrm{NN}}} = 2.76$ TeV as in the LHC Run 1. Two values for the inelastic nucleon-nucleon cross section are investigated: $\sigma_{\mathrm{NN}}^{\mathrm{inel}} = 6.4$ fm^2 from Ref. [162] and the $\sigma_{\mathrm{NN}}^{\mathrm{inel}} = 6.18$ fm^2 from the more recent Ref. [177].

6.2 Higher order Symmetric Cumulants in ALICE

The results shown in this section are derived from the ones released in Ref. [169]. While the formalism introduced in Section 4.1 can be applied to any number of flow harmonics, this experimental analysis is focused only on the case of three different amplitudes. This choice is motivated by the fact this is the next natural step after the studies of the two-harmonic SCs [114, 116]. Moreover, as it will be illustrated later in this section, the volume of data in the LHC10h sample is sufficient to get first meaningful predictions of the $\mathrm{SC}(k,l,m)$, but not enough to get reasonable statistical uncertainties in peripheral collisions.

6.2.1 Interpretation of the experimental results

The two panels of Fig. 6.1 present the centrality dependence of $\mathrm{SC}(k,l,m)$ and $\mathrm{NSC}(k,l,m)$ for different combinations of flow magnitudes. The results for $\mathrm{SC}(2,3,4)$ (black circles) and $\mathrm{SC}(2,3,5)$ (blue squares) are non-zero. They show an increase in magnitude with the centrality, although with opposite signs. It has to be stressed out that these are the first measurements of genuine correlations between more than two flow amplitudes. Furthermore, they have the potential to constrain the non-linear response in the higher flow harmonics. It has been shown that both ε_2 and ε_3 contribute in the expansion of v_5, while only ε_2^2 plays a role in v_4 (see Section 1.4). This implies that the genuine correlations observed in $\mathrm{SC}(2,3,5)$ — where all the harmonics are related through the non-linear response $v_5 \sim \varepsilon_2\varepsilon_3$ — and in $\mathrm{SC}(2,3,4)$ — where ε_3 is not linked to v_4 — are expected to come from different physics mechanisms. This latter point has also an impact on the NSCs themselves. The negative slope visible in $\mathrm{SC}(2,3,4)$ can be found in $\mathrm{NSC}(2,3,4)$ as well, while the positive trend of $\mathrm{SC}(2,3,5)$ is not present in $\mathrm{NSC}(2,3,5)$. Finally, it has to be noted that, in opposition to the previous methods used to constrain the non-linear response [178], the new information from the higher order SCs do not require any hypothesis on the nature of the two-harmonic correlations.

In the case of the correlations with higher order flow harmonics, the measurements for $\mathrm{SC}(2,4,6)$ and $\mathrm{SC}(3,4,5)$ are both in agreement with zero for the analysed centrality range. Two major points can be raised from this observation. These results could not have been predicted from the measurements between each pair of harmonics in $\mathrm{SC}(m,n)$. Moreover, they imply that the three-harmonic correlations (and not the three-harmonic cumulants) can be decomposed into a superposition of their respective two-harmonic measurements.

Another element of the SCs that can be studied is their signature. In the case of the two-harmonic SCs, v_m and v_n are said to be (anti-)correlated if the corresponding $\mathrm{SC}(m,n)$ is (negative) positive. The consequence of this sign on the relation between v_m and v_n (see Section 1.5) can then be easily understood by rewriting Eq. (2.62) as

$$\mathrm{SC}(m,n) = \left\langle \left(v_m^2 - \left\langle v_m^2 \right\rangle\right)\left(v_n^2 - \left\langle v_n^2 \right\rangle\right)\right\rangle . \tag{6.1}$$

This formulation means that, for $\mathrm{SC}(m,n) > 0$, if $v_m^2 > \langle v_m^2 \rangle$ is found in an event, there is an increased probability to find $v_n^2 > \langle v_n^2 \rangle$ in the same event. This pattern is denoted by $(+,+)$. The same logic applies as well in the case of the negative signs, leading to the pattern $(-,-)$. Moreover, $\mathrm{SC}(m,n) < 0$ leads to the two patterns $(+,-)$ and $(-,+)$.

This concept can then be generalised to the situation with three different harmonics. There, Eq. (4.1) can be rewritten under the form

$$\mathrm{SC}(k,l,m) = \left\langle \left(v_k^2 - \left\langle v_k^2 \right\rangle\right)\left(v_l^2 - \left\langle v_l^2 \right\rangle\right)\left(v_m^2 - \left\langle v_m^2 \right\rangle\right)\right\rangle . \tag{6.2}$$

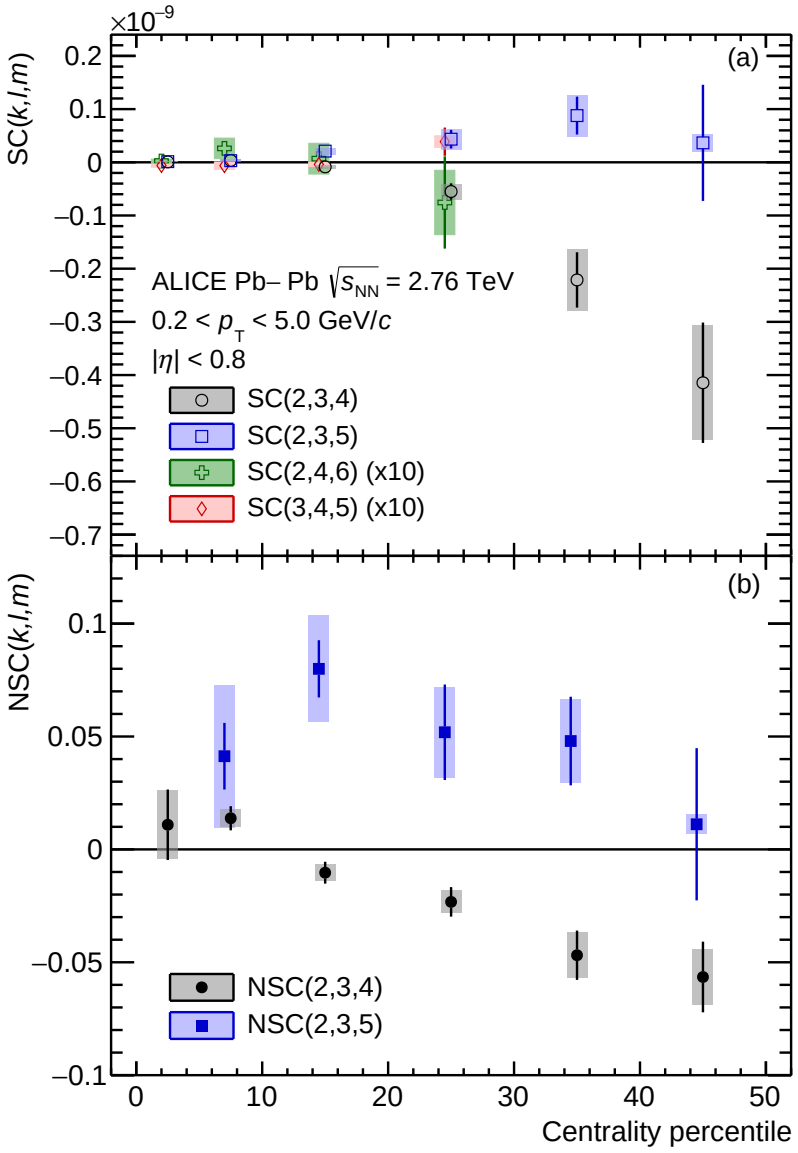

Figure 6.1: Centrality dependence of several combinations of flow amplitudes for $\mathrm{SC}(k,l,m)$ (a) and $\mathrm{NSC}(k,l,m)$ (b) in Pb–Pb collisions at $\sqrt{s_{\mathrm{NN}}} = 2.76$ TeV with ALICE [169].

The reasoning used in the previous case can again be applied here. Only the patterns $(+,+,+)$ and $(+,-,-)$ are allowed if $\mathrm{SC}(k,l,m) > 0$, with $(+,+,+)$ the notation for "if for an event $v_k^2 > \langle v_k^2 \rangle$ and $v_l^2 > \langle v_l^2 \rangle$ are found, then there is an enhancement of the probability to find $v_m^2 > \langle v_m^2 \rangle$". Furthermore, if $\mathrm{SC}(k,l,m) < 0$, then only the patterns $(+,+,-)$ and $(-,-,-)$ are possible. Finally, it has to be noted that only the two- and the three-harmonic SCs can be rewritten in these forms. For four and more harmonics, this is not possible anymore.

The signatures of the combinations of harmonics shown in Fig. 6.1 are persistent within uncertainties for the full centrality range. This implies that the relations between the three harmonics could only vary between two possible event-by-event patterns as a function of the centrality.

More importantly, these signatures give also new information, which cannot be extracted from the previous two-harmonic measurements. The observable $\mathrm{SC}(2,3,4)$ is taken here as an

example of this argument. The pairs of harmonics that can be created with v_2, v_3 and v_4 are SC(3, 2), SC(4, 2) and SC(4, 3). It is known from the previous systematic studies on the two-harmonic SCs in Ref. [116] that they follow the patterns $(+,-)$, $(+,+)$ and $(+,-)$ respectively (Fig. 6.2). These sequences would lead to the two possible three-harmonic patterns $(+,+,-)$ and

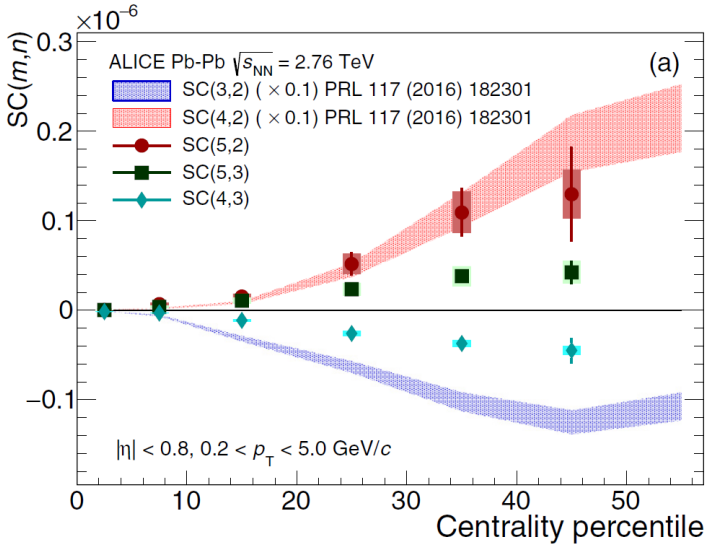

Figure 6.2: Centrality dependence of various combinations of two-harmonic Symmetric Cumulants [116].

$(+,-,-)$ (from the permutation of $(-,+,-)$) and therefore, the sign of the resulting SC(2, 3, 4) could be either negative or positive. However, the measurements of SC(2, 3, 4) clearly indicate a negative sign, hence the newly accessible information.

6.2.2 Comparison with hydrodynamic predictions

The experimental results presented above can now be compared with the predictions from the theoretical models introduced in Section 6.1 (Fig. 6.3). Both the EKRT (blue band) and the iEBE-VISHNU (black band) models can describe the overall trend of all the analysed observables in the centrality dependence. However, it has to be noted that they predict SC(2, 4, 6) to be strictly positive when the data are compatible with zero. Quantitatively, EKRT is found to be in better agreement for SC(2, 3, 4) (panel (a)) and SC(2, 3, 5) (panel (c)) than iEBE-VISHNU where the two observables are underestimated. The predictions for their normalised counterparts are, however, in better agreement with the data and the results from EKRT.

As stated in Chapters 2 and 4, it is possible to compare the predictions at initial and final states to get information about the hydrodynamic non-linear response. The explanation for this argument is the following. As seen in Section 1.4, if the values of the eccentricities ε_n are small, it is possible to relate them to the flow amplitudes with $v_n = k_n \varepsilon_n$. For the elliptic $n = 2$ and the triangular $n = 3$ harmonics, this approximation is sufficient. However, for higher order harmonics, non-linear behaviour cannot be neglected. By doing the ratio between the SCs and the averages of the implied amplitudes, the linear components of the response cancel out. Any observation of a variation between the NSCs at initial state and final state is then a sign of non-linear response. Figure 6.3 also show the initial state of EKRT (pink band) and T$_\mathrm{R}$ENTo used as initial conditions for iEBE-VISHNU (green band) for NSC(2, 3, 4) and NSC(2, 3, 5). For both pairs of models, the difference between the two sets of predictions shows the development of genuine correlations between v_2, v_3 and v_4 during the hydrodynamic evolution of the QGP.

This behaviour is also hinted in the case of NSC(2, 3, 5).

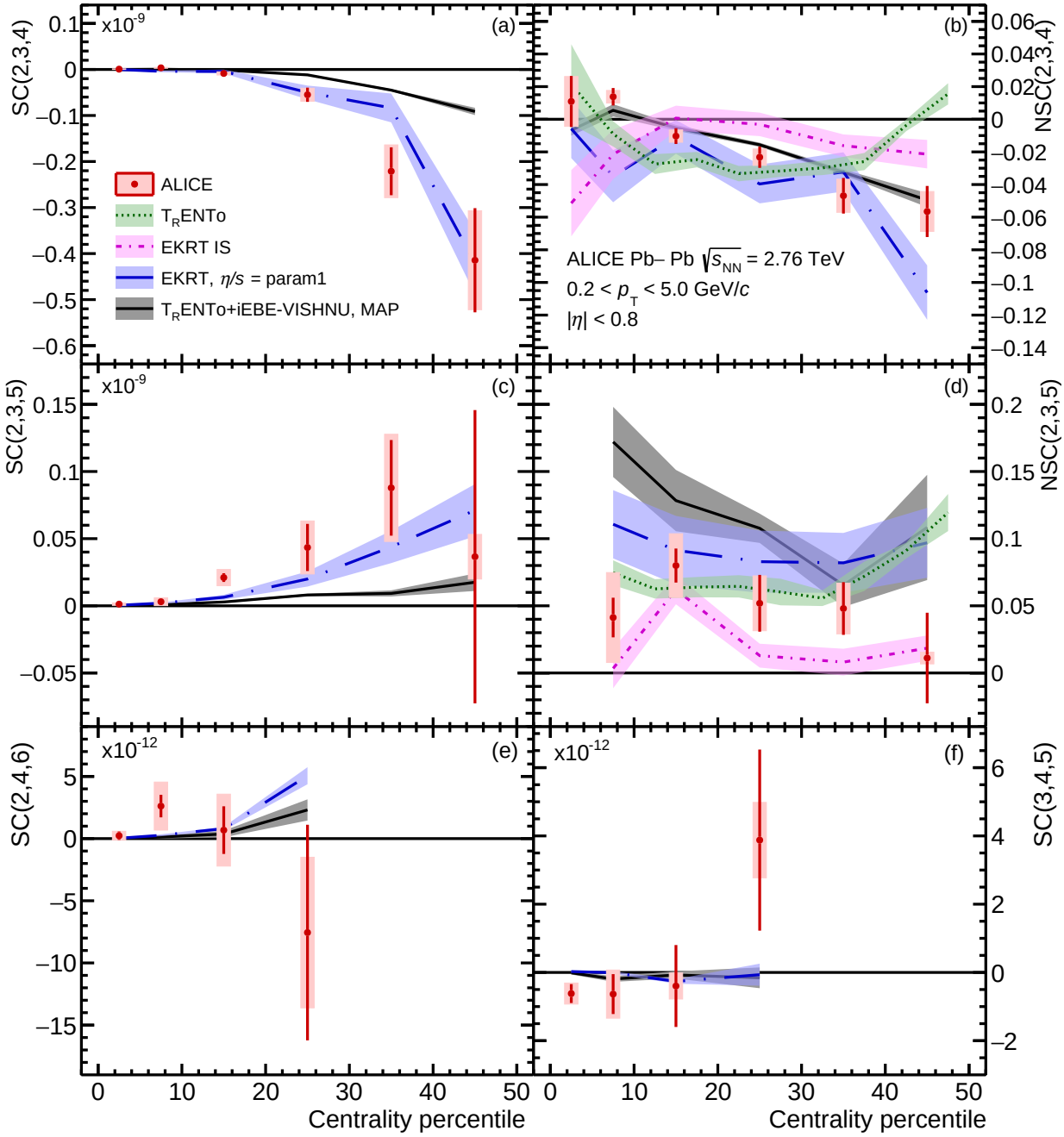

Figure 6.3: Predictions from the theoretical models for the centrality dependence of the SC(k, l, m) and NSC(k, l, m) shown in Fig. 6.1 [169].

6.3 Predictions for the Asymmetric Cumulants

This last section presents the first theoretical predictions obtained for various combinations of two-harmonic ACs. Some of the measurements shown here are presented in Refs. [125, 157].

6.3.1 Comparisons for the initial state

The predictions for various combinations of two-harmonic ACs are illustrated in Figs. 6.4–6.9. The panels in the left column show the results for the initial state, going from the lowest to the highest order of AC. Some global features can be distinguished for all combinations. The

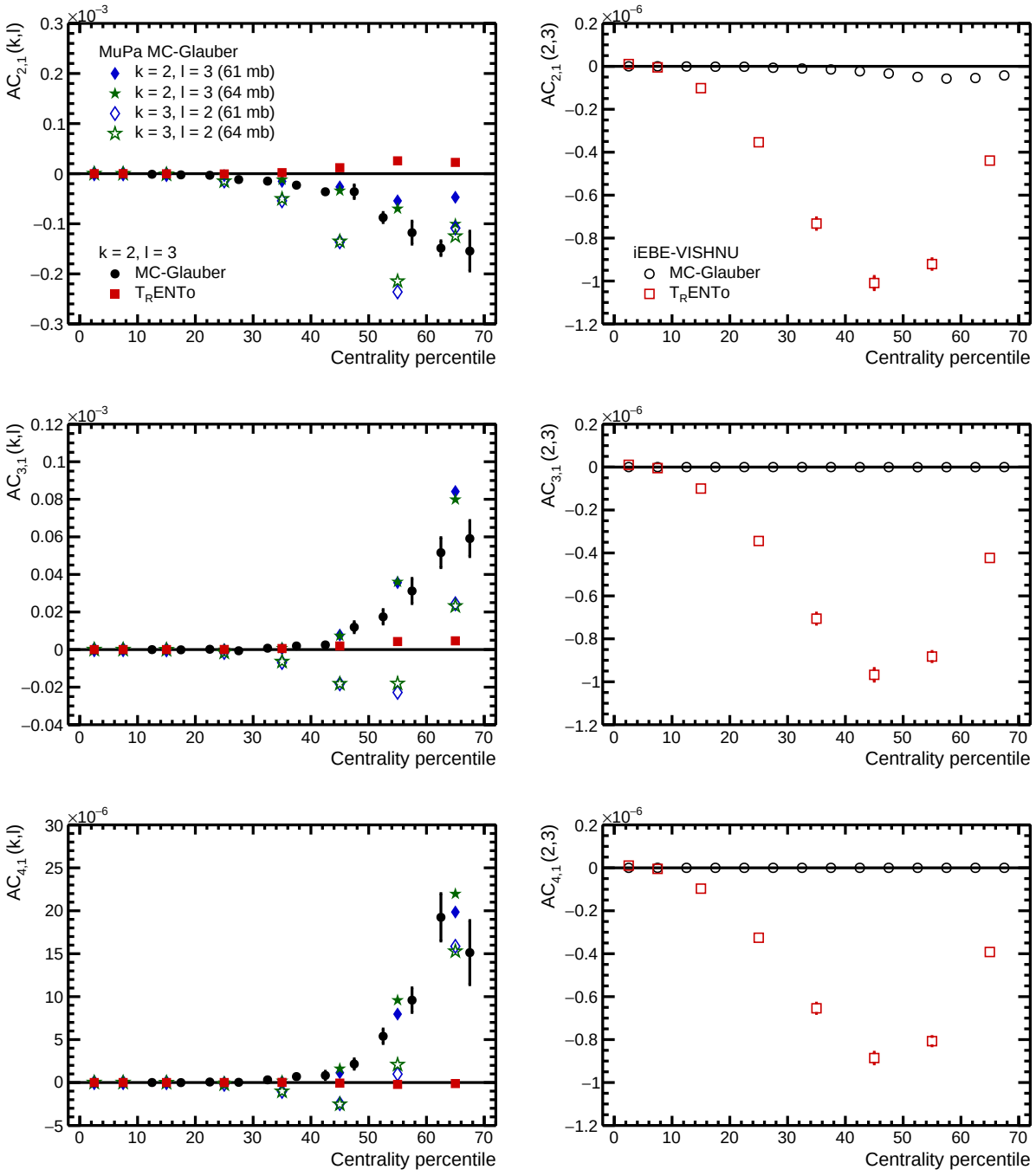

Figure 6.4: Predictions for the centrality dependence of the initial state (*left*) and the final state (*right*) of $\mathrm{AC}_{2,1}(2,3)$ (*top*), $\mathrm{AC}_{3,1}(2,3)$ (*middle*) and $\mathrm{AC}_{4,1}(2,3)$ (*bottom*). Results for MuPa-Glauber courtery of M. Lesch. Results for iEBE-VISHNU courtesy of S.F. Taghavi [125].

deviation from zero of the predictions from T$_\mathrm{R}$ENTo (red squares) is generally closer to zero

than the ones from the Glauber models (black, blue and green markers). A decrease of the amplitudes of the genuine correlations with the order of the AC is seen for all models. This can be explained by the fact that higher order ACs like $AC_{4,1}$ probe correlations with higher moments of the flow amplitudes.

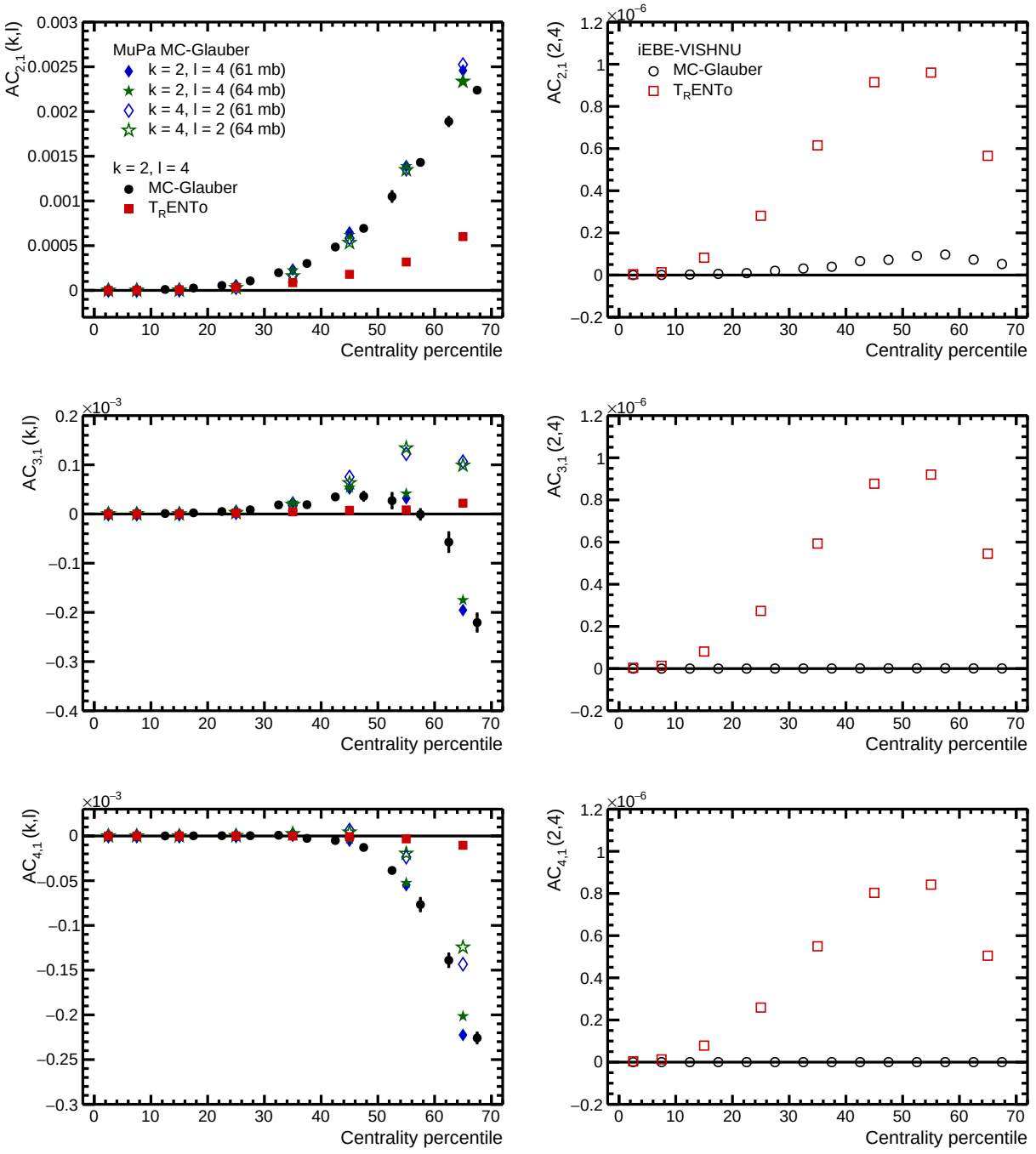

Figure 6.5: Predictions for the centrality dependence of the initial state (*left*) and the final state (*right*) of $AC_{2,1}(2,4)$ (*top*), $AC_{3,1}(2,4)$ (*middle*) and $AC_{4,1}(2,4)$ (*bottom*). Results for MuPa-Glauber courtery of M. Lesch. Results for iEBE-VISHNU courtesy of S.F. Taghavi [125].

For some of the proposed combinations of amplitudes, a change of signature can also be observed in one of the three moments of ACs ($AC_{2,1}(2,3)$ in Fig. 6.4, $AC_{2,1}(2,4)$ in Fig. 6.5 and

$AC_{4,1}(4,5)$ in Fig. 6.9). Furthermore, the predictions from the *MuPa MC-Glauber* models (blue

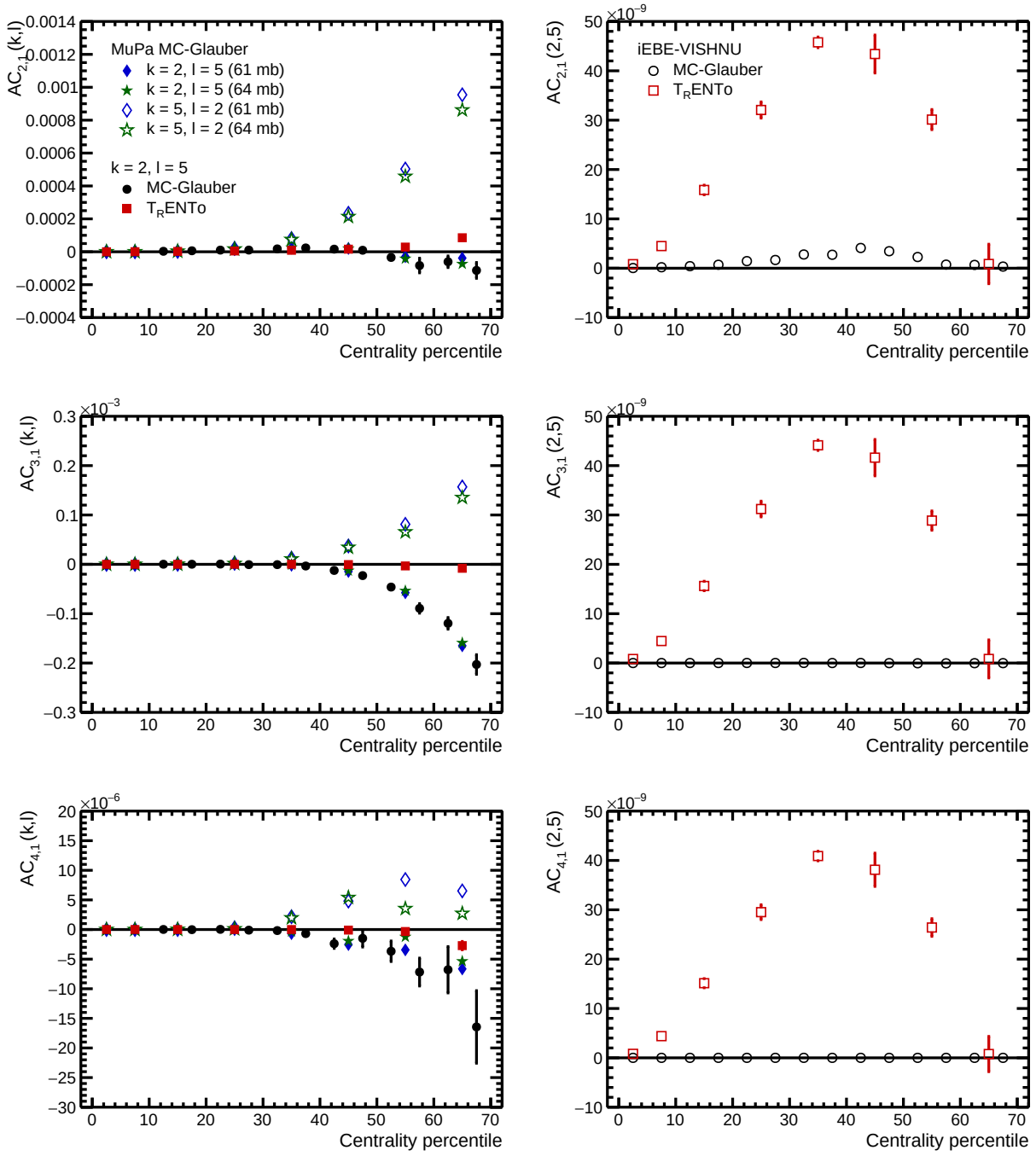

Figure 6.6: Predictions for the centrality dependence of the initial state (*left*) and the final state (*right*) of $AC_{2,1}(2,5)$ (*top*), $AC_{3,1}(2,5)$ (*middle*) and $AC_{4,1}(2,5)$ (*bottom*). Results for MuPa-Glauber courtery of M. Lesch. Results for iEBE-VISHNU courtesy of S.F. Taghavi [125].

and green filled markers) are generally in agreement with the results from the published MC-Glauber (black circles). Small to no effects can be seen between the two different cross-sections in the *MuPa MC-Glauber*. It has also to be noted that the *MuPa MC-Glauber* predictions for $AC_{2,1}(4,2)$, $AC_{4,1}(4,2)$, $AC_{2,1}(4,3)$, and $AC_{3,1}(4,3)$ are also compatible with the ones from the same model with the inverted harmonics.

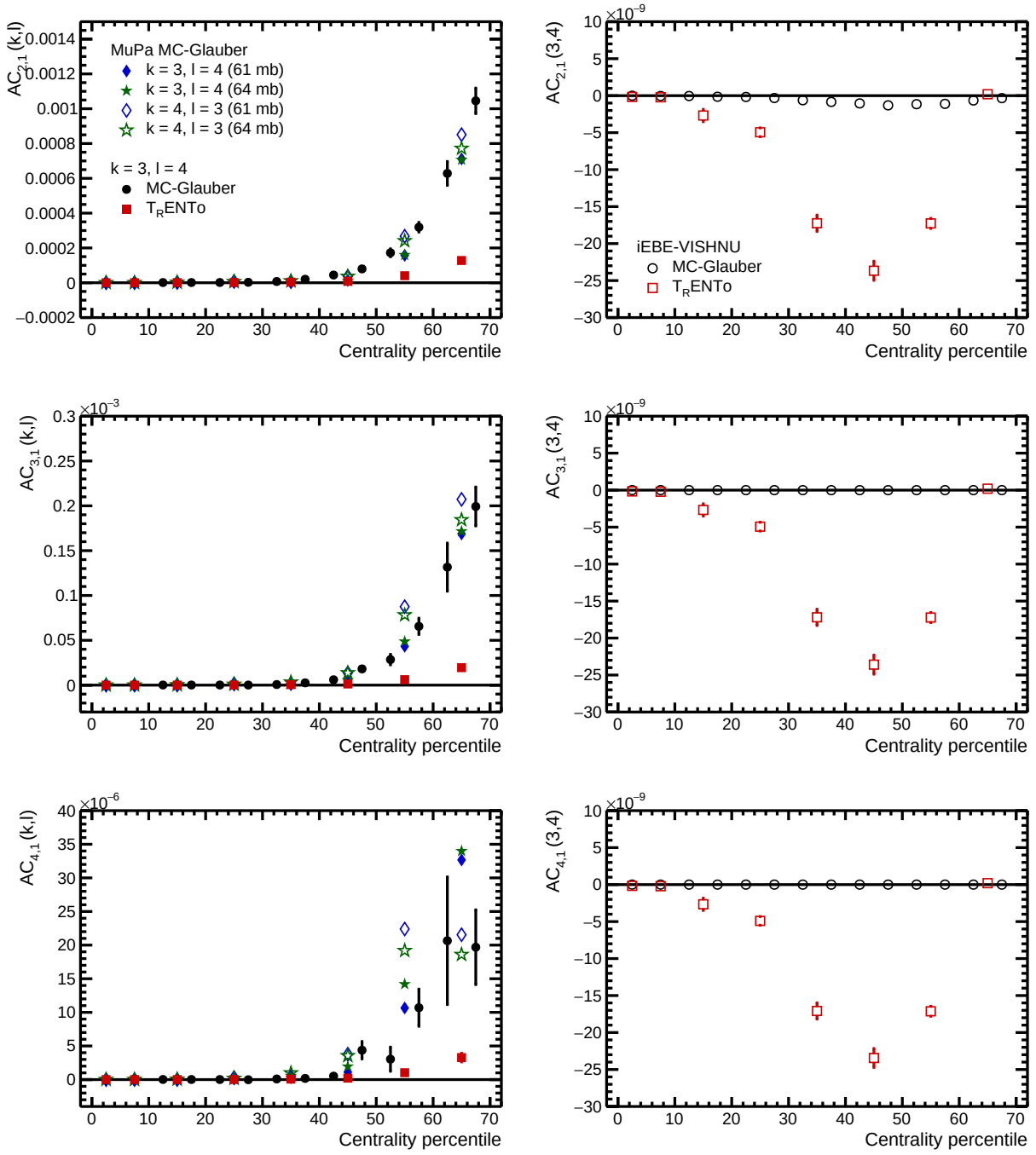

Figure 6.7: Predictions for the centrality dependence of the initial state (*left*) and the final state (*right*) of $\mathrm{AC}_{2,1}(3,4)$ (*top*), $\mathrm{AC}_{3,1}(3,4)$ (*middle*) and $\mathrm{AC}_{4,1}(3,4)$ (*bottom*). Results for MuPa-Glauber courtery of M. Lesch. Results for iEBE-VISHNU courtesy of S.F. Taghavi [125].

6.3.2 Comparisons for the final state

The right panels in Figs. 6.4–6.9 present the predictions for the final state from iEBE-VISHNU using MC-Glauber or T$_\mathrm{R}$ENTo as initial state. All combinations present similar behaviours, with the predictions from T$_\mathrm{R}$ENTo+iEBE-VISHNU showing a large amplitude, with an increase and a decrease as a function of the centrality — excepted for $\mathrm{AC}_{a,1}(4,5), a = 2,3,4$

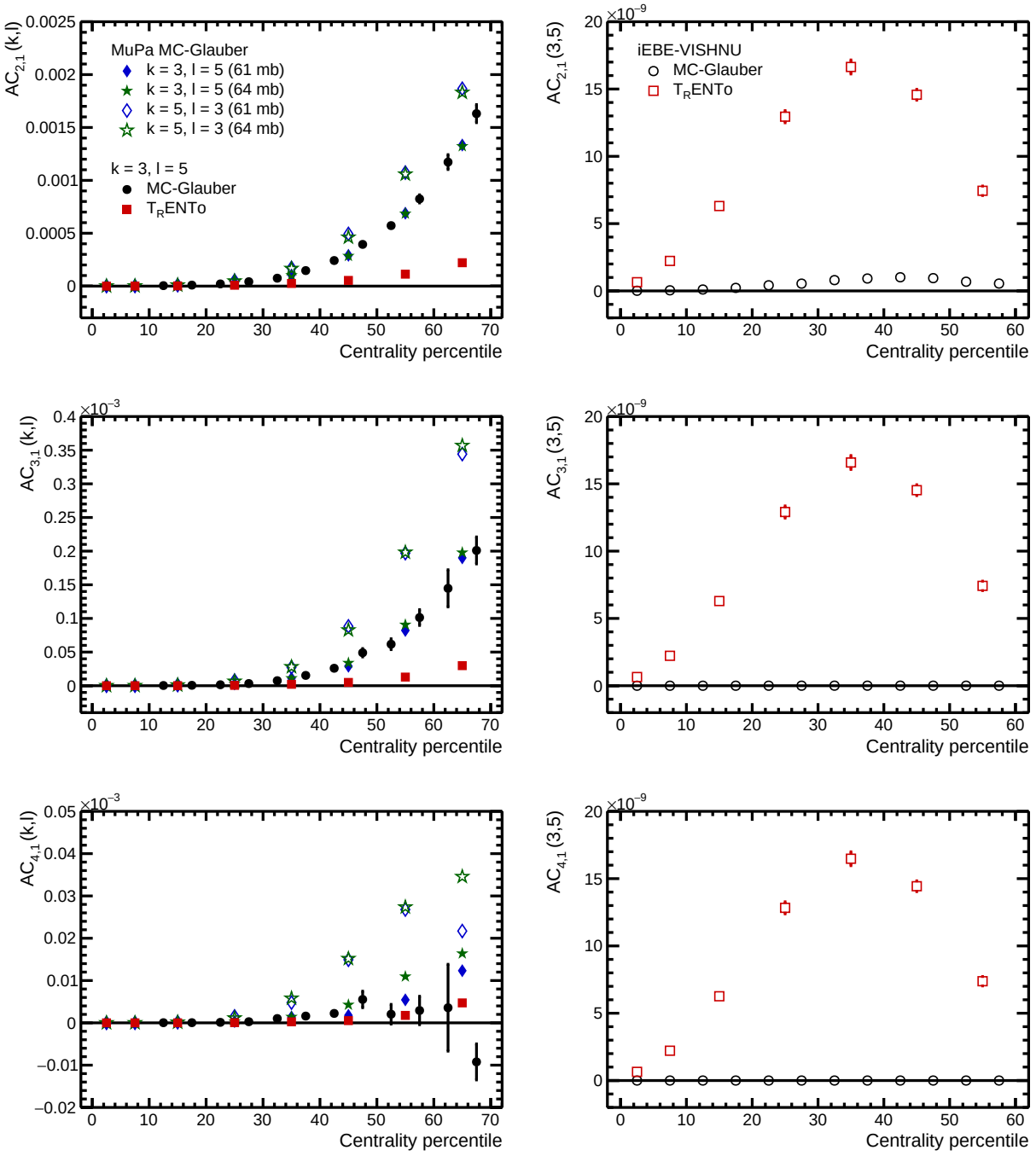

Figure 6.8: Predictions for the centrality dependence of the initial state (*left*) and the final state (*right*) of $\mathrm{AC}_{2,1}(3,5)$ (*top*), $\mathrm{AC}_{3,1}(3,5)$ (*middle*) and $\mathrm{AC}_{4,1}(3,5)$ (*bottom*). Results for MuPa-Glauber courtery of M. Lesch. Results for iEBE-VISHNU courtesy of S.F. Taghavi [125].

which only shows an increase — while MC-Glauber+iEBE-VISHNU is closer to zero with small to nearly no amplitude of variation. However, it has to be stressed out that all the results presented in this section are preliminaries. More thorough studies are needed in this direction before any final statement can be done on the ACs.

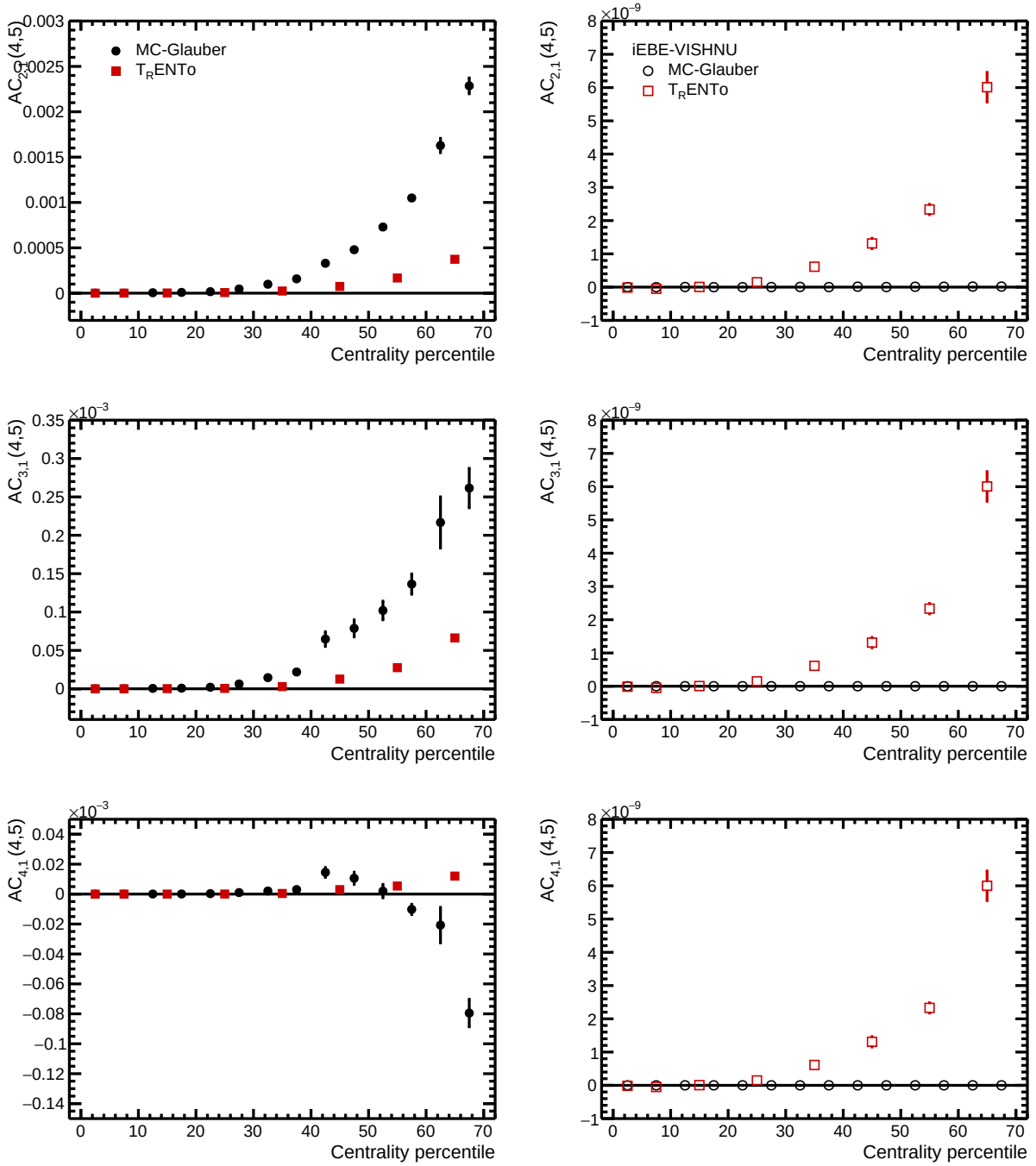

Figure 6.9: Predictions for the centrality dependence of the initial state (*left*) and the final state (*right*) of $\mathrm{AC}_{2,1}(4,5)$ (*top*), $\mathrm{AC}_{3,1}(4,5)$ (*middle*) and $\mathrm{AC}_{4,1}(4,5)$ (*bottom*). Results for iEBE-VISHNU courtesy of S.F. Taghavi [125].

Chapter 7

Summary

This thesis presents the development of a new alternative approach for the measurements of the genuine correlations between different flow amplitudes, based on the mathematical formalism of cumulants from Kubo. The starting point of this method is the observation that the well-known two-harmonic Symmetric Cumulants (SCs) are cumulants of the two flow amplitudes v_m^2 and v_n^2, instead of the azimuthal angles as it was the case for the old approach. From this statement, the SCs have been generalised to any number of flow harmonics, while preserving their cumulants properties. For these purposes, two sets of expressions have been obtained: the definitions in terms of flow amplitudes which are sufficient for theoretical studies and their counterpart with the azimuthal angles to use in experimental analyses. The validity of this new theoretical framework has been demonstrated with the help of toy MC studies and realistic HIJING simulations, besides the mathematical derivations of the required properties. This approach has then been extended to the broader case of the genuine correlations between distinct moments of two and more flow amplitudes, the Asymmetric Cumulants (ACs). Again, mathematical proofs, as well as toy and realistic MC simulations, have ensured the legitimacy of the method.

Collective anisotropic flow has always been one of the tools used to probe the initial conditions and system properties of the quark–gluon plasma (QGP) created in heavy-ion collisions. Recent measurements of single flow amplitudes with multiparticle cumulants have shown their sensitivity to these system properties, namely the average of the ratio of the shear viscosity over entropy density, $\langle \eta/s \rangle$. The possibility to study the genuine correlations between two different flow amplitudes through the SCs and their access to new information like the temperature dependence of η/s has been a new milestone in the flow community. This shows that recent developments in the theoretical and experimental techniques used in such analyses have been, and still are, crucial to obtain observables sensitive to the properties of this strongly interacting system with the least systematic biases as possible. This work — and this novel method — are thus in line with this idea by giving access to new and independent information and constraints which were inaccessible with previous techniques.

Furthermore, asking the proposed observables to be valid cumulants of only the flow amplitudes ensures a straightforward interpretation of the results. A zero value directly means an absence of genuine correlations between the corresponding flow magnitudes, while the opposite conclusion can be reached if non-zero results are observed. As it does not remove the robustness against nonflow correlations or require higher order azimuthal correlators than its traditional counterpart, this ease in the interpretation of the new approach represents a great advantage in flow studies.

Another step achieved in this thesis is the first measurement of the event-by-event genuine

correlations between three different flow amplitudes using the SCs discussed above. These results have been obtained in the Pb–Pb collisions at $\sqrt{s_{\mathrm{NN}}} = 2.76$ TeV measured by ALICE in 2010. This choice of dataset has been motivated by its excellent data taking conditions. The absence of dead zones in the TPC (as it is the case in 2011) ensured a flat acceptance in azimuthal angles and removes the need to correct for non-uniform acceptance effects. Furthermore, while 2015 and 2018 Pb–Pb datasets are larger, leading to an increase of the statistical precision, they also contain pile-up and distortion effects which need to be corrected. Therefore, this makes the 2010 dataset a good and clean sample to get a first look at novel flow observables.

As these measurements result from the generalisation of the two-harmonics SCs, the event and track selections have been widely based on the criteria used in the former studies. All-inclusive charged tracks reconstructed solely from the information from the TPC, the so-called TPC-only tracks, have been selected in the kinematic range $0.2 < p_{\mathrm{T}} < 5.0$ GeV/c and $|\eta| < 0.8$ commonly used in integrated flow analyses in ALICE. Additional criteria related to the detectors have been employed to ensure a good quality of the reconstructed tracks and events. A total of 8.2×10^6 minimum bias events in the centrality range 0—50% have been kept after the full selection for the analysis itself.

Four distinct combinations of harmonics have been measured with the SCs in the final state. Both SC$(2,3,4)$ and SC$(2,3,5)$ have shown a clear presence of genuine correlations. Besides, their signatures, negative and positive respectively, are constant for the full analysed centrality range. It has also been demonstrated how these signatures are new information which could not have been predicted with certainty from the previous two-harmonic SCs results. Furthermore, another result accessible only with the new SCs is the agreement of SC$(2,4,6)$ and SC$(3,4,5)$ with zero for their full centrality range. This is unprecedented, as the corresponding two-by-two genuine correlations are all non-zero over the same range.

Finally, these data have been compared to the predictions from two theoretical hydrodynamic models with different initial conditions: T$_{\mathrm{R}}$ENTo+iEBE-VISHNU, and EKRT. Several additional and independent information, and constraints, can be extracted from such comparisons. First, these models have been tuned to reproduce with a good agreement the previous flow measurements. However, their predictions for the three-harmonic SCs have revealed some, in some cases quite important, deviations with the experimental data. This means that these new results can then be used to improve the tuning of these models. Second, the comparisons of the initial and final state predictions using the normalised SCs have also shown great potential in flow studies. The difference observed between the two states for NSC$(2,3,4)$ has illustrated the development of genuine correlations during the hydrodynamic evolution of the QGP medium. The same behaviour has also been hinted in the case of NSC$(2,3,5)$. Finally, this latter combination of harmonics has also another interest on its own. It is known that the fifth flow amplitude v_5 presents a non-linear contribution from the second and third eccentricities, ϵ_2 and ϵ_3 respectively, in the form $\epsilon_2\epsilon_3$. The study of the genuine correlations between v_2, v_3 (both of which are linearly related to their corresponding eccentricities) and v_5 has therefore the great potential to give more information on this non-linear response.

These measurements have been the first look at the generalised SCs and have proved the feasibility of the new approach in flow analyses. Differential studies, in terms of transverse momentum, pseudorapidity and particle identification, using the Run 2 Pb–Pb data sample are already planned. Despite the additional challenges represented by the needed corrections on the data, these measurements will benefit from the increased size of the dataset, allowing possible exclusions of some tunings for the theoretical models. Similar studies will also be established for the two- and three-harmonic ACs, potentially giving access to new information on the nature of the genuine correlations between the flow amplitudes as well as new constraints on the initial conditions and system properties of the QGP.

Less close from now, the future collisions in Run 3, and corresponding increases of energy and luminosity will be of great help in such precision techniques and allow the measurements of even higher order SCs and ACs.

Appendix A

List of Publications

1. **Higher order Symmetric Cumulants**
   C. Mordasini, A. Bilandzic, D. Karakoç and S.F. Taghavi
   Phys. Rev. C 102 (2020) 024907 ; arXiv:1901.06968 [nucl-ex]

2. **Event-by-event multi-harmonic correlations of different flow amplitudes in Pb—Pb collisions at $\sqrt{s_{\mathrm{NN}}} = 2.76$ TeV**
   ALICE Collaboration [PC: A. Bilandzic, D.J. Kim, C. Mordasini (chair), S.F. Taghavi]
   Submitted to PRL ; arXiv:2101.02579 [nucl-ex]

3. **Multivariate cumulants in flow analyses: The Next Generation**
   A. Bilandzic, M. Lesch, C. Mordasini and S. F. Taghavi
   In preparation to be submitted to PRC ; arXiv:2101.05619v1 [physics.data-an]

4. **Extended Studies on Asymmetric Cumulants**
   C. Mordasini
   In preparation

Appendix B

Demonstrations

In this appendix, all the demonstrations mentioned in Section 1.4 and in Chapter 2 are presented.

B.1 Exact relation for the flow amplitudes v_n

The relation to prove here is the one of Eq. (1.14), recalled here:

$$v_n = \langle \cos\left[n\left(\varphi - \Psi_n\right)\right]\rangle .$$

The Fourier series in Eq. (1.13) can be expressed in a simplified way as

$$f(\varphi) = \frac{1}{2\pi}\left[1 + 2\sum_{n=1}^{\infty} v_n \cos\left(n(\varphi - \Psi_n)\right)\right], \tag{B.1}$$

with φ the azimuthal angles of the detected particles, v_n the flow amplitudes and Ψ_n the symmetry planes. The mean of a random variable x is defined as

$$\langle x\rangle \equiv \int_0^{2\pi} x f(x) dx. \tag{B.2}$$

Using the definition of the mean on the right-handed side (RHS) of Eq. (1.13) gives

$$\begin{aligned}
\langle\cos[n(\varphi - \Psi_n)]\rangle &= \int_0^{2\pi} d\varphi \cos[n(\varphi - \Psi_n)] f(\varphi) \\
&= \frac{1}{2\pi}\int_0^{2\pi} d\varphi \cos[n(\varphi - \Psi_n)]\left\{1 + 2\sum_{m=1}^{\infty} v_m \cos[m(\varphi - \Psi_m)]\right\} \\
&= \frac{1}{2\pi}\int_0^{2\pi} d\varphi \cos[n(\varphi - \Psi_n)] \\
&+ \frac{1}{\pi}\int_0^{2\pi} d\varphi \sum_{m=1}^{\infty} v_m \cos[n(\varphi - \Psi_n)]\cos[m(\varphi - \Psi_m)],
\end{aligned} \tag{B.3}$$

where the definition of the Fourier series (B.1) has been used to get the second equality.

The first term of the RHS is zero. For the second term, the orthogonality relation of trigonometry,

$$\int_0^{2\pi} dx \cos(mx + \alpha)\cos(nx + \beta) = \pi \cos(\alpha - \beta)\delta_{mn}, \tag{B.4}$$

where m, n are nonzero integers, α, β are arbitrary and δ_{mn} is the Kronecker delta symbol, is used. This gives

$$\langle \cos[n(\varphi - \Psi_n)] \rangle = \sum_{m=1}^{\infty} v_m \cos(-\Psi_n + \Psi_m)\delta_{mn} = v_n, \tag{B.5}$$

which is the desired result. □

B.2 Two-particle correlations in terms of Q-vectors

This section shows the demonstration of Eq. (2.14), which is repeated here for completion purposes.

$$\langle 2 \rangle_{n,-n} = \frac{1}{\binom{M}{2}2!} \left[|Q_n|^2 - M \right]. \tag{B.6}$$

The first part of the proof consists to show that

$$\langle 2 \rangle_{n,-n} = \frac{1}{\binom{M}{2}2!} \sum_{\substack{j,k=1 \\ j \neq k}}^{M} \mathrm{e}^{in(\varphi_j - \varphi_k)}. \tag{B.7}$$

This is achieved with the following derivation. The most general form for a two-particle correlator of the single harmonic n is given by (Eq. (2.11))

$$\langle 2 \rangle_{n,-n} = \frac{\sum_{\substack{j,k=1 \\ j \neq k}}^{M} w_j w_k \mathrm{e}^{in(\varphi_j - \varphi_k)}}{\sum_{\substack{j,k=1 \\ j \neq k}}^{M} w_j w_k}. \tag{B.8}$$

For unit particle weights $w_j, w_k = 1$, the denominator becomes

$$\sum_{\substack{j,k=1 \\ j \neq k}}^{M} 1 = M(M-1) = \binom{M}{2} 2!, \tag{B.9}$$

where $\binom{M}{2}$ is the binomial coefficient. Inserting this result into the general definition above returns Eq. (B.7). This result is then used to prove the initial equation, Eq. (2.14). The right-handed term can be rewritten as the sum over all combinations of azimuthal angles of M particles minus the sum of terms where the particles are taken identical ($j = k$), i.e.

$$\begin{aligned}
\frac{1}{\binom{M}{2}2!} \sum_{\substack{j,k=1 \\ j \neq k}}^{M} \mathrm{e}^{in(\varphi_j - \varphi_k)} &= \frac{1}{\binom{M}{2}2!} \left(\sum_{j,k=1}^{M} \mathrm{e}^{in(\varphi_j - \varphi_k)} - \sum_{j=1}^{M} \mathrm{e}^{in0} \right) \\
&= \frac{1}{\binom{M}{2}2!} \left(\sum_{j=1}^{M} \mathrm{e}^{in\varphi_j} \sum_{k=1}^{M} \mathrm{e}^{-in\varphi_k} - M \right) \\
&= \frac{1}{\binom{M}{2}2!} \left(Q_n Q_n^* - M \right) \\
&= \frac{1}{\binom{M}{2}2!} \left(|Q_n|^2 - M \right), \qquad \square
\end{aligned} \tag{B.10}$$

where the definition of the Q-vector Q_n (Eq. (2.13)),

$$Q_n \equiv \sum_{k=1}^{M} \mathrm{e}^{in\varphi_k}. \tag{B.11}$$

has been used.

B.3 Semi-invariance of SC(m, n)

This section shows how to the two-harmonic SCs fail to meet the semi-invariance requirement for multivariate cumulants when it is applied with the flow amplitudes v_m and v_n as the stochastic variables.

Consider two constants c_m and c_n. The semi-invariance criterion for SC(m,n) can be expressed as follows:

$$\begin{aligned}
\left\langle (v_m + c_m)^2 (v_n + c_n)^2 \right\rangle - \left\langle (v_m + c_m)^2 \right\rangle \left\langle (v_n + c_n)^2 \right\rangle &= \left\langle (v_m + c_m)^2 (v_n + c_n)^2 \right\rangle \\
&\quad - \left\langle \left(v_m^2 + 2c_m v_m + c_m^2 \right) \right\rangle \left\langle \left(v_n^2 + 2c_n v_n + c_n^2 \right) \right\rangle \\
&= \left\langle v_m^2 v_n^2 \right\rangle - \left\langle v_m^2 \right\rangle \left\langle v_n^2 \right\rangle \\
&\quad + 2c_m \left(\left\langle v_m v_n^2 \right\rangle - \langle v_m \rangle \left\langle v_n^2 \right\rangle \right) \\
&\quad + 2c_n \left(\left\langle v_m^2 v_n \right\rangle - \left\langle v_m^2 \right\rangle \langle v_n \rangle \right) \\
&\quad + 4c_m c_n \left(\langle v_m v_n \rangle - \langle v_m \rangle \langle v_n \rangle \right) \\
&\neq \mathrm{SC}(m,n). \qquad \square
\end{aligned} \tag{B.12}$$

This derivation proves that SC(m,n) is not a valid cumulant of the flow amplitudes v_m and v_n, but of the flow amplitudes squared v_m^2 and v_n^2, as it has been shown for SC(k,l,m) in Section 4.1.

Appendix C

Additional Figures for the Asymmetric Cumulants

C.1 Nonflow scaling up to $M_{final} = 550$

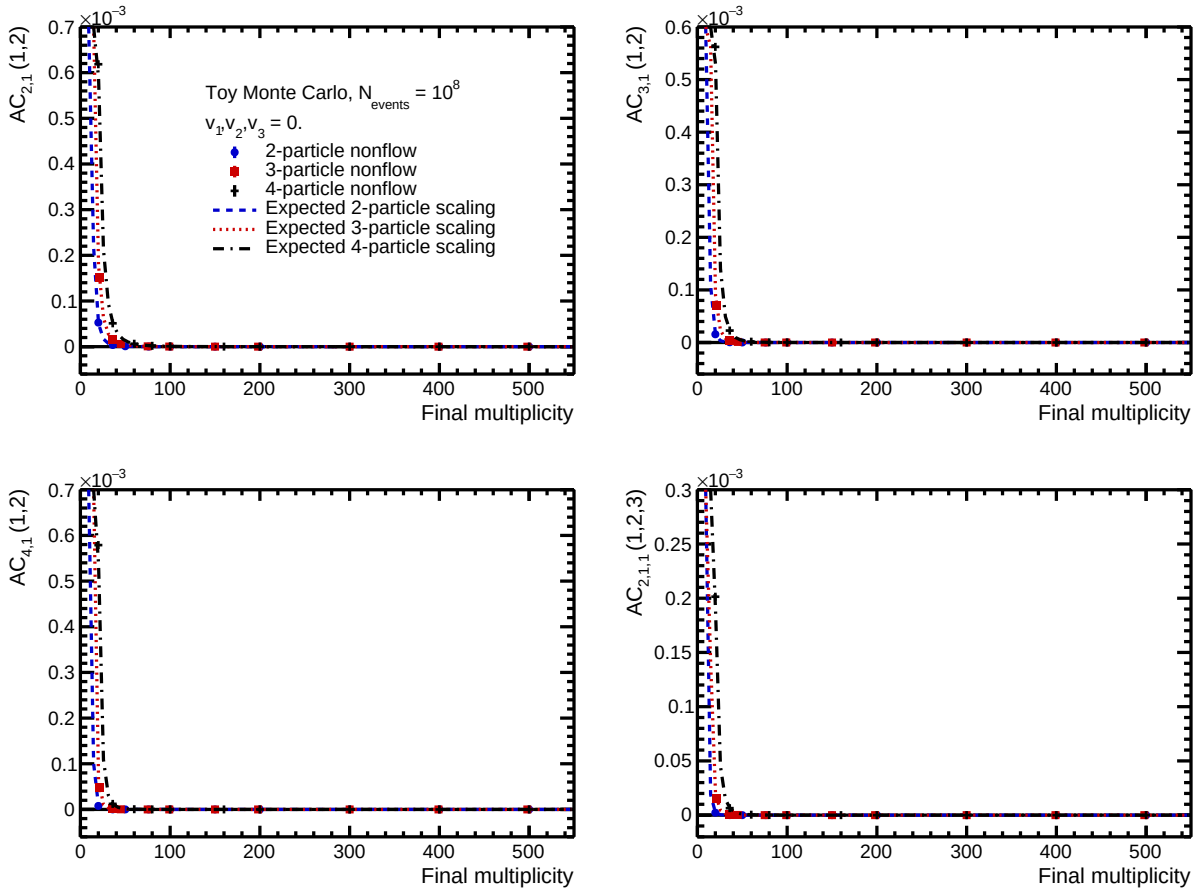

Figure C.1: Multiplicity dependence of the various ACs for strong few-particle correlations with the fit of the corresponding nonflow scaling. Alternative version of Fig. 4.17.

Appendix D

Technical Details for the Experimental Analysis

This appendix presents the technical information concerning the acquisition of the experimental results. The code used to run on the Grid and obtain the multiparticle correlators needed for the computation of the SCs and the ACs is the class *AliAnalysisTaskTwoMultiCorrelations.(h, cxx)* can be found in the Github repository https://github.com/alisw/AliPhysics/blob/master/PWG/FLOW/Tasks/. The two main parts of the experimental analysis have been obtained with the versions *vAN-20190625-1*, *vAN-20200207-1* and *vAN-20201214-1* of the AliPhysics software. The first analysis daily tag has been used to get the preliminary results showed at the Quark Matter 2019 conference, while the second one corresponds to the version of the checks presented in Ref. [169]. The third one, finally, is the last analysis tag used to get the final results through the LEGO Train framework. The final results for the SCs can be found in the wagons *CF-CF_PbPb-9083*, *CF-CF_PbPb-9129* and *CF-CF_PbPb_MC_AOD-2778*.

As stated in Chapter 5, the analysis has been conducted on the Pb–Pb dataset at $\sqrt{s_{\mathrm{NN}}} = 2.76$ TeV taken in 2010. This corresponds in the internal naming scheme of ALICE to the LHC10h dataset. The reconstruction is the pass 2 and the filtering is the AOD160, both of which are the latest configuration available for this data taking period. Among the 90 runs indicated as *good* in the Run Condition Table, the following 88 are included in this work:

139510, 139507, 139505, 139503, 139465, 139438, 139437, 139360, 139329, 139328, 139314, 139310, 139309, 139173, 139107, 139105, 139038, 139037, 139036, 139029, 139028, 138872, 138871, 138870, 138837, 138732, 138730, 138666, 138662, 138653, 138652, 138638, 138624, 138621, 138583, 138582, 138578, 138534, 138469, 138442, 138439, 138438, 138396, 138364, 138275, 138225, 138201, 138197, 138192, 138190, 137848, 137844, 137752, 137751, 137724, 137722, 137718, 137704, 137693, 137692, 137691, 137686, 137685, 137639, 137638, 137608, 137595, 137549, 137544, 137541, 137539, 137531, 137443, 137441, 137440, 137439, 137434, 137432, 137431, 137430, 137243, 137236, 137235, 137232, 137231, 137230, 137162, 137161.

It has to be noted that the quality of the runs indicated in the Run Condition Table is a decision from the Central QA. This procedure done centrally on the data is made to check the quality of each run and classify them done between the ones that are not usable in physics analysis, the ones that can be used with caution (for instance in certain analyses only) and the ones that are good for all analyses.

The computation of the particle weights used to correct for detector effects in the ALICE data has been done with HIJING simulations. The production anchored to the LHC10h dataset is the LHC11a10a_bis, with AOD162 as the latest available filtering. The list of analysed runs

is the same as the one above. The origin of the rejection of the "good" runs 137546 and 137530 come from this HIJING production. Some issues (empty bins in some centrality ranges e.g.), which were affecting the final corrections, have been found during the quality assurance of the dataset.

Appendix E

Support Figures for the Estimation of the Barlow Test

This Appendix gathers the tables used to determine the systematic uncertainties of the three-harmonic SCs and NSCs shown in Section 6.2, with the exception of SC$(2,3,4)$ presented as an example in Section 5.6.2. The corresponding support figures can be found in the ALICE internal analysis notes in Ref. [167].

Table E.1: Summary of the systematic uncertainties for each trial for the observable NSC$(2,3,4)$. The columns 0–5%, 5–10% and 10–20% summarise the absolute variations, while 20–50% contains the relative variations (see text). An en-dash "—" indicate a trial without a statistically significant deviation.

Trial	**0–5%**	**5–10%**	**10–20%**	**20–50%**
Centrality	2.97×10^{-3}	-1.87×10^{-3}	2.258×10^{-3}	15.5%
PV_z	-4.37×10^{-3}	-1.36×10^{-3}	-8.31×10^{-4}	3.2%
N_{TPC}	—	—	—	—
χ^2/NDF	—	—	—	—
DCA_{xy}	-3.14×10^{-3}	-2.15×10^{-3}	1.92×10^{-3}	12.4%
DCA_z	—	—	—	—
++/- -	—	—	—	—
Filter	1.40×10^{-2}	2.23×10^{-3}	2.18×10^{-3}	8.1%
Overall	1.53×10^{-2}	3.86×10^{-3}	3.76×10^{-3}	21.7%

Table E.2: Summary of the systematic uncertainties for each trial for the observable SC(2, 3, 5). The columns 0–5%, 5–10% and 10–20% summarise the absolute variations, while 20–50% contains the relative variations (see text). An en-dash "—" indicate a trial without a statistically significant deviation.

Trial	**0–5%**	**5–10%**	**10–20%**	**20–50%**
Centrality	-2.15×10^{-13}	-2.12×10^{-13}	-7.11×10^{-13}	21.1%
PV_z	—	—	—	—
N_{TPC}	8.49×10^{-13}	-1.04×10^{-12}	-3.02×10^{-12}	13.9%
χ^2/NDF	—	—	—	—
DCA_{xy}	-2.55×10^{-13}	2.35×10^{-12}	4.84×10^{-12}	35.7%
DCA_z	-3.73×10^{-14}	8.46×10^{-13}	9.33×10^{-13}	9.6%
++/- -	—	—	—	—
Filter	1.67×10^{-13}	-1.07×10^{-12}	1.72×10^{-12}	7.8%
Overall	9.28×10^{-13}	2.92×10^{-12}	6.07×10^{-12}	45.5%

Table E.3: Values of the systematic uncertainties for each trial for NSC(2,3,5). The columns 0–5%, 5–10% and 10–20% contain absolute variations and 20–50% relative variations as described above. A dash indicates a trial not included in the overall value due to not have significant statistical deviation.

Trial	**0–5%**	**5–10%**	**10–20%**	**20–50%**
Centrality	-1.14×10^{-2}	-2.88×10^{-3}	-2.69×10^{-3}	19.6%
PV_z	—	—	—	—
N_{TPC}	4.13×10^{-2}	-1.48×10^{-2}	-1.08×10^{-2}	11.3%
χ^2/NDF	5.26×10^{-3}	-3.51×10^{-3}	2.31×10^{-3}	12.4%
DCA_{xy}	1.90×10^{-2}	2.56×10^{-2}	9.31×10^{-3}	21.4%
DCA_z	-2.62×10^{-3}	1.10×10^{-2}	2.53×10^{-3}	8.4%
++/- -	—	—	—	—
Filter	3.03×10^{-2}	-1.02×10^{-2}	1.84×10^{-2}	18.9%
Overall	5.61×10^{-2}	3.35×10^{-2}	2.37×10^{-2}	39.4%

Table E.4: Values of the systematic uncertainties for each trial for SC(2,4,6). All the values are the absolute difference between systematic trials and default. A dash indicates a trial not included in the overall value due to not have significant statistical deviation.

Trial	**0–5%**	**5–10%**	**10–20%**	**20–50%**
Centrality	2.72×10^{-13}	-1.40×10^{-12}	1.98×10^{-12}	-2.30×10^{-12}
PV_z	1.18×10^{-13}	-4.95×10^{-14}	1.17×10^{-12}	1.93×10^{-12}
N_{TPC}	—	—	—	—
χ^2/NDF	4.92×10^{-14}	2.54×10^{-13}	9.32×10^{-13}	-2.10×10^{-12}
DCA_{xy}	—	—	—	—
DCA_z	—	—	—	—
++/- -	—	—	—	—
Filter	-1.96×10^{-13}	-1.30×10^{-12}	1.49×10^{-12}	-4.82×10^{-12}
Overall	3.59×10^{-13}	1.93×10^{-12}	2.89×10^{-12}	6.06×10^{-12}

Table E.5: Values of the systematic uncertainties for each trial for SC(3,4,5). All the values are the absolute difference between systematic trials and default. A dash indicates a trial not included in the overall value due to not have significant statistical deviation.

Trial	**0–5%**	**5–10%**	**10–20%**	**20–50%**
Centrality	—	—	—	—
PV_z	—	—	—	—
N_{TPC}	—	—	—	—
χ^2/NDF	4.11×10^{-14}	-1.94×10^{-14}	2.97×10^{-13}	2.86×10^{-13}
DCA_{xy}	2.61×10^{-13}	-7.03×10^{-13}	2.09×10^{-13}	5.69×10^{-13}
DCA_z	—	—	—	—
++/- -	—	—	—	—
Filter	1.60×10^{-13}	5.18×10^{-14}	1.19×10^{-13}	9.03×10^{-13}
Overall	3.09×10^{-13}	7.05×10^{-13}	3.82×10^{-13}	1.10×10^{-12}

Bibliography

[1] Arbuzov, A., "Quantum Field Theory and the Electroweak Standard Model," *CERN Yellow Rep. School Proc.* **3** (2018) 1–35.
Cited on page 1.

[2] Englert, F. and Brout, R., "Broken Symmetry and the Mass of Gauge Vector Mesons," *Phys. Rev. Lett.* **13** (1964) 321–323.
Cited on page 1.

[3] Higgs, Peter W., "Broken Symmetries and the Masses of Gauge Bosons," *Phys. Rev. Lett.* **13** (1964) 508–509.
Cited on page 1.

[4] Guralnik, G. S. and Hagen, C. R. and Kibble, T. W. B., "Global Conservation Laws and Massless Particles," *Phys. Rev. Lett.* **13** (1964) 585–587.
Cited on page 1.

[5] **ATLAS** Collaboration, Aad, G. *et al.*, "Observation of a new particle in the search for the Standard Model Higgs boson with the ATLAS detector at the LHC," *Phys. Lett. B* **716** (2012) 1–29, arXiv:1207.7214 [hep-ex].
Cited on page 1.

[6] **CMS** Collaboration, Chatrchyan, S. *et al.*, "Observation of a New Boson at a Mass of 125 GeV with the CMS Experiment at the LHC," *Phys. Lett. B* **716** (2012) 30–61, arXiv:1207.7235 [hep-ex].
Cited on page 1.

[7] Lubej, M., "A pretty diagram of the Standard Model." http://www-f9.ijs.si/~lubej/. [Online, accessed June 12, 2020].
Cited on page 2.

[8] P. Skands, "Introduction to QCD," in *Proceedings, 2nd Asia-Europe-Pacific School of High-Energy Physics (AEPSHEP 2014): Puri, India, November 04–17, 2014*, pp. 341–420. 2013. arXiv:1207.2389 [hep-ph].
Cited on pages 2 and 3.

[9] G. F. Sterman, "Some Basic Concepts of Perturbative QCD," *Acta Phys. Polon. B* **39** (2008) 2151–2172, arXiv:0807.5118 [hep-ph].
Cited on pages 2, 3, and 5.

[10] **Belle** Collaboration, S. Choi *et al.*, "Observation of a resonance-like structure in the $pi^{\pm}\psi'$ mass distribution in exclusive $B \to K\pi^{\pm}\psi'$ decays," *Phys. Rev. Lett.* **100** (2008) 142001, arXiv:0708.1790 [hep-ex].
Cited on page 3.

[11] **LHCb** Collaboration, R. Aaij *et al.*, "Observation of $J/\psi p$ Resonances Consistent with Pentaquark States in $\Lambda_b^0 \to J/\psi K^- p$ Decays," *Phys. Rev. Lett.* **115** (2015) 072001, arXiv:1507.03414 [hep-ex].
Cited on page 3.

[12] S. Sarkar, H. Satz, and B. Sinha, eds., *The physics of the quark-gluon plasma*, vol. 785. 2010.
Cited on pages 3, 6, 8, and 9.

[13] **Particle Data Group** Collaboration, M. Tanabashi *et al.*, "Review of Particle Physics," *Phys. Rev. D* **98** no. 3, (2018) 030001.
Cited on pages 3 and 4.

[14] D. J. Gross and F. Wilczek, "Ultraviolet behavior of non-abelian gauge theories," *Phys. Rev. Lett.* **30** (1973) 1343–1346.
Cited on page 3.

[15] H. D. Politzer, "Reliable perturbative results for strong interactions?," *Phys. Rev. Lett.* **30** (1973) 1346–1349.
Cited on pages 3 and 5.

[16] H. D. Politzer, "Asymptotic freedom: An approach to strong interactions," *Physics Reports* **14** no. 4, (1974) 129–180.
Cited on page 3.

[17] J. Greensite, *An Introduction to the Confinement Problem*, vol. 821 of *Lecture Notes in Physics*. Springer Berlin Heidelberg, 2011.
Cited on page 4.

[18] D. H. Rischke, "The Quark gluon plasma in equilibrium," *Prog. Part. Nucl. Phys.* **52** (2004) 197–296, arXiv:nucl-th/0305030.
Cited on pages 5 and 6.

[19] F. Karsch and E. Laermann, "Thermodynamics and in medium hadron properties from lattice QCD," arXiv:hep-lat/0305025.
Cited on page 5.

[20] H. Satz, *Extreme States of Matter in Strong Interaction Physics: An Introduction*, vol. 945 of *Lecture Notes in Physics*. Springer International Publishing, Cham, 2018.
Cited on pages 5, 6, and 9.

[21] R. Pasechnik and M. Šumbera, "Phenomenological Review on Quark–Gluon Plasma: Concepts vs. Observations," *Universe* **3** no. 1, (2017) 7, arXiv:1611.01533 [hep-ph].
Cited on pages 5, 6, and 11.

[22] T. Kolar, "Qcd matter phase diagram," 2014.
Cited on page 5.

[23] J. C. Collins and M. Perry, "Superdense Matter: Neutrons Or Asymptotically Free Quarks?," *Phys. Rev. Lett.* **34** (1975) 1353.
Cited on page 6.

[24] P. Braun-Munzinger and J. Wambach, "The Phase Diagram of Strongly-Interacting Matter," *Rev. Mod. Phys.* **81** (2009) 1031–1050, arXiv:0801.4256 [hep-ph].
Cited on page 6.

[25] K. Fukushima and T. Hatsuda, "The phase diagram of dense QCD," *Rept. Prog. Phys.* **74** (2011) 014001, arXiv:1005.4814 [hep-ph].
Cited on page 6.

[26] B. C. Barrois, "Superconducting Quark Matter," *Nucl. Phys. B* **129** (1977) 390–396.
Cited on page 6.

[27] M. G. Alford, A. Schmitt, K. Rajagopal, and T. Schäfer, "Color superconductivity in dense quark matter," *Rev. Mod. Phys.* **80** (2008) 1455–1515, arXiv:0709.4635 [hep-ph].
Cited on page 6.

[28] M. Gell-Mann, "A Schematic Model of Baryons and Mesons," *Phys. Lett.* **8** (1964) 214–215.
Cited on page 6.

[29] G. Zweig, "An SU(3) model for strong interaction symmetry and its breaking. Version 1,".
Cited on page 6.

[30] G. Zweig, *An SU(3) model for strong interaction symmetry and its breaking. Version 2*, pp. 22–101. 1964.
Cited on page 6.

[31] N. Itoh, "Hydrostatic Equilibrium of Hypothetical Quark Stars," *Prog. Theor. Phys.* **44** (1970) 291.
Cited on page 6.

[32] N. Cabibbo and G. Parisi, "Exponential Hadronic Spectrum and Quark Liberation," *Phys. Lett. B* **59** (1975) 67–69.
Cited on page 6.

[33] E. V. Shuryak, "Theory of Hadronic Plasma," *Sov. Phys. JETP* **47** (1978) 212–219.
Cited on page 6.

[34] E. V. Shuryak, "Quark-Gluon Plasma and Hadronic Production of Leptons, Photons and Psions," *Sov. J. Nucl. Phys.* **28** (1978) 408.
Cited on page 6.

[35] A. Bzdak, S. Esumi, V. Koch, J. Liao, M. Stephanov, and N. Xu, "Mapping the Phases of Quantum Chromodynamics with Beam Energy Scan," *Phys. Rept.* **853** (2020) 1–87, arXiv:1906.00936 [nucl-th].
Cited on page 6.

[36] E. V. Shuryak, "Physics of hot hadronic matter and quark - gluon plasma," *Nucl. Phys. A* **525** (1991) 3–22.
Cited on page 6.

[37] E. Shuryak, "Strongly coupled quark-gluon plasma in heavy ion collisions," *Rev. Mod. Phys.* **89** (2017) 035001, arXiv:1412.8393 [hep-ph].
Cited on pages 6, 7, and 10.

[38] D. M. Lee, "Probing the big bang at the relativistic heavy ion collider (RHIC) (or probing the big bang 13.7 billion years later)," *Journal of Physics: Conference Series* **213** (2010) 012012.
Cited on page 6.

[39] U. W. Heinz and M. Jacob, "Evidence for a new state of matter: An Assessment of the results from the CERN lead beam program," arXiv:nucl-th/0002042.
Cited on pages 6 and 15.

[40] E. V. Shuryak, "What RHIC experiments and theory tell us about properties of quark-gluon plasma?," *Nucl. Phys. A* **750** (2005) 64–83, arXiv:hep-ph/0405066.
Cited on pages 6 and 10.

[41] U. W. Heinz, "'RHIC serves the perfect fluid': Hydrodynamic flow of the QGP," in *Workshop on Extreme QCD*, pp. 3–12. 2005. arXiv:nucl-th/0512051.
Cited on pages 6 and 16.

[42] U. Heinz and R. Snellings, "Collective flow and viscosity in relativistic heavy-ion collisions," *Ann. Rev. Nucl. Part. Sci.* **63** (2013) 123–151, arXiv:1301.2826 [nucl-th].
Cited on pages 6, 10, 13, and 15.

[43] P. Kovtun, D. T. Son, and A. O. Starinets, "Viscosity in strongly interacting quantum field theories from black hole physics," *Phys. Rev. Lett.* **94** (2005) 111601, arXiv:hep-th/0405231.
Cited on page 6.

[44] Y. Aoki, G. Endrodi, Z. Fodor, S. Katz, and K. Szabo, "The Order of the quantum chromodynamics transition predicted by the standard model of particle physics," *Nature* **443** (2006) 675–678, arXiv:hep-lat/0611014.
Cited on page 6.

[45] F. Karsch, "Lattice simulations of the thermodynamics of strongly interacting elementary particles and the exploration of new phases of matter in relativistic heavy ion collisions," *J. Phys. Conf. Ser.* **46** (2006) 122–131, arXiv:hep-lat/0608003.
Cited on page 6.

[46] A. Bzdak and V. Koch, "Mapping the qcd phase diagram with statistics-friendly distributions,"
Phys. Rev. C **100** (2019) 051902.
Cited on page 6.

[47] **STAR** Collaboration, M. Sumbera, "Results from STAR Beam Energy Scan Program," *Acta Phys. Polon. Supp.* **6** (2013) 429–436, arXiv:1301.7224 [nucl-ex].
Cited on page 6.

[48] **PHENIX** Collaboration, J. Mitchell, "Transverse Energy Measurements from the Beam Energy Scan in PHENIX," *Nucl. Phys. A* **956** (2016) 842–845, arXiv:1601.00904 [nucl-ex].
Cited on page 6.

[49] **STAR** Collaboration, L. Adamczyk *et al.*, "Beam Energy Dependence of the Third Harmonic of Azimuthal Correlations in Au+Au Collisions at RHIC," *Phys. Rev. Lett.* **116** no. 11, (2016) 112302, arXiv:1601.01999 [nucl-ex].
Cited on page 6.

[50] S. M. Sanches, D. A. Fogaça, and F. S. Navarra, "The time evolution of the quark gluon plasma in the early universe," *Journal of Physics: Conference Series* **630** (2015) 012028.
Cited on page 6.

[51] J. Lattimer and M. Prakash, "The physics of neutron stars," *Science* **304** (2004) 536–542, arXiv:astro-ph/0405262.
Cited on page 7.

[52] M. Schaumann *et al.*, "First Xenon-Xenon Collisions in the LHC," in *9th International Particle Accelerator Conference*, p. MOPMF039. 2018.
Cited on page 7.

[53] Z. Citron *et al.*, "Report from Working Group 5: Future physics opportunities for high-density QCD at the LHC with heavy-ion and proton beams," *CERN Yellow Rep. Monogr.* **7** (2019) 1159–1410, arXiv:1812.06772 [hep-ph].
Cited on page 7.

[54] S. T. Heckel, *Mean transverse-momentum fluctuations from soft particles produced in pp, p−Pb and Pb−Pb collisions at the LHC*. PhD thesis, 2019.
http://cds.cern.ch/record/2718563. Presented 08 Jul 2019.
Cited on page 7.

[55] H. Petersen, J. Steinheimer, G. Burau, M. Bleicher, and H. Stöcker, "Fully integrated transport approach to heavy ion reactions with an intermediate hydrodynamic stage," *Phys. Rev. C* **78** (2008) 044901.
Cited on page 7.

[56] MADAI, "Heavy-ion collisions."
https://madai.phy.duke.edu/indexaae2.html?page_id=503.
Cited on page 7.

[57] S. A. Voloshin, A. M. Poskanzer, and R. Snellings, *Collective phenomena in non-central nuclear collisions*, vol. 23, pp. 293–333. 2010. arXiv:0809.2949 [nucl-ex].
Cited on pages 7 and 8.

[58] W. Broniowski and W. Florkowski, "Geometric relation between centrality and the impact parameter in relativistic heavy ion collisions," *Phys. Rev. C* **65** (2002) 024905, arXiv:nucl-th/0110020.
Cited on page 8.

[59] A. Bialas, M. Bleszynski, and W. Czyz, "Multiplicity Distributions in Nucleus-Nucleus Collisions at High-Energies," *Nucl. Phys. B* **111** (1976) 461–476.
Cited on page 8.

[60] M. L. Miller, K. Reygers, S. J. Sanders, and P. Steinberg, "Glauber modeling in high energy nuclear collisions," *Ann. Rev. Nucl. Part. Sci.* **57** (2007) 205–243, arXiv:nucl-ex/0701025.
Cited on pages 8 and 105.

[61] B. Alver, M. Baker, C. Loizides, and P. Steinberg, "The PHOBOS Glauber Monte Carlo," arXiv:0805.4411 [nucl-ex].
Cited on page 8.

[62] C. Loizides, "Glauber modeling of high-energy nuclear collisions at the subnucleon level," *Phys. Rev. C* **94** (2016) 024914.
Cited on page 8.

[63] E. Iancu, "QCD in heavy ion collisions," in *2011 European School of High-Energy Physics*, pp. 197–266. 2014. arXiv:1205.0579 [hep-ph].
Cited on pages 9 and 10.

[64] E. Iancu and R. Venugopalan, *The Color glass condensate and high-energy scattering in QCD*, pp. 249–363. 2003. arXiv:hep-ph/0303204.
Cited on page 9.

[65] F. Gelis, E. Iancu, J. Jalilian-Marian, and R. Venugopalan, "The Color Glass Condensate," *Ann. Rev. Nucl. Part. Sci.* **60** (2010) 463–489, arXiv:1002.0333 [hep-ph].
Cited on page 9.

[66] S. Bhattacharyya, D. Biswas, S. K. Ghosh, R. Ray, and P. Singha, "Systematics of chemical freeze-out parameters in heavy-ion collision experiments," *Phys. Rev. D* **101** no. 5, (2020) 054002, arXiv:1911.04828 [hep-ph].
Cited on page 10.

[67] J. I. Kapusta, "Quark - gluon plasma in the early universe," in *International School of Astrophysics 'Daniel Chalonge' 8th Course: Opening the 3rd Millennium, Phase Transitions in the Early Unverse: Theory and Observations*, pp. 103–121. 12, 2000. arXiv:astro-ph/0101516.
Cited on page 10.

[68] L. Landau, "On the multiparticle production in high-energy collisions," *Izv. Akad. Nauk Ser. Fiz.* **17** (1953) 51–64.
Cited on page 10.

[69] P. F. Kolb and U. W. Heinz, "Hydrodynamic description of ultrarelativistic heavy ion collisions," arXiv:nucl-th/0305084.
Cited on page 10.

[70] B. Schenke, P. Tribedy, and R. Venugopalan, "Fluctuating Glasma initial conditions and flow in heavy ion collisions," *Phys. Rev. Lett.* **108** (2012) 252301, arXiv:1202.6646 [nucl-th].
Cited on page 10.

[71] B. Zhang, C. Ko, B.-A. Li, and Z.-w. Lin, "A multiphase transport model for nuclear collisions at RHIC," *Phys. Rev. C* **61** (2000) 067901, arXiv:nucl-th/9907017.
Cited on page 10.

[72] X.-N. Wang and M. Gyulassy, "HIJING: A Monte Carlo model for multiple jet production in p p, p A and A A collisions," *Phys. Rev. D* **44** (1991) 3501–3516.
Cited on pages 11, 61, and 103.

[73] M. Gyulassy and X.-N. Wang, "HIJING 1.0: A Monte Carlo program for parton and particle production in high-energy hadronic and nuclear collisions," *Comput. Phys. Commun.* **83** (1994) 307, arXiv:nucl-th/9502021.
Cited on pages 11, 61, and 103.

[74] B. Zhang, "ZPC 1.0.1: A Parton cascade for ultrarelativistic heavy ion collisions," *Comput. Phys. Commun.* **109** (1998) 193–206, arXiv:nucl-th/9709009.
Cited on page 11.

[75] L. Yan, "A flow paradigm in heavy-ion collisions," *Chin. Phys. C* **42** no. 4, (2018) 042001, arXiv:1712.04580 [nucl-th].
Cited on pages 11, 12, and 13.

[76] P. Sorensen, "Implications of space-momentum correlations and geometric fluctuations in heavy-ion collisions," *J. Phys. G* **37** (2010) 094011, arXiv:1002.4878 [nucl-ex].
Cited on page 11.

[77] B. Alver and G. Roland, "Collision geometry fluctuations and triangular flow in heavy-ion collisions," *Phys. Rev. C* **81** (2010) 054905, arXiv:1003.0194 [nucl-th]. [Erratum: Phys.Rev.C 82, 039903 (2010)].
Cited on pages 11 and 16.

[78] D. Teaney and L. Yan, "Triangularity and dipole asymmetry in relativistic heavy ion collisions," *Phys. Rev. C* **83** (2011) 064904.
Cited on page 11.

[79] R. S. Bhalerao, M. Luzum, and J.-Y. Ollitrault, "Determining initial-state fluctuations from flow measurements in heavy-ion collisions," *Phys. Rev. C* **84** (2011) 034910, arXiv:1104.4740 [nucl-th].
Cited on pages 11, 13, and 25.

[80] J.-Y. Ollitrault, "Anisotropy as a signature of transverse collective flow," *Phys. Rev. D* **46** (1992) 229–245.
Cited on pages 11 and 12.

[81] R. Nouicer, "New State of Nuclear Matter: Nearly Perfect Fluid of Quarks and Gluons in Heavy Ion Collisions at RHIC Energies," *Eur. Phys. J. Plus* **131** no. 3, (2016) 70, arXiv:1512.08993 [nucl-ex].
Cited on page 12.

[82] M. Luzum, "Flow fluctuations and long-range correlations: elliptic flow and beyond," *J. Phys. G* **38** (2011) 124026, arXiv:1107.0592 [nucl-th].
Cited on page 13.

[83] N. Borghini, P. M. Dinh, and J.-Y. Ollitrault, "Flow analysis from multiparticle azimuthal correlations," *Phys. Rev. C* **64** (2001) 054901, arXiv:nucl-th/0105040.
Cited on pages 12, 17, 24, and 29.

[84] **ALICE** Collaboration, S. Acharya *et al.*, "Non-linear flow modes of identified particles in Pb-Pb collisions at $\sqrt{s_{\mathrm{NN}}} = 5.02$ TeV," *JHEP* **06** (2020) 147, arXiv:1912.00740 [nucl-ex].
Cited on page 13.

[85] **ALICE** Collaboration, S. Acharya *et al.*, "Linear and non-linear flow modes of charged hadrons in Pb-Pb collisions at $\sqrt{s_{\mathrm{NN}}} = 5.02$ TeV," *JHEP* **05** (2020) 085, arXiv:2002.00633 [nucl-ex].
Cited on page 13.

[86] H. Niemi, G. Denicol, H. Holopainen, and P. Huovinen, "Event-by-event distributions of azimuthal asymmetries in ultrarelativistic heavy-ion collisions," *Phys. Rev. C* **87** no. 5, (2013) 054901, arXiv:1212.1008 [nucl-th].
Cited on pages 14 and 18.

[87] D. Teaney and L. Yan, "Non linearities in the harmonic spectrum of heavy ion collisions with ideal and viscous hydrodynamics," *Phys. Rev. C* **86** (2012) 044908, arXiv:1206.1905 [nucl-th].
Cited on page 13.

[88] S. Voloshin and Y. Zhang, "Flow study in relativistic nuclear collisions by Fourier expansion of Azimuthal particle distributions," *Z. Phys. C* **70** (1996) 665–672, arXiv:hep-ph/9407282.
Cited on pages 13 and 14.

[89] A. M. Poskanzer and S. A. Voloshin, "Methods for analyzing anisotropic flow in relativistic nuclear collisions," *Phys. Rev. C* **58** (1998) 1671–1678, arXiv:nucl-ex/9805001.
Cited on pages 14 and 23.

[90] H. Gutbrod, B. Kolb, H. Schmidt, A. M. Poskanzer, H. Ritter, and K. Kampert, "A New Component of the Collective Flow in Relativistic Heavy Ion Collisions," *Phys. Lett. B* **216** (1989) 267–271.
Cited on page 15.

[91] D. Brill *et al.*, "Azimuthally anisotropic emission of pions in symmetric heavy ion collisions," *Phys. Rev. Lett.* **71** (1993) 336–339.
Cited on page 15.

[92] **E877** Collaboration, J. Barrette *et al.*, "Energy and charged particle flow in a 10.8-A/GeV/c Au + Au collisions," *Phys. Rev. C* **55** (1997) 1420–1430, arXiv:nucl-ex/9610006. [Erratum: Phys.Rev.C 56, 2336–2336 (1997)].
Cited on pages 15 and 17.

[93] **NA49** Collaboration, H. Appelshauser *et al.*, "Directed and elliptic flow in 158-GeV / nucleon Pb + Pb collisions," *Phys. Rev. Lett.* **80** (1998) 4136–4140, arXiv:nucl-ex/9711001.
Cited on page 15.

[94] **WA98** Collaboration, M. Aggarwal *et al.*, "Collective flow in 158-A-GeV Pb + Pb collisions," *Nucl. Phys. A* **638** (1998) 459–462.
Cited on page 15.

[95] **E895** Collaboration, C. Pinkenburg *et al.*, "Elliptic flow: Transition from out-of-plane to in-plane emission in Au + Au collisions," *Phys. Rev. Lett.* **83** (1999) 1295–1298, arXiv:nucl-ex/9903010.
Cited on page 15.

[96] **NA49** Collaboration, A. M. Poskanzer *et al.*, "Centrality dependence of directed and elliptic flow at the SPS," *Nucl. Phys. A* **661** (1999) 341–344, arXiv:nucl-ex/9906013.
Cited on page 15.

[97] **FOPI** Collaboration, N. Bastid, "Results from FOPI on nuclear collective flow in heavy ion collisions at SIS energies," *AIP Conf. Proc.* **610** no. 1, (2002) 546–550.
Cited on page 15.

[98] J.-Y. Ollitrault, "Determination of the reaction plane in ultrarelativistic nuclear collisions," *Phys. Rev. D* **48** (1993) 1132–1139, arXiv:hep-ph/9303247.
Cited on page 15.

[99] P. F. Kolb, "v_4 : a small, but sensitive observable for heavy ion collisions," *Phys. Rev. C* **68** (2003) 031902.
Cited on page 16.

[100] **STAR** Collaboration, J. Adams *et al.*, "Azimuthal anisotropy at RHIC: The First and fourth harmonics," *Phys. Rev. Lett.* **92** (2004) 062301, arXiv:nucl-ex/0310029.
Cited on pages 16 and 17.

[101] **ALICE** Collaboration, K. Aamodt *et al.*, "Higher harmonic anisotropic flow measurements of charged particles in Pb-Pb collisions at $\sqrt{s_{NN}}$=2.76 TeV," *Phys. Rev. Lett.* **107** (2011) 032301, arXiv:1105.3865 [nucl-ex].
Cited on pages 16 and 18.

[102] N. Borghini, P. M. Dinh, and J.-Y. Ollitrault, "New method for measuring azimuthal distributions in nucleus-nucleus collisions," *Phys. Rev. C* **63** (2001) 054906, arXiv:nucl-th/0007063.
Cited on pages 17, 24, 28, 29, and 30.

[103] N. Borghini, P. M. Dinh, and J.-Y. Ollitrault, "Flow analysis from cumulants: A Practical guide," in *International Workshop on the Physics of the Quark Gluon Plasma*. 10, 2001. arXiv:nucl-ex/0110016.
Cited on pages 17 and 29.

[104] **NA49** Collaboration, C. Alt *et al.*, "Directed and elliptic flow of charged pions and protons in Pb + Pb collisions at 40-A-GeV and 158-A-GeV," *Phys. Rev. C* **68** (2003) 034903, arXiv:nucl-ex/0303001.
Cited on page 17.

[105] **PHENIX** Collaboration, S. Afanasiev *et al.*, "Systematic Studies of Elliptic Flow Measurements in Au+Au Collisions at s**(1/2) = 200-GeV," *Phys. Rev. C* **80** (2009) 024909, arXiv:0905.1070 [nucl-ex].
Cited on page 17.

[106] **PHENIX** Collaboration, A. Adare *et al.*, "Measurements of Higher-Order Flow Harmonics in Au+Au Collisions at $\sqrt{s_{NN}}$ = 200 GeV," *Phys. Rev. Lett.* **107** (2011) 252301, arXiv:1105.3928 [nucl-ex].
Cited on page 17.

[107] **ATLAS** Collaboration, G. Aad *et al.*, "Measurement of event-plane correlations in $\sqrt{s_{NN}}$ = 2.76 TeV lead-lead collisions with the ATLAS detector," *Phys. Rev. C* **90** no. 2, (2014) 024905, arXiv:1403.0489 [hep-ex].
Cited on pages 17 and 19.

[108] A. Bilandzic, M. Lesch, and S. F. Taghavi, "New estimator for symmetry plane correlations in anisotropic flow analyses," *Phys. Rev. C* **102** (2020) 024910, arXiv:2004.01066 [nucl-ex].
Cited on page 17.

[109] P. Huo, J. Jia, and S. Mohapatra, "Elucidating the event-by-event flow fluctuations in heavy-ion collisions via the event shape selection technique," *Phys. Rev. C* **90** no. 2, (2014) 024910, arXiv:1311.7091 [nucl-ex].
Cited on page 18.

[110] A. Bilandzic, C. H. Christensen, K. Gulbrandsen, A. Hansen, and Y. Zhou, "Generic framework for anisotropic flow analyses with multiparticle azimuthal correlations," *Phys. Rev. C* **89** no. 6, (2014) 064904, arXiv:1312.3572 [nucl-ex].
Cited on pages 18, 25, 26, 27, 34, and 73.

[111] J. Schukraft, A. Timmins, and S. A. Voloshin, "Ultra-relativistic nuclear collisions: event shape engineering," *Phys. Lett. B* **719** (2013) 394–398, arXiv:1208.4563 [nucl-ex].
Cited on page 19.

[112] **ATLAS** Collaboration, G. Aad *et al.*, "Measurement of the correlation between flow harmonics of different order in lead-lead collisions at $\sqrt{s_{NN}}$=2.76 TeV with the ATLAS detector," *Phys. Rev. C* **92** no. 3, (2015) 034903, arXiv:1504.01289 [hep-ex].
Cited on page 19.

[113] **ATLAS** Collaboration, S. Radhakrishnan, "Measurement of the correlation between flow harmonics of different order in lead–lead collisions at $\sqrt{s_{NN}}$=2.76 TeV with ATLAS," *Nucl. Phys. A* **956** (2016) 328–331.
Cited on page 19.

[114] **ALICE** Collaboration, J. Adam *et al.*, "Correlated event-by-event fluctuations of flow harmonics in Pb-Pb collisions at $\sqrt{s_{\rm NN}} = 2.76$ TeV," *Phys. Rev. Lett.* **117** (2016) 182301, arXiv:1604.07663 [nucl-ex].
Cited on pages 19, 20, 33, 34, 81, 84, 91, 93, 94, 95, 104, and 106.

[115] **ALICE** Collaboration, Y. Zhou, "Measurements of correlations of anisotropic flow harmonics in Pb–Pb Collisions with ALICE," *Nucl. Phys. A* **956** (2016) 296–299, arXiv:1512.05397 [nucl-ex].
Cited on page 19.

[116] **ALICE** Collaboration, S. Acharya *et al.*, "Systematic studies of correlations between different order flow harmonics in Pb-Pb collisions at $\sqrt{s_{\rm NN}} = 2.76$ TeV," *Phys. Rev. C* **97** no. 2, (2018) 024906, arXiv:1709.01127 [nucl-ex].
Cited on pages 19, 33, 81, 104, 106, and 108.

[117] C. Mordasini, A. Bilandzic, D. Karakoç, and S. F. Taghavi, "Higher order Symmetric Cumulants," *Phys. Rev. C* **102** (2020) 024907, arXiv:1901.06968 [nucl-ex].
Cited on pages 19, 28, 47, 48, 50, 51, 53, 54, 55, 61, 62, and 105.

[118] H. Niemi, K. Eskola, and R. Paatelainen, "Event-by-event fluctuations in a perturbative QCD + saturation + hydrodynamics model: Determining QCD matter shear viscosity in ultrarelativistic heavy-ion collisions," *Phys. Rev. C* **93** no. 2, (2016) 024907, arXiv:1505.02677 [hep-ph].
Cited on pages 19, 20, and 104.

[119] J. Jia, "Event-shape fluctuations and flow correlations in ultra-relativistic heavy-ion collisions," *J. Phys. G* **41** no. 12, (2014) 124003, arXiv:1407.6057 [nucl-ex].
Cited on page 21.

[120] A. Bilandzic, N. van der Kolk, J.-Y. Ollitrault, and R. Snellings, "Event-plane flow analysis without non-flow effects," *Phys. Rev. C* **83** (2011) 014909, arXiv:0801.3915 [nucl-ex].
Cited on page 23.

[121] A. Bilandzic, R. Snellings, and S. Voloshin, "Flow analysis with cumulants: Direct calculations," *Phys. Rev. C* **83** (2011) 044913, arXiv:1010.0233 [nucl-ex].
Cited on pages 27 and 54.

[122] P. M. Dinh, N. Borghini, and J.-Y. Ollitrault, "Effects of HBT correlations on flow measurements," *Phys. Lett. B* **477** (2000) 51–58, arXiv:nucl-th/9912013.
Cited on page 28.

[123] N. Borghini, P. M. Dinh, and J.-Y. Ollitrault, "Are flow measurements at SPS reliable?," *Phys. Rev. C* **62** (2000) 034902, arXiv:nucl-th/0004026.
Cited on page 28.

[124] R. Kubo, "Generalized Cumulant Expansion Method," *Journal of the Physical Society of Japan* **17** no. 7, (1962) 1100–1120.
Cited on pages 30, 47, and 48.

[125] A. Bilandzic, M. Lesch, C. Mordasini, and S. F. Taghavi, "Multivariate cumulants in flow analyses: The Next Generation," arXiv:2101.05619 [physics.data-an].
Cited on pages 30, 31, 47, 48, 79, 109, 110, 111, 112, 113, 114, and 115.

[126] **ALICE** Collaboration, K. Aamodt *et al.*, "Elliptic flow of charged particles in Pb-Pb collisions at 2.76 TeV," *Phys. Rev. Lett.* **105** (2010) 252302, arXiv:1011.3914 [nucl-ex].
Cited on pages 33 and 93.

[127] L. Evans and P. Bryant, "LHC Machine," *JINST* **3** (2008) S08001.
Cited on pages 35 and 36.

[128] CERN, "Where did it all begin?."
https://home.cern/about/who-we-are/our-history.
Cited on page 35.

[129] C. P. Office, "CERN Accelerating science," 2017.
https://home.cern/resources/brochure/cern/lhc-guide.
Cited on pages 35 and 36.

[130] J. Wozniak, "The Architecture of the Next CERN Accelerator Logging Service - The Databricks Blog," *Databricks* (2017) . https://databricks.com/blog/2017/12/14/the-architecture-of-the-next-cern-accelerator-logging-service.html.
Cited on page 36.

[131] W. Herr and B. Muratori, "Concept of luminosity,".
https://cds.cern.ch/record/941318.
Cited on page 37.

[132] "About the ATLAS Experiment," 2019. https://atlas.cern/discover/about.
Cited on page 37.

[133] **CMS** Collaboration, "CMS personal webpage." https://cms.cern/.
Cited on page 37.

[134] **LHCb** Collaboration, "LHCb - Large Hadron Collider beauty experiment."
http://lhcb-public.web.cern.ch/.
Cited on page 37.

[135] "LHCf." https://home.cern/science/experiments/lhcf.
Cited on page 37.

[136] "TOTEM." https://home.cern/fr/science/experiments/totem.
Cited on page 37.

[137] "MoEDAL." https://home.cern/fr/science/experiments/moedal.
Cited on page 37.

[138] **ALICE** Collaboration, P. Cortese *et al.*, "ALICE: Physics performance report, volume I," *J. Phys. G* **30** (2004) 1517–1763.
Cited on pages 37, 38, 39, 40, 41, 42, and 44.

[139] **ALICE** Collaboration, C. W. Fabjan *et al.*, "ALICE: Physics performance report, volume II," *J. Phys. G* **32** (2006) 1295–2040.
Cited on pages 37 and 46.

[140] **ALICE** Collaboration, K. Aamodt *et al.*, "The ALICE experiment at the CERN LHC," *Journal of Instrumentation* **3** no. 08, (2008) S08002–S08002.
Cited on pages 37, 38, 39, 45, and 46.

[141] **ALICE** Collaboration, Y. Kharlov, "Physics with the ALICE experiment," *Phys. Atom. Nucl.* **76** (2013) 1497–1506, arXiv:1203.1984 [nucl-ex].
Cited on page 37.

[142] A. Kalweit, "Highlights from the ALICE experiment," *Nucl. Phys. A* **982** (2019) 1–7.
Cited on page 37.

[143] "3D ALICE Schematic RUN2 - with Description."
https://alice-figure.web.cern.ch/.
Cited on page 38.

[144] **ALICE** Collaboration, K. Aamodt *et al.*, "Alignment of the ALICE Inner Tracking System with cosmic-ray tracks," *JINST* **5** (2010) P03003, arXiv:1001.0502 [physics.ins-det].
Cited on pages 39 and 40.

[145] **ALICE** Collaboration, "Upgrade of the ALICE Time Projection Chamber," Tech. Rep. CERN-LHCC-2013-020. ALICE-TDR-016, 2013.
https://cds.cern.ch/record/1622286.
Cited on page 41.

[146] **ALICE TPC** Collaboration, P. Gasik, "Development of GEM-based Read-Out Chambers for the upgrade of the ALICE TPC," *JINST* **9** (2014) C04035.
Cited on page 42.

[147] **ALICE TPC** Collaboration, M. Aggarwal *et al.*, "Particle identification studies with a full-size 4-GEM prototype for the ALICE TPC upgrade," *Nucl. Instrum. Meth. A* **903** (2018) 215–223, arXiv:1805.03234 [physics.ins-det].
Cited on page 42.

[148] **ALICE** Collaboration, E. Abbas *et al.*, "Performance of the ALICE VZERO system," *JINST* **8** (2013) P10016, arXiv:1306.3130 [nucl-ex].
Cited on pages 42 and 43.

[149] **ALICE** Collaboration, K. Aamodt *et al.*, "Centrality dependence of the charged-particle multiplicity density at midrapidity in pb-pb collisions at $\sqrt{s_{\mathrm{NN}}} = 2.76$ TeV," *Phys. Rev. Lett.* **106** (2011) 032301.
Cited on page 43.

[150] I. Altsybeev and V. Kovalenko, "Classifiers for centrality determination in proton-nucleus and nucleus-nucleus collisions," *EPJ Web Conf.* **137** (2017) 11001, arXiv:1612.00312 [physics.data-an].
Cited on pages 43 and 44.

[151] **ALICE** Collaboration, P. Saiz, L. Aphecetche, P. Buncic, R. Piskac, J. E. Revsbech, and V. Sego, "AliEn - ALICE environment on the GRID," *Nucl. Instrum. Meth. A* **502** (2003) 437–440.
Cited on page 45.

[152] **ALICE** Collaboration, M. Zimmermann, "The ALICE analysis train system," *J. Phys. Conf. Ser.* **608** no. 1, (2015) 012019, arXiv:1502.06381 [hep-ex].
Cited on page 45.

[153] R. Brun, F. Bruyant, M. Maire, A. C. McPherson, and P. Zanarini, *GEANT 3: user's guide Geant 3.10, Geant 3.11; rev. version.* CERN, Geneva, 1987.
https://cds.cern.ch/record/1119728.
Cited on page 45.

[154] **GEANT4** Collaboration, S. Agostinelli *et al.*, "GEANT4–a simulation toolkit," *Nucl. Instrum. Meth. A* **506** (2003) 250–303.
Cited on page 45.

[155] **ALICE** Collaboration, I. Hrivnacova, O. Datskova, A. Gheata, A. Morsch, and E. Sicking, "The ALICE Geant4 simulation," *J. Phys. Conf. Ser.* **331** (2011) 032016.
Cited on page 45.

[156] M. Richter, M. Krzewicki, and G. Eulisse, "Data handling in the alice o2 event processing," *EPJ Web of Conferences* **214** (2019) 01035.
Cited on page 46.

[157] C. Mordasini, "Extended Studies on Asymmetric Cumulants,". In preparation.
Cited on pages 47, 71, 72, 73, 74, 75, 77, 78, 79, and 109.

[158] Wolfram Research, Inc., "Mathematica, Version 12.1."
https://www.wolfram.com/mathematica. Champaign, IL, 2020.
Cited on pages 53 and 71.

[159] S. F. Taghavi, "One Package For All Multi-Harmonic Cumulants,"
arXiv:2005.04742 [nucl-th].
Cited on page 66.

[160] Z. Moravcova, K. Gulbrandsen, and Y. Zhou, "Generic algorithm for multi-particle cumulants of azimuthal correlations in high energy nucleus collisions,"
arXiv:2005.07974 [nucl-th].
Cited on page 67.

[161] **ALICE** Collaboration, A. Toia, "Bulk Properties of Pb-Pb collisions at $\sqrt{s_{NN}} = 2.76$ TeV measured by ALICE," *J. Phys. G* **38** (2011) 124007, arXiv:1107.1973 [nucl-ex].
Cited on page 82.

[162] **ALICE** Collaboration, B. Abelev *et al.*, "Centrality determination of Pb-Pb collisions at $\sqrt{s_{NN}} = 2.76$ TeV with ALICE," *Phys. Rev. C* **88** no. 4, (2013) 044909, arXiv:1301.4361 [nucl-ex].
Cited on pages 82 and 105.

[163] **ALICE** Collaboration, B. B. Abelev *et al.*, "Performance of the ALICE Experiment at the CERN LHC," *Int. J. Mod. Phys. A* **29** (2014) 1430044, arXiv:1402.4476 [nucl-ex].
Cited on page 89.

[164] R. J. Barlow, *Statistics: A Guide to the Use of Statistical Methods in the Physical Sciences (Manchester Physics Series)*. WileyBlackwell, reprint ed., 1989.
Cited on page 95.

[165] R. Barlow, "Systematic errors: Facts and fictions," in *Conference on Advanced Statistical Techniques in Particle Physics*, pp. 134–144. 2002. arXiv:hep-ex/0207026.
Cited on page 95.

[166] G. Cowan, *Statistical Data Analysis*. Clarendon (Oxford), Oxford, 1998 (ISBN: 0-19-850156-0 or 0-19-850155-2 in paperback).
Cited on page 96.

[167] C. Mordasini, "Multi-harmonic correlations in ALICE," *ALICE Public & Analysis Notes* (2021) . https://alice-notes.web.cern.ch/node/969.
Cited on pages 97 and 131.

[168] K. Eskola, K. Kajantie, P. Ruuskanen, and K. Tuominen, "Scaling of transverse energies and multiplicities with atomic number and energy in ultrarelativistic nuclear collisions," *Nucl. Phys. B* **570** (2000) 379–389, arXiv:hep-ph/9909456.
Cited on page 104.

[169] **ALICE** Collaboration, S. Acharya *et al.*, "Event-by-event multi-harmonic correlations of different flow amplitudes in Pb-Pb collisions at $\sqrt{s_{\rm NN}} = 2.76$ TeV," arXiv:2101.02579 [nucl-ex].
Cited on pages 104, 105, 106, 107, 109, and 129.

[170] J. S. Moreland, J. E. Bernhard, and S. A. Bass, "Alternative ansatz to wounded nucleon and binary collision scaling in high-energy nuclear collisions," *Phys. Rev. C* **92** no. 1, (2015) 011901, arXiv:1412.4708 [nucl-th].
Cited on page 104.

[171] C. Shen, Z. Qiu, H. Song, J. Bernhard, S. Bass, and U. Heinz, "The iEBE-VISHNU code package for relativistic heavy-ion collisions," *Comput. Phys. Commun.* **199** (2016) 61–85, arXiv:1409.8164 [nucl-th].
Cited on page 105.

[172] P. Huovinen and P. Petreczky, "QCD Equation of State and Hadron Resonance Gas," *Nucl. Phys. A* **837** (2010) 26–53, arXiv:0912.2541 [hep-ph].
Cited on page 105.

[173] F. Cooper and G. Frye, "Comment on the Single Particle Distribution in the Hydrodynamic and Statistical Thermodynamic Models of Multiparticle Production," *Phys. Rev. D* **10** (1974) 186.
Cited on page 105.

[174] S. Bass *et al.*, "Microscopic models for ultrarelativistic heavy ion collisions," *Prog. Part. Nucl. Phys.* **41** (1998) 255–369, arXiv:nucl-th/9803035.
Cited on page 105.

[175] M. Bleicher *et al.*, "Relativistic hadron hadron collisions in the ultrarelativistic quantum molecular dynamics model," *J. Phys. G* **25** (1999) 1859–1896, arXiv:hep-ph/9909407.
Cited on page 105.

[176] M. Lesch, "Symmetry-planes correlations in flow analyses," 2019. https://www.das.ktas.ph.tum.de/DasDocs/Public/Bachelor_Theses/MarcelLesch_bachelor.pdf.
Bachelor thesis.
Cited on page 105.

[177] **ALICE** Collaboration, "Centrality determination in heavy ion collisions,". http://cds.cern.ch/record/2636623.
Cited on page 105.

[178] L. Yan and J.-Y. Ollitrault, "$\nu_4, \nu_5, \nu_6, \nu_7$: nonlinear hydrodynamic response versus LHC data," *Phys. Lett. B* **744** (2015) 82–87, arXiv:1502.02502 [nucl-th].
Cited on page 106.